学位論文

Probing Cosmic Dark Matter and Dark Energy with Weak Gravitational Lensing Statistics

(弱重力レンズ統計を用いた暗黒エネルギーと暗黒物質の観測的検証)

平成 26 年 12 月博士 (理学) 申請

東京大学大学院理学系研究科
物理学専攻
白崎正人

Abstract

An array of recent astrophysical observations established the standard cosmological model called ΛCDM model. The energy content of the present-day universe is dominated by dark energy and dark matter and its nature and physical properties are not known. In order to reveal the mysterious dark components in the universe, several observational programs are proposed and still in research. Gravitational lensing is expected to be the main subject in future cosmology surveys for constraints on cosmological parameters, which provide important clues to the dark components in the universe.

Gravitational lensing is a powerful method to study matter distribution in the universe, from which one can extract information on the basic cosmological parameters. However, the statistical method to make the best use of gravitational lensing data in upcoming surveys is still under debate. This problem originates from non-Gaussianity of the matter density field due to non-linear gravitational growth. In this thesis, we explore the applicability and the utility of two statistical approaches for understanding dark matter and dark energy with gravitational lensing measurement.

For cosmological constraints related to the nature of dark energy, we study morphological statistics called Minkowski functionals (MFs) to extract the non-Gaussian information of gravitational lensing using numerical simulations and observational data. We find that systematic effects in observation need to be well-calibrated in using MFs, although MFs can be a powerful statistics beyond the conventional approach with two-point correlation function for cosmological constraints. We then put a constraint on mean matter density in the present universe with lensing MFs measured from Canada-France-Hawaii Telescope Lensing survey (CFHTLenS). We also make the forecast on the nature of dark energy with MFs in upcoming surveys with sky coverage of 20,000 square degrees. Combined with two-point correlation function, MFs can constrain the equation of state of dark energy with a precision level of ∼3-4%.

In order to constrain the properties of dark matter, we study the cross-correlation of gravitational lensing and another possible probe of dark matter distribution, the extragalactic gamma-ray background (EGB). Dark matter annihilation is among the potential contributors to the EGB. The cross-correlation is a powerful probe of signatures of dark matter annihilation, because both gravitational lensing and gamma-ray emission originate directly from the same DM distribution in the universe. Therefore, measurement of the cross-correlation can be used to derive constraints on dark matter annihilation cross-section. We perform the first measurement of the cross-correlation using the real data set obtained from CFHTLenS and the Fermi Large Area Telescope. We find that the measured cross-correlation is consistent with a null signal. Comparing the result to theoretical predictions based on structure formation, we place an independent constraint on dark matter annihilation. We also show that future lensing surveys will increase sensitivity to probe annihilation cross section and be useful to constrain on the canonical value of annihilation cross section for wide range of mass of dark matter.

Acknowledgements

I am grateful to my supervisor Professor Naoki Yoshida for his continuous support and encouragement. Through fruitful discussions with him, I have learned many things in cosmology, astrophysics, data analysis, and computational skills. He originally led me to the interesting research area, observational cosmology. I also would like to express special thanks to my collaborators, Takashi Hamana and Shunsaku Horiuchi. If it had not been for their kindly support and useful discussions with them, I could not have completed this thesis. I would like to thank Masahiro Takada, Chiaki Hikage, Masayuki Tanaka, Kazuhiro Nakazawa, and Zoltan Haiman for useful and helpful discussions. Masanori Sato kindly provided us with their ray-tracing simulations data. I am thankful to all of members of in Kavli Institute for the Physics and Mathematics of the Universe (Kavli IPMU), the University of Tokyo Theoretical Astrophysics Group (UTAP) and Research Center for the Early Universe (RESCEU).

My graduate research is supported by Research Fellowships of the Japan Society for the Promotion of Science (JSPS) for Young Scientists. Numerical computations presented in this thesis were in part carried out on the general-purpose PC farm at Center for Computational Astrophysics, CfCA, of National Astronomical Observatory of Japan. The analysis presented in this thesis is based on observations obtained with MegaPrime/MegaCam, a joint project of CFHT and CEA/IRFU, at the Canada-France-Hawaii Telescope (CFHT) which is operated by the National Research Council (NRC) of Canada, the Institut National des Sciences de l'Univers of the Centre National de la Recherche Scientifique (CNRS) of France, and the University of Hawaii. The research used the facilities of the Canadian Astronomy Data Centre operated by the National Research Council of Canada with the support of the Canadian Space Agency. CFHTLenS data processing was made possible thanks to significant computing support from the NSERC Research Tools and Instruments grant program.

Finally, I wish to thank my father, my mother, my sister and all my friends who have supported me.

Contents

List of Figures

List of Tables

Chapter 1

Introduction

1.1 Cosmic Acceleration

In 1917, Albert Einstein first considered the cosmological model with his theory of General Relativity [4]. There, he adopted the simple assumptions: the universe would be static and homogeneous on large scales. In order to realize the static universe with a matter-filled space, he introduced the additional constant in the field equation, which is so-called the *cosmological constant*. Is the cosmological constant really needed in order to make the universe static? This question have been answered by the discovery of the expanding universe [5]. In 1929, Edwin Hubble reported the relation of distance and radial velocity among galaxies. His finding is summarized as

$$cz = H_0 d, \tag{1.1}$$

where c is light speed, d represents the distance to galaxy and z is the redshift of galaxy. H_0 is some constant number known as Hubble constant. Since cz corresponds to the radial velocity of galaxy moving away from us, the coherent motion of galaxies discovered by Hubble provided the evidence of the expansion of the universe. Therefore, the original motivation to introduce the cosmological constant were removed at that time. The situation, however, have been changed as the observational cosmology developed. To tell the truth, a number of observational studies indicates that the expansion of the universe is *accelerating*. Such observational results seem to be in conflict with the simple cosmological model without the cosmological constant. In this chapter, we summarize the representative observational results which revealed the cosmic acceleration.

1.1.1 Type Ia supernovae

Supernova is one of the most energetic phenomena in the universe, which is thought to occur late in life of a massive star. Type Ia supernovae are among the most interesting supernovae in context of observational cosmology. Type Ia supernovae have no absorption line of hydrogen with the presence of silicon in their spectrum. A white dwarf in a binary system can increase its mass by up to the Chandrasekhar mass limit with accretion from a binary companion or the merger of two white dwarfs. Once its mass exceeds the Chandrasekhar mass, gravitational collapse induces a runaway fusion reaction and leads to complete explosion of the white dwarf, that is Type Ia supernova.

The absolute magnitude of Type Ia supernovae at peak luminosity is roughly constant with some dispersion (e.g., [6, 7, 8]). The observed dispersion can be reduced by the novel technique based on the empirical correlation between the intrinsic magnitude and the shape of light curve (i.e. more luminous supernovae tend to decline its luminosity slower [9]). These results guarantee the usefulness of Type Ia supernovae as *standard candle*, which enable us to measure the distance precisely. With appropriate corrections (e.g., dust extinction, K-correction for redshifting effect, and so on), the observational programs have been conducted on for measuring the distance of Type Ia supernovae at higher redshift [10, 11].

Effort is rewarded. The two independent detailed analysis of tens of Type Ia supernovae at cosmological redshifts have been utilized to measure the luminosity distance of those objects [12, 13]. Their conclusion is that a universe curved by ordinary matter (the simple expectation from Ref. [5]) is ruled out at high significance. The observed luminosity distances can be explained by the cosmological model with ordinary matter *and* the cosmological constant.

1.1.2 Baryon acoustic oscillations

According to the discovery by Hubble [5], the early universe should be in the state of very large matter density and very high temperature. The model with such initial state of a universe is so called Big-Bang cosmology. In the Big-Bang cosmology, baryons and photons had experienced non-thermal processes as the universe expands or the temperature of radiation decreases [14]. Once electron and proton combined to form hydrogen atom, photons were able to travel through the space, i.e. the universe become transparent [15]. This epoch is called recombination epoch. Thus, the photon emitted when hydrogen atom formed contains the information of the earliest universe that we can observe from measurements of radiation field. This last-scattered photon is currently

called cosmic microwave background (CMB), which is one of the essential pieces of the Big-Bang cosmology.

At last scattering surface where CMB photons were released, there remains various interesting features in spatial variation of CMB temperature [16]. Baryonic acoustic oscillation is an example illustrative of the property of CMB photons. Before hydrogen atom formed, a photon-baryon fluid had played an important role to determine the dynamics of the universe. When the primeval fluctuations exist in the fluid, gravity affects the growth of perturbation, whereas radiation pressure resists. This simple framework finally induces the acoustic waves in the photon-baryon fluid, and the oscillating feature on the anisotropy of CMB sky. The oscillation have been actually conformed by CMB analysis in harmonic space (e.g., [17]). The characteristic scale of acoustic oscillation is determined by the sound horizon of the photon-baryon fluid at last scattering surface. Thus, the sound horizon at last scattering surface can be measured by the detailed analysis of CMB temperature anisotropy.

There exists another tracer of baryonic acoustic oscillation. Galaxies are expected to form in high matter density region where matter have been assembled initially. Since baryons have experienced acoustic oscillation in the early universe and should be abound at the acoustic peak, galaxy clustering would also show imprint of baryonic acoustic oscillation. SDSS collaboration [18] performed the correlation analysis of 46,748 galaxies and clearly detected the feature of the acoustic peak in galaxy correlation function. With the sound horizon measured from CMB, we can regard the acoustic peak found in galaxy clustering as *standard ruler*. The idea is very simple; ruler looks smaller as it is more distant. Considering two different cases where ruler locates enables us to determine the expansion rate of the universe. The current measurement of CMB (e.g., [19]) and galaxy clustering (e.g., [20]) is in favor with the presence of the cosmological constant.

1.2 Astrophysical Evidence of Dark Matter

First astrophysical implication on the existence of *dark* matter is found in Ref. [21]. Fritz Zwicky analyzed the velocity dispersion of galaxies in the Coma cluster and estimated the mass in the system from the virial theorem. He found that the ratio of mass and luminosity of member galaxies in this system to be ~ 400 solar masses per solar luminosity, which is larger than that of the solar neighborhood by a factor of 100. Theoretically, in 1970's, numerical studies (e.g., Ref. [22]) indicated that the existence of dark mass seems to be required for the gravitational stability of the disk of galaxy. Also, the observed anisotropies on cosmic microwave background in 1980's (e.g., [23, 24, 25]) seemed to be inconsistent with the cosmological model which is composed of simple baryonic matter.

Here, we summarize some examples of astrophysical "evidences" of the existence of dark matter (without attempting to be complete). The following astrophysical evidences are one of the reasons why most astronomers believe that dark matter exists *if we can not see it.*

1.2.1 Rotation curves of galaxies

The observation of the 21 cm line of HI clouds in galaxies in 1980's (e.g., [26]) provide us the new insight of matter distribution at galactic scales.

In Newtonian dynamics, the circular velocity of an object with off-centric distance of r is given by

$$v(r) = \sqrt{\frac{GM(r)}{r}}, \tag{1.2}$$

where $M(r)$ is the inner mass which is defined by $M(r) = \int \mathrm{d}r 4\pi r^2 \rho(r)$, and $\rho(r)$ describes the matter density profile in the system of interest. If the measured light distribution would exactly trace the matter distribution in galaxies, the circular velocity would decrease as $\sim \sqrt{1/r}$ beyond the optical disc. However, the observed circular velocity of HI clouds in spiral galaxies reaches to almost constant value as r increases. This is so-called flat rotational curve problem. One of the solution to this problem is to suppose invisible mass distribution in halo region of galaxies. If one assume $M(r) \propto r$ or $\rho(r) \propto r^{-2}$ in outer region, the observed circular velocity can be explained. However, there is another solution of this problem actually. That is the modified Newtonian dynamics (MOND) which can solve the flat rotational curve problem with an appropriate parameter (e.g., [27]). In order to distinguish these two models, we require another observational data which clearly shows the baryonic and dark matter distribution separated. In fact, we have already found such observational data, as known as bullet cluster [28, 29]. We revisit how we know the invisible dark matter distribution later.

1.2.2 Mass estimate of clusters of galaxies

Clusters of galaxies are one of the most important targets in terms of dark matter as Zwicky demonstrated in 1930's [21]. Modern astrophysical techniques enables us to study the mass distribution in clusters of galaxies in more sophisticated ways.

X-ray emission is one of the promising observables to estimate the mass of a galaxy cluster. Suppose the virialized object which holds the thermal equilibrium. In such

system, the virial theorem should hold

$$k_B T_{\rm eq} = \frac{1}{2}\frac{G m_p M_{\rm cl}}{R_{\rm cl}}, \tag{1.3}$$

where m_p is proton mass and $M_{\rm cl}$ and $R_{\rm cl}$ represent the mass and the radius of cluster, respectively. For typical clusters, the virial temperature is given by

$$k_B T_{\rm eq} \sim 2\,{\rm keV}\left(\frac{M_{\rm cl}}{10^{14}\,M_\odot}\right)\left(\frac{R_{\rm cl}}{2\,{\rm Mpc}}\right)^{-1}, \tag{1.4}$$

which corresponds to X-ray. Thus, the observation of the X-ray emission profile of galaxy cluster is aimed at measuring the mass under the hydrostatic equilibrium. Combining with optical luminosity of member galaxies, one can constrain on the mass-to-luminosity ratio over various samples of galaxy clusters (e.g., [30, 31]).

An alternative method for mass estimation is based on gravitational lensing. Gravitational lensing is known as the relativistic effect on trajectory of photon in the universe. According to General Relativity, intervening mass distribution can affect the path of photon emitted from distant objects. This effect would be observed by the distortion of images of source objects, or arc like images in some cases. Thus, the detailed analysis of images of background galaxies behind galaxy clusters can be useful to reconstruct the mass distribution of galaxy clusters itself. Such reconstruction technique are adopted to very interesting system, so-called bullet cluster [28, 29]. Bullet cluster has very unique characteristics of the gas distribution inferred from X-ray observation. It is found that a pair of clusters are colliding and the hot interstellar gas has a shock front. Ref. [29] adopted the mass reconstruction technique to this system and first showed the *direct* evidence of dark matter, of which density distribution clearly separated from gas density distributions.

1.2.3 Global energy budget of universe

Precise measurements of anisotropies on cosmic microwave background (CMB) are one of the most stringent cosmological probes. Although anisotropies in the temperature fluctuation are of a level of 10^{-5}, the physics of CMB can be understood in a simple but robust framework based on General Relativity and fluid dynamics [16]. The expected angular dependence of anisotropies can be well characterized by six parameters, which represent the fundamental quantities. Such parameters include the *mean* matter density and the baryonic matter density of universe. Recent measurement of cosmic microwave background (e.g., [19]) determines the mean density of dark matter and baryonic matter

as follows;

$$\Omega_{\rm cdm}h^2 = 0.1138 \pm 0.0045, \tag{1.5}$$

$$\Omega_{\rm b}h^2 = 0.02264 \pm 0.00050, \tag{1.6}$$

where the former represents the (normalized) mean density of dark matter and the latter is for baryonic matter. These results indicate that we must consider the non-baryonic matter to explain the observed CMB anisotropies and the significance of the existence of dark matter is $0.1138/0.0045 \sim 25\sigma$.

1.3 Cosmology with Gravitational Lensing

Entering the twenty-first century, technological progress enables us to conduct wider and/or deeper surveys. Statistical analysis with a huge sample reveals the dynamics (e.g., [32, 33]) and the composition (e.g., [19, 34, 35]), of the universe.

The "standard" cosmological model called ΛCDM model is currently consistent with the observational results[1]. In this concordance model, an exotic form of energy, now called dark energy, dominates the present universe and causes the cosmic acceleration. If dark energy density does not evolve in time as the universe expands, such energy is essentially equivalent to the cosmological constant introduced by Einstein. Dark matter is invisible mass and is considered to be a different form from normal matter like stars and planets. A large part of galaxy and cluster of galaxies seems to be made up of dark matter. Dark matter plays an important role in the formation of rich structure in the universe.

Next goal of observational cosmology is, probably, to understand the nature of dark energy and the physical properties of dark matter. Gravitational lensing is one of the important cosmological tools to tackle the problem.

Gravitational lensing provides a powerful method to probe matter distribution in the universe. Accoording to gravitational lensing, intervening large-scale structures induce small image distortion of distant galaxies. The small distortion is called cosmic shear which contains, in principle, rich information on the matter distribution at small and large scales. Gravitational lensing also has the advantage of not requiring any assumptions such as the relation between luminosity and mass and/or hydrostatic equilibrium. This indicates that it is an optimal tool to investigate dark matter distribution in the universe. The strength of lensing effect is also sensitive to the distance to background

[1] At small scale (less than galactic scales), the validity of ΛCDM model is controversial (see, e.g., [36] for review).

galaxies and lensing objects. It can thus be utilized to provide the meaningful information of both expansion history and gravitational growth of structure in the universe.

Although cosmic shear contains rich cosmological information, image distortion induced by gravitational lensing is very small in general. Therefore, we need the statistical analysis of cosmic shear signal over a large number of distant galaxies in order to extract cosmological information from gravitational lensing. The conventional statistics of cosmic shear are two-point correlation function or power spectrum. If the statistical property of cosmic shear field follows Gaussian, this quantity can describe all the information of cosmic shear. However, this is not the case in reality because cosmic shear has non-Gaussian information either of primordial origin (e.g., [37]) or caused by non-linear gravitational growth [38]. We have not understood yet how to make the best use of gravitational lensing for constraints on the nature of dark energy and dark matter. In this thesis, we explore the applicability and the utility of statistical analyses of gravitational lensing for understanding dark matter and dark energy.

Many proposals are found in literature. The statistical analyses differ between the two classes.

1. *Extension of two-point statistics*

   Ref. [39] shows the prospects of two-point statistics of cosmic shear in terms of measurement of cosmological parameters. Ref. [40] proposed the simple extension of the method in Ref. [39] in order to extract the redshift information of large-scale structure. This methodology is called tomography which causes the improvement of the cosmological parameter estimation due to reconstruction of the structure along the line of sight. Ref. [41] shows the potential contaminant in tomography, called intrinsic alignment. Intrinsic alignment of galaxy's shape could be caused by correlation between the ellipticity of galaxy and the tidal field at large scale. This alignment induces the additional correlation of shape of galaxy between two different redshifts. The impact of intrinsic alignment on two-point statistics of cosmic shear have been investigated with both theoretical (e.g., [42]) and observational method (e.g., [43]). Also, various systematics associated with the shape measurement can affect a cosmic shear analysis [44, 45]

   Another extension is the cross-correlation of the shape of background galaxies and the position of foreground galaxies. This method is called galaxy-galaxy lensing which have been proposed for purpose of measuring galaxy mass [46]. Refs. [47, 48] have recognized this technique as a direct probe of the relation between the mass and the light, as known as galaxy bias. Ref. [49] has derived the constraint on cosmological parameters with combination of the information of galaxy clustering and

galaxy bias estimated from galaxy-galaxy lensing. This combined analysis is another path to extract the dark matter clustering directly. In order to maximize the information content we can gain from this method, more sophisticated algorithm is proposed in Ref. [50] and have been applied to the real data set [51]. Similar method can be applied to observables of clusters of galaxies and the expected cosmological constraints would be comparable with current CMB measurements [52]. Joint analysis of three different statistics (i.e. two point correlation of galaxy, two point correlation of cosmic shear, and galaxy-galaxy lensing) have been studied in e.g., Ref. [53].

2. *Higher-order statistics*

   Cosmic shear contains the information of non-linear gravitational growth as well. This information typically appear as non-Gaussian property of cosmic shear. In order to extract non-Gaussianity of cosmic shear, a promising way is to consider the higher-order statistics beyond two-point statistics.

   Three-point statistics or bispectrum of cosmic shear is one of the candidates. Refs. [54, 55] show that the skewness of lensing field can, in principle, break the degeneracy between cosmological parameter dependences found in two-point statistics of cosmic shear. The cosmological information content in bispectrum of lensing field and the utility of bispectrum tomography with power spectrum have been discussed in Refs. [56, 57].

   Peak statistics in lensing field are also useful to constrain on cosmological parameters. In Ref. [58], the authors utilize a large set of numerical simulations and show that peaks of lensing field can be associated with massive clusters along the line of sight. Thus, number of lensing field peaks would be correlated with number of very massive object in the universe such as galaxy clusters and be sensitive to cosmological parameters [59, 60]. Refs. [61, 62] have investigated cosmological information obtained from combined analysis of peak count and angular correlation of cosmic shear. In addition to number counts, the correlation of peaks and cross correlation of peak and cosmic shear would provide fruitful cosmological information [63]. Some systematical effects in peak statistics have been studied in detail [64, 65, 66].

1.4 Objective of This Thesis

Future lensing surveys are aimed at measuring cosmic shear over a wide area of more than a thousand square degrees. Such ongoing observational programs include Subaru Hyper Suprime-Cam (HSC)[1], the Dark Energy Survey (DES)[2], and the Large Synoptic

Survey Telescope (LSST)[3]. Space missions such as Euclid and WFIRST are also promising. In these programs, the statistical error of shape measurement of galaxies would be improved dramatically. It is therefore crucial to construct the well-calibrated and accurate statistical approach of cosmic shear for providing important clues to the mysterious dark component.

In this thesis, we examine the two different methods of gravitational lensing for constraints on the nature of dark energy and dark matter. Each statistical analysis can be categorized in "higher-order statistics" or "extension of two-point statistics" as we mentioned in Section 1.3.

In order to reveal the nature of dark energy, we study the cosmological information content of morphological statistics of comic shear field, called Minkowski funtionals (MFs). We extend the previous morphological studies by including various observational effects such as sky masking, systematics associated with shape measurement, photometric redshift errors, and shear calibration correction. We generate a large set of mock cosmic shear data with numerical simulations to study possible systematics in detail one by one. We then apply all the methods developed and examined in numerical simulations to the real data obtained by Canada-France-Hawaii Telescope Lensing survey (CFHTLenS).

In order to explore the physical property of dark matter, we study the cross-correlation of cosmic shear and another possible probe of dark matter distribution, the extragalactic gamma-ray background (EGB). The origin of EGB is still unclear and the potential contributors to the EGB includes the emission due to dark matter annihilation. One of the most plausible candidates for dark matter is a weak interacting massive particle (WIMP). WIMP with the mass of 10 GeV – 10 TeV can naturally explain the abundance of dark matter today if their annihilation cross section is the same order as the cross section for weak interaction. If dark matter particles annihilate into standard model particles, they will produce gamma rays that contribute to the observed EGB. The dark matter distribution that causes cosmic shear would also be a gamma-ray source. Thus, the cross-correlation of cosmic shear and the EGB can be a powerful probe of signature of dark matter annihilation. We perform the first measurement of the cross-correlation using the real data set obtained from CFHTLenS and the Fermi Large Area Telescope. Comparing the result to theoretical predictions based on structure formation, we place a *cosmological* constraint on dark matter annihilation with our measurement.

The rest of the thesis is organized as follows. In Chapter 2, we summarize the basics of structure formation. In Chapter 3, we describe the formulation of weak gravitational

[1]http://www.naoj.org/Projects/HSC/j_index.html
[2]http://www.darkenergysurvey.org/
[3]http://www.lsst.org/lsst/

lensing and summarize how to perform statistical analyses with observables. In Chapter 4, we show the results of the impact of observational effects on lensing MFs. Various effects are investigated with numerical simulations and the real data set. The analysis presented in Section 4 is based on Refs. [1, 2]. In Chapter 5, we present the cross correlation analysis of cosmic shear and extragalactic gamma-ray background. We there summarize the detail of theoretical model and methodology. A large part of Section 5 is based on Ref. [3]. Concluding remarks and discussions are given in Chapter 6.

Chapter 2

Structure Formation

2.1 The standard cosmological model

2.1.1 Friedmann equation

The universe has a rich variety of structure. We know that galaxies are made of stars, and galaxies show a tendency to cluster into groups. Clusters of galaxies are a building block of larger structure such as superclusters and filaments. Even though the universe has the hierarchical structure, the matter distribution in the universe on a *sufficient* large scale should be homogenous and isotropic. This assumption is called the cosmological principle. In four space-time dimensions, the Friedmann-Lemaître-Robertson-Walker (FLRW) metric fulfills the requirement of the cosmological principle, i.e. a homogeneity and isotropy of space. This metric is given by

$$\mathrm{d}s^2 = -c^2\mathrm{d}t^2 + a^2(t)\left[\frac{\mathrm{d}r^2}{1-Kr^2} + r^2(\mathrm{d}\theta^2 + \sin^2\theta\mathrm{d}\phi^2)\right], \tag{2.1}$$

where $a(t)$ is the scale factor and K is the spatial curvature of the space. The spatially closed, flat and open universe correspond to the case of $K > 0$, $K = 0$ and $K < 0$, respectively. In the FLRW metric, the scale factor determines the time evolution of the space. In this thesis, we normalize as $a = 1$ at the present. In an expanding universe, it is useful to define the *comoving* distance χ as follows;

$$\mathrm{d}\chi^2 \equiv \frac{\mathrm{d}r^2}{1-Kr^2}. \tag{2.2}$$

With the definition of the comoving distance, the proper distance r is described as a function of χ, which is given by

$$r(\chi) = \begin{cases} \sinh(\sqrt{-K}\chi)/\sqrt{-K} & (K<0) \\ \chi & (K=0) \\ \sin(\sqrt{K}\chi)/\sqrt{K} & (K>0) \end{cases} . \tag{2.3}$$

The time evolution of $a(t)$ can be determined by the Einstein equations;

$$G_{\mu\nu} = R_{\mu\nu} - \left(\frac{1}{2}R - \Lambda\right) g_{\mu\nu} = \frac{8\pi G}{c^4} T_{\mu\nu}. \tag{2.4}$$

Let us consider the case of a perfect isotropic fluid under the FLRW metric. In this case, the energy-momentum tensor is given by

$$T_{\mu\nu} = (\rho + p) u_\mu u_\nu + p g_{\mu\nu}, \tag{2.5}$$

with density ρ and pressure p. The time-time and the space-space components of the Einstein equations then leads to

$$\left(\frac{\dot{a}}{a}\right)^2 = \frac{8\pi G}{3c^2}\rho - \frac{c^2 K}{a^2} + \frac{\Lambda c^2}{3}, \tag{2.6}$$

$$\frac{\ddot{a}}{a} = -\frac{4\pi G}{3c^2}(\rho + 3p) + \frac{\Lambda c^2}{3}, \tag{2.7}$$

where $\dot{}$ denotes $\mathrm{d}/\mathrm{d}t$. Eqs. (2.6) and (2.7) would reduce to the single equation as

$$\dot{\rho} = -3(\rho + p)\frac{\dot{a}}{a}. \tag{2.8}$$

The property of the fluid is specified by its equation of state, that is $p = w\rho$. The parameter w is zero for non-relativistic pressure-less components such as dark matter, while w is set to be one third for relativistic components, e.g., radiation. Using Eq. (2.8) and w of each component, we can derive the time evolution of the density as: $\rho_{\mathrm{m}} \propto a^{-3}$ for non-relativistic component and $\rho_\gamma \propto a^{-4}$ for relativistic one. In this thesis, we call non-relativistic components "matter" and relativistic components "radiation". In general, the time evolution of energy density $\rho(t)$ is given by

$$\rho \propto \exp\left(-3\int \frac{\mathrm{d}a'}{a'}(1 + w(a'))\right). \tag{2.9}$$

Suppose that a hypothetical fluid corresponding to cosmological constant Λ. We can obtain the following conditions of energy fluid from Eqs. (2.6) and (2.7):

$$\rho_\Lambda = \frac{\Lambda c^4}{8\pi G}, \tag{2.10}$$

$$w_{\rm DE} \equiv \frac{p_\Lambda}{\rho_\Lambda} = -1. \tag{2.11}$$

Hence, we can regard cosmological constant effectively as the energy fluid specified by Eqs. (2.10) and (2.11). Hereafter, we introduce dark energy ρ_Λ instead of cosmological constant. The density of dark energy with the same properties as Λ does not evolve in time.

In modern cosmology, the expansion history of the universe can be described by the following parameters called cosmological parameters: Hubble parameter H, density parameter Ω_α, critical density $\rho_{\rm c}$ and the curvature parameter $\Omega_{\rm K}$. The definition of these parameters are summarized as follows:

$$H = \frac{\dot{a}}{a}, \tag{2.12}$$

$$\Omega_\alpha = \frac{\rho_\alpha}{\rho_c}, \tag{2.13}$$

$$\rho_{\rm c} = \frac{3H^2}{8\pi G}, \tag{2.14}$$

$$\Omega_{\rm K} = \frac{Kc^2}{a^2H^2}. \tag{2.15}$$

$$\tag{2.16}$$

With these parameters, Eq. (2.6) is given by

$$H^2(a) = H_0^2\left[\frac{\Omega_{\rm m0}}{a^3} + \frac{\Omega_{\gamma 0}}{a^4} - \frac{\Omega_{\rm K0}}{a^2} + \Omega_{\Lambda 0}\exp\left\{-3\int\frac{{\rm d}a'}{a'}(1+w_{\rm DE}(a'))\right\}\right], \tag{2.17}$$

where the index 0 denotes the present value of each parameter. Once cosmological parameters are specified at present, the expansion history of the universe can be determined by Eq. (2.17). In the following, we summarize the expansion rate of the universe at the dominant epoch of radiation Ω_γ, matter Ω_m, curvature K and dark energy Ω_Λ.

1. *Radiation domination*

$$a = (2H_0)^{1/2}\Omega_{\gamma 0}^{1/4}t^{1/2}. \tag{2.18}$$

2. *Matter dominatation*

$$a = \left(\frac{9}{4}H_0^2\Omega_{\rm m0}\right)^{1/3} t^{2/3}. \tag{2.19}$$

3. *Curvature domination*

   Curvature can dominate the universe when $\Omega_\Lambda = 0, K < 0, a > -\Omega_{\rm m0}/\Omega_{\rm K0}$.

$$a = H_0\Omega_{\rm K0}^{1/2} t \tag{2.20}$$

4. *Dark energy domination*

   We consider the case of $w_{\rm DE} = -1$ for simplicity.

$$a = \exp\left[\Omega_{\Lambda 0}^{1/2} H_0 (t - t_0)\right] \tag{2.21}$$

Current astrophysical observations yield the present value of dark energy density $\Omega_{\Lambda 0} \sim 0.7$. The simplest candidate of dark energy with $w_{\rm DE} = -1$ is thought to be vacuum energy. However, if dark energy is vacuum energy, there appears to be a huge discrepancy between the observed amount of dark energy and the expected amount of vacuum energy at the present. This is one of the main motivation of other proposals for the candidate of dark energy. Among various models of dark energy, $w_{\rm DE}(a)$ is one of the key parameters to identify dark energy. It is crucial to determine $w_{\rm DE}(a)$ precisely by observation for understanding what dominates the present universe and why the current expansion of the universe is accelerating. In practice, the following parameterization of $w_{\rm DE}(a)$ is often used:

$$w_{\rm DE}(a) = w_0 + w_1(1 - a) + \cdots . \tag{2.22}$$

In this thesis, we pay particular attention to constraints on the parameter of w_0.

2.1.2 Cosmological redshift and angular-diameter distance

Here, we consider cosmological redshift as the time coordinate and define the angular diameter distance. Cosmological redshift is caused by a stretch of the wavelength of photon due to the expansion of the universe. Consider that the photon emitted at $t = t_1$ from the point (r_1, θ_1, ϕ_1). The photon path in a FLRW universe is determined by null

geodesics, i.e. $\mathrm{d}s = 0$ in Eq. (2.1). It is given by

$$\int_{t_1}^{t_0} \frac{c\mathrm{d}t}{a(t)} = \int_0^{r_1} \frac{\mathrm{d}r}{1 - Kr^2}, \tag{2.23}$$

where t_0 is the arrival time of photon and we set $\mathrm{d}\theta = \mathrm{d}\phi = 0$ because of homogeneity and isotropy of space. The right hand side of Eq. (2.23) is independent of the time. This leads to the following equation when considering the case of another emitted time $t_1 + \delta t_1$ and arrival time $t_0 + \delta t_0$:

$$\int_{t_1}^{t_0} \frac{c\mathrm{d}t}{a(t)} = \int_{t_1+\delta t_1}^{t_0+\delta t_0} \frac{c\mathrm{d}t}{a(t)}. \tag{2.24}$$

Suppose that the evolution of $a(t)$ is negligible during δt_1 and δt_0. Then, we can obtain the following relation with the Tayler expansion of Eq. (2.24) around t_0 and t_1:

$$\frac{\delta t_1}{a(t_1)} = \frac{\delta t_0}{a(t_0)}. \tag{2.25}$$

This result can be described in terms of redshift z as follows:

$$1 + z = \frac{\lambda_0}{\lambda_1} = \frac{1}{a(t_1)}, \tag{2.26}$$

where the wavelength of photon λ_i is defined by $c\delta t_i$ and $a(t_0)$ is set to be unity.

We next define the angular diameter distance d_A. The angular diameter distance to an object is defined by the object's size ℓ and the apparent angular size of the object $\Delta\theta$. In the FLRW metric, the relation of ℓ between $\Delta\theta$ is given by

$$\ell = ar\Delta\theta = \frac{r}{1+z}\Delta\theta. \tag{2.27}$$

Thus, d_A is obtained by

$$d_\mathrm{A} = \frac{\ell}{\Delta\theta} = \frac{r}{1+z}. \tag{2.28}$$

In general, the angular diameter distance between two redshifts z_1 and z_2 ($z_1 < z_2$) can be calculated by

$$d_\mathrm{A}(z_1, z_2) = \frac{r(z_1, z_2)}{1+z_2}, \tag{2.29}$$

where $r(z_1, z_2)$ is defined by $\displaystyle\int_{z_1}^{z_2} \frac{c\mathrm{d}z}{H(z)}$.

2.2 Growth of matter density

2.2.1 Evolution of density fluctuations

We can not explain the rich structure of the universe observed today only assuming FLRW metric because FLRW metric describes the *homogeneous* universe. According to the observation of cosmic microwave background (CMB), there exist tiny fluctuations in the CMB temperature map. These fluctuations are expected to amplify its amplitude mainly due to gravitational growth and develop the rich structure of the universe such as galaxies and clusters of galaxies. The gravitational growth of density fluctuations is governed by the fluid equation and the Poisson equation under the background expansion of the universe with FLRW metric. The matter density of fluid $\rho(\boldsymbol{x}, t)$ can be decomposed into the homogeneous and inhomogeneous part;

$$\rho(\boldsymbol{x}, t) = \bar{\rho}(t) + \delta\rho(\boldsymbol{x}, t), \tag{2.30}$$

$$\delta\rho(\boldsymbol{x}, t) \equiv \bar{\rho}(t)\delta(\boldsymbol{x}, t), \tag{2.31}$$

where $\bar{\rho}$ and $\delta\rho$ are the homogeneous and inhomogeneous part, respectively. The fluid equation and the Poisson equation under the background FLRW universe are given by

$$\dot{\delta} + \frac{1}{a}\nabla \cdot [(1+\delta)\boldsymbol{u}] = 0, \tag{2.32}$$

$$\dot{\boldsymbol{u}} + \frac{\dot{a}}{a}\boldsymbol{u} + \frac{1}{a}(\boldsymbol{u}\cdot\nabla)\boldsymbol{u} = -\frac{\nabla p}{a\bar{\rho}(1+\delta)} - \nabla\frac{\Phi}{a}, \tag{2.33}$$

$$\Delta\Phi = 4\pi G\bar{\rho}a^2\delta, \tag{2.34}$$

where $\boldsymbol{u}$ is the velocity field of matter fluid, $\Phi = \phi + \frac{a\ddot{a}}{2}x^2$, ϕ represents the gravitational potential and ∇ is the derivative operator by the comoving coordinate $\boldsymbol{x}$. The evolution of density fluctuations can be determined by a set of non-linear equations Eqs. (2.32), (2.33) and (2.34).

2.2.2 Linear perturbation

It is difficult to determine the evolution of matter density analytically in general. However, perturbations of matter density can be understood with the linearized equations when the amplitude of perturbations is sufficiently small, i.e. $\delta \ll 1$. For matter components with $p = 0$, we can obtain the following equation of δ by considering the first order of Eqs. (2.32), (2.33) and (2.34)

$$\ddot{\delta} + 2\frac{\dot{a}}{a}\dot{\delta} - 4\pi G\bar{\rho}\delta = 0. \tag{2.35}$$

Thus, the evolution of δ is determined as a function of time over various physical scales at the level of the first order in Eqs. (2.32), (2.33) and (2.34). The linear growth of δ would be affected by the expansion history of the universe. Here, we summarize the linear growth of δ in various cosmological models.

1. *Radiation domination and equality epoch*

   Let us consider the evolution of δ from radiation domination to the equality time. The equality time is defined by the cosmic epoch when the energy density of radiation in the universe is equal to that of matter. At this epoch, a mixture of radiation and matter dominates the universe. Hubble parameter H is then calculated by

$$\begin{aligned} H(a) &= H_0\sqrt{\Omega_{\rm m0}a^{-3}+\Omega_{\gamma 0}a^{-4}} \\ &= \frac{H_0\Omega_{\rm m0}^{1/2}}{a^2}\sqrt{a+a_{eq}}, \end{aligned} \tag{2.36}$$

   where $a_{\rm eq}$ is the scale factor at the equality time, defined by $a_{\rm eq}=\Omega_{\gamma 0}/\Omega_{\rm m0}$. We can rewrite Eq. (2.35) by the new time coordinate $y=a/a_{\rm eq}$ instead of t as follows;

$$\frac{{\rm d}^2\delta}{{\rm d}y^2}+\frac{2+3y}{2y(1+y)}\frac{{\rm d}\delta}{{\rm d}y}-\frac{3\delta}{2y(1+y)}=0. \tag{2.37}$$

   There are two kinds of solutions of Eq. (2.37). One is given by

$$\delta \propto 1+\frac{3y}{2}, \tag{2.38}$$

   and another is expressed as

$$\delta \propto \left(1+\frac{3y}{2}\right)\ln\left(\frac{\sqrt{1+y}+1}{\sqrt{1+y}-1}\right)-3\sqrt{1+y}. \tag{2.39}$$

   This result indicates that the density fluctuation of matter density can grow *gradually* (i.e. by a factor of 2.5) in radiation domination.

2. *Matter Domination*

   In matter domination, Hubble parameter H is equal to $2/(3t)$. Using the relation between $\bar{\rho}$ and the time at this epoch ($\bar{\rho}=1/(6\pi G t^2)$), we can rewrite Eq. (2.35) as follows;

$$\ddot{\delta}+\frac{4}{3t}\dot{\delta}-\frac{2}{3t^2}\delta=0. \tag{2.40}$$

We can solve Eq. (2.40) by considering the case of $\delta \propto t^n$. The solution can be expressed as

$$\delta = At^{2/3} + Bt^{-1}. \tag{2.41}$$

Thus, the evolution of δ is determined by $\delta \propto t^{2/3} \propto a$.

3. *ΛCDM model*

Here, we consider the case of ΛCDM model that is consistent with current multiple astrophysical observations. In this model, the radiation density $\Omega_{\gamma 0}$ and the curvature K is negligible and the equation state of dark energy $w_{\rm DE}$ is set to be -1. Therefore, Hubble parameter H is given by

$$H(a) = H_0\sqrt{\Omega_{\rm m0}a^{-3} + \Omega_{\Lambda 0}}. \tag{2.42}$$

One can find that Eq. (2.42) is actually the specific solution of Eq. (2.35) in ΛCDM model with the relation of $4\pi G\bar{\rho} = 3/2H^2\Omega_{\rm m}$. Hence, one can obtain another solution of Eq. (2.35) by assuming $D(a) = H(a)f(a)$. The solution is given by

$$D(a) \propto H(a)\int^a \frac{{\rm d}a'}{(a'H(a'))^3}. \tag{2.43}$$

Note that $H(a)$ represents the decline of the linear growth and $D(a)$ describes the linear growth of δ in ΛCDM model. We also extend ΛCDM model by considering $w_{\rm DE} = const. \neq -1$. In this model, the linear growth of matter density perturbation can be expressed as

$$D(a) \propto aF\left(-\frac{1}{3w_{\rm DE}}, \frac{w_{\rm DE}-1}{2w_{\rm DE}}, 1-\frac{5}{6w_{\rm DE}}, x\right), \tag{2.44}$$

$$x = -\frac{\Omega_{\Lambda 0}}{\Omega_{\rm m0}}a^{-3w_{\rm DE}}, \tag{2.45}$$

where $F(\alpha, \beta, \gamma, x)$ is known as the hypergeometric function. An integral giving the hypergeometric function is

$$F(\alpha,\beta,\gamma,x) = \frac{\Gamma(\gamma)}{\Gamma(\alpha)\Gamma(\gamma-\beta)}\int_0^1 t^{\beta-1}(1-t)^{\gamma-\beta-1}(1-tx)^{-\alpha}{\rm d}t. \tag{2.46}$$

We here emphasize that all the results above are correct only when matter overdensity δ is significantly small, i.e. $\delta \ll 1$. We can not predict the evolution of δ in the way as shown above once the amplitude of δ becomes larger and the mode coupling of δ (the coupling term such as $\delta \cdot \boldsymbol{u}$ etc.) becomes important.

2.2.3 Non-linear perturbation

The spherical collapse model is one of the simplest models to describe non-linear growth of matter density in the universe. Suppose that matter density around a given point distributes in a spherical manner. The gravitational force at a shell with a offset distance of r from the center of system can be determined by the inner mass M within this shell. The equation of motion for the shell is given by

$$\frac{\mathrm{d}^2 r}{\mathrm{d}t^2} = -\frac{GM}{r^2}, \tag{2.47}$$

and the solution of the above equation under the condition of $\mathrm{d}r/\mathrm{d}t > 0$ and $r = 0$ at $t = 0$ is

$$r = A^2(1 - \cos\theta), \tag{2.48}$$

$$t = \frac{A^3}{\sqrt{GM}}(\theta - \sin\theta). \tag{2.49}$$

When considering the matter domination for simplicity, one can find that the overdensity within the shell is given by

$$\delta = \frac{9GMt^2}{2r^3} - 1 = \frac{9}{2}\frac{(\theta - \sin\theta)^2}{(1 - \cos\theta)^3} - 1, \tag{2.50}$$

where we use the relation of mean matter density and cosmic time i.e. $\bar{\rho} = 1/(6\pi G t^2)$. As you can see from Eq. (2.48), the shell will expand from $\theta = 0$ to $\theta = \pi$ and then contrast from $\theta = \pi$. Finally, the overdensity within this shell would diverge when $\theta = 2\pi$. Let us assume this system would be virialized through the contraction of each shell and the formation of object with a finite size of r_{vir} occurs. In this scenario, the following relations should be realized according to the energy conservation of system and the virial theorem;

$$2K_{\mathrm{vir}} + U_{\mathrm{vir}} = 0, \tag{2.51}$$

$$K_{\mathrm{vir}} + U_{\mathrm{vir}} = U_{\mathrm{turn}}, \tag{2.52}$$

where U_{turn} is the potential energy of the shell at $\theta = \pi$ and K_{vir} and U_{vir} represent the kinematic energy and the potential energy of shell, respectively. These equations provide $r_{\mathrm{vir}} = A^2$. Thus, broadly speaking, the overdensity when the system is virialized can be evaluated as

$$\Delta_{\mathrm{vir}} = \frac{3M}{4\pi r_{\mathrm{vir}}^3}\frac{1}{\bar{\rho}(t_{\mathrm{coll}})} - 1 = 18\pi^2 - 1 \simeq 177, \tag{2.53}$$

where $t_{\rm coll}$ is the free fall time given by $t(\theta = 2\pi) = 2A^3/\sqrt{GM}$. Therefore, we can estimate the overdensity within an virialized region as ~ 177.

It is useful to consider the *linear* overdensity in a virialized system. The linear density in the spherical model is defined by the lowest order of Eq. (2.50) in terms of θ,

$$\delta_{\rm L}(t) = \frac{3}{20}\left(\frac{6\sqrt{GM}}{A^3}t\right)^{2/3}. \tag{2.54}$$

The linear overdensity at $t = t_{\rm coll}$ is $\sim$1.69.

We can easily extend the above calculation to the case of various cosmological models. Ref. [67] provided the useful fitting formula in ΛCDM model as follows;

$$\Delta_{\rm vir} \simeq 18\pi^2(1 + 0.4093 w_{\rm f}^{0.9052}), \tag{2.55}$$

$$\delta_{\rm L} \simeq \frac{3(12\pi)^{2/3}}{20}(1 - 0.00123\log_{10}\Omega_{\rm f}), \tag{2.56}$$

$$w_{\rm f} = \frac{1}{\Omega_{\rm f}} - 1, \tag{2.57}$$

$$\Omega_{\rm f} = \frac{\Omega_{\rm m0}(1+z)^3}{\Omega_{\rm m0}(1+z)^3 + \Omega_{\Lambda 0}}. \tag{2.58}$$

How does matter distribute in virialized system such as galaxy and cluster of galaxies? Ref. [68] has performed cosmological N-body simulation with various cosmological model and the authors found that matter density profile of virialized dark matter halo can be described by the *universal* function as follows;

$$\rho_h(r) = \frac{\rho_s}{(r/r_s)(1 + r/r_s)^2}, \tag{2.59}$$

where ρ_s and r_s are the scale density and the scale radius, respectively. These parameters can be condensed into one parameter, the concentration $c_{\rm vir}(M, z)$, by the use of two halo mass relations; namely, $M = 4\pi r_{\rm vir}^3 \Delta_{\rm vir}(z)\rho_{\rm crit}(z)/3$, where $r_{\rm vir}$ is the virial radius corresponding to the overdensity criterion $\Delta_{\rm vir}(z)$ as shown, e.g, in Eq. (2.55), and $M = \int dV\, \rho_h(\rho_s, r_s)$ with the integral performed out to $r_{\rm vir}$. At present, the density profile shown in Eq. (2.59) is called NFW profile. NFW profile have been conformed for wide range of mass scales (from earth-size halos to clusters of galaxies) at different epochs in current (dark matter only) N-body simulations [69, 70, 71, 72]. Once NFW profile is assumed, one can easily calculate the various observables such as rotation curve of galaxies (e.g., [73, 74]), gravitational lensing effect of clusters of galaxies (e.g., [75]), hot gas distribution in galaxy clusters (e.g., [76]), and two-point statistics of density perturbations (e.g., [77]).

2.3 Statistics of matter density perturbation

2.3.1 Two point statistics

One needs the statistical method to investigate gravitational growth of density perturbations in the universe with a large data set obtained from photometric and/or spectroscopic astronomical surveys. One of the simplest statistics is two point correlation function. Two point correlation function represents the clustering of astrophysical sources such as galaxies, which is defined by

$$\xi(|\boldsymbol{x}_1 - \boldsymbol{x}_2|) = \langle \delta_g(\boldsymbol{x}_1)\delta_g(\boldsymbol{x}_2)\rangle, \tag{2.60}$$

$$\delta_g(\boldsymbol{x}) = (n(\boldsymbol{x}) - \bar{n})/\bar{n}, \tag{2.61}$$

where $n(\boldsymbol{x})$ is the number density of objects and $\bar{n}$ represents the mean number density. In general, number density of astrophysical objects $n(\boldsymbol{x})$ can be biased from underlying matter density $\rho(\boldsymbol{x})$. We here consider the simplest case that $n(\boldsymbol{x})$ can be proportional to $\rho(\boldsymbol{x})$, i.e. matter overdensity δ is equal to δ_g.

It is useful to consider two point correlation function in fourier space instead of real space. In fourier space, density perturbation $\tilde{\delta}(\boldsymbol{k})$ is related to $\delta(\boldsymbol{x})$ as follows;

$$\delta(\boldsymbol{x}) = \frac{1}{(2\pi)^3}\int \mathrm{d}^3k\ \tilde{\delta}(\boldsymbol{k})\exp(i\boldsymbol{k}\cdot\boldsymbol{x}), \tag{2.62}$$

$$\tilde{\delta}(\boldsymbol{k}) = \int \mathrm{d}^3x\ \delta(\boldsymbol{x})\exp(-i\boldsymbol{k}\cdot\boldsymbol{x}). \tag{2.63}$$

Thus, two point correlation between two different wave numbers $\boldsymbol{k}$ and $\boldsymbol{k}'$ is given by

$$\langle\tilde{\delta}(\boldsymbol{k})\tilde{\delta}(\boldsymbol{k}')\rangle = (2\pi)^3\delta_D^{(3)}(\boldsymbol{k}+\boldsymbol{k}')\int \mathrm{d}^3r\ \xi(r)\exp(-i\boldsymbol{k}\cdot\boldsymbol{r}), \tag{2.64}$$

where $\delta_D^{(3)}(\boldsymbol{r})$ represents three-dimensional dirac function. The integral in Eq. (2.64) is called power spectum and often is denoted by $P(k)$. Power spectrum depends on only the amplitude of $\boldsymbol{k}$ if the universe is isotropic.

The initial condition of power spectrum of matter density is usually assumed to be a power law function, i.e. $P_{\mathrm{init}}(k) \propto k^{n_s}$. This originates from early works by Harrison [78] and Zeldovich [79] in 1970's (The similar approximation is also found in Ref. [80]). In their prescription, all perturbations that come within the horizon have the same amplitude. In this case, n_s is found to be unity and the case of $n_s = 1$ is called Harrison–Zeldovich spectrum. Most of inflation models also predict the power law type of primordial power spectrum.

The shape of power spectrum would be affected by growth of primordial density perturbation through various physical processes. In the linear regime (i.e. $\delta \ll 1$), power spectrum would be modified in an independent way of wave number mode k because the evolution of δ can be determined by a function of time not k as shown in Eq. (2.35). Thus, overdensity $\tilde{\delta}(k, a)$ should be decomposed into a function of k and a as follows;

$$\tilde{\delta}(k, a) = \frac{T(k)D(a)}{D(a_{\rm init})}\tilde{\delta}(k, a_{\rm init}), \tag{2.65}$$

where $D(a)$ is the growth factor given by the solution of Eq. (2.35) and $T(k)$ represents the evolution of density perturbation at different scales, which is called the transfer function. Therefore, power spectrum at a given k and a can be written as

$$P(k, a) = \frac{T^2(k)D^2(a)}{D^2(a_{\rm init})}P_{\rm init}(k). \tag{2.66}$$

Note that the above formula should be valid in the linear regime (i.e. $\delta \ll 1$). In order to obtain the specific shape of $T(k)$, we need to solve the Boltzmann equation coupled with General Relativity. Although it is difficult to derive $T(k)$ analytically, one can obtain $T(k)$ numerically with the Boltzmann equation solver [81] or the fitting formula shown in Ref. [82].

The normalization of power spectrum is determined by observations. One possible way is based on the variance of smoothed overdensity $\sigma_{\rm R}$ with comoving scale of R Mpc/h at present. $\sigma_{\rm R}$ is given by

$$\sigma_{\rm R}^2 = \int \frac{{\rm d}^3k}{(2\pi)^3}\ P(k, a = 1)|W_{\rm R}(k)|^2 \tag{2.67}$$

where $W_{\rm R}(k)$ is the window function, which is set to be the top-hat function in practice. $R = 8$ Mpc/h is the conventional scale for the normalization of power spectrum. We can also use another observational result in the early universe, e.g., the power spectrum of primordial curvature perturbation generated by inflation at some pivot wave number of k_0. In matter domination, power spectrum of curvature perturbation is related to one of matter density through Poisson equation as follows;

$$\frac{4\pi k^3 P(k, a)}{(2\pi)^3} = \Delta^2_{\mathcal{R}}(k_0)\left(\frac{2c^2k^2}{5H_0^2\Omega_{\rm m0}}\right)^2 D^2(a)T^2(k)\left(\frac{k}{k_0}\right)^{-1+n_s} \tag{2.68}$$

$$\Delta^2_{\mathcal{R}}(k) = \frac{4\pi k^3 P_{\mathcal{R}}(k)}{(2\pi)^3} \tag{2.69}$$

where $P_{\mathcal{R}}(k_0)$ represents power spectrum of curvature perturbation which is determined by observations.

2.3.2 Mass function and Halo bias

The abundance of massive objects such as clusters of galaxies is one of the powerful tools to probe cosmology at lower redshift. Let us consider the number of virialized objects with mass range of $M \sim M + \mathrm{d}M$ which is called mass function. One of the simplest way to calculate the mass function is Press-Schechter formalism [83]. In Press-Schechter formalism, virialized objects with mass of M are assumed to form where the density perturbation in an sphere with radii of $R = (3M/4\pi\bar{\rho})^{1/3}$ is larger than the critical value δ_c. δ_c is often considered to be ~ 1.69 as shown in Eq. (2.54).

Smoothed density perturbation with smoothing scale of R is given by

$$\delta_{\mathrm{R}}(\boldsymbol{x}) = \int \mathrm{d}^3x' \; W_{\mathrm{R}}(|\boldsymbol{x} - \boldsymbol{x}'|)\delta(\boldsymbol{x}'), \tag{2.70}$$

where $W_{\mathrm{R}}(|\boldsymbol{x} - \boldsymbol{x}'|)$ represents window function for smoothing. Top-hat window function is often used in literature. Suppose that smoothed density perturbation follows Gaussian, the probability of formation of virialized objects with mass of $M = 4\pi/3\bar{\rho}R^3$ can be written as

$$F(M) = 2\int_{\delta_c}^{\infty} \mathrm{d}\delta_{\mathrm{R}} \frac{1}{\sqrt{2\pi\sigma_{\mathrm{R}}^2}} \exp\left(-\frac{1}{2}\frac{\delta_{\mathrm{R}}^2}{\sigma_{\mathrm{R}}^2}\right) = 2 \times \frac{1}{2}\mathrm{erfc}\left(\frac{\delta_c}{\sqrt{2}\sigma_{\mathrm{R}}}\right), \tag{2.71}$$

where σ_{R} is the variance of smoothed density perturbation given by Eq. (2.67). The factor of 2 in Eq. (2.71) is the multiplicative correction so that $F(0)$ would be equal to unity when $R \to 0$. (Note that $\sigma_{\mathrm{R}} \to \infty$ with limit of $R \to 0$.) In this thesis, $n(M)\mathrm{d}M$ denotes the number density of virialized objects with mass range of $M - M + \mathrm{d}M$. Thus, the mass fraction of virialized objects with mass of M can be written as $n(M)M\mathrm{d}M/\bar{\rho}$. This fraction should be equal to be $F(M + \mathrm{d}M) - F(M) = |\partial F/\partial M|_M \, \mathrm{d}M$. Therefore, we can evaluate $n(M)$ by equating $n(M)M\mathrm{d}M/\bar{\rho}$ with $|\partial F/\partial M|_M \, \mathrm{d}M$;

$$\begin{aligned} n(M) &= -\frac{\bar{\rho}}{M}\frac{\partial F}{\partial M} \\ &= -\frac{\bar{\rho}}{M}\sqrt{\frac{2}{\pi}}\frac{\delta_c}{\sigma_{\mathrm{R}}^2}\exp\left(-\frac{1}{2}\frac{\delta_c^2}{\sigma_{\mathrm{R}}^2}\right)\frac{\partial \sigma_{\mathrm{R}}}{\partial M} \\ &= f_{\mathrm{PS}}\left(\frac{\delta_c}{\sigma_{\mathrm{R}}}\right)\frac{\bar{\rho}}{M^2}\left|\frac{\mathrm{d}\ln\sigma_{\mathrm{R}}^{-1}}{\mathrm{d}\ln M}\right|, \end{aligned} \tag{2.72}$$

$$f_{\mathrm{PS}}(\nu) = \sqrt{\frac{2}{\pi}}\nu e^{-\nu^2/2}. \tag{2.73}$$

Although Press-Schechter formalism relies on various approximations, it can explain overall feature of mass function found in cosmological N-body simulation. The detailed shape of mass function have been calibrated with numerical simulations (e.g., [84, 85,

86]). There are some previous works based on the analytic approach with ellipsoidal collapse model [87, 88]. In the case of ellipsoidal collapse model, $f_{\rm PS}$ can be replaced with the following function;

$$f_{\rm ST}(\nu) = A\sqrt{\frac{2\alpha}{\pi}}\left[1+\left(\alpha\nu^2\right)^{-p}\right]\nu e^{-\alpha\nu^2/2}, \tag{2.74}$$

where α and p represent the parameter of ellipsoidal collapse model and A is the normalization factor. Numerical simulation have been utilized for calibration of these parameters, which are given by $A = 0.322$, $\alpha = 0.707$, and $p = 0.3$.

Virialized objects such as galaxies and galaxy clusters are *biased* tracer of underlying matter distribution. Thus, the clustering of virialized objects would be different from one of matter density perturbation. The peak-background split formalism [89] give a simple framework to calculate the clustering of virialized objects at large scale. One can split underlying density perturbation into long-wavelength mode δ_ℓ and short-wavelength mode δ_s;

$$\rho(\boldsymbol{q}) = \bar{\rho}(1+\delta_\ell+\delta_s), \tag{2.75}$$

where $\boldsymbol{q}$ represents the coordinate in the Lagrangian space. The number density of virialized object with mass of M at the position of $\boldsymbol{q}$ would be modulated by presence of the long-wavelength mode of density perturbation. Hence, the simple model of the number density field of virialized objects is given by a local shift in the density threshold, i.e. replacing δ_c with $\delta_c - \delta_\ell(\boldsymbol{q})$ in Eq. (2.72). In this context, the number density contrast of virialized objects in the Lagrangian space is given by

$$\delta_h(\boldsymbol{q}|M) = \frac{n_h(\boldsymbol{q}|M)}{n(M)} - 1, \tag{2.76}$$

where $n_h(\boldsymbol{q}|M)$ is the number density field of objects with mass of M at $\boldsymbol{q}$ and $n(M)$ represents the mean number density which is given by e.g., Eq. (2.72). By expanding this equation into Taylor series of δ_ℓ in Eq. (2.76), one can relate δ_h with δ_ℓ as follows;

$$\delta_h(\boldsymbol{q}|M) = b_L(M)\delta_\ell(\boldsymbol{q}), \tag{2.77}$$

$$b_L = \frac{1}{n(M)}\left(\frac{\partial n_h}{\partial\delta_\ell}\right)_{\delta_\ell=0}. \tag{2.78}$$

b_L is the large-scale bias of virialized objects in Lagrangian space. In Eulerian space, one needs to add the correction of the Eulerian space clustering. Therefore, the total or Eulerian bias is given by $b = b_L + 1$. b_L can be calculated once the function form of mass function is specified. For example, in the case of the functional form in Eq. (2.73),

b_L is given by

$$b_L(M) = \frac{\nu^2 - 1}{\delta_c}, \tag{2.79}$$

where ν is given by $\delta_c/\sigma_R(M)$.

Chapter 3

Weak Gravitational Lensing

3.1 Basic Equation

According to General Relativity, the path of photon from a distant object would be affected by intervening matter distribution between the object and us. This relativistic effect is called gravitational lensing and more effective when photon goes through more massive objects along the line of sight. Photon from *every* galaxy at a cosmological distance would experience gravitational lensing effect due to large-scale structure in the universe. Hence, the image of distant galaxies would be distorted by multiple deflections of the path of photon. Although the distortion of images is very weak in general, we can extract the information of matter density distribution along the line of sight with statistical analysis of image of galaxies.

Let us consider the path of photon from a distant source object in the presence of inhomogeneous matter distribution. The path of a light ray can be determined by the null geodesic equation;

$$\frac{\mathrm{d}^2 x^\mu}{\mathrm{d}\lambda^2} = -\Gamma^\mu_{\alpha\beta}\frac{\mathrm{d}x^\alpha}{\mathrm{d}\lambda}\frac{\mathrm{d}x^\beta}{\mathrm{d}\lambda}, \tag{3.1}$$

$$g_{\mu\nu}\frac{\mathrm{d}x^\mu}{\mathrm{d}\lambda}\frac{\mathrm{d}x^\nu}{\mathrm{d}\lambda} = 0, \tag{3.2}$$

where $\Gamma^\mu_{\alpha\beta}$ represents the Christoffel symbol given by a function of metric $g_{\mu\nu}$,

$$\Gamma^\mu_{\alpha\beta} = \frac{g^{\mu\nu}}{2}\left(g_{\mu\alpha,\beta} + g_{\mu\beta,\alpha} - g_{\alpha\beta,\mu}\right), \tag{3.3}$$

where $\partial g_{\mu\alpha}/\partial x^\beta = g_{\mu\alpha,\beta}$ and so on. In this chapter, Roman letter (e.g., i, j) is running from 1 to 3 and Greek character (e.g., α, β) is running from 0 to 3. When gravitational potential Φ is very small, the metric of inhomogeneous expanding universe can be

described as follows;

$$\mathrm{d}s^2 = -\left(1+\frac{2\Phi}{c^2}\right)c^2\mathrm{d}t^2 + a^2(t)\left(1-\frac{2\Phi}{c^2}\right)\left[\mathrm{d}\chi^2 + r(\chi)^2\mathrm{d}\sigma^2\right]. \tag{3.4}$$

We can approximate $\mathrm{d}\sigma^2$ as $(\mathrm{d}\theta^1)^2 + (\mathrm{d}\theta^2)^2$ when the deflection angle of interest is small (this approximation is valid because the typical value of θ is of the order of arc-minutes for distant galaxies). Suppose that the position of a light ray $x^i = (\theta^1, \theta^2, \chi)$, the derivative with respect to affine parameter can be written as follows;

$$\begin{aligned}\frac{\mathrm{d}}{\mathrm{d}\lambda} &= \frac{\mathrm{d}\chi}{\mathrm{d}\lambda}\frac{\mathrm{d}}{\mathrm{d}\chi} \\ &= \frac{\mathrm{d}\chi}{\mathrm{d}x^0}\frac{\mathrm{d}x^0}{\mathrm{d}\lambda}\frac{\mathrm{d}}{\mathrm{d}\chi} \\ &= -\frac{P^0}{a}\frac{\mathrm{d}}{\mathrm{d}\chi},\end{aligned} \tag{3.5}$$

where $P^0 = \mathrm{d}x^0/\mathrm{d}\lambda$. Therefore, the transverse components ($i = 1, 2$) of the null geodesic equation can be expressed as the differential equation with respect to comoving distance χ. We can obtain the following equation by expanding Taylor series about θ^1, θ^2, and Φ/c^2 up to first order in the geodesic equation;

$$\frac{\mathrm{d}^2(r\theta^i)}{\mathrm{d}\chi^2} + Kr\theta^i = -\frac{2}{c^2}\frac{\partial\Phi}{\partial(r\theta^i)}. \tag{3.6}$$

The solution of Eq. (3.6) is given by

$$\beta^i = \theta^i - \frac{2}{c^2}\int_0^\chi \mathrm{d}\chi'\partial_i\Phi(\chi')\frac{r(\chi-\chi')}{r(\chi)}, \tag{3.7}$$

where β^i is the *unlensed* position of source on sky and ∂_i is the derivative with respect to $r\theta^i$. Eq. (3.7) is the basic equation in *weak* gravitational lensing.

When we denote the observed position of a source object as $\boldsymbol{\theta}$ and the true position as $\boldsymbol{\beta}$, we can characterize the distortion of image of a source object by the following 2D matrix:

$$A_{ij} = \frac{\partial\beta^i}{\partial\theta^j} \equiv \begin{pmatrix} 1-\kappa-\gamma_1 & -\gamma_2 \\ -\gamma_2 & 1-\kappa+\gamma_1 \end{pmatrix}, \tag{3.8}$$

where κ is convergence and γ is shear. The component of A_{ij} can be decomposed as

$$A_{ij} = \begin{pmatrix} 1-\kappa & 0 \\ 0 & 1-\kappa \end{pmatrix} + \begin{pmatrix} -\gamma_1 & -\gamma_2 \\ -\gamma_2 & +\gamma_1 \end{pmatrix}, \tag{3.9}$$

where the first part of the right-hand side represents an amplification of the size of the image and the second part discribes an anisotropic stretching of its shape.

By using Eq. (3.7), we can relate each component of A_{ij} to the second derivative of the gravitational potential as follows;

$$\begin{aligned} A_{ij} &= \delta_{ij} - \Phi_{ij}, && (3.10)\\ \Phi_{ij} &= \frac{2}{c^2}\int_0^\chi \mathrm{d}\chi' g(\chi,\chi')\partial_i\partial_j\Phi(\chi'), && (3.11)\\ g(\chi,\chi') &= \frac{r(\chi-\chi')r(\chi')}{r(\chi)}. && (3.12) \end{aligned}$$

We can find $2\kappa = \Phi_{11} + \Phi_{22}$ from the above equations. On the other hand, gravitational potential Φ can be related to matter density perturbation according to Poisson equation;

$$\Delta\Phi = \frac{3H_0^2}{2}\Omega_{\mathrm{m0}}\frac{\delta}{a}. \tag{3.13}$$

Therefore, convergence can be expressed as the weighted integral of δ along the line of sight;

$$\begin{aligned} \kappa &= \frac{1}{c^2}\int_0^\chi \mathrm{d}\chi' g(\chi,\chi')[\Delta - \partial_\chi^2]\Phi \\ &= \frac{3}{2}\left(\frac{H_0}{c}\right)^2\Omega_{\mathrm{m0}}\int_0^\chi d\chi' g(\chi,\chi')\frac{\delta}{a} - \frac{1}{c^2}\int_0^\chi \mathrm{d}\chi' g(\chi,\chi')\partial_\chi^2\Phi. && (3.14) \end{aligned}$$

We can safely neglect the term related to the second derivative with respect to χ when considering small angle separation [90]. Thus, convergence κ can be written as

$$\kappa = \frac{3}{2}\left(\frac{H_0}{c}\right)^2\Omega_{\mathrm{m0}}\int_0^\chi \mathrm{d}\chi' g(\chi,\chi')\frac{\delta}{a}. \tag{3.15}$$

The relation between convergence and shear in fourier space is given by

$$\begin{aligned} \tilde{\gamma}(\boldsymbol{k}) &= \tilde{\gamma_1}(\boldsymbol{k}) + i\tilde{\gamma_2}(\boldsymbol{k}) \\ &= \frac{k_1^2 - k_2^2 + ik_1k_2}{k^2}\tilde{\kappa}(\boldsymbol{k}), && (3.16)\\ \tilde{\kappa}(\boldsymbol{k}) &= \tilde{\gamma_1}(\boldsymbol{k})\cos 2\phi_{\boldsymbol{k}} + \tilde{\gamma_2}(\boldsymbol{k})\sin 2\phi_{\boldsymbol{k}}, && (3.17) \end{aligned}$$

where $\tilde{X}(\boldsymbol{k})$ is the fourier coefficient of $X(\boldsymbol{\theta})$ and $\boldsymbol{k} = (k_1, k_2) = k(\cos\phi_{\boldsymbol{k}}, \sin\phi_{\boldsymbol{k}})$. Inverse fourier transform of Eq. (3.17) provides that (e.g., [91])

$$\begin{aligned} \kappa(\boldsymbol{\theta}) &= -\frac{1}{\pi}\int \mathrm{d}^2\theta' \mathcal{R}\mathrm{e}\left[D^*(\boldsymbol{\theta}-\boldsymbol{\theta'})\gamma(\boldsymbol{\theta'})\right], && (3.18)\\ D(\boldsymbol{z}) &= \frac{z_1^2 - z_2^2 + 2iz_1z_2}{z^4}. && (3.19) \end{aligned}$$

One of the most common observables is the angle average of lensing quantities around some objects like galaxy or galaxy clusters. From Eq. (3.10), we can derive the following equations by taking a polar coordinate $(\theta_1, \theta_2) = (\theta\cos\phi, \theta\sin\phi)$;

$$\kappa = \frac{1}{2}\left(\Phi_{\theta\theta} + \frac{1}{\theta}\Phi_\theta + \frac{1}{\theta^2}\Phi_{\phi\phi}\right), \tag{3.20}$$

$$\gamma_t = -\frac{1}{2}\left(\Phi_{\theta\theta} - \frac{1}{\theta}\Phi_\theta - \frac{1}{\theta^2}\Phi_{\phi\phi}\right), \tag{3.21}$$

$$\gamma_\times = \partial_\theta\left(\frac{1}{\theta}\Phi_\phi\right), \tag{3.22}$$

where the origin is set to be the center of the object. Here, γ_t and $\gamma_\times$ represents the tangential and cross component of shear which are defined as

$$\gamma_t = -\gamma_1\cos 2\phi - \gamma_2\sin 2\phi, \tag{3.23}$$

$$\gamma_\times = \gamma_1\sin 2\phi - \gamma_2\cos 2\phi. \tag{3.24}$$

Then, the average of κ, γ_t and $\gamma_\times$ within an annulus $[\theta, \theta + \mathrm{d}\theta]$ is given by

$$\langle\kappa\rangle(\theta) = \frac{1}{2}\left(\langle\Phi_{\theta\theta}\rangle + \frac{1}{\theta}\langle\Phi_\theta\rangle\right), \tag{3.25}$$

$$\langle\gamma_t\rangle(\theta) = -\frac{1}{2}\left(\langle\Phi_{\theta\theta}\rangle - \frac{1}{\theta}\langle\Phi_\theta\rangle\right), \tag{3.26}$$

$$\langle\gamma_\times\rangle(\theta) = 0, \tag{3.27}$$

where $\langle X\rangle(\theta)$ is given by $\int_0^{2\pi} X(\theta,\phi)\mathrm{d}\phi/2\pi$ and we use the fact that $\langle\Phi_\phi\rangle = 0$. Hence, for a given point on sky, one can test any systematic effects on cosmic shear measurement by checking whether $\langle\gamma_\times\rangle = 0$ or not. Also, $\langle\kappa\rangle$ and $\langle\gamma_t\rangle$ are related as follows;

$$\langle\gamma_t\rangle(\theta) = -\langle\kappa\rangle(\theta) + \bar{\kappa}(\theta), \tag{3.28}$$

where $\bar{\kappa}(\theta)$ represents the circler average of convergence defined by

$$\begin{aligned}\bar{\kappa}(\theta) &= \frac{1}{\pi\theta^2}\int_0^\theta 2\pi\mathrm{d}\theta'\theta'\langle\kappa\rangle(\theta),\\ &= \frac{1}{\theta^2}\int_0^\theta \mathrm{d}\theta'\partial_{\theta'}\left(\theta'\Phi_{\theta'}\right),\\ &= \frac{1}{\theta}\langle\Phi_\theta\rangle.\end{aligned} \tag{3.29}$$

3.2 Observable

Here, we consider the relationship between the observable and the cosmological signal in weak lensing measurement.

Weak lensing measurement roughly consists of two methods: measurement of shape of images and measurement of size and magnitude of images. Gravitational lensing causes amplification of size and distortion of shape of an image. The size amplification is called magnification and leads to fluctuation in the size and the magnitude of distant galaxies. In a magnitude-limited survey, number density of background galaxies is expected to change by the magnification due to foreground matter density distribution. This magnification effect have been already detected by cross correlation analysis of background and foreground populations (e.g., [92, 93]) and use of a tight scaling relation between galaxy's properties such as apparent size and surface brightness [94]. Nevertheless, at present, the shape measurement of distant galaxies is more commonly used in weak gravitational lensing measurement. In the following, we focus on the shape of image of a distant object in terms of measurement of shear γ [95, 96].

Suppose the observed surface brightness of galaxies $f(\boldsymbol{\theta})$, we can define the center of an image $\bar{\theta}_i$ as follows;

$$\bar{\theta}_i \equiv \frac{\int \mathrm{d}^2\theta\, W(\theta)\, \theta_i\, f(\boldsymbol{\theta})}{\int \mathrm{d}^2\theta\, W(\theta)\, f(\boldsymbol{\theta})}, \tag{3.30}$$

where $W(\theta)$ determines the apparent size of image. Then, the quadruple moment of image can be evaluated by

$$Q_{ij}^{(\mathrm{obs})} \equiv \frac{\int \mathrm{d}^2\theta\, W(\theta)(\theta_i - \bar{\theta}_i)(\theta_j - \bar{\theta}_j) f(\boldsymbol{\theta})}{\int \mathrm{d}^2\theta\, W(\theta) f(\boldsymbol{\theta})}. \tag{3.31}$$

The position of observed galaxies would change due to gravitational lensing effect by foreground matter distribution. When the *unlensed* position is denoted by $\boldsymbol{\beta}$, we can define the quadruple moment of images on source plane $\boldsymbol{\beta}$. The surface brightness on source plane $f^{(s)}(\boldsymbol{\beta})$ should be equal to the observed surface brightness according to conservation of photon energy;

$$f(\boldsymbol{\theta}) = f^{(s)}(\boldsymbol{\beta}). \tag{3.32}$$

Therefore, the quadruple moment on source plane is given by

$$\begin{aligned} Q_{ij}^{(s)} &= \frac{\int \mathrm{d}^2\beta\, W(\beta)(\beta_i - \bar{\beta}_i)(\beta_j - \bar{\beta}_j) f^{(s)}(\boldsymbol{\beta})}{\int \mathrm{d}^2\beta\, W(\beta) f^{(s)}(\boldsymbol{\beta})} \\ &= \frac{\int \mathrm{d}^2\theta \det A\; W(A\theta)\, A_{ik}(\theta_k - \bar{\theta_k})\, A_{j\lambda}(\theta_\lambda - \bar{\theta_\lambda}) f(\boldsymbol{\theta})}{\int \mathrm{d}^2\theta \det A\; W(A\theta) f(\boldsymbol{\theta})} \\ &= A_{ik}(\bar{\theta}) Q_{k\lambda} A_{j\lambda}(\bar{\theta}). \end{aligned} \tag{3.33}$$

Here, we define two good measures of ellipticity $\boldsymbol{\epsilon} = \epsilon_1 + i\epsilon_2$ as

$$\epsilon_1 \equiv \frac{Q_{11} - Q_{22}}{Q_{11} + Q_{22} + 2\sqrt{Q_{11}Q_{22} - 2Q_{12}^2}}, \tag{3.34}$$

$$\epsilon_2 \equiv \frac{2Q_{12}}{Q_{11} + Q_{22} + 2\sqrt{Q_{11}Q_{22} - 2Q_{12}^2}}. \tag{3.35}$$

This complex parameter $\boldsymbol{\epsilon}$ can be defined in the same way on source plane. Thus, the relation of ellipticity between source plane and observed plane is given by

$$\boldsymbol{\epsilon} = \frac{\boldsymbol{\epsilon}_{\rm int} + \boldsymbol{g}}{1 + \boldsymbol{g}^* \boldsymbol{\epsilon}_{\rm int}}, \tag{3.36}$$

where we use Eq. (3.33) and the above relation is valid for $|\boldsymbol{g}| \leq 1$. Complex reduced shear $\boldsymbol{g}$ is defined by

$$\boldsymbol{g} \equiv \frac{\gamma_1}{1-\kappa} + i\frac{\gamma_2}{1-\kappa}. \tag{3.37}$$

In the weak lensing regime (i.e. $\kappa, \gamma_i \ll 1$), the observed ellipticity can be an estimator of shear as follows;

$$\boldsymbol{\epsilon} = \boldsymbol{\gamma} + \boldsymbol{\epsilon}_{\rm int}, \tag{3.38}$$

where $\boldsymbol{\epsilon}_{\rm int}$ represents the intrinsic ellipticity of source galaxies. The current ground-based observations indicate $\sigma_{\rm int} = \sqrt{\langle |\boldsymbol{\epsilon}_{\rm int}|^2 \rangle} \simeq 0.4$ (e.g., [97]). This value is much larger than the expected signal of cosmic shear of each galaxy by a factor of $\sim 10 - 100$. Thus, the statistical analysis of galaxy's ellipticity is crucial to extract the cosmological information from the shape measurement of galaxies.

3.3 Statistics

3.3.1 Two Point Correlation Function

In the presence of the intrinsic ellipticity called shape noise, we need to perform some statistical analysis of ellipticities of source galaxies in order to use it as cosmological probe. The conventional statistical quantity is two point correlation function of ellipticity of galaxies. Here, we will summarize the formulation of two point correlation function of ellipticity of galaxies.

First of all, we will start to consider the convergence power spectrum, i.e. two point correlation in fourier space. The convergence power specturm contains the information of the power spectrum of density fluctuation δ because convergence relates to δ through Eq. (3.15). Although we consider the specific case that all the sources locate at the same redshift in Eq. (3.15), source galaxies have the distribution of redshift in practice. We can take into account the effect of redshift distribution of source galaxies on Eq. (3.15) as follows;

$$\kappa(\boldsymbol{\theta}) = \int_0^{\chi_H} \mathrm{d}\chi\ q(\chi)\delta(\chi, r(\chi)\boldsymbol{\theta}), \tag{3.39}$$

$$q(\chi) \equiv \frac{3}{2}\left(\frac{H_0}{c}\right)^2 \Omega_{\mathrm{m}0} W_{\mathrm{GL}}(\chi)\frac{r(\chi)}{a(\chi)}, \tag{3.40}$$

$$W_{\mathrm{GL}}(\chi) = \int_\chi^{\chi_H} \mathrm{d}\chi' G(\chi')\frac{r(\chi'-\chi)}{r(\chi')}, \tag{3.41}$$

where $G(\chi)$ represents the redshift distribution of source galaxies and χ_H is the comoving distance up to $z \to \infty$. Let us calculate the convergence power spectrum with Eq. (3.39). The two point correlation function of convergence is defined by

$$\langle\kappa(\boldsymbol{\theta})\kappa(\boldsymbol{\theta}')\rangle = \int \mathrm{d}\chi q(\chi) \int \mathrm{d}\chi' q(\chi')\langle\delta(\chi, r(\chi)\boldsymbol{\theta})\delta(\chi', r(\chi')\boldsymbol{\theta}')\rangle. \tag{3.42}$$

The fourier transform of the above equation provides the relation between the convergence power spectrum and matter density power spectrum. We can obtain the following equation by fourier transforming of δ;

$$\begin{aligned}\langle\kappa(\boldsymbol{\theta})\kappa(\boldsymbol{\theta}')\rangle &= \int \mathrm{d}\chi\ q(\chi) \int \mathrm{d}\chi'\ q(\chi') \int \frac{\mathrm{d}^3k}{(2\pi)^3} \int \frac{\mathrm{d}^3k'}{(2\pi)^3}\langle\delta(\chi, \boldsymbol{k})\delta(\chi', \boldsymbol{k}')\rangle \\ &\times \exp\left[-ir(\chi)\boldsymbol{k}_\perp \cdot \boldsymbol{\theta} - ir(\chi')\boldsymbol{k}'_\perp \cdot \boldsymbol{\theta}' - ik_\parallel \chi - ik'_\parallel \chi'\right],\end{aligned} \tag{3.43}$$

where $\boldsymbol{k}_\perp$ and $k_\parallel$ represent the wave vector in the perpendicular and the parallel direction on the line of sight, respectively. Assuming that the comoving distance $r(\chi)$ does not change significantly at angular scale of interest, i.e. $r(\chi') \simeq r(\chi), q(\chi') = q(\chi)$, we can

calculate the two point correlation of convergence as

$$\langle\kappa(\boldsymbol{\theta})\kappa(\boldsymbol{\theta}')\rangle = \int \mathrm{d}\chi\, q^2(\chi) \int \frac{\mathrm{d}^2 k_\perp}{(2\pi)^2} P(\chi, k_\perp) \exp\left[-ir(\chi)\boldsymbol{k}_\perp \cdot (\boldsymbol{\theta}-\boldsymbol{\theta}')\right]. \tag{3.44}$$

The power spectrum in two dimensional space is expressed as

$$P_\kappa(\ell) = \int \mathrm{d}^2\theta \langle\kappa(\boldsymbol{\theta})\kappa(\boldsymbol{\theta}')\rangle e^{i\boldsymbol{\ell}\cdot(\boldsymbol{\theta}-\boldsymbol{\theta}')}. \tag{3.45}$$

Therefore, the convergence power spectrum is given by

$$P_\kappa(\ell) = \int \mathrm{d}\chi \frac{q^2(\chi)}{r^2(\chi)} P\left(\chi, \frac{\ell}{r(\chi)}\right). \tag{3.46}$$

We can also calculate the power spectrum of γ_i by using Eq. (3.11). Here, we generalize Eq. (3.11) in the same way as Eq. (3.39);

$$\Phi_{ij}(\boldsymbol{\theta}) = \int_0^{\chi_H} \mathrm{d}\chi W_\Phi(\chi)\partial_i\partial_j\Phi(\chi'), \tag{3.47}$$

$$W_\Phi(\chi) = \frac{2}{c^2} r(\chi) \int_\chi^{\chi_H} \mathrm{d}\chi'\, G(\chi') \frac{r(\chi-\chi')r(\chi')}{r(\chi)}. \tag{3.48}$$

Then, the power spectrum of Φ_{ij} is defined by

$$\langle\Phi_{ij}(\boldsymbol{\ell})\Phi_{lm}(\boldsymbol{\ell}')\rangle = (2\pi)^2\delta^{(2)}(\boldsymbol{\ell}+\boldsymbol{\ell}')P^\Phi_{ijlm}(\ell) \tag{3.49}$$

with the two-dimensional power spectrum of

$$P^\Phi_{ijlm}(\ell) = \int_0^{\chi_H} \mathrm{d}\chi \frac{W_\Phi^2}{r^2} \frac{\ell_i\ell_j\ell_l\ell_m}{r^4} P_\Phi(k=\ell/r), \tag{3.50}$$

where $P_\Phi(k)$ represents the power spectrum of gravitational potential. We can easily obtain the power spectrum of lensing quantities κ and γ_i in terms of $P_\Phi(k)$ as follows;

$$P_\kappa(\ell) = \frac{\ell^4}{4} \int_0^{\chi_H} \mathrm{d}\chi \frac{W_\Phi^2}{r^6} P_\Phi(k=\ell/r), \tag{3.51}$$

$$P_{\gamma_1}(\ell_1,\ell_2) = P_\kappa(\ell)\cos^2(2\phi_\ell), \tag{3.52}$$

$$P_{\gamma_2}(\ell_1,\ell_2) = P_\kappa(\ell)\sin^2(2\phi_\ell), \tag{3.53}$$

where $\ell_1 = \ell\cos(\phi_\ell)$ and $\ell_2 = \ell\sin(\phi_\ell)$. Therefore, the two point correlation function of γ_i is given by

$$\begin{aligned}
\langle\gamma_1(0)\gamma_1(\boldsymbol{\theta})\rangle &= \frac{1}{16\pi}\int_0^\infty \mathrm{d}\ell\,\ell^5 \int_0^{\chi_H} \mathrm{d}\chi\,\frac{W_\Phi^2}{r^6}P_\Phi(k=\ell/r) \\
&\quad \times\left[J_0(\ell\theta) + J_4(\ell\theta)\cos(4\phi)\right], \qquad (3.54)\\
\langle\gamma_2(0)\gamma_2(\boldsymbol{\theta})\rangle &= \frac{1}{16\pi}\int_0^\infty \mathrm{d}\ell\,\ell^5 \int_0^{\chi_H} \mathrm{d}\chi\,\frac{W_\Phi^2}{r^6}P_\Phi(k=\ell/r) \\
&\quad \times\left[J_0(\ell\theta) - J_4(\ell\theta)\cos(4\phi)\right], \qquad (3.55)\\
\langle\gamma_1(0)\gamma_2(\boldsymbol{\theta})\rangle &= \frac{1}{16\pi}\int_0^\infty \mathrm{d}\ell\,\ell^5 \int_0^{\chi_H} \mathrm{d}\chi\,\frac{W_\Phi^2}{r^6}P_\Phi(k=\ell/r) \\
&\quad \times\left[J_4(\ell\theta)\sin(4\phi)\right], \qquad (3.56)
\end{aligned}$$

where $J_0(x)$ ($J_4(x)$) is the zero-th (fourth) bessel function and $\theta_1 = \theta\cos\phi$ and $\theta_2 = \theta\sin\phi$.

Then, we can construct the correlation functions of shear which is defined the tangential and cross component of $\gamma = \gamma_1 + i\gamma_2$ as

$$\begin{aligned}
\gamma_t &\equiv -\mathcal{R}e(\gamma \mathrm{e}^{-2i\phi}), \qquad (3.57)\\
\gamma_\times &\equiv -\mathcal{I}m(\gamma \mathrm{e}^{-2i\phi}). \qquad (3.58)
\end{aligned}$$

Finally, we can obtain the linear combination of the cross-correlation function of γ_t and $\gamma_\times$ as follows [98];

$$\begin{aligned}
\xi_\pm(\theta) &\equiv \langle\gamma_t(0)\gamma_t(\boldsymbol{\theta})\rangle \pm \langle\gamma_\times(0)\gamma_\times(\boldsymbol{\theta})\rangle, \qquad (3.59)\\
&= \frac{1}{2\pi}\int \mathrm{d}\ell\,\ell P_\kappa(\ell) J_{0,4}(\ell\theta), \qquad (3.60)
\end{aligned}$$

where the Bessel function J_0 (J_4) corresponds to the correlation function of ξ_+ (ξ_-). Eq. (3.59) can relate to the convergence power spectrum (i.e. Eq. (3.46)) and is a function of separation angle only. Thus, $\xi_\pm$ is easily measurable in practice and enables us to compare with theoretical prediction for a given cosmological model.

Ref. [99] shows that the two point correlation functions are estimated in an unbiased way by averaging over pairs of galaxies. In practice, the estimator $\hat{\xi}_\pm$ is calculated by

$$\begin{aligned}
\hat{\xi}_\pm(\theta) &= \frac{1}{N_p(\theta)}\sum_{ij} w_i w_j \left(\epsilon_t(\boldsymbol{\theta}_i)\epsilon_t(\boldsymbol{\theta}_j) \pm \epsilon_\times(\boldsymbol{\theta}_i)\epsilon_\times(\boldsymbol{\theta}_j)\right)\Delta_\theta(\boldsymbol{\theta}_i - \boldsymbol{\theta}_j), \qquad (3.61)\\
N_p(\theta) &= \sum_{ij} w_i w_j \Delta_\theta(\boldsymbol{\theta}_i - \boldsymbol{\theta}_j), \qquad (3.62)
\end{aligned}$$

where w_i is weight related to shape measurement, $\Delta_\theta(\boldsymbol{\phi}) = 1$ for $\theta - \Delta\theta/2 \le \phi \le \theta - \Delta\theta/2$ and zero otherwise, and $\epsilon_{t,\times}(\boldsymbol{\theta}_i)$ is the tangential and cross component of ith source

galaxy's ellipticity. The expectation value of this estimator is evaluated by an ensemble average of the shear field γ. According to Eq. (3.38), an ensemble average $\langle \epsilon_{ti}\epsilon_{tj} \pm \epsilon_{\times i}\epsilon_{\times j} \rangle$ is given by

$$\langle \epsilon_{ti}\epsilon_{tj} \pm \epsilon_{\times i}\epsilon_{\times j} \rangle = \sigma^2_{\rm int}\delta_{ij} + \xi_{\pm}(\theta), \tag{3.63}$$

where we here assume the source ellipticity to be oriented randomly. Thus, we can see that this estimator is unbiased, i.e. $\langle \hat{\xi}_{\pm}(\theta) \rangle = \xi_{\pm}(\theta)$. Then, we can calculate the covariance of $\hat{\xi}_{\pm}$, which is defined by

$$\mathrm{Cov}(\hat{\xi}_{\pm}, \theta_1, \hat{\xi}_{\pm}, \theta_2) \equiv \langle (\hat{\xi}_{\pm}(\theta_1) - \xi_{\pm}(\theta_1))(\hat{\xi}_{\pm}(\theta_2) - \xi_{\pm}(\theta_2)) \rangle. \tag{3.64}$$

In the calculation of Eq. (3.64), the four point correlation function of ellipticity appears. The four point correlation function of ellipticity can be given by

$$\begin{aligned} \langle \epsilon_{\alpha i}\epsilon_{\beta j}\epsilon_{\mu k}\epsilon_{\nu \ell} \rangle &= \langle \gamma_{\alpha i}\gamma_{\beta j}\gamma_{\mu k}\gamma_{\nu \ell} \rangle + \langle \epsilon_{{\rm int},\alpha i}\epsilon_{{\rm int},\beta j}\epsilon_{{\rm int},\mu k}\epsilon_{{\rm int},\nu \ell} \rangle + \frac{\sigma^2_{\rm int}}{2}\big(\delta_{j\ell}\delta_{\beta\nu}\langle \gamma_{\alpha i}\gamma_{\mu k} \rangle \\ &\quad + \delta_{jk}\delta_{\beta\mu}\langle \gamma_{\alpha i}\gamma_{\nu \ell} \rangle + \delta_{i\ell}\delta_{\alpha\nu}\langle \gamma_{\beta j}\gamma_{\mu k} \rangle + \delta_{ik}\delta_{\alpha\mu}\langle \gamma_{\beta j}\gamma_{\nu \ell} \rangle\big), \end{aligned} \tag{3.65}$$

where the above equation is valid for $i \neq j$ and $k \neq \ell$ and Greek letters represent 1 or 2. It is difficult to calculate the four point correlation of the shear field without numerical simulations at present [100]. Here, assuming that the shear field and the source ellipticity are Gaussian, we can write the four point correlation as the product of the two point function as follows;

$$\begin{aligned} \langle \epsilon_{\alpha i}\epsilon_{\beta j}\epsilon_{\mu k}\epsilon_{\nu \ell} \rangle &= \langle \gamma_{\alpha i}\gamma_{\beta j} \rangle \langle \gamma_{\mu k}\gamma_{\nu \ell} \rangle + \langle \gamma_{\alpha i}\gamma_{\mu k} \rangle \langle \gamma_{\beta j}\gamma_{\nu \ell} \rangle + \langle \gamma_{\alpha i}\gamma_{\nu \ell} \rangle \langle \gamma_{\beta j}\gamma_{\mu k} \rangle \\ &+ \left(\frac{\sigma^2_{\rm int}}{2}\right)^2 (\delta_{ik}\delta_{j\ell}\delta_{\alpha\mu}\delta_{\beta\nu} + \delta_{i\ell}\delta_{jk}\delta_{\alpha\nu}\delta_{\beta\mu}) + \frac{\sigma^2_{\rm int}}{2}\big(\delta_{j\ell}\delta_{\beta\nu}\langle \gamma_{\alpha i}\gamma_{\mu k} \rangle \\ &+ \delta_{jk}\delta_{\beta\mu}\langle \gamma_{\alpha i}\gamma_{\nu \ell} \rangle + \delta_{i\ell}\delta_{\alpha\nu}\langle \gamma_{\beta j}\gamma_{\mu k} \rangle + \delta_{ik}\delta_{\alpha\mu}\langle \gamma_{\beta j}\gamma_{\nu \ell} \rangle\big). \end{aligned} \tag{3.66}$$

From Eq. (3.66) and the fact that

$$\epsilon_{ti}\epsilon_{tj} + \epsilon_{\times i}\epsilon_{\times j} = \epsilon_{1i}\epsilon_{1j} + \epsilon_{2i}\epsilon_{2j}, \tag{3.67}$$

$$\epsilon_{ti}\epsilon_{tj} - \epsilon_{\times i}\epsilon_{\times j} = (\epsilon_{1i}\epsilon_{1j} - \epsilon_{2i}\epsilon_{2j})\cos 4\phi_{ij} + (\epsilon_{1i}\epsilon_{1j} + \epsilon_{2i}\epsilon_{2j})\sin 4\phi_{ij}, \tag{3.68}$$

where ϕ_{ij} is the polar angle of $\boldsymbol{\theta}_i - \boldsymbol{\theta}_j$, we can express the covariance of $\hat{\xi}_\pm$ as follows;

$$\begin{aligned}
\mathrm{Cov}(\hat{\xi}_+, \theta_1, \hat{\xi}_+, \theta_2) &= \frac{1}{N_p(\theta_1)N_p(\theta_2)}\Big[\sigma^4_{\rm int}\delta_{\theta_1\theta_2}\sum_{ij} w_i^2 w_j^2 \Delta_{\theta_1}(ij) \\
&+ 2\sigma^2_{\rm int}\sum_{ijk} w_i^2 w_j w_k \Delta_{\theta_1}(ij)\Delta_{\theta_2}(ik)\xi_+(jk) \\
&+ \sum_{ijk\ell} w_i w_j w_k w_\ell \Delta_{\theta_1}(ij)\Delta_{\theta_2}(k\ell) \\
&\qquad \times\big(\xi_+(i\ell)\xi_+(jk) + \cos\left[4(\phi_{i\ell}-\phi_{jk})\right]\xi_-(i\ell)\xi_-(jk)\big)\Big], \qquad (3.69) \\
\mathrm{Cov}(\hat{\xi}_-, \theta_1, \hat{\xi}_-, \theta_2) &= \frac{1}{N_p(\theta_1)N_p(\theta_2)}\Big[\sigma^4_{\rm int}\delta_{\theta_1\theta_2}\sum_{ij} w_i^2 w_j^2 \Delta_{\theta_1}(ij) \\
&+ 2\sigma^2_{\rm int}\sum_{ijk} w_i^2 w_j w_k \Delta_{\theta_1}(ij)\Delta_{\theta_2}(ik)\xi_+(jk)\cos\left[4(\phi_{ij}-\phi_{ik})\right] \\
&+ \sum_{ijk\ell} w_i w_j w_k w_\ell \Delta_{\theta_1}(ij)\Delta_{\theta_2}(k\ell) \\
&\qquad \times\big(\cos\left[4(\phi_{ij}-\phi_{i\ell}-\phi_{jk}+\phi_{k\ell})\right]\xi_-(i\ell)\xi_-(jk) \\
&\qquad\qquad + \cos\left[4(\phi_{ij}-\phi_{k\ell})\right]\xi_+(i\ell)\xi_+(jk)\big)\Big], \qquad (3.70) \\
\mathrm{Cov}(\hat{\xi}_+, \theta_1, \hat{\xi}_-, \theta_2) &= \frac{1}{N_p(\theta_1)N_p(\theta_2)}\Big[2\sigma^2_{\rm int}\sum_{ijk} w_i^2 w_j w_k \Delta_{\theta_1}(ij)\Delta_{\theta_2}(ik)\xi_-(jk)\cos\left[4(\phi_{ik}-\phi_{jk})\right] \\
&+ 2\sum_{ijk\ell} w_i w_j w_k w_\ell \Delta_{\theta_1}(ij)\Delta_{\theta_2}(k\ell)\cos\left[4(\phi_{i\ell}-\phi_{k\ell})\right]\xi_-(i\ell)\xi_+(jk)\Big], \qquad (3.71)
\end{aligned}$$

where we use the result of Eqs. (3.54), (3.55), and (3.56).

3.3.2 Lensing Mass Reconstruction

Reconstruction of mass density (or convergence) field from observed ellipticity of galaxies is first proposed in Ref. [101] (KS92). The primary motivation of the reconstruction of mass density in KS92 is to investigate mass distribution in clusters and the method proposed in KS92 have been applied to real data set by Ref. [102]. However, Seitz and Schneider have pointed out that the reconstruction algorithm in KS92 would be problematic in practice because of the boundary artifacts on finite sky coverage [91]. They then have proposed the modification of the method in KS92 by taking into account the finite field in observation.

On the other hand, instead of the reconstruction of convergence field itself, Ref. [103] has proposed the statistical analysis based on the *smoothed* convergence field with some smoothing function for the purpose of detection of dark matter concentration. The statistics of the smoothed convergence field are currently known as the powerful tool to measure the abundance of dark matter haloes (e.g., [104, 105, 106]) and the higher-order

moments of underlying dark matter field (e.g., [107, 108]). In the following, we focus on the smoothed convergence field as a cosmological probe.

Let us first define the smoothed lensing convergence field:

$$\mathcal{K}(\boldsymbol{\theta}) = \int \mathrm{d}^2\phi \; \kappa(\boldsymbol{\theta} - \boldsymbol{\phi}) U(\boldsymbol{\phi}), \tag{3.72}$$

where U is the filter function to be specified below. We can calculate the same quantity by smoothing the shear field γ as

$$\mathcal{K}(\boldsymbol{\theta}) = \int \mathrm{d}^2\phi \; \gamma_t(\boldsymbol{\phi} : \boldsymbol{\theta}) Q_t(\boldsymbol{\phi}), \tag{3.73}$$

where γ_t is the tangential component of the shear at position $\boldsymbol{\phi}$ relative to the point $\boldsymbol{\theta}$. The filter function for the shear field Q_t is related to U by

$$Q_t(\theta) = \int_0^\theta \mathrm{d}\theta' \; \theta' U(\theta') - U(\theta). \tag{3.74}$$

We consider Q_t to be defined with a finite extent. In this case, one finds

$$U(\theta) = 2 \int_\theta^{\theta_o} \mathrm{d}\theta' \; \frac{Q_t(\theta')}{\theta'} - Q_t(\theta), \tag{3.75}$$

where θ_o is the outer boundary of the filter function.

In this thesis, we consider the truncated Gaussian filter (for U) as

$$U(\theta) = \frac{1}{\pi\theta_G^2} \exp\left(-\frac{\theta^2}{\theta_G^2}\right) - \frac{1}{\pi\theta_o^2}\left(1 - \exp\left(-\frac{\theta_o^2}{\theta_G^2}\right)\right), \tag{3.76}$$

$$Q_t(\theta) = \frac{1}{\pi\theta^2}\left[1 - \left(1 + \frac{\theta^2}{\theta_G^2}\right)\exp\left(-\frac{\theta^2}{\theta_G^2}\right)\right], \tag{3.77}$$

for $\theta \leq \theta_o$ and $U = Q_t = 0$ elsewhere. Throughout this thesis, we adopt $\theta_G = 1$ arcmin and $\theta_o = 15$ arcmin. Note that this choice of θ_G is considered to be an optimal smoothing scale for the detection of massive galaxy clusters using weak-lensing for source redshift of $z_{\mathrm{source}} = 1.0$ [58].

It is important to use appropriately the weight associated with shape measurement when making smoothed convergence maps. In practice, we can estimate $\mathcal{K}$ by generalizing Eq. (3.73):

$$\mathcal{K}(\boldsymbol{\theta}_i) = \frac{\sum_j Q_t(\boldsymbol{\phi}_j) w_j \epsilon_t(\boldsymbol{\phi}_j : \boldsymbol{\theta}_i)}{\sum_j Q_t(\boldsymbol{\phi}_j) w_j}, \tag{3.78}$$

where the summation in Eq. (3.78) is taken over all the source galaxies that are located within θ_o from ith pixel.

3.3.3 Minkowski Functionals

In 1970's–1980's, there has been a debate about the nature of the topology of large scale structure in the universe. At that time, there were two competing models: the hierarchical clustering model [109] and the cell structure model [110]. The former model appears in a cold dark matter (CDM) scenario, i.e. high-density regions would be seen as isolated clumps and low-density regions are connected. The latter model predicts that the largest structure first forms and then fragment into smaller objects. The cell structure model is so-called "top-down" type model of structure formation in the universe. In order to examine the connectedness of the high- and the low-density regions in the universe, Ref. [111] has proposed a measure of topology by using of a density contour of galaxy distribution and they have found that both the high- and low-density region are connected, which can be explained naturally by the initial *Gaussian* condition in the inflationary models. The more qualitative studies in measuring the topology of galaxy distribution have been presented in, e.g., Refs. [112, 113, 114]. In particular, Gott et al. (1989) [114] have applied their developed technique of measuring of topology to real data set and they have found that the CDM model give a good fit to the observed measure of the topology of galaxy distribution.

On the other hand, the measure of two dimensional topology has been initiated in e.g., Refs. [115, 116, 117]. Coles (1988) [115] has studied the statistical geometry of the two-dimensional random field in order to examine the conventional assumption that the primordial density fluctuations are a Gaussian random field. This interesting idea has been applied to the current data of comic microwave background [118, 119] and the topological analysis on sky can be a powerful probe to constrain on *non-Gaussianity* in underlying random field.

Minkowski functionals (MFs) are among the most useful statistics to extract non-Gaussian information from a two-dimensional or three-dimensional field. MFs are morphological statistics for some smoothed random field above a certain threshold. In general, for a given D-dimensional smoothed field $\mathbb{S}^D$, one can calculate $D+1$ MFs V_i. On $\mathbb{S}^2$, one can thus define 2+1 MFs V_0, V_1, and V_2. For a given threshold, V_0, V_1, and V_2 describe the fraction of area, the total boundary length of contours, and the integral of the geodesic curvature K_g along the contours, respectively. MFs are defined,

for threshold ν, as

$$V_0(\nu) \equiv \frac{1}{4\pi}\int_{Q_\nu} \mathrm{d}S, \tag{3.79}$$

$$V_1(\nu) \equiv \frac{1}{4\pi}\int_{\partial Q_\nu} \frac{1}{4}\mathrm{d}\ell, \tag{3.80}$$

$$V_2(\nu) \equiv \frac{1}{4\pi}\int_{\partial Q_\nu} \frac{1}{2\pi}K_g \mathrm{d}\ell, \tag{3.81}$$

where Q_ν and ∂Q_ν represent the excursion set and the boundary of the excursion set for a smoothed field $u(\boldsymbol{\theta})$. They are given by

$$Q_\nu = \{\boldsymbol{\theta} \,|\, u(\boldsymbol{\theta}) > \nu\}, \tag{3.82}$$

$$\partial Q_\nu = \{\boldsymbol{\theta} \,|\, u(\boldsymbol{\theta}) = \nu\}. \tag{3.83}$$

Here, geodesic curvature is defined as

$$K_g \equiv |\nabla_{\dot{\zeta}}\dot{\zeta}|, \tag{3.84}$$

where $\dot{\zeta}$ is the tangent vector along the contour curve ζ and $\nabla_{\dot{\zeta}}$ represents the covariant derivative along the curve. Note that V_2 equals to the genus statistic in a two-dimensional space as found in e.g., Ref. [120]. The genus statistic has been used as the measure of topology in the three-dimensional galaxy distribution [112, 113, 114] and the two-dimensional anisotropy of cosmic microwave background [115]. The genus statistic $G_2(\nu)$ in a two-dimensional space is defined by

$$\begin{aligned} G_2(\nu) = \Big[&(\text{the number of contours surrounding regions higher than the threshold value } \nu) \\ - \;&(\text{the number of contours surrounding regions lower than the threshold value } \nu)\Big], \end{aligned} \tag{3.85}$$

per unit area of the surface. We summarize the schematic picture of MFs for two-dimensional random field in Figure 3.1.

For a two-dimensional Gaussian random field, we can calculate the expectation values for MFs analytically [121];

$$V_0(\nu) = \frac{1}{2}\left[1 - \mathrm{erf}\left(\frac{\nu-\mu}{\sigma_0}\right)\right], \tag{3.86}$$

$$V_1(\nu) = \frac{1}{8\sqrt{2}}\frac{\sigma_1}{\sigma_0}\exp\left(-\frac{(\nu-\mu)^2}{\sigma_0^2}\right), \tag{3.87}$$

$$V_2(\nu) = \frac{\nu-\mu}{2(2\pi)^{3/2}}\frac{\sigma_1^2}{\sigma_0^3}\exp\left(-\frac{(\nu-\mu)^2}{\sigma_0^2}\right), \tag{3.88}$$

where $\mu = \langle u \rangle$, $\sigma_0^2 = \langle u^2 \rangle - \mu^2$, and $\sigma_1^2 = \langle |\nabla u|^2 \rangle$.

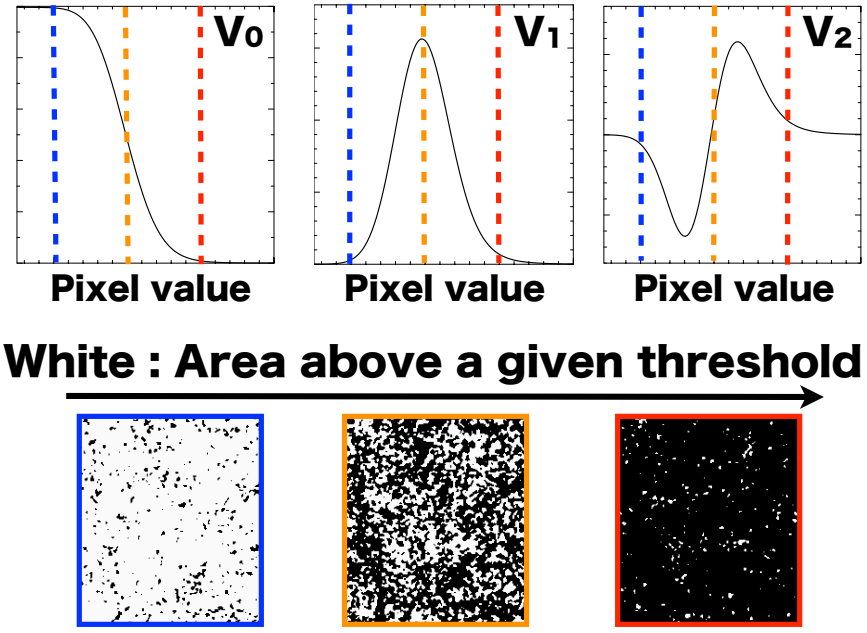

FIGURE 3.1: The schematic picture of Minkowski functionals (MFs). The upper panels show each MF for a given threshold. The blue, yellow and red line represent lower, medium and higher threshold, respectively. The lower panels show that three examples of the excursion sets on the hypothetical two-dimensional random field. In lower panels, white region shows area with a pixel value above a threshold and threshold increases from left to right.

In general, the expectation values for MFs can be expressed as [120]

$$V_k(\nu) = \frac{1}{(2\pi)^{(k+1)/2}} \frac{\omega_2}{\omega_{2-k}\omega_k} \left(\frac{\sigma_1}{\sqrt{2}\sigma_0}\right)^k e^{-x^2/2} v_k(x) \tag{3.89}$$

$$\omega_k = \frac{\pi^{k/2}}{\Gamma(k/2+1)}, \tag{3.90}$$

where $x = (\nu - \mu)/\sigma_0$ and ω_k represents the volume of the unit ball in the k-dimensioanl space, thus $\omega_0 = 1, \omega_1 = 2$, and $\omega_2 = \pi$. v_k in a general random field can be obtained by the cumulant expansion theorem of the multiplicative probability function of the series of spatial derivatives of u [120]:

$$v_k(x) = v_k^{(0)}(x) + v_k^{(1)}(x)\sigma_0 + v_k^{(2)}(x)\sigma_0^2 + \cdots, \tag{3.91}$$

where $v_k^{(0)} = H_{k-1}$ and H_k is the k-th Hermite polynomial. Here, $v_k^{(1)}$ is given by

$$v_k^{(1)}(x) = \frac{S}{6} H_{k+2}(x) - \frac{kS_{\rm I}}{4} H_k(x) - \frac{k(k-1)S_{\rm II}}{4} H_{k-2}(x), \tag{3.92}$$

where $S, S_{\rm I}$ and $S_{\rm II}$ are defined by

$$S = \frac{\langle F^3\rangle}{\sigma_0^4}, \tag{3.93}$$

$$S_{\rm I} = \frac{\langle F^2\nabla^2 F\rangle}{\sigma_0^2\sigma_1^2}, \tag{3.94}$$

$$S_{\rm II} = \frac{2\langle|\nabla F|^2\nabla^2 F\rangle}{\sigma_1^4}, \tag{3.95}$$

where $F = (u-\mu)/\sigma_0$. From Eq. (3.92), one can expect that MFs contain the information of higher-order moments of an underlying random field.

Ref. [122] constructed the estimator of MFs in pixelated maps as follows;

$$V_i(F_0) = \frac{1}{N_{\rm pix}}\sum_{j=1}^{N_{\rm pix}}\mathscr{I}_i(F_0,\boldsymbol{\theta}_j), \tag{3.96}$$

$$\mathscr{I}_0(F_0,\boldsymbol{\theta}_j) = \Theta(F-F_0), \tag{3.97}$$

$$\mathscr{I}_1(F_0,\boldsymbol{\theta}_j) = \frac{1}{4}(\delta F_0)^{-1}\left(\Theta(F-F_0+\delta F_0/2)-\Theta(F-F_0-\delta F_0/2)\right) \times \sqrt{F_x^2+F_y^2}, \tag{3.98}$$

$$\mathscr{I}_2(F_0,\boldsymbol{\theta}_j) = \frac{1}{2\pi}(\delta F_0)^{-1}\left(\Theta(F-F_0+\delta F_0/2)-\Theta(F-F_0-\delta F_0/2)\right) \times \frac{2F_xF_yF_{xy}-F_x^2F_{yy}-F_y^2F_{xx}}{F_x^2+F_y^2}, \tag{3.99}$$

where $N_{\rm pix}$ is the number of pixels on the map and $F_x = (\partial F/\partial\theta_x)_{\theta_x=\theta_{x,j}}$ and $F_x = (\partial F/\partial\theta_y)_{\theta_y=\theta_{y,j}}$.

There are several previous studies on MFs of weak gravitational lensing. Matsubara and Jain (2001) [123] and Sato et al. (2001) [124] studied $\Omega_{\rm m0}$-dependence of weak lensing MFs. While these studies mainly focus on the relatively weak non-Gaussian information of lensing MFs, Taruya et al. (2002) [125] have considered the highly non-Gaussian information and constructed the phenomenological model of lensing MFs based on numerical simulations. More recently, Kratochvil et al. (2012) [126] showed that the lensing MFs contain significant cosmological information, beyond the power-spectrum, whereas Ref. [127] showed weak lensing MFs can be used to constrain the statistical properties of the primordial density fluctuations.

According to these works, lensing MFs is receiving renewed attention as a cosmological probe in upcoming galaxy imaging surveys. However, cosmic shear field or convergence field show highly non-Gaussian feature due to the nature of non-linear gravitational growth of matter density fluctuations. Thus, it is difficult to construct the theoretical

template of lensing MFs by the analytic approach. The simplest but powerful methodology is to utilize a large set of mock weak lensing catalogs which are taken into account non-linearity due to gravitational growth and observational effects (e.g., intrinsic ellipticity of sources and finite sky coverage, etc.) simultaneously. In this thesis, we try to construct the theoretical template of lensing MFs with mock galaxy lensing catalogs and examine the utility and the applicability of lensing MFs as a cosmological probe.

3.4 Numerical Simulation of Weak Lensing

Here, we summarize the algorithm to simulate weak lensing effects of distant source objects with cosmological N-body simulations.

We first run a number of cosmological N-body simulations to generate a three-dimensional matter density field. We use the parallel Tree-Particle Mesh code `Gadget2` [128]. We generate the initial conditions using a parallel code developed by Refs. [129, 130], which employ the second-order Lagrangian perturbation theory, e.g., [131]. The initial redshift is set to $z_{\rm init} = 50$, where we compute the linear matter transfer function using `CAMB` [81]. Our fiducial cosmology adopts the following parameters: matter density $\Omega_{\rm m0} = 0.279$, dark energy density $\Omega_{\Lambda 0} = 0.721$, the amplitude of curvature fluctuations $A_s = 2.41 \times 10^{-9}$ at the pivot scale $k = 0.002{\rm Mpc}^{-1}$, the parameter of the equation of state of dark energy $w_0 = -1$, Hubble parameter $h = 0.700$ and the scalar spectral index $n_s = 0.972$. These parameters are consistent with the WMAP nine-year results [19]. To investigate the degeneracy of the cosmological parameters in lensing statistics, we also run the same set of simulations but with slightly different $\Omega_{\rm m0}$, w_0 and A_s. The simulation parameters are summarize in Table 3.1.

For ray-tracing simulations of gravitational lensing, we generate light-cone outputs using multiple simulation boxes in the following manner. Our small- and large-volume simulations are placed to cover the past light-cone of a hypothetical observer with some angular extent, similarly to the methods in Refs. [132, 133].

All the quantities associated with weak lensing effects can be determined by the lens equation as shown in Eq. (3.7). According to the lens equation, the deflection angle can be described by the weighted integral of gravitational potential along a line of sight. In the standard multi-plane algorithm, the integral found in the lens equation is devided into N intervals with the separated comoving distance of $\Delta\chi$. The surface matter density on lens planes is obtained by the projection of the three-dimensional matter density field realized in N-body simulations. Hence, the surface matter density on p-th lens plane

$\Sigma^p(\boldsymbol{\theta})$ is calculated by

$$\Sigma^p(\boldsymbol{\theta}) = \int_{\chi_{p-1}}^{\chi_p} \mathrm{d}\chi\, \delta(\chi\boldsymbol{\theta}, \chi), \tag{3.100}$$

where $\delta = \rho/\bar{\rho} - 1$, χ_p is the comoving distance of p-th lens plane and $\boldsymbol{\theta}$ represents the angular coordinate on sky. According to Poisson equation, $\Sigma^p(\boldsymbol{\theta})$ can be related to the two-dimensional gravitational potential as follows;

$$\nabla^2\Phi^p(\boldsymbol{\theta}) = \frac{3\Omega_m H_0^2}{c^2}\Sigma^p(\boldsymbol{\theta}), \tag{3.101}$$

where $\Phi^p(\boldsymbol{\theta})$ is the gravitational potential on p-th lens plane. One can obtain the first and second derivatives of $\Phi^p(\boldsymbol{\theta})$ under the periodic boundary condition by fourier-transforming Eq. (3.101). The derivatives of $\Phi^p(\boldsymbol{\theta})$ is used to evaluate the distortion tensor and the deflection angle on n-th lens plane;

$$\boldsymbol{\theta}^n = \boldsymbol{\theta}^1 - \sum_{p=1}^{n-1} \frac{r(\chi_n - \chi_p)}{a(\chi_p)r(\chi_n)} \nabla_\perp \Phi^p \tag{3.102}$$

$$\mathbf{A}^n = \mathbf{I} - \sum_{p=1}^{n-1} \frac{r(\chi_p)r(\chi_n - \chi_p)}{a(\chi_p)r(\chi_n)} \mathbf{U}^p, \tag{3.103}$$

$$\mathbf{U}^p_{ij} = \begin{pmatrix} \Phi^p_{,11} & \Phi^p_{,12} \\ \Phi^p_{,12} & \Phi^p_{,22} \end{pmatrix} \tag{3.104}$$

$$\Phi^p_{,ij} \equiv \frac{\partial^2 \Phi^p}{\partial x_i \partial x_j}, \tag{3.105}$$

where $x_i = \chi\theta_i$ and $\mathbf{A}^n$ and $\boldsymbol{\theta}^n$ represent the distortion tensor and the deflection angle on n-th lens plane, respectively. In practice, we evaluate the matter density field in N-body simulations with the triangular shaped cloud (TSC) assignment scheme [134]. Then, the surface matter density is obtained as follows in Eq. (3.100) and the derivatives of the gravitational potential on each plane is provided by Eq. (3.101). In these steps, the pixelation on the surface matter density maps is required. Therefore, we have the following numerical parameters in weak lensing simulations: the number of particles in N-body simulation $N_{\rm sim}$, the box size of N-body simulation on a side $L_{\rm box}$, an angular extent in lensing simulations $\theta_{\rm sim}$, the comoving width in multi-plane algorithm $\Delta\chi$, and the number of pixels in the surface matter density maps on each lens plane $N_{\rm pix}$. First of all, $\theta_{\rm sim}$ can be determined by the request how large sky coverage is needed. In this thesis, $\theta_{\rm sim}$ is set to be 10 deg, which is large enough to consider the case of the current lensing data set. $N_{\rm sim}$, $L_{\rm box}$, $N_{\rm pix}$ and $\Delta\chi$ are associated with generating the surface mass density on each lens plane. Let us consider the simple case: $L_{\rm box}$ is chosen so that they are multiples of $\Delta\chi$. In this case, Ref. [133] tested some cases and

found that $N_{\rm sim}/(L_{\rm box}/\Delta\chi) \sim O(1) \times N_{\rm pix}$ is optimal in considering the case of source redshift of $z_{\rm source} \sim 1$ and the spatial resolution of ~ 0.1 arcmin. In order to take into account the objects with mass of $\sim 10^{14}\, M_\odot h^{-1}$ appropriately in simulations, the mass of particle in N-body simulation should be set to an order of $\sim 10^{11}\, M_\odot h^{-1}$ at least. From these conditions, we choose that $N_{\rm sim} = 512^3$, $L_{\rm box} = 480$ or $960\ h^{-1}$Mpc (to cover $10 \times 10\,{\rm deg}^2$, from $z = 0$ to 3), $\Delta\chi = 120\ h^{-1}$Mpc, and $N_{\rm pix} = 8192^2$. The similar set-up has been tested in e.g., Ref. [38]. The configuration of our simulation is found in Figure 3.2. Note that we reduce the number of pixel on a side by a factor of 2 in the step of Eq. (3.102) and Eq. (3.103). This is because the path of each ray does not necessarily pass through the pixel on each lens plane due to the deflection of path of each ray. Therefore, the angular grid size of our maps is $10\,{\rm deg}/4096 \sim 0.15$ arcmin and 4096^2 rays are traced backward from the observer point. For each ray, we first computed ray positions on all lens planes in an iterative manner, using the lens equation Eq. (3.102). The derivatives of gravitational potentials on a ray position are linearly interpolated from four nearest grids on the pre-computed maps with 8192^2 pixels. We use outputs from independent realizations when generating the light-cone outputs. We also randomly shift the simulation boxes in order to avoid the same structure appearing multiple times along a line of sight. In total, 40 independent shear maps are generated from four N-body simulations for each cosmological model.

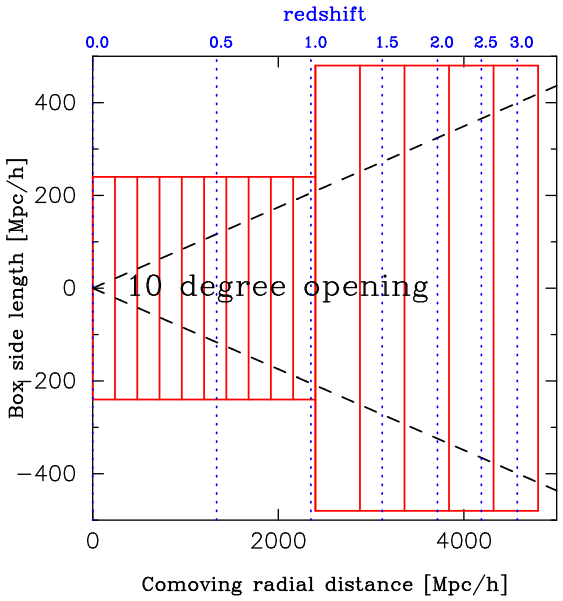

FIGURE 3.2: The configuration of our ray-tracing simulation. Each red line shows a boundary of N-body simulations. We avoid the overlap of N-body boxes along the line of sight with use of a part of box.

	$\Omega_{\rm m0}$	w_0	$A_s \times 10^9$	σ_8	# of N-body sims	# of maps
Fiducial	0.279	-1.0	2.41	0.823	4	40
High $\Omega_{\rm m0}$	0.304	-1.0	2.41	0.878	4	40
Low $\Omega_{\rm m0}$	0.254	-1.0	2.41	0.763	4	40
High w_0	0.279	-0.8	2.41	0.768	4	40
Low w_0	0.279	-1.2	2.41	0.862	4	40
High A_s	0.279	-1.0	2.51	0.840	4	40
Low A_s	0.279	-1.0	2.31	0.806	4	40

TABLE 3.1: Cosmological parameters for our N-body simulations used in this thesis. We also show the resulting σ_8. For each parameter set, we run 4 N-body realizations and generate 40 weak-lensing shear maps. We utilize the set of simulations shown here to generate the mock weak lensing catalog for CFHTLenS data.

Chapter 4

Weak Lensing Morphological Analysis

Here, we will study the true utility and applicability of weak lensing Minkowski functionals (MFs) in terms of statistical tool for *precision* cosmology. The previous studies on weak lensing MFs shown in Section. 3.3.3 often consider idealized cases. However, there are many observational effects in real weak lensing measurements, for example, imperfect shape measurement due to seeing and optical distortion, selection effects of galaxies, uncertain redshift distribution of galaxies due to photometric redshift error (e.g., [135]), noise-rectification biases (e.g., [136, 137, 138]), and complicated survey geometry due to masked regions. Refs. [44, 139] have studied some of these effects on cosmic shear power spectrum analysis. A comprehensive study of observational effects on lensing MFs is also necessary for purpose of making the best use of the data from upcoming wide cosmological surveys.

4.1 Impact of Masked Region

First, we investigate the impact of masked regions on the measurement of weak lensing MFs. Masking effect on sky could be one of the major systematics because MFs are defined by morphological quantities such as contours. We use a large set of numerical simulations of weak lensing to examine the masking effect. We then compare the measured MFs from real data obtained from a Subaru survey with the results of our ray-tracing simulations that include the effect of masked regions as same as the observed sky.

4.1.1 Estimation of Lensing MFs from Cosmic Shear Data

The smoothed lensing map (i.e. $\mathcal{K}$) would be constructed from the observed ellipticity of source galaxies by the method in Section. 3.3.2. In the measurement of lensing MFs, we convert a weak lensing field $\mathcal{K}$ to $x = (\mathcal{K} - \langle\mathcal{K}\rangle)/\sigma_0$ where σ_0 is the standard deviation of $\mathcal{K}$. In binning the thresholds, we set $\Delta x = 0.2$ from $x = -5$ to $x = 5$. We then follows the method shown in Section. 3.3.3 in order to estimate the lensing MFs from $\mathcal{K}$ field. The above normalization can affect the MFs through the variance of σ_0 for each field. In light of this problem, there is an alternative definition of the threshold suggested in Ref. [112] as follows:

$$f = (2\pi)^{-1/2} \int_{\nu_V}^{\infty} e^{-t^2/2} \mathrm{d}t, \tag{4.1}$$

where ν_V is a density contour with a certain threshold and f represents the fraction of volume. We can apparently avoid the normalization issue by using ν_V instead of x for measurement of MFs. However, even with ν_V, it is difficult to eliminate the effect of the variance between multiple fields because we have to use the $f - \nu_V$ mapping for each field or for each sample, rather than by using some global quantity calculated for all the samples. Here, we have tested the effect of the sample variance of σ_0 on MFs against ν_V and x with 1000 Gaussian simulations[1].

Figure 4.1 shows the comparison of the mean of V_2 over our 1000 Gaussian maps with the Gaussian prediction given by Eq. (3.88). For the Gaussian prediction, we evaluate the quantities $\langle\mathcal{K}\rangle$, σ_0 and σ_1 by averaging over 1000 realizations; these quantities serve as "global" values. The error bars in each panel represent the variance of V_2 around the global mean. The three top panels show the different cases that the MFs are plotted as a function of, from left to right, $\mathcal{K} - \langle\mathcal{K}\rangle$, $(\mathcal{K} - \langle\mathcal{K}\rangle)/\sigma_0$, and ν_V, respectively. The apparent variation of the MF in the middle and right panels is partly caused by the variance of the measured σ_0 for each field. The lower panels represent the difference between the mean V_2 and the Gaussian prediction. The difference should be compared with the field variance, namely error bars. We find that the difference from the Gaussian prediction is larger than the field variance when the MFs are evaluated with normalization as $(\mathcal{K} - \langle\mathcal{K}\rangle)/\sigma_0$ or by using ν_V associated with volume fraction (see, Eq. (4.1)). As a matter of course, the Gaussian prediction describes the mean MFs well as long as the MFs are evaluated *without* normalization of $\mathcal{K}$ by σ_0 (left panel). However, we cannot use *unnormalized* weak lensing field $\mathcal{K}$ on morphological analysis when we compare

[1] We generate the Gaussian convergence maps for ΛCDM cosmology. In Gaussian simulation, we use the fitting formula of Ref. [140] to calculate the matter power spectrum $P(k; z)$. We then obtain the convergence power spectrum by integrating the matter power spectrum over redshift z with a weighting function for the source redshift $z_{\rm source} = 1$. Each map is defined on 2048^2 grid points with an angular grid size of 0.15 arcmin.

theoretical predictions with the observation of a limited area (with masks). This is because theoretical predictions for MFs are always given as a function of some normalized threshold. This means that one needs either to de-normalize the theoretical prediction by using an appropriate variance for the observed field, or to normalize the observed $\mathcal{K}$ in some way. In other words, field-to-field variance of the weak lensing MFs is originated partly from the variance σ_0. Thus, in cosmological parameter estimation with such measurement, one should take into account the field variance of σ_0. In the rest of this thesis, we simply use the normalized field $x = (\mathcal{K} - \langle\mathcal{K}\rangle)/\sigma_0$ for estimation of MFs. When estimating lensing MFs on a $\mathcal{K}$ map with mask, we discard the pixels within $2\theta_G$ from the boundaries of mask, because $\mathcal{K}$ data on the vicinity of the mask boundaries are affected by the lack of shear data.

4.1.2 Data

4.1.2.1 Suprime-Cam

In this section, we summarize i'-band data from the Subaru/Suprime-Cam data archive SMOKA[1]. The observation have been performed in the contiguous area with at least four pointings. In the observation, the exposure time for each pointing is longer than 1800 sec and the seeing full width at half-maximum (FWHM) is better than 0.65 arcsec. The same data are found in Table A1 in Ref. [141], denoted to "COSMOS".

In this thesis, we use the data only within a 15 arcmin radius from the field center of Suprime-Cam, because the elongation of point spread function (PSF) becomes significant outside of the central area, which makes PSF correction inaccurate in the shape measurement. Then we performed mosaic stacking with `SCAMP` [142] and `SWarp` [143]. We use `SExtractor` [144] and $hfindpeaks$ of the software `IMCAT` software [145], and then we merged the two catalogs by matching positions of the detected objects with a tolerance of 1 arcsec.

For weak lensing analysis, we adopt the KSB method (e.g., [145, 146, 147]). We selected stars in the standard way by finding the appropriate branch in the magnitude half-light radius (rh) plane, along with the detection significance cut $S/N > 10$. Number density of stars is ~ 1 arcmin^{-2}. We then select the galaxy images by the following three conditions; (i) the detection significance of $S/N > 3$ and $\nu > 10$ where ν is an estimate of the peak significance given by $hfindpeaks$, (ii) rh is larger than the stellar branch, and (iii) the AB magnitude is in the range of $22 < i' < 25$ (where MAG_AUTO given by `SExtractor` is used for the magnitude and slightly different from [141]). The resulting

[1] http://smoka.nao.ac.jp/

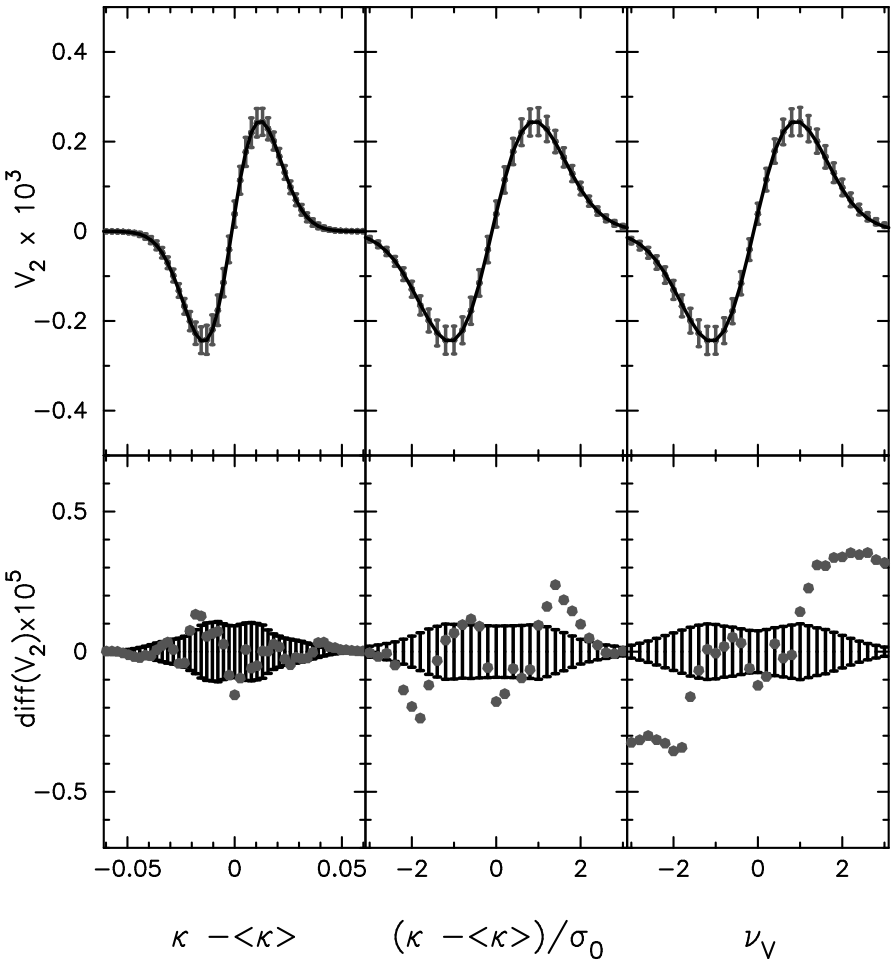

FIGURE 4.1: The effect of sample variance of field variance σ_0 on weak lensing MFs (taken from [1]). The three panels show the comparison of the mean V_2 over 1000 maps with the Gaussian prediction of Eq. (3.88) for three different estimations of V_2. In the left panel, V_2 is calculated without normalization, while that in the middle panel is calculated for each $\mathcal{K}$ field normalized by its variance and that in the right panel is calculated for each ν_V. The gray points in the lower panels represent the differences between the mean V_2 and the Gaussian prediction. The differences should be compared with the variance of V_2 estimated from our 1000 gaussian maps (black error bars), that is the standard deviation of V_2 divided by $\sqrt{1000}$.

number density of galaxies $n_{\rm gal}$ is then 15.8 arcmin^{-2}. We measured the shapes of the objects with *getshapes* in `IMCAT`, and corrected for the PSF with the KSB method. The *rms* of the galaxy ellipticities after the PSF correction is found to be 0.314.

We next define data and masked regions by the observed positions of the source galaxies as follows. We consider the pixelated map on the observation area with rectangular pixels of width 0.15 arcmin. For each pixel, we check whether there is a galaxy within $\theta_D = 0.4$ arcmin from the pixel center or not. We set the value of θ_D so that mean number of galaxies within $\pi\theta_D^2$ would be equivalent to $\sim 3\sigma$ confidence levels of poisson distribution (i.e. $n_{\rm gal}\pi\theta_D^2/\sqrt{n_{\rm gal}\pi\theta_D^2} \simeq 3$). If we can find no galaxies, then the pixel is

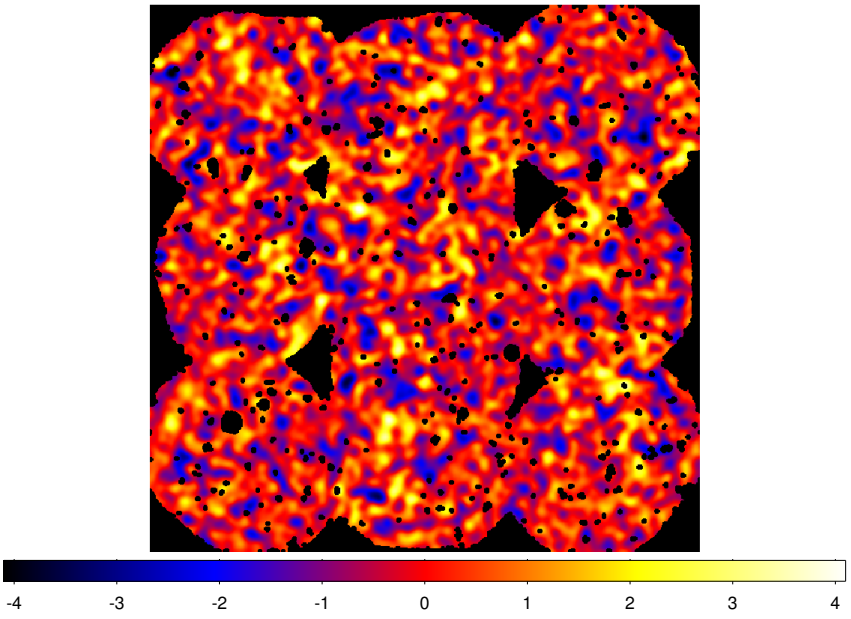

FIGURE 4.2: The lensing field $\mathcal{K}$ reconstructed from the Subaru Suprime-Cam data. The ellipticity of 102342 source galaxies are used for reconstruction of the convergence $\mathcal{K}$. The masked survey area (black portion) is found to be 0.34 deg^2. The color bar represents the value of $(\mathcal{K} - \langle\mathcal{K}\rangle)/\sigma_0$.

marked as a mask pixel. After performing the procedure for all the pixels, the marked pixels are masked regions, whereas the other pixels are data regions. However, we do not mask "isolated" masked pixels whose surrounding pixels are all data pixels.

We computed weak lensing convergence field $\mathcal{K}$ from the galaxy ellipticity data as in Eq. (3.73) on regular grids with a grid spacing of 0.15 arcmin. Figure 4.2 shows the resulting mass map and masked regions. The masked regions cover 0.34 deg^2 in total. The area on unmasked regions are 1.79 deg^2. Note that we use only 0.575 deg^2 in unmasked regions for lensing MFs analysis because we remove the pixels within $2\theta_G = 2$ arcmin from the mask boundaries.

4.1.2.2 Ray-tracing Simulation from Sato et al. (2009)

In order to study the impact of masked regions on lensing MFs, we use 1000 weak gravitational lensing ray-tracing simulations from Ref. [38][2]. The ray-tracing simulations are to cover a past light-cone of a hypothetical observer with an angular extent of $5^\circ \times 5^\circ$, from redshift $z = 0$ to $z = 3.5$, similarly to the methods in Section. 3.4. We use the ray-tracing simulations with the source redshift of $z_{\rm source} = 1$. Each map is defined on

[2] For the simulations, the authors in Ref. [38] adopted the cosmological model which is consistent with WMAP three-years results [148].

2048^2 grid points with an angular grid size of 0.15 arcmin. Details of the ray-tracing simulations are found in Ref. [38].

It is well-known that the intrinsic ellipticity of source galaxies is one of the main contaminants on lensing shear maps. We take into account the noise by adding random ellipticities drawn from a two-dimensional Gaussian to the simulated shear data. The root-mean-square of intrinsic ellipticities is set to be 0.314 and we set the number of source galaxies is 15.8 arcmin^{-2}. Note that these values are obtained from the actual weak lensing observations in Section 4.1.2.1.

4.1.3 Bias due to Masking Effect

We then discuss the overall effect of masking on the lensing MFs. Here, we utilize ray-tracing simulations of weak gravitational lensing in Section 4.1.2.2. We focus on non-Gaussian features in the case with masked regions. The total non-Gaussianity probed by the lensing MFs $\Delta V_i^{\rm obs}$ is given by

$$\Delta V_i^{\rm obs} = V_i(\text{masked}) - V_i^G(\text{masked}), \tag{4.2}$$

where V_i(masked) is i-th MF on a masked map and V_i^G(masked) is the Gaussian term of V_i(masked).

One can then decompose $\Delta V_i^{\rm obs}$ into three components:

$$\begin{aligned}
\Delta V_i^{\rm obs} &= \Delta V_i^{\rm gravity} + \Delta V_i^{\rm bias} - \Delta V_i^{\rm bias,G}, && (4.3)\\
\Delta V_i^{\rm gravity} &= V_i(\text{unmasked}) - V_i^G(\text{unmasked}), && (4.4)\\
\Delta V_i^{\rm bias} &= V_i(\text{masked}) - V_i(\text{unmasked}), && (4.5)\\
\Delta V_i^{\rm bias,G} &= V_i^G(\text{masked}) - V_i^G(\text{unmasked}), && (4.6)
\end{aligned}$$

where $\Delta V_i^{\rm gravity}$ is the non-Gaussianity induced by non linear gravitational growth, $\Delta V_i^{\rm bias}$ represents the mask bias of MFs for non-Gaussian maps, and $\Delta V_i^{\rm bias,G}$ describes the Gaussian term of $\Delta V_i^{\rm bias}$. In order to evaluate these quantities, we first consider V_i^G(masked) and V_i^G(unmasked). We measure the following three quantities from 1000 masked ray-tracing maps:

$$\mu = \langle \mathcal{K} \rangle,\ \sigma_0^2 = \langle \mathcal{K}^2 \rangle - \mu^2,\ \sigma_1^2 = \langle |\nabla \mathcal{K}|^2 \rangle. \tag{4.7}$$

The same quantities are also measured for the unmasked lensing maps. We can then estimate V_i^G(masked) and V_i^G(unmasked) using these quantities and the theoretical formula Eq. (3.86)-Eq. (3.88). For the Gaussian terms, we also take into account the correction

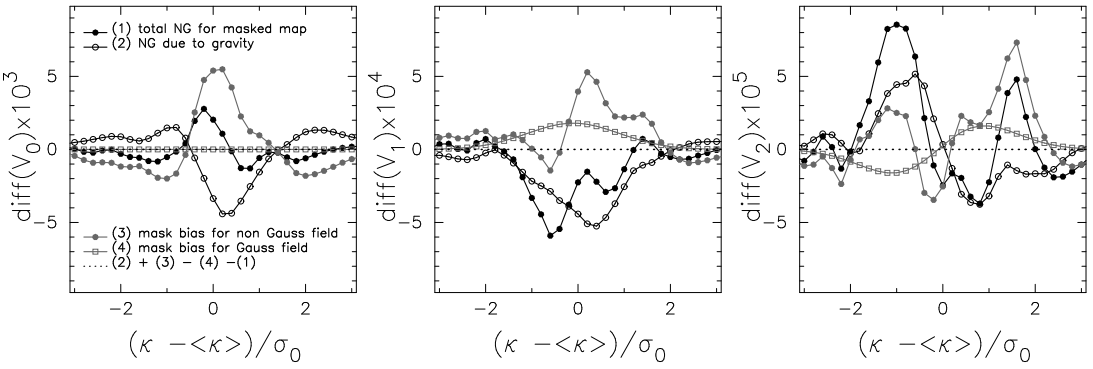

FIGURE 4.3: The differences between the lensing MFs on masked ray-tracing simulation maps and the Gaussian term (taken from [1]). In this figure, the various components are plotted: the total non-Gaussianity obtained from the masked maps $\Delta V_i^{\rm obs}$ (black line with closed circle), the non-Gaussianity caused by non-linear gravitational growth $\Delta V_i^{\rm gravity}$ (black line with open circle), the bias of lensing MFs due to masked regions for ray-tracing maps $\Delta V_i^{\rm bias}$ (gray line with closed circle), and the Gaussian term of $\Delta V_i^{\rm bias}$ (gray line with open square). The definition of each component is given by Eq. (4.2)-Eq. (4.6).

of the finite binning effect pointed out by Ref. [149]. The correction is caused by the fact that the threshold ν to calculate the MFs V_1 and V_2 is not continuous but discrete with some finite width. We calculate the correction by integrating the analytic formula (Eq. (3.87),Eq. (3.88)) for finite binning width (see Ref. [149] for details). V_i(masked) and V_i(unmasked) can be estimated directly from masked and unmasked maps with the estimated V_i^G(masked) and V_i^G(unmasked). We show the various non-Gaussian contributions (Eq. (4.3)-Eq. (4.6)) calculated directly from 1000 masked ray-tracing maps in Figure 4.3. It is shown that $\Delta V_i^{\rm bias}$ is comparable to $\Delta V_i^{\rm gravity}$ in the ray-tracing maps. We also find that the mask bias $\Delta V_i^{\rm bias}$ contributes significantly to the observed non-Gaussianity $\Delta V_i^{\rm obs}$. Note that $\Delta V_i^{\rm bias,G}$ is sub-dominant although not negligible for V_1 and V_2. This indicates clearly that the mask bias can be a significant contaminant for cosmological parameter estimation with the lensing MFs. The bias is expected to be induced for the following two reasons: (i) sky masking effectively reduce the number of sampling Fourier modes of cosmic shear and (ii) masked regions introduce scatter of the variance of the reconstructed weak lensing mass field. The former can be corrected analytically at least for a Gaussian random field as shown in the Appendix A, while numerical simulations are needed to include the latter effect accurately. In the following, we include the bias effect when comparing simulation data and observations.

4.1.4 Impact of Masking on Cosmological Parameter Estimation

We next consider cosmological information content in the lensing MFs with sky masking. The cumulative signal-to-noise ratio S/N is often used for study of information content.

S/N is defined by

$$(S/N)^2 = \boldsymbol{\mu}^t \boldsymbol{C}^{-1} \boldsymbol{\mu}, \tag{4.8}$$

where $\boldsymbol{\mu}$ is a data vector that consists of the lensing MFs V_0, V_1, and V_2, and $\boldsymbol{C}$ is the covariance matrix. In order to calculate $(S/N)^2$, the data vector are constructed from a set of lensing MFs as

$$\begin{aligned}\{\mu_i\} = \{&V_0(x_1), ..., V_0(x_{10}), V_1(x_1), ..., V_1(x_{10}), \\ &V_2(x_1), ..., V_2(x_{10})\},\end{aligned} \tag{4.9}$$

where $x_i = (\mathcal{K}_i - \langle\mathcal{K}\rangle)/\sigma_0$ is the binned normalized lensing field. We calculate the covariance matrix of MFs using 1000 ray-tracing simulations.

We show the cumulative signal-to-noise ratio S/N as a function of x_i in Figure 4.4. One can find that clearly the information content is reduced by a factor of two in the case with mask. We can explain the degradation by the reduced effective area. The solid line corresponds to S/N by scaling $\boldsymbol{C}^{-1}$ with the effective survey area. It closely matches the S/N calculated directly from the masked maps. For a Gaussian random field, it is expected that the variance of MFs should be inversely proportional to the effective survey area (e.g., [150, 151]). Thus, we expect that the effective survey area mainly would determine how much cosmological information we can gain from weak lensing MFs.

We further perform the following analysis to investigate the effect of the mask bias on cosmological parameter estimation. For each realization r of our simulations, the χ^2 value can be calculated as follows,

$$\chi^2(r) = (\mu_i(r) - \mu_i^{\rm theory})\boldsymbol{C}^{-1}(\mu_j(r) - \mu_j^{\rm theory}), \tag{4.10}$$

where $\mu_i(r)$ represents the estimated lensing MFs from each realization r and $\mu_i^{\rm theory}$ is the theoretical template for a given cosmology. In practice, we assume that $\mu_i^{\rm theory}$ corresponds to the average over our 1000 ray-tracing simulations with or without masks. We estimate the lensing MFs $\mu_i(r)$ for each masked map, and then we use the covariance matrices of the MFs obtained from a total of 1000 masked maps. If $\mu_i(r)$ follows the Gaussian distribution, the distribution of $\chi^2(r)$ should follow a genuine χ^2 distribution. Hence, we can discuss the impact of bias due to masking on cosmological constraints by comparing the resulting distribution of $\chi^2(r)$ for $\mu_i^{\rm theory}$ estimated from unmasked maps.

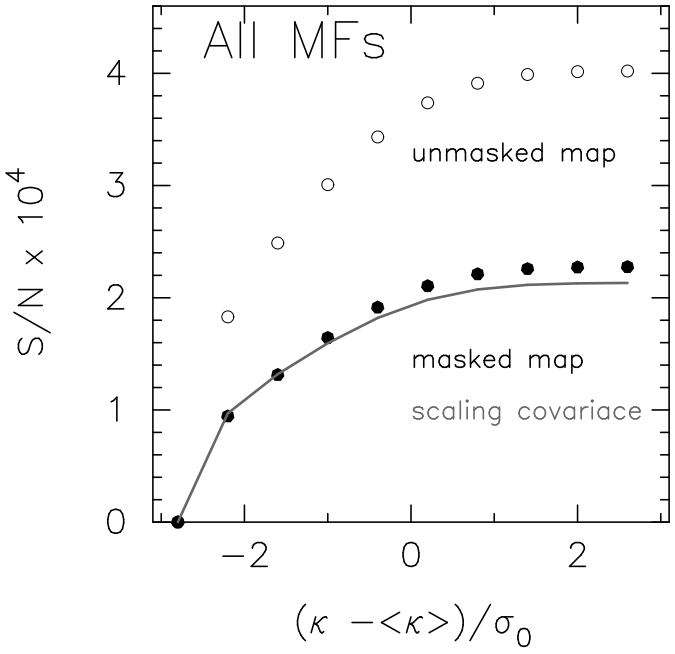

FIGURE 4.4: The cumulative signal-to-noise ratio for the weak lensing MFs (taken from [1]). The horizontal axis shows the maximum value of binned lensing field used in the calculation of S/N. The open circles represent the S/N for unmasked 'clean' lensing maps whereas the black points correspond to the case with masked regions. The solid line is S/N estimated with scaling the covariance matrices of MFs with the effective survey area. In this figure, the masked regions are same as the Subaru Suprime-Cam data (see Figure 4.2).

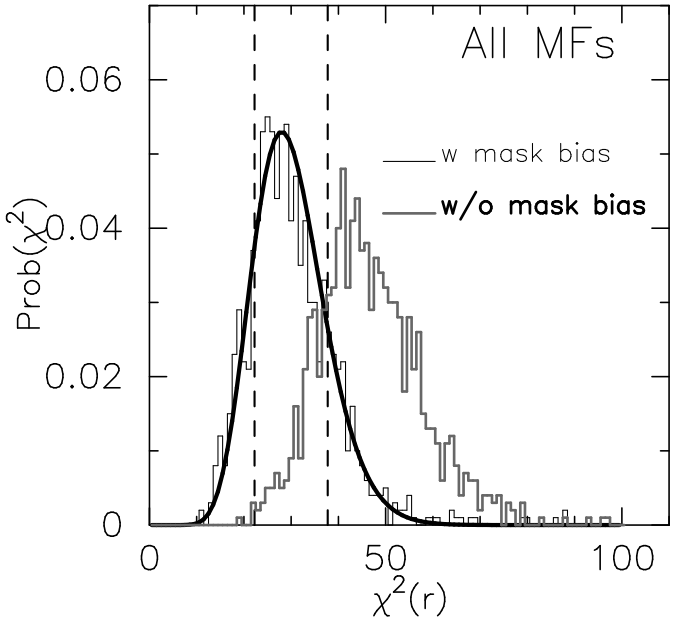

FIGURE 4.5: The distribution of $\chi^2(r)$ for $\mu_i^{\rm theory}$ evaluated for 1000 masked maps (black histogram) with that for $\mu_i^{\rm theory}$ evaluated for 1000 unmasked maps (taken from [1]). In this figure, the thick solid lines represent a genuine chi-square distribution with 30 degrees of freedom, and dashed line shows the one sigma region.

We show the resulting distribution of $\chi^2(r)$ for our 1000 masked ray-tracing simulations in Figure 4.5. The black histogram corresponds to the probability of $\chi^2(r)$ for the corresponding model using the average MFs over the masked maps whereas the gray one is for the unmasked maps. The thick solid line represents a genuine χ^2 distribution with 30 degrees of freedom, and the dashed line is the 1σ region for the χ^2 values. We find an excellent agreement between the thin histogram and the solid line. This means that the binned lensing MFs $\mu_i(r)$ can be described well by a Gaussian distribution. Interestingly, most of the resulting $\chi^2(r)$ without mask lie outside 1σ regions. When we do not include bias due to masked regions, 55.3%, 59.4%, 74.9% and 85.4% of the realizations lies outside 1σ regions of the χ^2 values for V_0, V_1, V_2 and all MFs. Therefore, we conclude that the bias of lensing MFs due to masked regions can crucially affect a cosmological parameter estimation.

4.1.5 Application to Subaru Suprime-Cam Data

Here, we test whether we can extract cosmological information from masked noisy shear data using the lensing MFs. In this section, we utilize available Subaru Suprime-Cam data. In order to compare with the observed lensing map and the simulated maps, we include two observational effects directly in our simulations, i.e., masked regions and shape noises as described in Section 4.1.2.2. Figure 4.6 shows the comparison with the lensing MFs for the Subaru data and those calculated for the ray-tracing simulations. The MFs V_0, V_1, and V_2 are plotted in the top panels. In the bottom panels, the thick error bars represent the cosmic variance of lensing MFs estimated from our 1000 simulated maps, whereas the thin error bars describe the sum of the cosmic variance and the statistical error. The statistical error is estimated from 1000 randomized realizations, in which the ellipticity of each source galaxy is rotated randomly. We find the statistical error is approximately ~ 1.5 times the cosmic variance for each bin. In order to quantify the consistency of our results, a so-called χ^2 analysis is performed. We compute the χ^2 statistics for the observed lensing MFs,

$$\chi^2 = (d_i - m_i){\boldsymbol{C}_{\rm cv+stat}}^{-1}(d_j - m_j) \tag{4.11}$$

where d_i is the lensing MFs in the i-th bin for observation, m_i is the theoretical model, and $\boldsymbol{C}_{\rm cv+stat}$ is the covariance matrix of lensing MFs including the cosmic variance and the statistical error. We again estimated the cosmic variances from 1000 ray-tracing simulations and the statistical errors from 1000 randomized galaxy catalogs, respectively. We estimate m_i by averaging the MFs over 1000 ray-tracing simulations. We adopt 10 linear binning in the range of $x = [-3, 3]$ for each MF. For the binning, we have a large number of simulations enough to evaluate the covariance matrix of the lensing

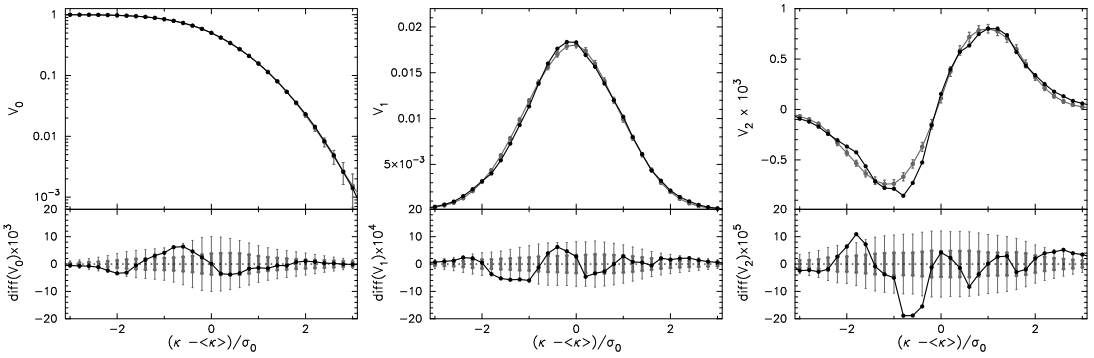

FIGURE 4.6: The comparison the observed MFs with those from cosmological ray-tracing simulations (taken from [1]). In the upper panels, the black line corresponds to the observed lensing MFs and the gray one shows the simulation results. The gray error bars represent the cosmic variance obtained from 1000 ray-tracing simulations. In the lower panels, the black line shows the difference between the obtained MFs and the simulation results. The thin error bars indicate the sum of the cosmic variance and the statistical error while the thick error bars show only the cosmic variance. 1000 randomized galaxy catalogues have been used for estimation of the statistical errors.

MFs. The resulting value of χ^2 per number of freedoms is found to be $\chi^2/n_{\rm dof} = 3.35/10, 9.69/10, 12.8/10$ and $29.6/30$ for V_0, V_1, V_2 and all the MFs. Thus, we conclude that the observed lensing MFs are consistent with the standard ΛCDM cosmology in the case of the observation with the small sky coverage (i.e. 0.575 deg^2).

4.2 Statistical and Systematic Error of Minkowski Functionals

In Section 4.1, we present the effect of masked regions on the measurement of weak lensing MFs. There, we showed that sky masking induces large non-Gaussianities, which could compromise measurement of the *true* non-Gaussianity associated with gravitational growth. This result leads that it is important to include directly realistic observational effects in order to apply the lensing MFs to data from future cosmology surveys. Here, we further explore several observational effects using the real data set from the Canada-France-Hawaii Lensing Survey (CFHTLenS). We use a large set of simulations described in Section 3.4 in order to study possible systematics in detail one by one. We finally present a forecast for future surveys such as Subaru HSC and LSST.

4.2.1 Mock weak lensing catalogs

4.2.1.1 Canada-France-Hawaii Telescope Lensing Survey

We use the data from the Canada-France-Hawaii Telescope Lensing Survey (CFHTLenS; [97]). CFHTLenS is a 154 deg^2 multi-color optical survey in the five optical bands $u^*, g', r', i',$ and z'. CFHTLenS has been optimized for weak-lensing analysis with a full multi-color depth of $i'_{AB} = 24.7$ with optimal sub-arcsecond seeing conditions. The survey consists of four regions called W1, W2, W3 and W4, with an area of $\sim$ 72, 30, 50 and 25 deg^2, respectively.

The CFHTLenS survey analysis mainly consists of the following processes: weak-lensing data processing with THELI [152], shear measurement with the *lens*fit [153], and photometric redshift measurement [154]. A detailed systematic error study of the shear measurements in combination with the photometric redshifts is presented in Ref. [97]. The additional error analyses of the photometric redshift measurements are presented in Ref. [155].

The ellipticities of the source galaxies in the data have been obtained with the *lens*fit algorithm. The *lens*fit performs a Bayesian model fitting to the imaging data by considering various ellipticity and size of a galaxy, and by taking into account the uncertainty of the centroid position. It also takes into account a forward convolution process expressed by convolving the galaxy model with the point-spread function (PSF) to estimate the posterior probability of the model given the data. The *lens*fit estimates the ellipticity ϵ of each galaxy as the mean likelihood of the model posterior probability after marginalizing over galaxy size, centroid position, and bulge fraction. Then, an inverse variance weight w is given by the variance of the ellipticity likelihood surface and the variance of the ellipticity distribution of the galaxy population. The *lens*fit algorithm has been tested with image simulations in detail. The observed ellipticities $\boldsymbol{\epsilon}^{\rm obs}$ with any shape measurement method are calibrated in practice as

$$\boldsymbol{\epsilon}^{\rm obs} = (1+m)\boldsymbol{\epsilon}^{\rm true} + \boldsymbol{c}, \tag{4.12}$$

where m is a multiplicative bias and $\boldsymbol{c}$ is an additive bias. In the case of *lens*fit, $\boldsymbol{c}$ is consistent with zero for a large set of simulated images but m cannot be negligible and it depends on both galaxy signal-to-noise ratio and size. On a weight average, this multiplicative bias corresponds to a 6 % correction. In terms of statistical quantities such as two point correlation function, this bias is easily corrected by multiplying an overall factor (see Ref. [153] for further details).

In the catalog of source galaxies of CFHTLenS, the photometric redshifts z_p are estimated by the `BPZ` code [156, Bayesian Photometric Redshift Estimation]. Ref. [155] has been shown that the true redshift distribution is well described by the sum of the probability distribution functions (PDFs) estimated from `BPZ`. The galaxy-galaxy lensing redshift scaling analysis in Ref. [97] confirms that contamination is unimportant for galaxies selected at $0.2 < z_p < 1.3$. In this redshift range, the weighted median redshift is found to be ~ 0.7 and the effective weighted number density $n_{\rm eff}$ is 11 per arcmin^2. In the following, we have used the source galaxies with $0.2 < z_p < 1.3$ to make the smoothed lensing mass map.

The effective survey area is an important quantity for lensing MFs. Ref. [97] performs systematic tests in order to find *clean* data in terms of two point correlation of cosmic shear. The fraction of data flagged by their procedure amounts to 25 % of the total CFHTLenS; this is indeed significant. In Section 4.1.4, it is shown that the effective survey area mainly determines the cosmological information content in the lensing MFs. More importantly, however, complicated geometries of the masked regions induce non-Gaussianities that contaminate the lensing MFs as shown in Figure 4.3. We thus have decided to use all the available data of CFHTLenS to make a wide *and* continuous map. We expect the systematics associated with the PSF to be relatively small compared to the masking effect on morphological statistics (see, e.g., Refs [97, 157]). When calculating the two point correlation function (2PCF), we use the *clean* sample of Ref. [97].

In order to construct the smoothed lensing convergence field $\mathcal{K}$, we use the estimator as in Eq. (3.73). We adopt the truncated Gaussian filter (for U) with the parameters of $\theta_G = 1$ arcmin and $\theta_o = 15$ arcmin. The weak-lensing convergence field $\mathcal{K}$ is then computed from the galaxy ellipticity data on regular grids with a grid spacing of 0.15 arcmin. In making the convergence map, we discard the pixels when the denominator in Eq. (3.73) is equal to zero. We define the boundaries by masking a pixel if the number of sources within θ_o from the pixel is less than $5\sqrt{15\pi\theta_o^2}$. This critical value effectively sets the signal-to-noise ratio of the number of sources inside a circle with radius of θ_o to be less than 5, on the assumption that the distribution of sources is approximated by a Poisson distribution. We repeat the above procedure for all the pixels. Note that the details of the procedure do not affect the final results significantly as long as we impose the same conditions to on all of the pixels, because our analysis is based on the comparison of two maps that have the same configuration of source positions. Figure 4.7 shows the obtained mass map in the CFHTLenS W1 field.

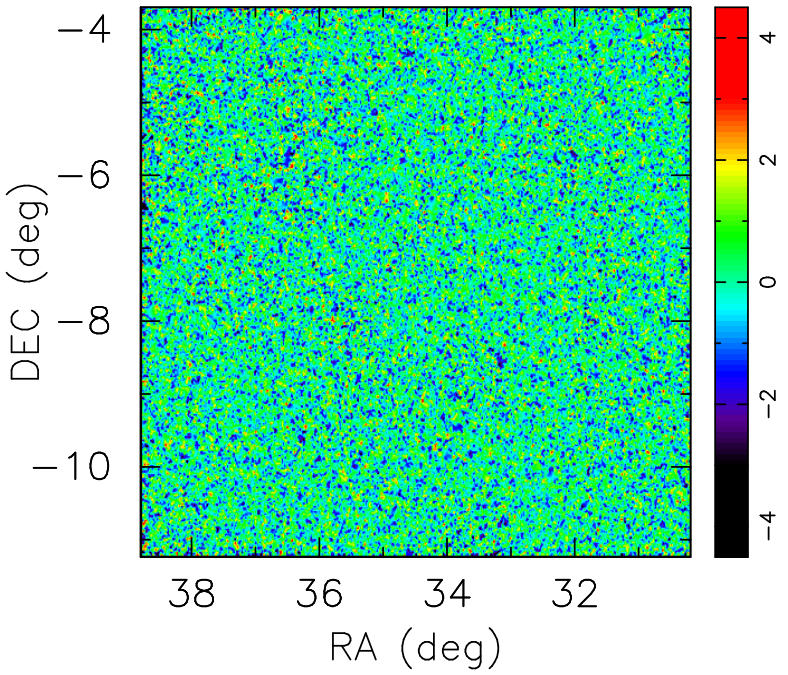

FIGURE 4.7: Reconstructed convergence field $\mathcal{K}$ in the CFHTLenS W1 field (taken from [2]). In this figure, the ellipticities of 2570270 source galaxies are used in the reconstruction of the $\mathcal{K}$ map. The color-scale bar represents the normalized value $(\mathcal{K} - \langle\mathcal{K}\rangle)/\sigma_0$.

4.2.1.2 Algorithm for mock catalogs

In order to study observational effects on weak-lensing morphological statistics, we generate realistic mock weak-lensing catalogs by combining ray-tracing simulations and the CFHTLenS data [157]. The main advantage of these mock catalogs is that we can directly use the observed positions on the sky of the source galaxies. This enables us to keep all the characteristics of the survey geometry the same as in CFHTLenS.

We locate the source galaxies in the pixel unit of our lensing map and then calculate the reduced shear signal $g = \gamma/(1-\kappa)$ at the galaxy positions. Ray-tracing is done up to the redshift of the galaxy as described in Section 3.4. In this step, a galaxy's redshift is set to be at the peak of the posterior PDF obtained from `BPZ`. This could cause systematic effects on morphological statistics originating from the inaccuracy of the photometric redshift estimation. We discuss the impact of the redshift distribution of sources on lensing morphological statistics later.

We next consider the intrinsic ellipticity that is known to be a major error source in cosmic shear measurement. To model the intrinsic ellipticity of each galaxy, we randomize the orientation of the observed ellipticity, while keeping its amplitude. The randomized ellipticity is then assigned as the intrinsic ellipticity $\epsilon_{\rm int}$ at each galaxy's position. The

final "observed" ellipticity is given by, as shown in Eq. (3.36),

$$\boldsymbol{\epsilon}_{\rm mock} = \frac{\boldsymbol{\epsilon}_{\rm int} + \boldsymbol{g}}{1 + \boldsymbol{g}^{*}\boldsymbol{\epsilon}_{\rm int}}, \tag{4.13}$$

where $\boldsymbol{\epsilon}_{\rm mock}$ is represented as a complex ellipticity.

Finally, we incorporate calibration correction in the shear measurement. We assign the weight associated with the shape measurement of *lens*fit and the shear calibration correction following Ref. [97]. The two factors determine the potential additive shear bias $\boldsymbol{c}$ and multiplicative bias m. We then apply the shear calibration correction to $\boldsymbol{\epsilon}_{\rm mock}$ by using bias factors m and $\boldsymbol{c}$ as

$$\boldsymbol{\epsilon}_{\rm mock} \rightarrow (1+m)\boldsymbol{\epsilon}_{\rm mock} + \boldsymbol{c}. \tag{4.14}$$

In this step, we assume that there is no correlation between $\boldsymbol{\epsilon}$ and $m, \boldsymbol{c}$. We have explicitly calculated the correlation between $\boldsymbol{\epsilon}$ and $m, \boldsymbol{c}$ at the source galaxy positions using the CFHTLenS data set, and found that there is indeed no significant correlation between the quantities.

Through the above procedures, we have successfully included the following observational effects in the morphological analysis that all or many of these effects are often ignored in previous works: (1) non-linear relation between the observed ellipticities and cosmic shear, (2) non-Gaussian distribution of the intrinsic ellipticities, (3) the masked survey area of CFHTLenS and the inhomogeneous angular distribution of the source galaxies, (4) imperfect shape measurements and (5) the redshift distribution of the source galaxies.

Figure 4.8 shows the two point correlation function measured from 40 mock catalogs. For simplicity, we estimate the two point correlation function without shape noises and calibration biases. Also, the weight associated with shape measurements is set to be unity. The colored points with error bars are the average $\xi_{\pm}$ in our mock lensing catalogs. The error bars show the standard deviation of estimator Eq. (3.61) over 40 realizations. For comparison, we also represent the theoretical prediction Eq. (3.60) with the model of non-linear matter power spectrum in Ref. [158]. Our mock catalogs provide a reasonable fit of the theoretical prediction with a level of two point statistics. In the following, we utilize these mock catalogs to discuss higher order statistics of interest, i.e. Minkowski functionals of smoothed convergence field.

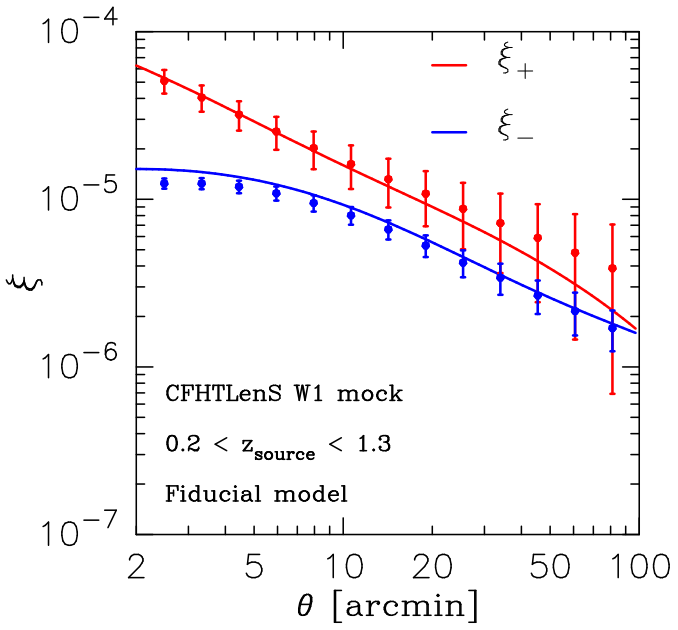

FIGURE 4.8: The two point correlation function of cosmic shear in our mock lensing catalogs. In this figure, we shows the average of $\xi_\pm$ over 40 realizations for our fiducial cosmological model. The points with error bars represent the results of $\xi_\pm$ measured from mock catalogs. The colored line is the theoretical prediction shown in Section 3.3.1.

4.2.2 Realistic forecast of cosmological constraints

4.2.2.1 Fisher analysis

In this section, we perform a Fisher analysis to produce a forecast for parameter constraints on $\Omega_{\rm m0}$, A_s, and w_0 with future weak-lensing surveys.

For a multivariate Gaussian likelihood, the Fisher matrix F_{ij} can be written as

$$F_{ij} = \frac{1}{2}\mathrm{Tr}\left[A_i A_j + C^{-1}M_{ij}\right], \tag{4.15}$$

where $A_i = C^{-1}\partial C/\partial p_i$, $M_{ij} = 2\left(\partial\mu/\partial p_i\right)\left(\partial\mu/\partial p_j\right)$, C is the data covariance matrix, μ represents the assumed model, and $\boldsymbol{p} = (\Omega_{\rm m0}, A_s, w_0)$ are the main parameters. Here, we consider only the second term in Eq. (4.15). Because C is expected to scale proportionally inverse to the survey area, the second term will be dominant for a large area survey (see, e.g., Ref. [159]). We model the theoretical template by averaging the MFs over 40 convergence maps with appropriate noises for each CFHTLenS field. Figure 4.9 shows the cosmological dependence of our model MFs thus calculated. We find the clear behavior of the MFs as a function of $\boldsymbol{p}$ even in the presence of various observational effects.

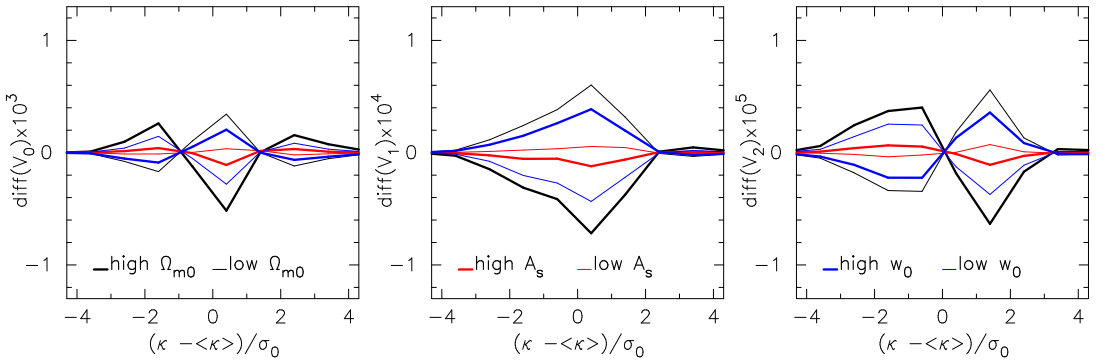

FIGURE 4.9: Variation of the lensing MFs for different cosmological parameters (taken from [2]). Each panel shows the differences of V_0, V_1, and V_2 with respect to those of our fiducial cosmology. In all of the panels, the thick (thin) black line represents the case of cosmological model with higher (lower) $\Omega_{\rm m0}$. The thick (thin) red one corresponds to the result of the cosmological model with higher (lower) A_s, and the thick (thin) blue one is for the model with higher (lower) w_0. For reference, the typical statistical errors of V_0,V_1, and V_2 at $(\mathcal{K} - \langle\mathcal{K}\rangle)/\sigma_0 = 0$ are $\sim 10^{-3}$, 10^{-4}, and 10^{-5}, respectively, for CFHTLenS.

We also calculate the model 2PCFs using the fitting formula of non-linear matter power spectrum of Ref. [158], on the assumption that the source redshift distribution is well approximated by the sum of the posterior PDF with $0.2 < z_p < 1.3$ given in Ref. [160].

To calculate the matrix M_{ij}, we approximate the first derivatives of the 2PCF and MFs with respect to cosmological parameter p_i as

$$\frac{\partial\mu}{\partial p_i} = \frac{\mu(p_i^{(0)} + \Delta p_i) - \mu(p_i^{(0)} - \Delta p_i)}{2\Delta p_i}, \tag{4.16}$$

where $\boldsymbol{p}^{(0)} = (0.279, 2.41 \times 10^{-9}, -1.0)$ gives our fiducial model parameters and we set $\Delta\boldsymbol{p} = (0.025, 0.1 \times 10^{-9}, 0.2)$.

We construct the data vector $\boldsymbol{D}$ from a set of binned MFs and 2PCFs,

$$\begin{aligned} D_i = \{&V_0(x_1), ..., V_0(x_{10}), V_1(x_1), ..., V_1(x_{10}), V_2(x_1), ..., V_2(x_{10}), \\ &\xi_+(\theta_1), ..., \xi_+(\theta_{10}), \xi_-(\theta_1), ..., \xi_-(\theta_{10})\}, \end{aligned} \tag{4.17}$$

where $x_i = (\mathcal{K}_i - \langle\mathcal{K}\rangle)/\sigma_0$ is the binned normalized lensing field. For the Fisher analysis, we use 10 bins in the range of $x_i = [-3, 3]$ [3]. In this range of x, Eq. (4.16) gives smooth estimates for M_{ij}. For the 2PCFs, we use 10 bins logarithmically spaced in the range of

[3] In principle, one can use regions with $x > 3$ as well. Such regions usually correspond to the positions of massive dark matter halos, which are thought to be sensitive to cosmological parameters. On the other hand, such regions are extremely rare, and thus the first derivatives in Eq. (4.16) are not evaluated accurately even with our large number of $\mathcal{K}$ maps. We thus do not use high $\mathcal{K}$ regions with $x > 3$ in the analysis.

$\theta_i = [0.9, 300]$ arcmin. A data vector has 50 elements, 3×10 MFs and 2×10 2PCFs, in total.

We therefore need a 50×50 data covariance matrix for the Fisher analysis. In order to estimate the sampling variance, we use 1000 shear maps made by Ref. [38] or in Section 4.1.2.2. The maps have almost the same design as our simulations, but are generated for slightly different cosmological parameters (consistent with WMAP three-years results [148]). The actual parameter differences are small, and also the dependence of the covariance matrix on cosmological parameters is expected to be weak. We model the intrinsic ellipticities by adding random ellipticities drawn from a two-dimensional Gaussian to the simulated shear data. We here set the rms of the intrinsic ellipticities to be 0.38 and the number of source galaxies is set to be 10 arcmin^{-2}. These are reasonable choices for the study here. In making the smoothed lensing map from the simulation outputs, we set the weight related to shape measurement to be unity. From the 1000 shear maps with appropriate noises, we can estimate the variances of the 2PCFs and MFs. The statistical errors can be estimated from randomized catalogs with rotating the observed orientation of the ellipticities. Using these randomized catalogs, the data covariance matrices in each CFHTLenS field can be estimated by the sum of sampling variance and the statistical error as

$$C_{\rm each} = C_{\rm cosmic} \left(\frac{A_{\rm each}\ {\rm deg}^2}{25\ {\rm deg}^2} \right)^{-1} + C_{\rm stat}, \tag{4.18}$$

where $C_{\rm cosmic}$ is sampling variance, $C_{\rm stat}$ represents the statistical error in each CFHTLenS field, and $A_{\rm each}$ corresponds to the effective survey area. In the following, we assume that the four CFHTLenS fields are independent of each other statistically. The total inverse covariance matrix for the whole CFHTLenS data is the sum of $C_{\rm each}^{-1}$ over the W1, W2, W3 and W4 fields. We forecast for future lensing surveys by simply scaling the data covariances by the survey area, assuming that the statistical error is identical to that in CFHTLenS. When calculating the inverse covariance, we include a debiasing correction, the so-called Anderson-Hartlap factor $\alpha = (n_{\rm real} - n_{\rm bin} - 2)/(n_{\rm real} - 1)$ with $n_{\rm rea} = 1000$ being the number of realization of simulation sets and $n_{\rm bin} = 50$ being the number of total bins in the data vector [161].

We expect that Eq. (4.18) provides a good approximation to the full covariance, but the accuracy needs to be addressed here. In the case of shear correlation functions, the covariance matrix consists of three components: a sampling variance, the statistical noise, and a third term coupling the two as shown in Section 3.3.1. However, because the MFs do not have the additivity of, e.g., $V_i(\nu_1 + \nu_2) = V_i(\nu_1) + V_i(\nu_2)$, it is not clear if the MF covariance can be expressed similarly as the sum of the three contributions. We thus resort to estimating the MF covariance in a direct manner by using the large set of

mock catalogs generated by the procedure shown in Section 4.2.1.2. Note that, in the procedure, we perform two randomization processes for a fixed cosmological model. One is to generate multiple realizations of the large scale structure (by N-body simulations) and the other is to randomize intrinsic ellipticities of the source galaxies. We perform each process separately, technically by fixing a random seed of the other process, to evaluate each term in Eq. (4.18). In principle, one can perform both of the processes simultaneously and derive the full covariance. However, this would require a huge number of mock catalogs. In Appendix C, we have done a simple but explicit check to validate that Eq. (4.18) indeed provides a reasonably good approximation. The details of our test and the result are shown there.

4.2.2.2 Forecast for Upcoming Survey

We now present a forecast for upcoming surveys such HSC and LSST. We first derive constraints on the cosmological parameters for a 154 deg^2 area survey, for which we have the full covariance matrix obtained in the previous sections. We then consider two wide surveys with an area coverage of 1400 deg^2 (HSC) and 20000 deg^2 (LSST). We simply scale the covariance matrix by a factor of 154/1400 or 154/20000 for them.

Let us begin with quantifying the statistical error associated with the real data. We have performed a Fisher analysis including the sampling variance and the statistical error. When including the statistical error, we found that the cosmological constraints are degraded by a factor of ~ 2 for the CHFTLens survey as shown in Figure 4.10. In Figure 4.10, the red error circle corresponds to the 1σ cosmological constraints including the sampling variance and the statistical error, while the blue one is obtained from the Fisher analysis without the statistical error.

We are now able to present a forecast for future lensing surveys covering larger sky areas on the assumption that the data covariance is same as that of CFHTLenS. Figure 4.11 shows the derived parameter constraints. The blue error circles corresponds to the 1σ constraints from the shear 2PCFs, whereas the red circles are cosmological constraints obtained from the lensing MFs. It is promising that, with Subaru HSC, we can constrain the dark energy equation of state w_0 with an error of $\Delta w_0 \sim 0.25$ by the lensing MFs *alone*. Table 4.1 summarizes the expected constraints by future surveys. Combining the 2PCFs and the MFs can improve the constraints by a factor of ~ 2 by breaking the degeneracy between the three parameters. It should be noted that this conclusion might seem slightly different from that of Ref. [126], who argue that adding the power spectrum does not effectively improve the constraints when all three MFs are already used. Our result suggests that combining the 2PCFs and the MFs improves cosmological parameter

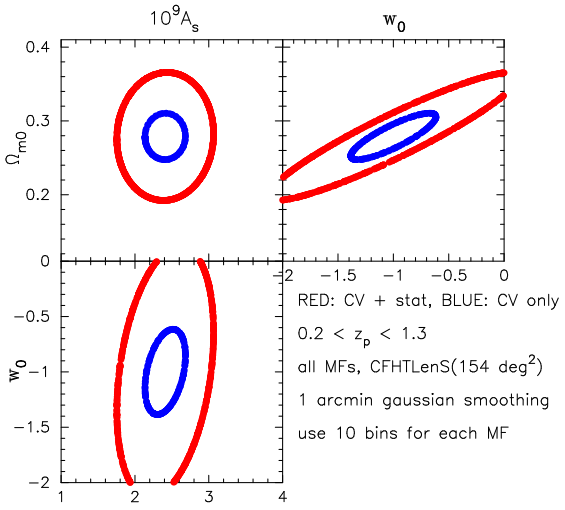

FIGURE 4.10: Impact of statistical errors on the cosmological parameter estimation (taken from [2]). Each panel shows the expected 1σ cosmological constraints by the lensing MFs in the CFHTLenS case. The red error circle presents forecast that includes sampling variance and the statistical error associated with the observational effects. The blue circle is obtained with only sampling variance included.

	$\Omega_{\rm m0}$	$A_s \times 10^9$	w_0
MFs only (1400 deg^2)	0.0190	0.143	0.248
MFs only (20000 deg^2)	0.00503	0.0380	0.0658
MFs + 2PCFs (1400 deg^2)	0.0110	0.132	0.139
MFs + 2PCFs (20000 deg^2)	0.00293	0.0351	0.0369

TABLE 4.1: The 1σ constraint on $\Omega_{\rm m0}$, A_s, and w_0, when marginalized over the other two parameters (taken from [2]). In this table, we take into account the sampling variance and the statistical error estimated from statistical analysis with CFHTLenS data. Two surveys are considered: one with a survey area of 1400 deg^2 (HSC) and another with 20000 deg^2 (LSST).

constraints appreciably. A precise account for the difference is not given by our analysis only, but there are many factors that can affect the parameter constraint. First of all, we characterize the amplitude of the matter power spectrum by the amplitude of curvature perturbations A_s at the cosmological recombination epoch whereas Ref. [126] adopt σ_8 at the present epoch as a parameter. The latter is the so-called derived parameter and has an internal degeneracy with $\Omega_{\rm m}$ and w_0. Our result suggests that including the 2PCFs in the analysis can better constrain A_s, which in turn yields tighter constraints on the other parameters. Furthermore, our analysis includes observational effects such as survey mask regions and the source distribution directly. Altogether, these differences make it difficult to compare our results with those of previous works that mostly adopt idealized configurations.

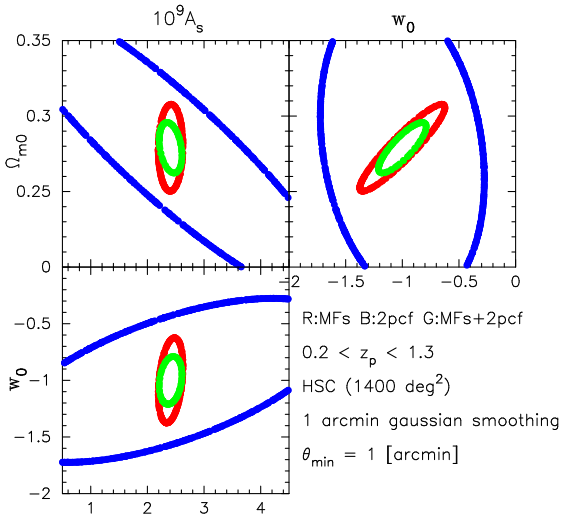

FIGURE 4.11: Forecast for cosmological parameter constants by lensing statistics for the Subaru Hyper Suprime Cam survey (1400 deg^2) (taken from [2]). The blue error circle shows the constraints from the 2PCFs, whereas the red one is expected from the MFs. We can improve cosmological constraints as indicated by the green circle by combining the two statistics. The data covariances for this plot are estimated from 1000 ray-tracing simulations and 1000 randomized catalogs based on the CFHTLenS data.

4.2.3 Possible Systematics

In this section, we examine the effect of known systematics on measurement of the MFs. We follow Ref. [44] to estimate the bias in the cosmological parameter due to some possible systematics

$$\delta p_\alpha = F^{-1}_{\alpha\beta} \sum_{i,j} C^{-1}_{ij} (D^{\rm test}_i - D^{\rm fid}_i) \frac{\partial D^{\rm fid}_j}{\partial p_\beta} \tag{4.19}$$

where δp_α is the bias in the αth cosmological parameter, $F_{\alpha\beta}$ is a Fisher matrix, $\boldsymbol{D}$ is the data vector and $\boldsymbol{C}$ is the data covariance. The data vector $\boldsymbol{D}^{\rm fid}$ is the theoretical template for the fiducial model and $\boldsymbol{D}^{\rm test}$ is the test data vector that includes a known systematics effect. In this section, we use the data vector $\boldsymbol{D}$ consisting of the lensing MFs only. For $\boldsymbol{D}^{\rm fid}$, we use the average MFs over 40 mock catalogs from our fiducial cosmological model described in Section 4.2.1.2. The mock samples are used as reference model, for which we have assumed that (1) the source galaxy redshift is well approximated by the peak of the posterior PDF of photometric redshift, and (2) the observed shear is perfectly calibrated by a functional form shown in Ref. [97]. We test these assumptions and quantify the net effects in a direct manner by generating and using another set of the mock catalogs for $\boldsymbol{D}^{\rm test}$ using the same N-body realizations as for our fiducial case.

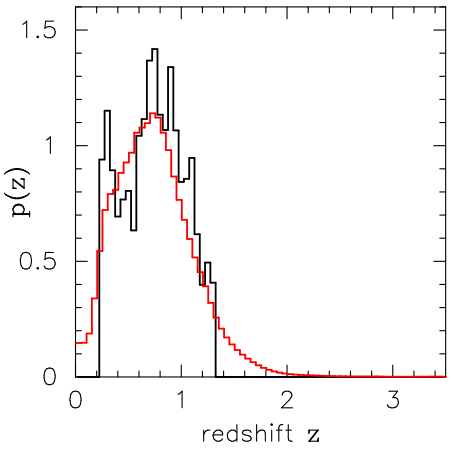

FIGURE 4.12: Redshift distribution function of sources $p(z)$ (taken from [2]). The red histogram corresponds to the sum of the posterior PDF over galaxies with $0.2 < z_p < 1.3$. The black one is calculated from the peak value of the posterior PDF, i.e., the best-fit photometric redshift. The mean redshift is slightly different: 0.69 for the black histogram and 0.748 for the red one.

4.2.3.1 Redshift Distribution

It is important to quantify the effect of the source redshift distribution and of the error in photometric redshifts on the lensing MFs, or indeed on any lensing statistics. We perform ray-tracing simulations by shooting rays to the farthest lens plane at $z = 3$, weighting the lensing kernel using a redshift distribution function of the sources. Specifically, we follow the same manner in Section 3.4 to simulate the weak-lensing effect but the lensing kernel is slightly different from their simulation because of the wider source redshift distribution. When one assume $z_p = 1$ so that the lensing kernel can be calculated by the simple expression, i.e., $r(\chi_s - \chi_l)r(\chi_l)/r(\chi_s)$, where χ_s and χ_l are the comoving distance of sources and of the lens, respectively. When one consider source redshift *distribution* $p(\chi)$, the lensing kernel for the lensing objects at χ_l should be replaced with $\int_{\chi_l}^{\chi_H} \mathrm{d}\chi_s p(\chi_s) r(\chi_s - \chi_l) r(\chi_l)/r(\chi_s)$. The source positions on the sky and all the other characteristics are kept the same as in the original mock catalogs, which themselves are derived from CHFTLenS. For the redshift distribution, we adopt the sum of the posterior PDF of photometric redshift for the galaxies with $0.2 < z_p < 1.3$. Figure 4.12 compares the integrated redshift distribution with the histograms of the source redshifts. The latter is used in the fiducial simulations. The test data vector $\boldsymbol{D}^{\mathrm{test}}$ is calculated by averaging the MFs over the new 40 catalogs with the posterior weight described above.

The main difference caused by the different redshift distributions is the amplitude of the standard deviation of $\mathcal{K}$. Figure 4.13 shows that the net difference is as large as those found for cosmological models differing by $\Delta w_0 = 0.2$; this can obviously be a significant source of error in cosmological parameter constraints with upcoming future surveys. We

estimate the resulting bias in the derived w_0 by using Eq. (4.19). The uncertainties in the photometric redshifts can indeed induce a $\Delta w_0 \sim 0.1$ bias in w_0. The exact values are summarized in Table 4.2.

We have also studied the effect of source redshift *clustering* on the lensing MFs. The results are presented in Appendix B. Briefly, the source redshift clustering is found to be a minor effect, but we note that it could cause non-negligible bias in "ultimate" galaxy imaging surveys, for example, the LSST lensing survey.

4.2.3.2 Shear Calibration Correction

We next study the effect of shear calibration correction. Here, we consider the standard correction that describes the calibration as $\epsilon = (1+m)\boldsymbol{\epsilon}_{\rm mock} + \boldsymbol{c}$ with a multiplicative component m and an additive component c. The former is calibrated by analyzing simulated images whereas the latter is calibrated empirically using the actual data. An ideal case would be one with $m = c = 0$, which might possibly be realized if a perfect calibration is done. We compare the lensing maps with and without the calibration factors m and c in order to quantify how important the shear calibration is. We simply reanalyze the fiducial mock catalogs by setting $m = c = 0$ for all of the source galaxies. The resulting 40 mock catalogs are used to obtain the data vector $\boldsymbol{D}^{\rm test}$ for this study.

We find that the additive calibration induces negligible effect but that the multiplicative calibration affects the lensing MFs appreciably. In the case of CFHTLenS, the multiplicative calibration results in a ~ 6 % correction with $\langle 1+m\rangle \simeq 0.94$. Note that m is a function of both the galaxy signal-to-noise ratio and the size. Thus the calibration differs from position to position and introduces effectively additional non-Gaussianities to the $\mathcal{K}$ map. Figure 4.13 shows that the non-Gaussianities actually cause biases in the lensing MFs. The biases cannot simply be described by the difference of the standard deviation of $\mathcal{K}$, i.e., by the normalization of the lensing MFs. The resulting bias in the cosmological parameter estimate is close to the 1σ level for an HSC-like survey as shown in Table 4.2. The study presented here suggests that the multiplicative correction needs to be included in *model* predictions of the MFs for producing robust forecasts for upcoming surveys. We here emphasize that our theoretical templates are based on mock catalogs that directly include the multiplicative correction obtained from the real observational data.

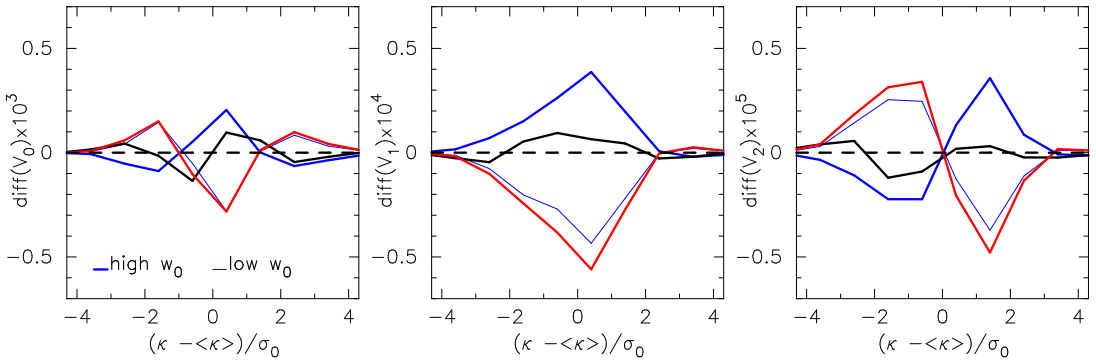

FIGURE 4.13: Impact of possible systematics on lensing MFs (taken from [2]). Each panel plots the differences of average MFs over 40 catalogs between the fiducial cosmology and another one that includes a given systematic. The red line presents the difference owing to source redshift distribution whereas the black one shows the effect of shear calibration correction on the lensing MFs. For comparison, the case of a cosmological model with higher (lower) w_0 is plotted as the thick (thin) blue line.

	$\Omega_{\rm m0}$	$A_s \times 10^9$	w_0
Redshift distribution	0.00707	-0.0254	-0.122
Calibration correction	-0.0224	0.110	-0.234

TABLE 4.2: The bias of cosmological parameter estimation due to possible systematics (taken from [2]). Here, we show the bias of $\Omega_{\rm m0}$, A_s, and w_0. We consider two possible systematics on morphological analysis of weak lensing data: one is the uncertainty of redshift of source galaxies and another corresponds to the calibration correction in shape measurement of galaxies.

4.3 Application to CFHTLenS

We then apply all the methods developed and examined in the previous sections to the CFHTLenS data. We have already shown in Section 4.2.2.2 that the statistical error in CFHTLenS degrades the constraints on cosmological parameters if we use only the lensing MFs. It would be ideal to utilize other cosmological probes to put tighter constraints. We will use the CMB data from WMAP.

Even though the likelihood analysis in this section includes the systematics studied in Section 4.2.3, our result could be "correctly" biased. Hence we need comprehensive studies to mitigate the effect of possible systematics for the more accurate cosmological constraints from lensing MFs. Although it is difficult to derive constraints on the cosmological parameters by lensing MFs correctly at present, we can test how helpful lensing MFs are for parameter estimation by using the current data set. In the following analysis, we simply assume the flat universe with w_0.

4.3.1 Data Sets

We utilize multiple data sets. As a probe of large-scale structure, we use data from the nine-year WMAP data release [19, 162]. We use the output of Monte Carlo Markov Chains (MCMC) derived from the likelihood analysis with the CMB temperature and polarization power- and cross-spectrum in the WMAP9 data. Note that the MCMC we use here does not include other external data sets, such as small-scale CMB measurements, galaxy redshift surveys, and Hubble constant. We then calculate the likelihood in the parameter space $\boldsymbol{p} = (\Omega_{\rm m0}, A_s, w_0)$ after marginalizing over the following three parameters: the reionization optical depth τ, scalar spectral index n_s and Hubble parameter H_0.

As a probe of matter distribution at low redshifts, we use the lensing MFs and the 2PCF calculated from the CFHTLenS data.

We evaluate a pixelated $\mathcal{K}$ map in the same manner as Section 4.2.1.1. We then convert $\mathcal{K}$ to $x = (\mathcal{K} - \langle\mathcal{K}\rangle)/\sigma_0$ where σ_0 is the standard deviation of $\mathcal{K}$. We follow the method in Ref. [149] to calculate the MFs from pixelated $\mathcal{K}$ maps. We set $\Delta x = 0.2$ from $x = -5$ to $x = 5$ for binning the threshold value. We construct the data vector and covariances in the same manner as in Section 4.2.2.1, but we assume no covariances between the MFs and the 2PCF. To validate the assumption, we have actually calculated the expected parameter constraints by the Fisher analysis with/without covariances between the MFs and the 2PCF. We have found that the approximation does not affect the final results significantly for the current data set. The error in $\Omega_{\rm m0}$ increases only by $\Delta\Omega_{\rm m0} = 5 \times 10^{-4}$.

We sample the posterior of the cosmological parameters from the lensing 2PCF data set using the Population Monte Carlo (PMC) using the publicly available code `COSMO_PMC` [163]. Details of the PMC are found in Ref. [164]. We adopt the method described in Ref. [159], which incorporates the cosmological dependence of the shear covariance. The same model parameters are adopted as in Ref. [160], with the smallest and largest angular bins being 0.9 and 300 arcmin. The following set of cosmological parameters are considered: $\boldsymbol{p} = (\Omega_{\rm m0}, \Omega_{\rm b0}, \sigma_8, H_0, n_s, w_0)$, where $\Omega_{\rm b0}$ is the baryon density and σ_8 normalizes the matter power spectrum. For comparison the result derived from CMB and that from the lensing MFs, we calculate the value of A_s at each sample point in parameter space by using the following relation:

$$A_s = A_{s,\rm fid}\left(\frac{\sigma_8}{\sigma_{8,\rm fid}}\right)^2 \frac{SD_+^2|_{\rm fid}}{SD_+^2}, \tag{4.20}$$

$$S = \int_0^\infty \frac{{\rm d}^3k}{(2\pi)^3} k^{n_s} T(k)^2 |W_8(k)|^2, \tag{4.21}$$

where D_+ is the linear growth factor of matter density, $T(k)$ is the transfer function, and $W_8(k)$ is the top-hat function with scale of 8 Mpc/h in the Fourier space. For the fiducial parameter set, we adopt the same parameters as the WMAP9 best-fit values.

In the PMC run, we perform 30 iterations to find a suitable importance function compared to the posterior. Also 100,000 sample points are generated for each iteration. To obtain a large sample set, we combine the PMC samples with the five highest value of perplexity p, which is the conventional diagnostic that indicates the quality and effectiveness of the sampling. The PMC run achieves $p > 0.7$ for the final samples; this criterion is the same as that adopted in the analysis in Ref. [160].

In the following, we study the following three cases: (1) likelihood analysis with the lensing MFs alone, (2) combined analysis with the lensing MFs and the 2PCF, and (3) combined analysis with the lensing MFs and CMB anisotropies. In the last analysis, we treat the lensing MFs data and the CMB data as being independent of each other.

4.3.2 Likelihood Analysis of Lensing MFs

In the maximum likelihood analysis, we assume that the data vector $\boldsymbol{D}$ is well approximated by the multivariate Gaussian distribution with covariance $\boldsymbol{C}$. This assumption is reasonable for the case of joint analysis of the CMB and lensing power spectrum [165]. In this case, the χ^2 statistics (log-likelihood) is simply given by

$$\chi^2 = (D_i - \mu_i(\boldsymbol{p}))C^{-1}(D_j - \mu_j(\boldsymbol{p})) \tag{4.22}$$

where $\boldsymbol{\mu}(\boldsymbol{p})$ is the theoretical prediction as a function of cosmological parameters. The theoretical prediction is computed in a three-dimensional parameter space. In sampling the likelihood function, we consider the limited parameter region as follows: $\Omega_{\rm m0} \in [0, 1]$, $A_s \times 10^9 \in [0.1, 8.0]$ and $w_0 \in [-6.5, 0.5]$. The sampling number in each parameter is set to 100.

In order to estimate the MFs components in $\boldsymbol{\mu}$, we assume that the lensing MFs depend linearly on the cosmological parameters with the first derivatives calculated from Eq. (4.16). We consider two components of the contribution of the data covariance in the likelihood analysis; one is the statistical error and sampling variance, which are estimated as in Section 4.2.2.1 while the other originates from the possible systematics as studied in Section 4.2.3. We denote the latter contribution as $\boldsymbol{C}^{\rm sys}$. We estimate $\boldsymbol{C}^{\rm sys}$ in a simple and direct manner using the differences of the MFs, as shown in Figure 4.13:

$$C_{ij}^{\rm sys} = \left[(D_i^{\rm zdist} - D_i^{\rm fid})^2 + (D_i^{\rm scc} - D_i^{\rm fid})^2\right] \delta_{ij}^{2D}, \tag{4.23}$$

	$\Omega_{\rm m0}$	σ_8
2PCF alone	$0.396\pm^{0.177}_{0.185}$	$0.695\pm^{0.203}_{0.202}$
MFs alone	0.295 ± 0.020	$0.855\pm^{0.060}_{0.060}$
MFs + 2PCF	0.282 ± 0.022	$0.782\pm^{0.042}_{0.042}$

TABLE 4.3: Cosmological parameter constraints obtained from the maximum likelihood analysis (taken from [2]). Weak lensing data set is obtained from CFHTLenS. We consider three analyses: Two-point correlation function (2PCF), Minkowski Functionals (MFs) and the combined analysis of 2PCF and MFs. The error bar corresponds to the 68% confidence level. Note that the concordance ΛCDM model is assumed in this table.

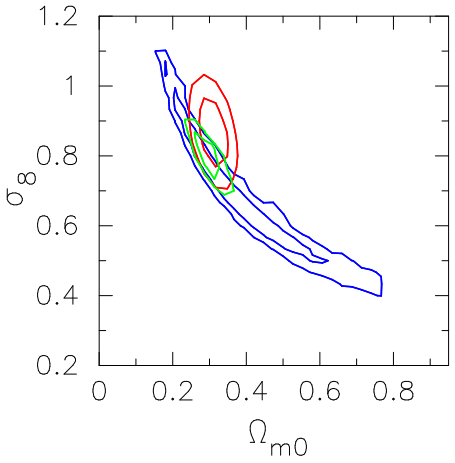

FIGURE 4.14: Marginalized 2D confidence level (68% and 95%) obtained from cosmic shear data (taken from [2]). The red region shows the cosmological results by lensing MFs alone and the blue region represents the cosmological constraints by 2PCF alone. The green circle corresponds to the result of our combined analysis with the lensing MFs and 2PCF. The concordance ΛCDM model (i.e., $w_0 = -1$) are assumed in this figure.

where $\boldsymbol{D}^{\rm fid}$ is the template MFs for our fiducial mock catalogs, $\boldsymbol{D}^{\rm zdist}$ is the average MFs over 40 catalogs reflecting the different source redshift distribution as shown in Figure 4.12, and $\boldsymbol{D}^{\rm scc}$ is estimated by averaging the MFs over 40 catalogs without shear calibration correction. The total covariance is the sum of the above two contributions.

4.3.3 Breaking Degeneracies

We would like to examine the ability of the lensing MFs to break degeneracies between cosmological parameters. We first consider the concordance ΛCDM model, i.e. $w_0 = -1$. Figure 4.14 presents the marginalized constraints on Ω_0 and σ_8 in the two-parameter plane. This figure shows clearly the lensing MFs can break the well-known degeneracy between Ω_0 and σ_8 that is apparent in the analysis using only the 2PCF. Interestingly, the marginalized constraints on each parameter can be improved by a factor of five

to eight by adding the MFs. The final constraints in the case of ΛCDM model are summarized in Table 4.3.

We expect that this improvement would be caused by the cosmological information from the higher-order moment of the $\mathcal{K}$ map. As shown in Section 3.3.3, the lensing MFs have the non-Gaussian correction originated from the third-order moment of $\mathcal{K}$. We here present the qualitative interpretation how we can break degeneracy between σ_8 and $\Omega_{\rm m0}$ by using the information from the higher-order moment of $\mathcal{K}$. As an order of magnitude calculations, we regard $\mathcal{K}$ as a quantity of $O(\Omega_{\rm m0}\delta)$ where δ is the matter over-density. In this case, the second-order moment of $\mathcal{K}$ would be expressed as $O(\Omega_{\rm m0}^2\langle\delta\delta\rangle) \sim \Omega_{\rm m0}^2\sigma_8^2$, while the third-order moment of $\mathcal{K}$ is given by $O(\Omega_{\rm m0}^3\langle\delta\delta\delta\rangle)$. At weakly non-linear regime, the three-point correlation function of δ would be calculated by the standard perturbation theory (e.g., [166]), which predicts $O(\langle\delta\delta\delta\rangle) \propto O(\langle\delta\delta\rangle^2) \sim \sigma_8^4$. As a result, the third-order moment of $\mathcal{K}$ would be the quantity of $O(\Omega_{\rm m0}^3\sigma_8^4)$. Therefore, in principle, we can break the degeneracy between $\Omega_{\rm m0}$ and σ_8 by combining with measurement of two- and three-point correlation of $\mathcal{K}$. Recently, Ref. [167] has measured the second- and third-order moments of $\mathcal{K}$ as a function of smoothing scale in $\mathcal{K}$ map by using CFHTLenS data set. They have confirmed that the 10% improvement of the constraint on $\sigma_8\Omega_{\rm m0}^\alpha$ where $\alpha \sim 0.5 - 0.7$ when using smoothed maps with smoothing scale of $2-15$ arcmin. Their result indicates that we can extract some cosmological information from higher-order moment of $\mathcal{K}$ in the realistic case. Our analysis presented here would correspond to the extended analysis in Ref. [167] by taking into account the moments higher than third-order one.

Figure 4.15 shows a simple comparison of lensing MFs. In this figure, we consider the two ΛCDM model: one is the best fit model shown in Table 4.3 and another model is consistent with lensing 2PCF with a $\sim 2\sigma$ level. In upper panel, we show the measured MFs with statistical and systematic errors by black points. Although the error bar is too small compared to the signal in upper panels, bottom panels clearly show the magnitude relation of error bars and signals. In bottom panel, we show the differences between our modelling MFs and the measured one. There, we simply assume that lensing MFs can be describe as the linear function of cosmological parameters. Even though we do not consider the detailed modeling of lensing MFs, Figure 4.15 implies that lensing MFs might be useful to improve the cosmological parameter estimation in a cosmic shear analysis.

Next, we explore models with a variant of dark energy. The equation of state parameter w_0 serves as an additional parameter here. The left panel in Figure 4.16 presents the marginalized constraints in the 2D plane by the lensing MFs and 2PCF. The red circle shows the result from the lensing MFs alone, whereas the green circle is the estimate

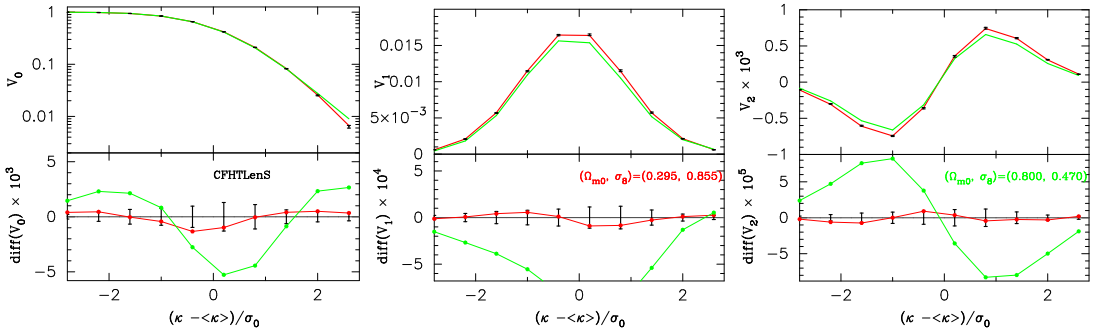

FIGURE 4.15: The comparison with our theoretical template and the observed MFs. In upper panel, the black point shows the observed MFs whereas the error bars are too small. The error bars include the statistical and systematic error described in Section 4.3.2. The colored line shows our model of lensing MFs based on mock catalogs. The red line corresponds to the best fit ΛCDM model and the green line represents the cosmological model with higher $\Omega_{\rm m0}$ and lower σ_8. Bottom panels show the differences of lensing MFs between our measurement and different models.

	$\Omega_{\rm m0}$	$A_s \times 10^9$	w_0
MFs alone	0.205 ± 0.060	$2.18\pm^{0.60}_{0.60}$	-2.2 ± 0.8
MFs + 2PCF	$0.256\pm^{0.054}_{0.046}$	$1.92\pm^{0.65}_{0.65}$	$-1.60\pm^{0.76}_{0.57}$
MFs + CMB	$0.290\pm^{0.016}_{0.028}$	2.39 ± 0.07	-0.90 ± 0.11

TABLE 4.4: The parameter constraints obtained from the maximum likelihood analysis of lensing MFs and others. The error bar indicates the 68% confidence level.

derived from combining the lensing MFs and 2PCF. Interestingly, with the lensing MFs alone, the data set favors a low w_0[4]. We have checked that our theoretical MF template can recover correctly the input cosmological parameters for the 40 mock data with a similar confidence level expected from the Fisher analysis. We thus argue that the trend of favoring low w_0 is likely attributed to the possible systematics as studied in Section 4.2.3, or to imperfect modeling of the dependence of the lensing MFs on the cosmological parameters.

The right panel of Figure 4.16 presents the 68% and 95% confidence regions obtained from our joint analysis with the WMAP9 CMB data. The red region represents the results from lensing MFs alone. The blue region is the result obtained from CMB, and the green one represents constraints by combining the both. These figures show clearly that the lensing MFs are useful to improve the cosmological constraints by breaking the parameter degeneracies. The marginalized constraints for the three parameters are summarized in Table 4.4.

[4] We have also examined which MFs (V_0, V_1, V_2) cause this trend. We have performed likelihood analysis using each MF only. Both V_1 and V_2 prefer lower w_0. The 68 % marginalized constraints on w_0 using each MF are found to be $-0.30\pm^{0.77}_{0.84}$, -3.31 ± 0.60, and $-2.48\pm^{0.91}_{0.84}$ for V_0, V_1, and V_2, respectively.

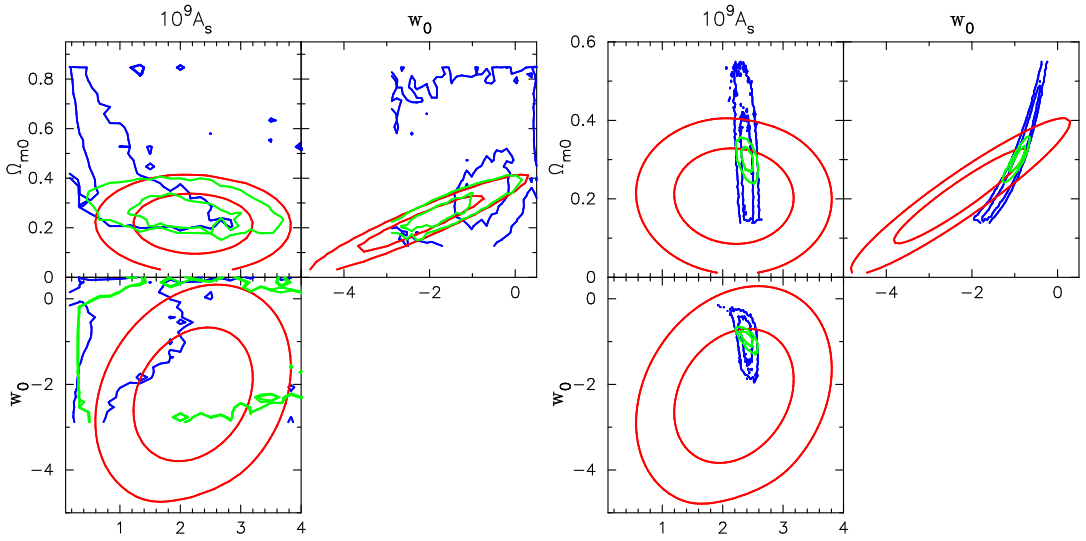

FIGURE 4.16: Marginalized 2D confidence level (68% and 95%) obtained from the lensing MFs and additional probes. The left panel shows the cosmological constraints by our combined analysis with the lensing MFs and the 2PCF. The right panel shows the result of the joint analysis with the lensing MFs and CMB. In each panel, the red region shows the constraint from the lensing MFs alone and the blue region shows those from the 2PCF or CMB alone. The green one shows the result of the combined analysis with the lensing MFs and another data set.

We derive the above cosmological constraints by assuming that our modeling of lensing MFs is correct. However, there are possible systematics in lensing MFs as shown in Section 4.2.3. We consider the possible bias in parameter estimation with our modeling of lensing MFs. As pointed out in Section 4.2.3, the uncertainty of photometric redshift and imperfect shape measurement of source galaxies would cause the biased parameter estimation with lensing MFs. For the main three parameters, we would evaluate the systematic uncertainty as summarized in Table 4.2: $\Delta\Omega_{\rm m0} = \pm 0.0224 \pm 0.00707$, $\Delta(A_s \times 10^9) = \pm 0.0254 \pm 0.110$, and $\Delta w_0 = \pm 0.122 \pm 0.234$. Here, the former error corresponds to the systematic error related with the uncertainty of photometric redshift, while the latter is the error associated with imperfect shape measurement. We can easily relate these uncertainties to the uncertainty of σ_8 by using Eq. (4.20): $\Delta\sigma_8 = \pm 0.042 \pm 0.064$. It is worth making further effort to reduce the systematic errors in measurement of the lensing MFs.

Chapter 5

Cross correlation with Dark Matter Annihilation Sources

Here, we present the first measurement of the cross-correlation between cosmic shear and the extragalactic gamma-ray background (EGB). This measurement is performed with the largest cosmic shear data set currently available from the Canada-France-Hawaii Lensing Survey (CFHTLenS) and gamma-ray photon data from the *Fermi* LAT telescope. The measured cross correlation is utilized to place constraints on the dark matter annihilation cross section. The resulting constraint is based on the information at cosmological scales, and is complementary to dark matter search in local galaxies. In this chapter, we assume the standard cosmological parameters $H_0 = 100h\,\mathrm{km\,s^{-1}}$ with $h = 0.7$, $\Omega_{\mathrm{m0}} = 0.279$, and $\Omega_\Lambda = 0.721$.

5.1 Dark Matter Annihilation

The existence of dark matter (DM) is supported with high significance by a number of astrophysical observations as shown in Section 1.2. While we still know little of the DM particle properties, if DM particles annihilate into standard model particles, as is typically expected for their production in the early universe, underlying matter density field in the universe will be a source of gamma rays.

5.1.1 Relic density

Here, we summarize the relic density of the annihilating dark matter. A particle in the early universe has to experience various interactions in efficient way. As the universe

expands and cools down, the local thermal equilibrium can not be maintained because the interaction rate can not overcome the expansion rate of the universe at some time. At that time, the particle is so-called *decoupled* and the time evolution of mean number density of the particle can be determined by the expansion rate of the universe.

The time evolution of number density of a particle can be determined by the Boltzmann equation. In the case of the annihilating DM, the governing equation is given by

$$\frac{\mathrm{d}n_{\mathrm{dm}}}{\mathrm{d}t} + 3Hn_{\mathrm{dm}} = -\langle\sigma v\rangle(n_{\mathrm{dm}}^2 - n_{\mathrm{dm,eq}}^2), \tag{5.1}$$

where n_{dm} is the number density of DM, $n_{\mathrm{dm,eq}}$ represents the number density at thermal equilibrium, H is Hubble constant and $\langle\sigma v\rangle$ is the annihilation cross section times the relative velocity averaged with the velocity distribution function. Here, $n_{\mathrm{dm,eq}}$ is given by the Maxwell-Boltzmann approximation:

$$n_{\mathrm{dm,eq}} = g\left(\frac{m_{\mathrm{dm}}T}{2\pi}\right)^{3/2}\exp\left(-\frac{m_{\mathrm{dm}}}{T}\right), \tag{5.2}$$

where g is the internal degrees of freedom, m_{dm} is the DM particle mass, and T represents the temperature of thermal equilibrium. It is useful to introduce the following new variables;

$$Y = \frac{n_{\mathrm{dm}}}{s}, \tag{5.3}$$

$$Y_{\mathrm{eq}} = \frac{n_{\mathrm{dm,eq}}}{s}, \tag{5.4}$$

where s is the entropy density $s = 2\pi g_* T^3/45$ and g_* represents the number of relativistic degrees of freedom. With Y and Y_{eq}, one can obtain the following equation from Eq. (5.1) during the radiation domination[1];

$$\frac{\mathrm{d}Y}{\mathrm{d}x} = -\frac{\langle\sigma v\rangle s}{Hx}\left(Y^2 - Y_{\mathrm{eq}}^2\right), \tag{5.5}$$

where we use the conservation of entropy per comoving volume and x is defined by m_{dm}/T. Furthermore, we introduce the variable $\Delta = Y - Y_{\mathrm{eq}}$ and finally obtain the equation as follows;

$$\frac{\mathrm{d}\Delta}{\mathrm{d}x} = -\frac{\mathrm{d}Y_{\mathrm{eq}}}{\mathrm{d}x} - f(x)\Delta(2Y_{\mathrm{eq}} + \Delta), \tag{5.6}$$

[1] During the radiation domination, the following equation holds; $t = 0.301 g_*^{-1/2}(m_{\mathrm{Pl}}/T^2)$ where m_{Pl} is the planck mass.

where $f(x)$ is given by

$$f(x) = \sqrt{\frac{\pi g_*}{45}} m_{\rm dm} m_{\rm Pl} \langle \sigma v \rangle x^{-2} \tag{5.7}$$

For simplicity, in this thesis, we consider the s-wave annihilation, i.e. the case where $\langle \sigma v \rangle$ is constant. In this case, Ref. [168] found the accurate approximate formula of Y in the limit of $x \to \infty$:

$$Y_\infty^{-1} = \sqrt{\frac{\pi g_*}{45}} m_{\rm dm} m_{\rm Pl} x_F^{-1} \langle \sigma v \rangle, \tag{5.8}$$

where x_F is evaluated at the freeze-out temperature where $\langle \sigma v \rangle n_{\rm dm}|_T = H|_T$. Then, one can estimate the present mean matter density of the annihilating DM as $\bar{\rho}_{\rm m0} = m_{\rm dm} s_0 Y_\infty$ where $s_0 = 2889.2\,{\rm cm}^{-3}$ is the present entropy density. Finally, the relic density of DM is given by

$$\Omega_{\rm m0} h^2 \simeq \frac{1.07 \times 10^9\,{\rm GeV}^{-1}}{m_{\rm Pl}} \frac{x_F}{\sqrt{g_*}} \frac{1}{\langle \sigma v \rangle}. \tag{5.9}$$

An order-of-magnitude estimate is found in Ref. [169]. That is given by

$$\Omega_{\rm m0} h^2 \simeq \frac{3 \times 10^{-27}\,{\rm cm}^3\,{\rm s}^{-1}}{\langle \sigma v \rangle}. \tag{5.10}$$

The above estimate and the current constraints on $\Omega_{\rm m0} h^2 \sim 0.1$ (e.g., [19]) lead to the canonical thermal cross-section of DM annihilation:

$$\langle \sigma v \rangle_{\rm themal} \simeq 3 \times 10^{-26}\,{\rm cm}^3\,{\rm s}^{-1}. \tag{5.11}$$

5.1.2 Gamma-ray intensity

The intensity is defined by the number of photons per unit energy, area, time, and solid angle. Thus, the contribution of DM annihilation to the intensity at gamma-rays I_γ can be expressed by

$$E_\gamma I_\gamma = \frac{c}{4\pi} \int {\rm d}z \frac{P_\gamma(E'_\gamma, z)}{H(z)(1+z)^4} e^{-\tau(E'_\gamma, z)}, \tag{5.12}$$

where E_γ is the observed gamma-ray energy, $E'_\gamma = (1+z)E_\gamma$ is the energy of the gamma ray at redshift z, $H(z) = H_0[\Omega_{\rm m0}(1+z)^3 + \Omega_\Lambda]^{1/2}$ is the Hubble parameter in a flat ΛCDM universe, and the exponential factor in the integral takes into account the effect of gamma-ray attenuation during propagation owing to pair creation on diffuse extragalactic photons. In this thesis, we adopt the model in Ref. [170] for the gamma-ray optical depth $\tau\left(E'_\gamma, z\right)$. The volume emissivity, denoted by P_γ, defined by the photon

energy emitted per unit volume, time, and energy range. Hence, P_γ is given by

$$P_\gamma(E_\gamma, z) = E_\gamma \frac{\mathrm{d}N_\gamma}{\mathrm{d}E_\gamma} \frac{\langle \sigma v \rangle}{2} \left[\frac{\rho_{\rm dm}(\boldsymbol{x}|z)}{m_{\rm dm}} \right]^2 , \tag{5.13}$$

where $\mathrm{d}N_\gamma/\mathrm{d}E_\gamma$ is the gamma-ray spectrum per annihilation and $\rho_{\rm dm}(\boldsymbol{x}|z)$ is the DM mass density distribution at redshift z as a function of spatial coordinate $\boldsymbol{x}$.

Since the DM annihilation rate is proportional to the DM density squared, highly overdense regions in the universe would dominate the volume emissivity. Therefore, it is useful to consider the intensity at gamma-ray in terms of an overdensity $\delta(z) = \rho_{\rm dm}/\bar{\rho}_{\rm dm}(z)$ where $\bar{\rho}_{\rm dm}(z) = \Omega_{\rm m0}\rho_{\rm crit,0}(1+z)^3$ and $\rho_{\rm crit,0}$ is the critical density today. Let us consider the mean intensity at gamma-ray originated from the DM annihilation. In order to calculate the mean value of Eq. (5.12), we need to evaluate the ensemble average of the overdensity squared, $\langle \delta^2(z) \rangle = \langle \rho^2_{\rm dm}(z) \rangle / \bar{\rho}^2_{\rm dm}(z)$. This factor is called the intensity multiplier (or the clumping factor), and characterizes the enhancement in the DM annihilation rate due to dense DM halos. It is obtained by integrating over the DM halo mass function $n(M, z)$,

$$\langle \delta^2(z) \rangle = \frac{1}{\bar{\rho}^2_{\rm dm}(z)} \int_{M_{\rm min}}^{\infty} \mathrm{d}M\, n(M, z) \int \mathrm{d}V \rho^2_{\rm dm}(r|M, z), \tag{5.14}$$

where $\rho_{\rm dm}(r|M, z)$ describes the density profile as a function of radius r for a DM halo with mass M at redshift z, and $M_{\rm min}$ is the smallest DM halo mass.

Therefore, the contribution to mean intensity of gamma-rays is obtained by

$$I_\gamma = \frac{\langle \sigma v \rangle}{8\pi} \int c\,\mathrm{d}z \frac{dN_\gamma}{dE_\gamma}\bigg|_{E'_\gamma} \frac{e^{-\tau(E'_\gamma, z)}}{H(z)(1+z)^3} \left(\frac{\bar{\rho}_{\rm dm}(z)}{m_{\rm dm}} \right)^2 \langle \delta^2(z) \rangle. \tag{5.15}$$

Eq. (5.15) clearly shows that the particle properties of DM – $m_{\rm dm}$, $\langle \sigma v \rangle$, and $\mathrm{d}N_\gamma/\mathrm{d}E_\gamma$ – are conveniently decoupled from the physics determining its spatial distribution, $\langle \delta^2(z) \rangle$. Note that Eq. (5.14) would provide us the contribution at "extragalactic scales". Although the galactic dark matter distribution would also contribute to the observed gamma-ray emission (see e.g., Ref. [171]), it is not of great importance as long as we consider the cross correlation analysis of cosmic shear, which is the subject of this thesis.

Estimates of the flux multiplier depend on the value of $M_{\rm min}$, the halo mass function, the DM density profile, and how the DM profile depend on halo mass and evolve in redshift. Among these, the value of $M_{\rm min}$ has the largest impact. The smallest DM halo mass could be determined from the DM particle properties, being the Jeans mass of dark matter particles. For supersymmetric neutralinos and $\sim$ MeV DM, this is some $10^{-6} M_\odot$ [172], while other DM particles have $M_{\rm min}$ that vary by orders of magnitudes [173, 174,

175]. However, the situation would be more complicated because of hierarchical structure formation thorough various processes such as accretion, stripping and mergers. These processes make some DM halos destructed. In particular, much of the smallest DM halos may be absorbed into larger halos and their central densities disrupted before they appreciably contribute to the extragalactic gamma-ray emission (e.g., [176, 177]). The DM Jeans mass is therefore simply a lower limit. Furthermore, the additional gamma-ray could be produced by interactions of the annihilation products with the environment. Such gamma-rays are called secondary gamma-rays. An example of secondary gamma-ray emission is when DM annihilation produces a positron, which, in turn, finds an electron in the galactic halo and annihilates to produce gamma rays. For secondary gamma-ray emission, the relevant minimum mass is set by the Jeans mass of the baryons, which is on the order of $\sim 10^6 M_\odot$ (e.g., [172]).

The gamma-ray emission due to DM annihilation is expected to be anisotropic because of the highly non-linear gravitational growth of the DM density distribution (e.g., [178]). Hence, the expected anisotropy should correlate with another tracer of the DM density distribution, e.g., gravitational lensing effects of distant galaxies called cosmic shear. Although the DM distribution in the universe can be traced in a number of ways, among the most powerful is gravitational lensing, which has the advantage of not requiring any assumptions such as the relation between luminosity and mass and/or hydrostatic equilibrium. The simple idea naturally occurs: *the DM distribution that generate cosmic shear would also be a gamma-ray source.* In Ref. [179], the authors first consider the cross-correlation between cosmic shear and the extragalactic gamma-ray background (EGB) and also explored how astrophysical sources contribute to the cross-correlation signal. Their conclusion is that even without detailed astrophysical modeling, the additional information derived by the cross-correlation would be helpful for exploring the DM contribution in extragalactic gamma-ray emission.

5.2 Extragalactic Gamma-ray Background

The origin of the extragalactic gamma-ray background (EGB) emission is among the most interesting problems in astrophysics. The EGB was first detected by the *OSO*-3 satellite [180] and subsequently deduced by the *SAS*-2 satellite [181] and the Energetic Gamma-Ray Experiment Telescope onboard the Compton Gamma-ray Observatory [182]. Most recently, the Large Area Telescope (LAT) onboard the *Fermi* Gamma-ray Space Telescope has derived the most accurate EGB based on new data and improved modeling of the Galactic gamma-ray foreground emission. The *Fermi* LAT observation

shows a featureless power-law spectrum for the EGB in the energy range 0.1–300 GeV [183].

Multiple astrophysical sources of gamma rays have been proposed as contributors to the EGB. Unresolved astrophysical point sources, such as blazars and star-forming galaxies (SFG), are guaranteed sources and have been investigated by many groups. However, the modeling of the sources' faint end distributions is non-trivial, and estimates of the contribution to the EGB from unresolved blazars range from ∼15 per cent to ∼100 per cent (e.g., [184, 185, 186]). On the other hand, the intrinsic spectral and flux properties of blazars constructed by *Fermi* LAT data, as well as the auto-correlation of EGB anisotropies [187], suggest that unresolved blazars can only contribute up to ∼20 per cent of EGB (e.g., [188, 189, 190, 191]). Similarly, the contribution from SFGs and radio galaxies to the EGB can be significant but is subject to large uncertainties [192, 193]. These previous works show that while the EGB intensity can be explained by the superposition of multiple astrophysical source classes, there appears to remain large uncertainties and thus, at present, an appreciable contribution from unknown or unconfirmed sources of gamma rays is allowed.

5.2.1 Data

In this thesis, we use *Fermi*-LAT Pass 7 Reprocessed gamma-ray photon data taken from August 2008 to January 2014[2]. Our interest is the cross correlation analysis of cosmic shear data obtained from CFHTLenS as summarized in Section 4.2.1.1. For each CFHTLenS patch, we download photons within a circle of radius 10° around the center of each region and work with a $14^\circ \times 14^\circ$ square region of interest (ROI). In analyzing the data, we use the Fermi Tools version `v9r32p5`[3]. Using the *gtmktime* tool, we remove data taken during non-survey modes and when the satellite rocking angle exceeds 52° with respect to the zenith (`DATA_QUAL=1`, `LAT_CONFIG=1`, and `ABS(ROCK_ANGLE)<52`). This standard procedure removes epochs with potentially significant contamination by the gamma-ray bright Earth limb. Unless otherwise stated, we work with only `ULTRACLEAN`-class photons, which are events that pass the most stringent quality cuts, and we use photons between 1–500 GeV in energy. In Section 5.4.1, we discuss using `SOURCE`-class photons. Then, using the *gtbin* tool, we bin the photons in a stereographic projection into pixels of $0.2^\circ \times 0.2^\circ$ and into 30 equal logarithmically-spaced energy bins. These binning sizes are taken from the official recommended values that are chosen to ensure

[2] We also performed the cross correlation analysis for Pass 7 Reprocessed gamma-ray photon data take from different two periods: August 2008 to May 2012 (data1) and May 2012 to January 2014 (data2). Even though we consider only CFHTLenS W1 field for this analysis, we find that the resulting signal is also consistent with a null signal. The value of chi-squared statistics for 10 bins is found to be 7.93 and 3.64 for data1 and data2, respectively.

[3] http://fermi.gsfc.nasa.gov/ssc/data/analysis/

reasonable analysis outcomes, namely, to ensure that rapid variations of the effective area with energy is taken into account (e.g., as discussed in the binned likelihood tutorial of the Fermi Analysis Threads). With the data selection cuts in place, we use the *gtltcube* tool to generate integrated live times and the *gtexpcube2* tool to generate the integrated exposure maps. Throughout, we work with the `P7REP_ULTRACLEAN_V15` instrument response function (IRF), unless otherwise stated.

In order to obtain the extragalactic diffuse photons, for each ROI we subtract the best fit Galactic foreground emission model from the raw data. We then mask out point sources using a mask of 2° radius around each point source. The mask size corresponds to a generous estimate of the PSF of the *Fermi*-LAT detector, which decreases with energy: the 68% containment angle is ~ 0.9 deg at 1 GeV and ~ 0.26 deg at 10 GeV, both for combined front and back conversion tracks. Since most point sources have steep spectra and hence dominated by low-energy photons, our adopted mask is chosen to be sufficiently larger than the containment angle at our lower energy limit of 1 GeV. When we adopt a smaller mask of 1° radius around each point source, we find that the final constraint would change with a level of only 10%.

We also estimate the best fit Galactic diffuse emission model separately for each ROI, by including all the point sources in the ROI in the 2FGL catalog, together with the recommended Galactic diffuse emission model (`gll_iem_v05`) and the recommended isotropic emission model (`iso_clean_v05`). We have checked that our four ROIs are sufficiently far from the large-scale diffuse gamma-ray sources such as the Fermi bubbles [194] which would otherwise complicate fitting. We find 9, 11, 11, and 12 point sources in W1, W2, W3 and W4 field, respectively. In order to perform a binned likelihood analysis, we use the *gtlike* tool by varying all point source spectra as well as the diffuse emission normalizations. We then use the *gtmodel* tool to generate photon counts maps based on the best fit Galactic diffuse model and exposure maps. Finally, we subtract these from the raw counts maps. We checked that the procedure yields a flux spectrum for the EGB, estimated as the raw counts minus a model without the isotropic component, divided by the exposure map, that is very similar to the -2.41 power-law spectrum of the EGB reported in Ref. [183]. In Figure 5.1, we show how the residuals of the raw counts minus the Galactic diffuse model, demonstrate structureless spatial maps in all four CFHTLenS fields.

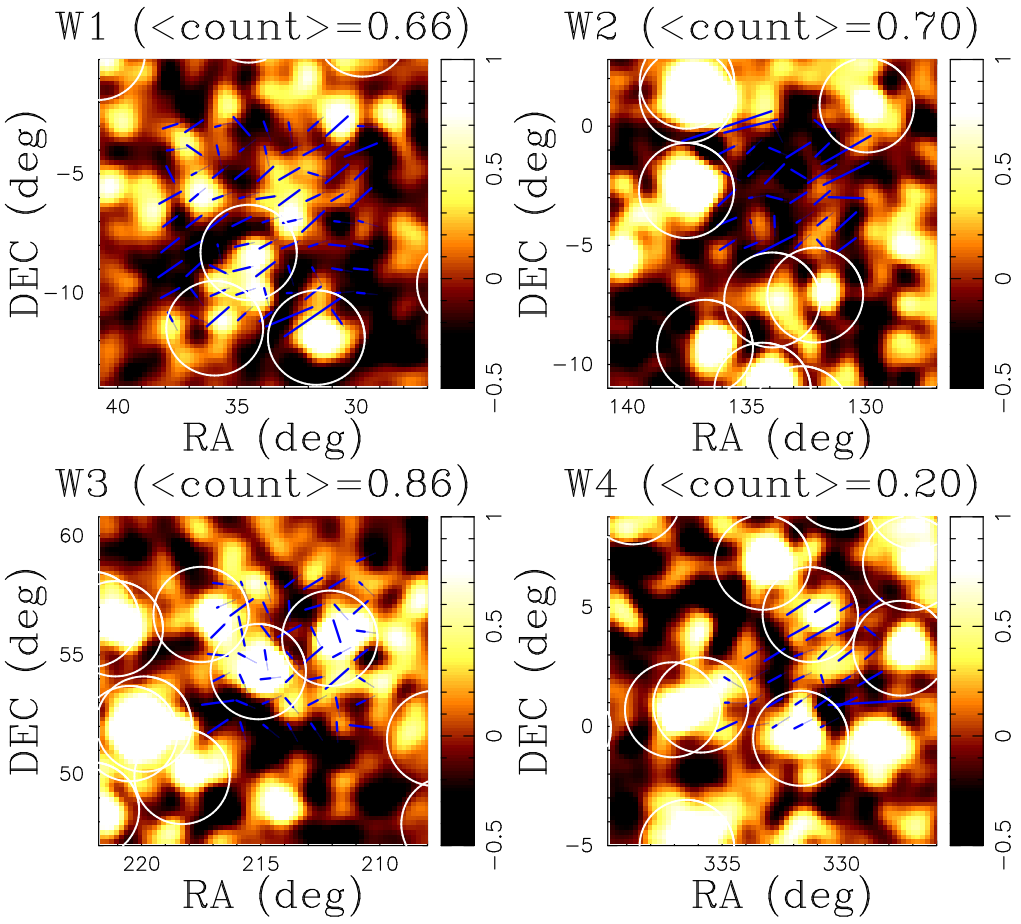

FIGURE 5.1: Residual maps in the CFHTLenS W1, W2, W3, and W4 fields, where residual is defined as the fluctuation in the EGB photon count map from its mean value (taken from [3]). In each panel, the color-scale bar represents both the positive and negative difference between the EGB count map and the mean of each field indicated above the panels: 0.66, 0.70, 0.86, and 0.20 in W1, W2, W3 and W4 fields, respectively. Overlaid by thick lines are the average ellipticities of source galaxies over 1 deg^2 with arbitrary scaling. The circles represent the point-source masked regions. For visualization purposes, a Gaussian smoothing is performed on the map with a width of 0.6 deg.

Ref. [195] modeled the point spread function (PSF) in the case of *Fermi*-LAT with the following functional form:

$$W_{\rm PSF}(\theta, E_\gamma) = A(E_\gamma)\left[f_{\rm core}K(x,\sigma_{\rm core},\gamma_{\rm core}) + (1-f_{\rm core})K(x,\sigma_{\rm tail},\gamma_{\rm tail})\right], \quad (5.16)$$

$$f_{\rm core} = \frac{1}{1+N_{\rm tail}\sigma_{\rm tail}^2/\sigma_{\rm core}^2}, \quad (5.17)$$

$$K(x,\sigma,\gamma) = \frac{1}{2\pi\sigma^2}\left(1-\frac{1}{\gamma}\right)\left[1+\frac{1}{2\gamma}\frac{x^2}{\sigma^2}\right]^{-\gamma}, \quad (5.18)$$

where x is a scaled-angular deviation defined by $x = \theta/S_{\rm P}(E_\gamma)$ and $A(E_\gamma)$ is the normalization factor such that $\int {\rm d}^2\theta\, W_{\rm PSF}(\theta, E_\gamma) = 1$. The scale factor $S_{\rm P}(E_\gamma)$ is found in

[195],

$$S_{\rm P}(E_\gamma) = \sqrt{\left[c_0 \left(\frac{E_\gamma}{100\,{\rm MeV}}\right)^{-\beta}\right]^2 + c_1^2}, \tag{5.19}$$

and the normalization is given by $A(E_\gamma) = [S_{\rm P}(E_\gamma)]^2$. In this thesis, we adopt the parameters estimated in the latest in-flight PSF for `ULTRACLEAN` photons[4], i.e., $c_0 = 3.16$ deg and $c_1 = 0.034$ deg for front-converting events, and $c_0 = 5.32$ deg and $c_1 = 0.096$ deg for back-converting events, along with $\beta = 0.8$, $N_{\rm tail} = 0.08639$, $\sigma_{\rm core} = 0.5399$, $\sigma_{\rm tail} = 1.063$, $\gamma_{\rm core} = 2.631$, and $\gamma_{\rm tail} = 2.932$ for both events [195].

5.3 Cross Correlation of Extragalactic Gamma-ray Background and Cosmic Shear

5.3.1 Theoretical model

In this section, we summarize our benchmark model for the cross-correlation signal between cosmic shear and the EGB. The theoretical framework for the angular power spectrum analysis of the EGB has been developed in Refs. [178, 179, 196, 197]. We calculate the cross-correlation of cosmic shear and the EGB as follows.

In general, the number of EGB photons along the line of sight $\boldsymbol{\theta}$ can be expressed by

$$\delta n(\boldsymbol{\theta}) = \int {\rm d}\chi \; g(\chi, \boldsymbol{\theta}) W_g(\chi), \tag{5.20}$$

where χ is the comoving distance, g is the relevant field for gamma-ray sources, and W_g is the window function. As shown in Section 5.1.2, for gamma-ray emission from DM annihilation, the relevant field is the overdensity squared δ^2. With Eq. (5.12), the window function in Eq. (5.20) is given by

$$W_g(\chi) = \int_{E_{\gamma,\rm min}}^{E_{\gamma,\rm max}} {\rm d}E_\gamma \; \frac{\langle\sigma v\rangle}{8\pi} \left(\frac{\bar{\rho}_{\rm dm,0}}{m_{\rm dm}}\right)^2 [1+z(\chi)]^3 \left.\frac{{\rm d}N_\gamma}{{\rm d}E_\gamma}\right|_{E'_\gamma} \exp\left[-\tau\left(E'_\gamma, \chi\right)\right] \eta(E_\gamma), \tag{5.21}$$

where $\bar{\rho}_{\rm dm,0}$ is the mean density of DM at present, $E'_\gamma = (1+z(\chi))E_\gamma$ and E_γ are the energy of the gamma ray when it is emitted at χ and when it is observed, respectively. Here, $\eta(E_\gamma)$ is the exposure which is the integral of effective area over time taking into account the orbits of *Fermi* and data cuts. We use a standard model of τ [170], and we estimate $\eta(E_\gamma)$ by averaging the exposure maps over the ROI in each of the

[4] made publicly available at
http://fermi.gsfc.nasa.gov/ssc/data/analysis/documentation/Cicerone/Cicerone_LAT_IRFs/IRF_PSF.html

CFHTLenS patches. For the gamma-ray spectrum per annihilation $\mathrm{d}N_\gamma/\mathrm{d}E_\gamma$, we adopt two characteristic spectra corresponding to annihilation with 100% branching ratios to $b\bar{b}$ and $\tau^+\tau^-$ final states. These are calculated with the `PPPC4DMID` package [198] that is based on `PYTHIA` (v8.135) and `HERWIG` (v6.510) event generators. The spectra are dominated by emission from the decay of neutral pions. These are *primary* gamma-ray emissions, and are distinguished from *secondary* emission. Also, the gamma-ray emission can be noticeably softened by the bremsstrahlung emission from leptonic final states [199]. We do not include secondary emission in this thesis simply because their effect depends strongly on the astrophysical environment and furthermore since they would be only critical for annihilation in regions of high baryon density, e.g., the planes of galaxies. Additional contributions can arise from three-body final states such as internal bremsstrahlung [200]. However, we do not include this because it can only be included in the framework of a precise DM model e.g., [198].

We next consider gravitational lensing by large-scale structure. Weak lensing convergence field is then given by

$$\kappa(\boldsymbol{\theta}) = \int \mathrm{d}\chi\, W_\kappa(\chi)\delta(\boldsymbol{\theta},\chi), \tag{5.22}$$

where window function for κ is given by

$$W_\kappa(\chi) = \frac{3}{2}\left(\frac{H_0}{c}\right)^2 \Omega_{\mathrm{m}0}(1+z(\chi)) \int_\chi^\infty \mathrm{d}\chi'\; p(\chi')g(\chi',\chi), \tag{5.23}$$

where we denote the source distribution by $p(\chi)$. In this thesis, for $p(\chi)$, we use the sum of the posterior probability distribution function of photometric redshift [160].

Using Eqs. (5.20) and (5.22) with Limber approximation [98, 201], we obtain the angular cross power spectrum of δn and κ as

$$P_{\delta n-\kappa}(\ell) = \int \frac{\mathrm{d}\chi}{\chi^2} W_g(\chi) W_\kappa(\chi) P_{\delta-\delta^2}(\ell/\chi, z(\chi)). \tag{5.24}$$

The direct observable in the present study is the cross-correlation function in real space, which is calculated as

$$\xi_{\delta n-\gamma_t}(\theta) = \int \frac{\mathrm{d}\ell\ell}{2\pi} P_{\delta n-\kappa}(\ell) J_2(\ell\theta), \tag{5.25}$$

where $J_2(x)$ represents the second-order Bessel function [52, 202].

We adopt the so-called halo model approach [77] to estimate the integrand $P_{\delta-\delta^2}(k,z)$ in Eq. (5.24). The halo model is a useful approach for incorporating the non-linear growth of the overdensity δ that determines the anisotropy of the EGB. With the halo model

approach, $P_{\delta-\delta^2}(k,z)$ can be expressed as a sum of two terms called the one-halo term and the two-halo term. The former represents the two-point correlation within a given DM halo, and the latter corresponds to the correlation due to clustering of DM haloes. These two terms can be written as, respectively,

$$\begin{aligned} P^{1h}_{\delta-\delta^2}(k,z) &= \left(\frac{1}{\bar{\rho}_m}\right)^3 \int_{M_{\rm min}} \mathrm{d}M\ n(M,z) M\ u(k|M,z) \\ &\qquad \times (1+b_{sh}(M)) v(k|M,z) \int \mathrm{d}V \rho_h^2(r|M,z), \qquad (5.26) \\ P^{2h}_{\delta-\delta^2}(k,z) &= P^{\rm lin}(k,z) \left(\frac{1}{\bar{\rho}_m}\right)^3 \left[\int_{M_{\rm min}} \mathrm{d}M\ n(M,z) b_h(M,z) M\ u(k|M,z)\right] \\ &\qquad \times \Big[\int_{M_{\rm min}} \mathrm{d}M\ n(M,z) b_h(M,z)(1+b_{sh}(M)) v(k|M,z) \\ &\qquad\qquad \int \mathrm{d}V \rho_h^2(r|M,z)\Big], \qquad (5.27) \end{aligned}$$

where $n(M,z)$ is the halo mass function, and $b_h(M,z)$ is the linear halo bias [87, 203]. We adopt the Navarro-Frenk-White (NFW) DM density profile as shown in Eq. (2.59). In this thesis, we adopt the functional form of the concentration parameter in Ref. [69]. The volume integral of the density squared with Eq. (2.59) is then

$$\int \mathrm{d}V \rho_h^2(r|M,z) = \frac{4\pi r_s^3 \rho_s^2}{3} \left[1 - \frac{1}{(1+c_{\rm vir})^3}\right]. \qquad (5.28)$$

Here, $u(k|M,z)$ and $v(k|M,z)$ describe the fourier transform of density profile and density squared profile, respectively. Both $u(k|M,z)$ and $v(k|M,z)$ are normalized so as to become unity in the limit of $k \to 0$. We use the fourier transform of normalized NFW profile for $u(k|M,z)$ as given in Ref. [77], and the functional form of $v(k|M,z)$ in Ref. [197]. Finally, b_{sh} is the boost factor, which is essentially equal to the flux multiplier $\langle\delta^2(z)\rangle$ described in Section 5.1.2. However, another important effect should be considered: the DM annihilation rate could be boosted due to subhalos that reside within halos. We adopt the fitting formula for b_{sh} provided by Ref. [204] that includes this extra effect. Based on recent high-resolution dissipationless N-body numerical simulations, they find that $b_{sh} = 1.6 \times 10^{-3} \left(M/M_\odot\right)^{0.39}$ provides a satisfactory fit.

The minimum halo mass $M_{\rm min}$ in Eq. (5.26) and Eq. (5.27) is one of the largest model uncertainties. As discussed in Section 5.1.2, it has a large range of possibilities. In this thesis, we consider two cases: a conservative case with $M_{\rm min} = 10^6 M_\odot$ that corresponds to the typical baryonic Jeans mass [172], and an optimistic case with $M_{\rm min} = 10^{-6} M_\odot$ which is the typical free streaming scale for neutralino DM. In our benchmark model, we find that the difference in $M_{\rm min}$ changes the amplitude of cross-correlation signal $\xi_{\delta n-\gamma_t}(\theta)$ by a factor of ~ 10. We regard this variation as our model uncertainty. Namely, the uncertainty of our benchmark model is a factor of ~ 10. Note that this model

uncertainty likely dominates over the systematic uncertainties in the Galactic diffuse template and those due to sample variance in our weak lensing shear measurement.

Recently, Refs. [205, 206] have argued that the halo profile concentration shows a peculiar dependence on the halo mass, and that the simple power-law extrapolation for concentration used in Ref. [204] results in an overestimate of the boost factor by a factor of ~ 50 depending on $M_{\rm min}$. Because most of the cross-correlation signal comes from clustering at large angular scales (see Figure 5.9 later in Section 5.5.2), our results are not strongly affected by the choice. Also, the universality of density profile of DM halo is still unclear. Although we assume the NFW profile in our benchmark model, there exist the different parameterizations of density profile ρ_h (e.g., [207]). Since the cross correlation signal is of the order of $\int {\rm d}V\, \rho_h^2$, the inner slope of density profile could affect the cross-correlation signal even at large angular scales. We discuss these points further in detail in Appendix D.

5.3.1.1 Astrophysical source contribution

Next, we consider astrophysical contributors to the EGB, i.e. blazars and SFGs. The contribution to $P_{\delta n-\kappa}(\ell)$ can be calculated as

$$P_{\delta n-\kappa}(\ell) = \int \frac{{\rm d}\chi}{\chi^2} W_{g,{\rm ast}}(\chi) W_\kappa(\chi) P_{\delta-L}(\ell/\chi, z(\chi)), \tag{5.29}$$

where $W_{g,{\rm ast}}(\chi)$ is the window function of gamma rays from astrophysical sources and $P_{\delta-L}(k,z)$ represents the three dimensional cross power spectrum of matter over density and luminosity. The weight function $W_{g,{\rm ast}}$ is given by

$$W_{g,{\rm ast}}(\chi) = \int_{E_{\rm min}}^{E_{\rm max}} \frac{{\rm d}E_\gamma}{4\pi}\, N_0(\chi) \left(\frac{E'_\gamma}{E_0}\right)^{-\alpha} \exp\left[-\tau\left(E'_\gamma, \chi\right)\right] \eta(E_\gamma), \tag{5.30}$$

where $E_0 = 100$ MeV, $E'_\gamma = (1+z(\chi))E_\gamma$, and $N_0(\chi)\,(E_\gamma/E_0)^{-\alpha}$ represents the gamma-ray energy distribution of the astrophysical sources. In modeling $P_{\delta-L}$, one can use a similar formalism to Eq. (5.26) and Eq. (5.27) but replacing the mass function $n(M,z){\rm d}M$ by the luminosity function $\Phi(L,z){\rm d}L$ [179]. Assuming blazars and SFGs are well approximated as point sources, $P_{\delta-L}$ can be divided into two terms,

$$P^{1h}_{\delta-L}(k,z) = \frac{1}{\bar\rho_m \langle L\rangle(\chi)} \int_{L_{\rm min}(z)}^{L_{\rm max}(z)} {\rm d}L\; \Phi(L,z) L\; u(k|M(L),z) \tag{5.31}$$

$$P^{2h}_{\delta-L}(k,z) = P^{\rm lin}(k,z) \left(\frac{1}{\bar\rho_m \langle L\rangle(\chi)}\right) \left[\int_{M_{\rm min}} {\rm d}M\; n(M,z) b_h(M,z) u(k|M,z)\right] \times \int_{L_{\rm min}(z)}^{L_{\rm max}(z)} {\rm d}L\; \Phi(L,z) L\; b_h(M(L),z), \tag{5.32}$$

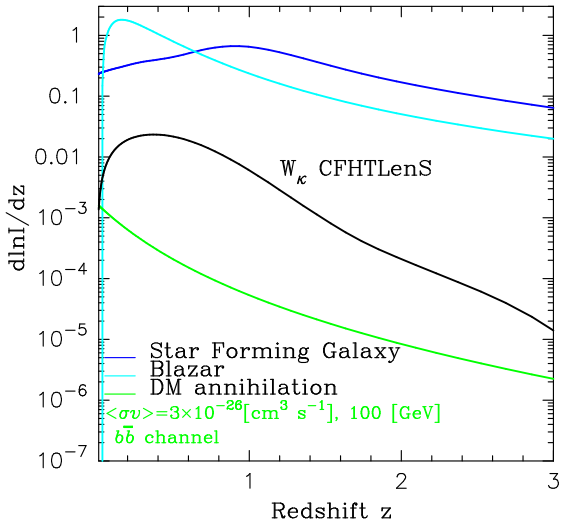

FIGURE 5.2: The effective redshift of cross correlation analysis. The black line shows the window function appeared in lensing convergence field (see, Eq. (5.22)). The colored line represents $\mathrm{d}\ln I/\mathrm{d}z$ for each contributor of EGB where I is the mean intensity. In this figure, we consider three contributions: SFG (blue), blazers (cyan), and DM annihilation (green). We assume that a 100 GeV DM annihilates into $b\bar{b}$ with annihilation cross section $\langle\sigma v\rangle = 3\times10^{-26}$ cm^3 s^{-1}.

where $\langle L\rangle(\chi)$ represents the mean luminosity at $z(\chi)$ and $M(L)$ is the mass-luminosity relation of astrophysical sources. We therefore need to set the specific functional form of $N_0(\chi)$, $\Phi(L,z)$, $M(L)$, and the power-law index of energy distribution of gamma-ray α in order to calculate $P_{\delta n-\kappa}(\ell)$ for each astrophysical source.

For the gamma-ray luminosity function of blazars, we adopt the luminosity-dependent density evolution model [185, 196] with parameters in Ref. [197]. We set the power law index α for blazars to be 2.4, which is consistent with the spectra of resolved blazars. The gamma-ray luminosity of blazars is evaluated as νL_ν at 100 MeV. In this case, N_0 is given by $\langle L\rangle/E_0^2$. We adopt the mass-luminosity relation $M(L) = 10^{11.3}M_\odot\left(L/10^{44.7}\text{ erg s}^{-1}\right)^{1.7}$ that yields the desired bias of blazer host halos [196]. We assume that there are no blazars fainter than the luminosity $L_{\rm min} = 10^{42}$ erg s^{-1} at any redshift. In estimating $L_{\rm max}(z)$, we assume a blazar can be resolved if the gamma-ray flux F at $E > 100$ MeV is larger than 2×10^{-9} cm^{-2} s^{-1}.

For the gamma-ray luminosity function of SFGs, we use the tight correlation between the infrared (IR) luminosity and the gamma-ray luminosity [192], and use the observed IR luminosity function [208]. We define gamma-ray luminosity in the energy range between 0.1 GeV and 100 GeV, and we assume a power-law spectrum with index $\alpha = 2.7$ for SFGs. This leads to $N_0(\chi) = (\langle L\rangle/E_0^2)(\alpha-2)/(1+z(\chi))^{2-\alpha}$ so that the mean luminosity is obtained as $\langle L\rangle = \int \mathrm{d}E_\gamma\, E_\gamma N_0(\chi)\,(E_\gamma/E_0)^{-\alpha}$ with the integral performed

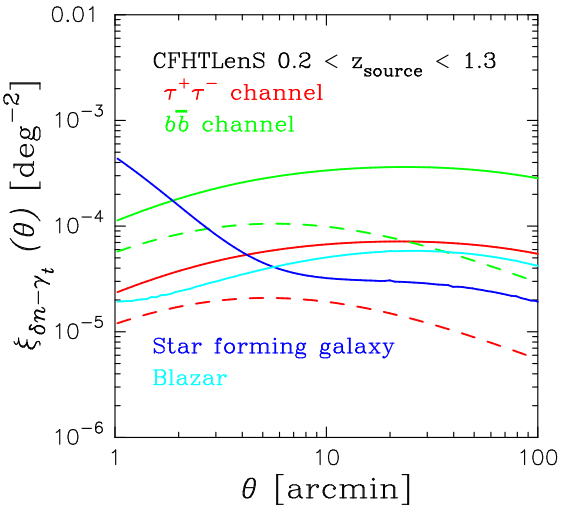

FIGURE 5.3: The expected cross-correlation signals of cosmic shear and important components of the EGB: from SFG (blue), blazers (cyan), and DM annihilation. For DM annihilation, the two cases are shown: a 100 GeV DM particle with annihilation cross section $\langle\sigma v\rangle = 3\times10^{-26}$ cm^3 s^{-1} and annihilation channels $\tau^+\tau^-$ (red) and $b\bar{b}$ (green). Furthermore the model uncertainty is also considered. In this figure, we set two values for the minimum halo mass; $M_{\rm min} = 10^{-6}M_\odot$ (solid) and $M_{\rm min} = 10^{6}M_\odot$ (dashed). This figure is taken from [3].

from $(1+z)E_0$ to $(1+z)E_1$, where $E_0 = 100$ MeV and $E_1 = 100$ GeV. We use the mass-luminosity relation for SFGs, $M(L) = 10^{12}M_\odot\left(L/10^{39}\text{ erg s}^{-1}\right)^{0.5}$ that is calibrated by the Milky Way properties [179]. The minimum luminosity is set to 10^{30} erg s^{-1} at any redshift, while the maximum luminosity is estimated in the same way as in the case of blazars.

We first present the effective redshift of cross correlation of cosmic shear and EGB. Figure 5.2 shows the mean intensity of EGB I from each contributor. There, $\mathrm{d}\ln I/\mathrm{d}z$ for SFG, blazer and DM annihilation are summarized as blue, cyan and green line, respectively. Also, we show the lensing kernel function found in Eq. (5.22) with source galaxy distribution in CFHTLenS. Clearly, we can extract the information at cosmological scales ($z = 0.2 - 0.4$) from cross correlation analysis. Then, in Figure 5.3, we summarize our benchmark model of cross-correlation signals in the case of DM annihilation with $m_{\rm dm} = 100$ GeV and $\langle\sigma v\rangle = 3\times10^{-26}$ cm^3 s^{-1}. In this figure, the results for two annihilation channels are shown, the $\tau^+\tau^-$ channel (red lines) and the $b\bar{b}$ channel (green lines). We represent the level of model uncertainty due to the minimum halo mass $M_{\rm min}$ by plotting both the optimistic case with $M_{\rm min} = 10^{-6}M_\odot$ (solid lines) and the conservative case with $M_{\rm min} = 10^{6}M_\odot$ (dashed lines). The figure clearly shows the sensitivity of the results on $M_{\rm min}$ and the different annihilation channels. The blue and cyan line in Figure 5.3 show the cross-correlation signals of cosmic shear and EGB contributed by unresolved SFGs and blazars, respectively. Clearly, the contribution from

astrophysical sources can be significant at all angular scales. We note that our adopted model of blazars is different from the one in the previous work of Ref. [179]. Our model reproduces the observed flux counts of resolved blazars, whereas the model in Ref. [179] is aimed at reproducing the flux counts as well as the anisotropy of the EGB [190]. The main difference lies in the faint slope of the gamma-ray luminosity function. Overall, our model predicts a larger contribution from blazers to the EGB intensity than the model of Ref. [179] by a factor of ~ 10. In this thesis, we first examine the case where DM annihilation is the sole contributor to the cross-correlation signal. Our analysis under this assumption should provide a conservative constraint on DM annihilation, because the cross-correlation signals due to astrophysical sources are expected to be positive unless the sources are distributed in an anti-correlated manner with respect the underlying DM density field. Furthermore, we find that the statistical error in the current dataset is larger than the expected cross-correlation signals due to astrophysical sources. Therefore, the final result is not strongly affected by the details of the modelling for the astrophysical sources.

5.3.1.2 Point spread function

Let us consider the smoothing effect of the point spread function. The observed number of EGB photons along a line of sight $\boldsymbol{\theta}$ is expressed by the convolution of the underlying number of EGB photons with the PSF of the detector,

$$\delta n^{\rm obs}(\boldsymbol{\theta}) = \int {\rm d}^2\theta' \, W_{\rm PSF}(\boldsymbol{\theta} - \boldsymbol{\theta}')\delta n(\boldsymbol{\theta}'), \tag{5.33}$$

where $\delta n^{\rm obs}$ is the observed number of EGB photons and $W_{\rm PSF}$ is the PSF. This induces an additional scale dependence of the weight function of EGB counts in Eq. (5.21) and Eq. (5.30). Taking into account the energy dependence of the PSF, the scale-dependent weight function is given by

$$\begin{aligned} W_g(\chi) \to W_g(\chi,\ell) &= \int_{E_{\gamma,\rm min}}^{E_{\gamma,\rm max}} {\rm d}E_\gamma \, \frac{\langle\sigma v\rangle}{8\pi}\left(\frac{\bar{\rho}_{\rm dm,0}}{m_{\rm dm}}\right)^2 [1+z(\chi)]^3 \left.\frac{{\rm d}N_\gamma}{{\rm d}E_\gamma}\right|_{E'_\gamma} \\ &\quad \times \exp\left[-\tau\left(E'_\gamma,\chi\right)\right]\eta(E_\gamma)\tilde{W}_{\rm PSF}(\ell,E_\gamma), \end{aligned} \tag{5.34}$$

$$\begin{aligned} W_{g,\rm ast}(\chi) \to W_{g,\rm ast}(\chi,\ell) &= \int_{E_{\rm min}}^{E_{\rm max}} \frac{{\rm d}E_\gamma}{4\pi} \, N_0(\chi)\left(\frac{E'_\gamma}{E_0}\right)^{-\alpha} \\ &\quad \times \exp\left[-\tau\left(E'_\gamma,\chi\right)\right]\eta(E_\gamma)\tilde{W}_{\rm PSF}(\ell,E_\gamma), \end{aligned} \tag{5.35}$$

where $\tilde{W}_{\rm PSF}(\ell, E_\gamma)$ is the fourier transform of the PSF.

The effect of the PSF on the cross-correlation analysis can be evaluated with the specific functional form shown in Eq. (5.16). Figure 5.4 shows the effect. In Figure 5.4, we

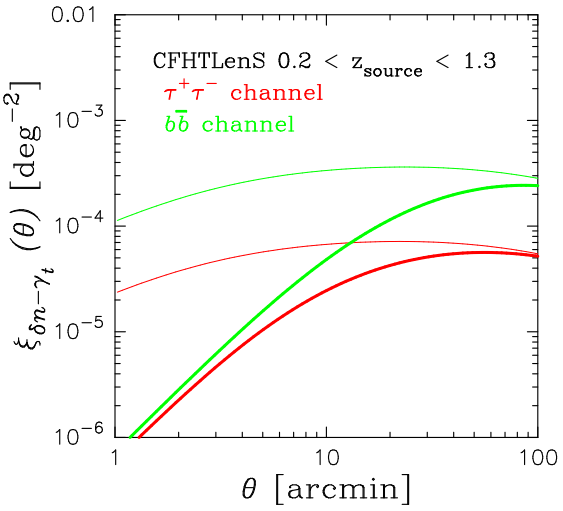

FIGURE 5.4: The smoothing effect due to the PSF on the cross-correlation signals of cosmic shear and EGB (taken from [3]). The thin lines show the original expected signal as in Figure 5.3: annihilation of a 100 GeV mass DM with annihilation cross section $\langle\sigma v\rangle = 3\times10^{-26}$ cm^3 s^{-1} and minimum halo mass $M_{\rm min} = 10^{-6}M_\odot$; red and green lines are for the $\tau^+\tau^-$ and $b\bar{b}$ channel, respectively. The thick lines represent the signal with smoothing due to the PSF.

consider the cross-correlation signal due to the annihilation of DM with $m_{\rm dm} = 100$ GeV and $\langle\sigma v\rangle = 3\times10^{-26}$ cm^3 s^{-1}. To account for the PSF, we first calculate the cross-correlation signals with the scale-dependent weight function in Eq. (5.34) and Eq. (5.35) for front- and back-converting events, respectively. We then average these two signals at a given angular separation assuming the number of front-converting events is equal to that of back-converting events. Clearly, the smoothing effect significantly affects the cross-correlation signal especially at smaller angular scales than the typical size of the PSF, i.e. ~ 50 arcmin. We also expect that the pixelization effect would be unimportant in our analysis, because the pixel size is smaller than the size of the PSF (the pixel size = 12 arcmin).

5.3.2 Cross-correlation estimator and covariance

We summarize the properties of the estimator for cross-correlation analysis. When we measures galaxies' ellipticities ($\boldsymbol{\epsilon}$) and counts extragalactic gamma-ray photons (δn) from an observed data set precisely, the cross-correlation estimator is expressed by

$$\hat{\xi}_{\delta n-\gamma_t}(\theta) = \frac{1}{N_{\rm p}(\theta)}\sum_i^{N_{\rm pixel}}\sum_j^{N_{\rm gal}}\delta n(\boldsymbol{\phi}_i)\epsilon_t(\boldsymbol{\phi}_j|\boldsymbol{\phi}_i)\Delta_\theta(\boldsymbol{\phi}_i-\boldsymbol{\phi}_j), \tag{5.36}$$

$$N_{\rm p}(\theta) = \sum_i^{N_{\rm pixel}}\sum_j^{N_{\rm gal}}\Delta_\theta(\boldsymbol{\phi}_i-\boldsymbol{\phi}_j), \tag{5.37}$$

where $N_{\rm pix}$ is the number of pixels in the gamma-ray counts map, $N_{\rm gal}$ is the number of galaxies, $\delta n(\boldsymbol{\phi}_i)$ is the observed number of EGB photons in pixel i in the gamma-ray counts map, and $\epsilon_t(\boldsymbol{\phi}_j|\boldsymbol{\phi}_i)$ is the tangential component of the j-th galaxy's ellipticity with respect to the i-th pixel of the gamma-ray counts map, defined by

$$\epsilon_t(\boldsymbol{\phi}_j|\boldsymbol{\phi}_i) = -\epsilon_1(\boldsymbol{\phi}_j)\cos(2\alpha_{ij}) - \epsilon_2(\boldsymbol{\phi}_j)\sin(2\alpha_{ij}), \tag{5.38}$$

where α_{ij} is defined as the angle measured from the right ascension direction to a line connecting the i-th pixel and the j-th galaxy. We define the function $\Delta_\theta(\boldsymbol{\phi}) = 1$ for $\theta - \Delta\theta/2 \leq \phi \leq \theta + \Delta\theta/2$ and zero otherwise. $N_{\rm p}(\theta)$ represents the effective pair number in cross-correlation analysis. We can find that this estimator is an unbiased estimator of of cross-correlation signal $\xi_{\delta n-\gamma_t}(\theta)$ by taking the ensemble average of Eq. (5.36).

In order to discuss statistical significances of the measured estimator from real data, one need to estimate the covariance of $\hat{\xi}_{\delta n-\gamma_t}(\theta)$. In particular, the covariance in the case of $\langle\hat{\xi}_{\delta n-\gamma_t}(\theta)\rangle = 0$ is required for detection of cross-correlation signals. The covariance matrix of Eq. (5.36) is defined by

$$\begin{aligned}
{\rm Cov}\left[\hat{\xi}_{\delta n-\gamma_t}(\theta_1), \hat{\xi}_{\delta n-\gamma_t}(\theta_2)\right] &= \langle(\hat{\xi}_{\delta n-\gamma_t}(\theta_1) - \xi_{\delta n-\gamma_t}(\theta_1))(\hat{\xi}_{\delta n-\gamma_t}(\theta_2) - \xi_{\delta n-\gamma_t}(\theta_2))\rangle \\
&= \frac{1}{N_{\rm p}(\theta_1)N_{\rm p}(\theta_2)}\Bigg[\sum_{i,j,k,\ell}\langle n(\boldsymbol{\phi}_i)\epsilon_t(\boldsymbol{\phi}_j|\boldsymbol{\phi}_i)n(\boldsymbol{\phi}_k)\epsilon_t(\boldsymbol{\phi}_\ell|\boldsymbol{\phi}_k)\rangle \\
&\qquad \times\Delta_{\theta_1}(\boldsymbol{\phi}_i - \boldsymbol{\phi}_j)\Delta_{\theta_2}(\boldsymbol{\phi}_k - \boldsymbol{\phi}_\ell)\Bigg] \\
&\qquad -\xi_{\delta n-\gamma_t}(\theta_1)\xi_{\delta n-\gamma_t}(\theta_2),
\end{aligned} \tag{5.39}$$

where i and k represent the indices of summation over gamma-ray counts, and j and ℓ are for galaxies. When two fields δn and $\boldsymbol{\epsilon}$ are independent of each other, the ensemble average $\langle\delta n\,\epsilon_t\,\delta n\,\epsilon_t\rangle$ would simply reduce the product of the ensemble average of each field, i.e. $\langle\delta n\,\delta n\rangle\langle\epsilon_t\,\epsilon_t\rangle$. For shape of galaxies, the two point correlation function $\langle\epsilon_t\,\epsilon_t\rangle$ would be expressed by the summation of intrinsic variance and the correlation signal due to large scale structure;

$$\langle\epsilon_t(\boldsymbol{\phi}_j)\epsilon_t(\boldsymbol{\phi}_\ell)\rangle = \frac{\sigma^2_{\rm int}}{2}\delta_{j\ell} + \xi_+(|\boldsymbol{\phi}_j - \boldsymbol{\phi}_\ell|), \tag{5.40}$$

where $\sigma_{\rm int}$ represents the variance of intrinsic shape of galaxies and $\xi_+(\theta)$ is the two point correlation signal due to weak gravitational lensing. In a concordance ΛCDM universe, $\xi_+(\theta)$ would be expected to be on the order of 10^{-4}. The latest cosmic shear measurement [160] confirmed this expectation with high significance and shows that the typical value of $\sigma_{\rm int}$ to be ~ 0.4. For extragalactic gamma-ray counts, the origin is still unknown. Hence, it is difficult to estimate the exact contribution to the two point

correlation function $\langle \delta n\, \delta n \rangle$. At least, we expect that Poisson processes would dominate on scales larger than the point spread function in gamma-ray surveys. We here assume that photon count fluctuations follow a Poisson distribution with mean corresponding to $\delta n^{\rm obs}(\boldsymbol{\phi})$, where $\delta n^{\rm obs}(\boldsymbol{\phi})$ is the observed gamma-ray count map. In this case, two point correlation function $\langle \delta n\, \delta n \rangle$ would be expressed by

$$\langle \delta n(\boldsymbol{\phi}_i)\delta n(\boldsymbol{\phi}_k)\rangle = \delta n^{\rm obs}(\boldsymbol{\phi}_i)\delta_{ik} + \delta n^{\rm obs}(\boldsymbol{\phi}_i)\delta n^{\rm obs}(\boldsymbol{\phi}_k), \tag{5.41}$$

where the first term represents Poisson fluctuations in count maps and the second term includes the effect of correlation due to the point spread function in gamma-ray surveys. Eq. (5.41) would be a reasonable approximation when considering scales larger than the size of point spread function, i.e. ~ 1 deg in our analysis.

Using Eqs. (5.40) and (5.41), and $\langle \hat{\xi}_{\delta n-\gamma_t}(\theta)\rangle = 0$, one can divide the covariance of our estimator into four contributions as follows:

$$\begin{aligned}
{\rm Cov}\left[\hat{\xi}_{\delta n-\gamma_t}(\theta_1), \hat{\xi}_{\delta n-\gamma_t}(\theta_2)\right] &= C_{\rm SN+p}(\theta_1,\theta_2) + C_{\rm WL+p}(\theta_1,\theta_2) \\
&\quad + C_{\rm SN+obs}(\theta_1,\theta_2) + C_{\rm WL+obs}(\theta_1,\theta_2), \quad (5.42)\\
C_{\rm SN+p}(\theta_1,\theta_2) &= \frac{1}{N_{\rm p}(\theta_1)N_{\rm p}(\theta_2)}\sum_{i,j}\delta n^{\rm obs}(\boldsymbol{\phi}_i)\frac{\sigma^2_{\rm int}}{2}\Delta_{\theta_1}(ij)\Delta_{\theta_2}(ij), \quad (5.43)\\
C_{\rm WL+p}(\theta_1,\theta_2) &= \frac{1}{N_{\rm p}(\theta_1)N_{\rm p}(\theta_2)}\sum_{i,j,\ell}\delta n^{\rm obs}(\boldsymbol{\phi}_i)\xi_+(|\boldsymbol{\phi}_j-\boldsymbol{\phi}_\ell|) \\
&\quad \times\Delta_{\theta_1}(ij)\Delta_{\theta_2}(i\ell), \quad (5.44)\\
C_{\rm SN+obs}(\theta_1,\theta_2) &= \frac{1}{N_{\rm p}(\theta_1)N_{\rm p}(\theta_2)}\sum_{i,j,k}\delta n^{\rm obs}(\boldsymbol{\phi}_i)\delta n^{\rm obs}(\boldsymbol{\phi}_k)\frac{\sigma^2_{\rm int}}{2} \\
&\quad \times\Delta_{\theta_1}(ij)\Delta_{\theta_2}(kj), \quad (5.45)\\
C_{\rm WL+obs}(\theta_1,\theta_2) &= \frac{1}{N_{\rm p}(\theta_1)N_{\rm p}(\theta_2)}\left[\sum_{i,j,k,\ell}\delta n^{\rm obs}(\boldsymbol{\phi}_i)n^{\rm obs}(\boldsymbol{\phi}_k)\xi_+(|\boldsymbol{\phi}_j-\boldsymbol{\phi}_\ell|)\right. \\
&\quad \left.\times\Delta_{\theta_1}(ij)\Delta_{\theta_2}(k\ell)\right], \quad (5.46)
\end{aligned}$$

where $\Delta_{\theta_1}(ij) = \Delta_{\theta_1}(\boldsymbol{\phi}_i - \boldsymbol{\phi}_j)$ and so on. According to the observational fact that ξ_+ is smaller than $\sigma^2_{\rm int}$ by a factor of 10^{-3}, the first term $C_{\rm SN+p}$ and the third term $C_{\rm SN+obs}$ would be the dominant contributions in Eq. (5.42). $C_{\rm SN+p}$ can be estimated from the observed galaxy catalogue and random count maps based on Poisson distribution. We can also estimate $C_{\rm SN+obs}$ by cross-correlating the observed photon counts and randomized galaxy catalogues. The estimation of $C_{\rm SN+p}$ and $C_{\rm SN+obs}$ from the real data set is found in Section 5.4.1.

5.4 Application to Real Data Sets

We consider the cross correlation function of cosmic shear and EGB with real data sets obtained from CFHTLenS surveys and *Fermi* LAT telescope. In this section, we have used the source galaxies with $0.2 < z_p < 1.3$ to measure the cross-correlation of cosmic shear and EGB. We use a total of 2570270, 679070, 1649718, and 770356 galaxies in the W1, W2, W3, and W4 fields, respectively.

5.4.1 Analysis

In order to calculate the cross-correlation of cosmic shear and EGB, we generalize the formula of Eq. (5.36) as follows:

$$\xi_{\delta n-\gamma_t}(\theta) = \frac{\sum_i^{N_{\rm pixel}} \sum_j^{N_{\rm gal}} (n^{\rm obs}(\boldsymbol{\phi}_i) - n^{\rm gm}(\boldsymbol{\phi}_i)) w_j \epsilon_t(\boldsymbol{\phi}_j|\boldsymbol{\phi}_i) \Delta_\theta(\boldsymbol{\phi}_i - \boldsymbol{\phi}_j)}{(1+K(\theta)) \sum_i^{N_{\rm pixel}} \sum_j^{N_{\rm gal}} w_j \Delta_\theta(\boldsymbol{\phi}_i - \boldsymbol{\phi}_j)}, \tag{5.47}$$

where $n^{\rm obs}(\boldsymbol{\phi}_i)$ is the observed number of photons in pixel i in the gamma-ray counts map, $n^{\rm gm}(\boldsymbol{\phi}_i)$ is the contribution from the Galactic emission model estimated using the *Fermi*-LAT diffuse template and detector modeling, and w_j is the weight related to the shape measurement. The overall factor $1 + K(\theta)$ in Eq. (5.47) is used to correct for the multiplicative shear bias m in the shape measurement with *lens*fit [153], which is given by

$$1 + K(\theta) = \frac{\sum_i^{N_{\rm pixel}} \sum_j^{N_{\rm gal}} w_j (1 + m(\boldsymbol{\phi}_j)) \Delta_\theta(\boldsymbol{\phi}_i - \boldsymbol{\phi}_j)}{\sum_i^{N_{\rm pixel}} \sum_j^{N_{\rm gal}} w_j \Delta_\theta(\boldsymbol{\phi}_i - \boldsymbol{\phi}_j)}. \tag{5.48}$$

We have checked that our estimator is consistent with a zero signal when applied to randomized shear catalogues and the observed photon count map. We have also tested a combination of random photon count map with the observed shear catalogue.

For binning in angular separation θ, we set the innermost separation bin to 1 arcmin and use 10 bins logarithmically spaced in $\Delta \log_{10} \theta = 0.2$. In calculating Eq. (5.47), we do not perform pixelization in the galaxy catalogue. We simply consider the center of each pixel in the gamma-ray map as the angular position of the gamma-ray photons to perform the summation in Eq. (5.47). To be precise, this induces an artificial smoothing

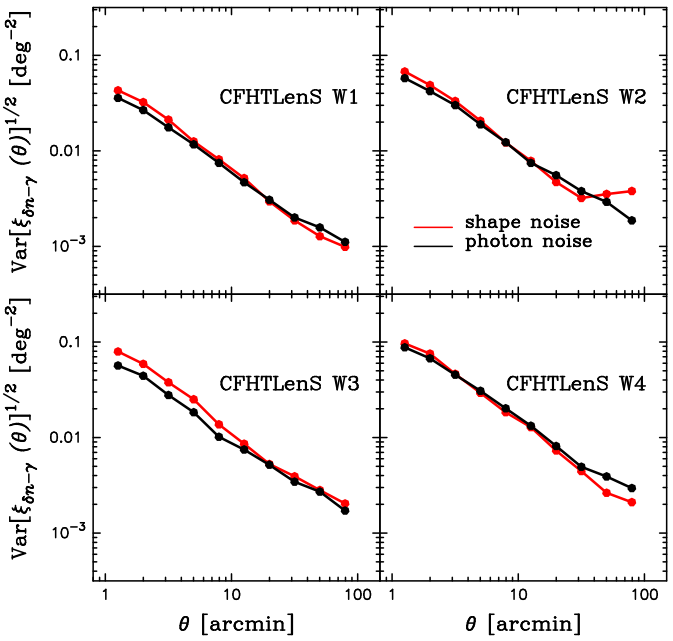

FIGURE 5.5: The variance of cross-correlation signals estimated from a set of randomized realizations and the observed map (taken from [3]). The red line in each panel shows the statistical error associated with the shape measurement. The black line represents the statistical error associated with the Poisson error from the finite number of gamma-ray counts.

over smaller scales than the pixel size in our gamma-ray map, i.e., 0.2 deg. However, we do not expect to detect physically important correlations over such small angular scales due to blurring by the PSF of the *Fermi*-LAT detector, as we show in Section 5.3.1. In this thesis, we take the PSF smoothing into account in theoretical models (see Figure 5.4). Note that the pixelization effect in the gamma-ray map is included in the covariance of our estimator. The pixelization effect is found to be unimportant in detection of the cross-correlation signals at large angular separations.

The statistical properties of our estimator Eq. (5.47) are summarized in Section 5.3.2. There, we summarize the exact formulation of the covariance of our estimator and derive two dominant contributions; they arise from the intrinsic shape variance of galaxies, called shape noise, and the finite number of photon counts per pixel in the gamma-ray maps, called photon noise. We utilize randomized shear catalogues in order to estimate the statistical errors associated with the shape noise. We generate 500 randomized shear catalogues by rotating the direction of each galaxy ellipticity but with fixed amplitude. We then estimate the covariance matrix C_{ij} of the estimator Eq. (5.47) by

$$C_{ij} = \frac{1}{N_{\rm re}-1}\sum_r (\xi^r_{\delta n-\gamma_t}(\theta_i) - \bar{\xi}_{\delta n-\gamma_t}(\theta_i))(\xi^r_{\delta n-\gamma_t}(\theta_j) - \bar{\xi}_{\delta n-\gamma_t}(\theta_j)), \tag{5.49}$$

where $\xi^r_{\delta n-\gamma_t}(\theta_i)$ is the estimator for the i-th angular bin obtained from the r-th realization, and $N_{\rm re} = 500$ is the number of randomized catalogues. The ensemble average of the i-th angular bin over 500 realizations, $\bar{\xi}_{\delta n-\gamma_t}(\theta_i)$, is simply given by

$$\bar{\xi}_{\delta n-\gamma_t}(\theta_i) = \frac{1}{N_{\rm re}} \sum_r \xi^r_{\delta n-\gamma_t}(\theta_i). \tag{5.50}$$

To estimate the statistical error associated with the photon count noise, we generate 500 randomized count maps assuming the photon counts in each pixel follows a Poisson distribution with a mean of $n^{\rm obs}(\boldsymbol{\phi})$. We repeat the cross-correlation analysis with the 500 count maps and the observed galaxy shear catalogue. We then estimate the statistical error related to the photon noise in the same manner shown in Eq. (5.49). In total, we estimate the statistical error associated with the shape measurement and the photon noise by summing these two contributions. Figure 5.5 shows the variance of the cross-correlation signal estimated from the two sets of randomized catalogs as described above. In each panel, the red line shows the contribution from the shape noise and the black line shows the variance due to the photon noise. Overall, the shape noise and the photon noise contribute to the statistical error of our estimator at similar levels.

The cross-correlation estimator adopted here is also dependent on the model for the foreground astrophysical diffuse emission of our own Galaxy. We therefore investigate alternate LAT diffuse models provided by the *Fermi* collaboration to assess differences in the estimated EGB photons. First we work with *Fermi* LAT Pass 7 reprocessed `SOURCE`-class photons. This class is made with a weaker set of cuts to remove cosmic-ray induced backgrounds. We analyze them adopting the appropriate diffuse model and IRF. Second, we work with the *Fermi* LAT Pass 7 photon pipeline instead of Pass 7 reprocessed photons with respectively the appropriate diffuse emission model (`gal_2yearp7v6_v0` and `iso_p7v6clean`) and IRF. In both cases, we first find the best fit diffuse model normalizations, subtract the best fit Galactic diffuse maps from the raw data, and then mask the point sources, to obtain finally the EGB photons. We have explicitly checked that the different Galactic diffuse models do not significantly affect our cross-correlation analyses at present. We discuss this issue later in Section 5.4.2.

It may be necessary to consider another important contribution to the covariance, i.e., the sampling variance. To estimate the sampling variance, one could use the halo model approach as shown in Section 5.3.1, but it is uncertain how the astrophysical sources are included in the model. We expect the sampling variance to be less important compared to the uncertainty of the halo model *itself*. In this thesis, we simply ignore the sampling variance but include the model uncertainty as presented in Section 5.3.1 when deriving the constraints on DM annihilation.

The PSF in optical imaging surveys is one of the major systematics of galaxy shape measurement. The optical PSF originates from diffraction, the atmospheric turbulence, optical aberration, the misalignment of CCD chips on a focal plane, and pixelization effects. Anisotropy of the PSF causes a coherent deformation of images that might mimic the tangential shear pattern due to large scale structure in the universe. Often in cosmic shear measurement, systematic effects are tested through statistical analyses of the 45° rotated component of galaxy ellipticities. This is because the 45° rotated component of cosmic shear should vanish statistically as shown in Section 3.1. In Section 5.4.2, we perform statistical analysis by using the 45° rotated component of galaxy ellipticities and we quantify systematics, if any, of the lensing data set.

5.4.2 Result

Here, we present the measurement of the cross-correlation signals of the cosmic shear and the EGB. Figure 5.6 shows the cross-correlation signals obtained for each CFHTLenS patch. In each panel of Figure 5.6, we also show the cross-correlation using another component of weak lensing shear that is rotated 45° from the tangential shear component. We refer to this component as $\gamma_\times$. In practice, $\gamma_\times$ is often used as an indicator of systematics in the shape measurement. In the case of *perfect* shape measurement and no intrinsic alignment, the correlation signal with $\gamma_\times$ should vanish statistically. In order to quantify the significance of the measured cross-correlation signals with respect to the statistical error, we use the χ^2 statistics defined by

$$\chi^2 = \sum_{i,j} \xi_{\delta n-\gamma_t}(\theta_i) C_{ij}^{-1} \xi_{\delta n-\gamma_t}(\theta_j), \tag{5.51}$$

where $\boldsymbol{C}^{-1}$ denotes the inverse covariance matrix estimated from the randomized realization shown in Section 5.4.1. In our analysis, the number of deg of freedom is 10. The resulting values of $\chi^2/n_{\rm dof}$ for γ_t and for $\gamma_\times$ are shown in each panel. The result is consistent with null detection in each CFHTLenS patch. We confirm that the combined four field together is also consistent with null detection ($\chi^2/n_{\rm dof} = [7.80 + 6.87 + 6.49 + 7.39]/40 = 28.55/40$ in total).

For the diffuse model subtraction, we have made an attempt to estimate the systematics by employing different gamma-ray datasets and different Galactic diffuse emission models. The resulting χ^2 values in each of the CFHTLenS patches are summarized in Table 5.1, and show how the typical systematic error associated with *Fermi* photon analysis are very small ($\Delta\chi^2 \sim 1$–5).

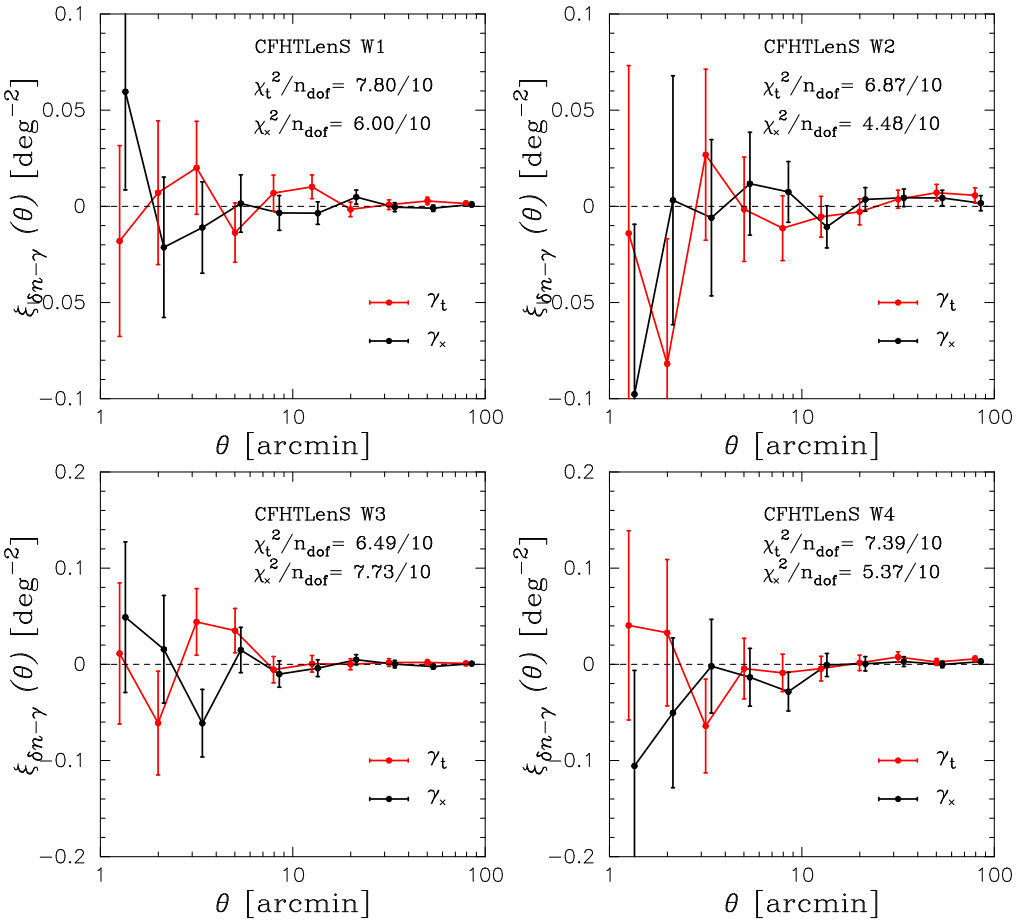

FIGURE 5.6: The cross-correlation signal of cosmic shear and the EGB. Each panel corresponds to each of the CFHTLenS patches W1-W4 (taken from [3]). The red points correspond to the result using tangential shear γ_+, while the black points are for $\gamma_\times$. The error bars represent the standard deviation estimated from our 500 randomized shear catalogues and 500 randomized photon count maps.

	SOURCE/Pass 7	SOURCE/Pass7 rep	ULTRACLEAN/Pass 7	ULTRACLEAN/Pass7 rep
W1	6.91/10	6.22/10	8.58/10	7.80/10
W2	12.26/10	12.32/10	6.98/10	6.87/10
W3	7.62/10	7.11/10	8.77/10	6.49/10
W4	12.88/10	12.95/10	7.57/10	7.39/10

TABLE 5.1: The impact of *Fermi* Galactic diffuse model on the cross-correlation analysis of cosmic shear and the EGB (taken from [3]). The χ^2 value of the cross-correlation signal in each CFHTLenS patch are summarized with different models and photon selections.

5.5 Constraint and Forecast

5.5.1 DM annihilation constraint

We are now able to use the null detection of the cross-correlation to place constraints on the DM annihilation cross-section. For this purpose, we use the maximum Likelihood analysis. We assume that the data vector $\boldsymbol{D}$ is well approximated by the multivariate Gaussian distribution with covariance $\boldsymbol{C}$. In this case, χ^2 statistics (log-likelihood) is given by

$$\chi^2(\boldsymbol{p}) = \sum_{i,j}(D_i - \mu_i(\boldsymbol{p}))C_{ij}^{-1}(D_j - \mu_j(\boldsymbol{p})), \tag{5.52}$$

where $\boldsymbol{\mu}(\boldsymbol{p})$ is the theoretical prediction as a function of parameters of interest. In this thesis, we use the halo model approach shown in Section 5.3.1 to calculate the theoretical prediction. For parameters of interest $\boldsymbol{p}$, we simply adopt the DM particle mass and the annihilation cross-section, $m_{\rm dm}$ and $\langle\sigma v\rangle$[5]. The data vector $\boldsymbol{D}$ consists of the measured cross-correlation signals with the range of $\theta = [1, 100]$ arcmin as

$$D_i = \{\xi_{\delta n-\gamma_t}(\theta_1), \xi_{\delta n-\gamma_t}(\theta_2), ..., \xi_{\delta n-\gamma_t}(\theta_{10})\}, \tag{5.53}$$

where θ_i is the i-th bin of angular separation. The inverse covariance matrix $\boldsymbol{C}^{-1}$ includes the statistical error of the shape measurement and the photon Poisson error. In our likelihood analysis, we assume that the four CFHTLenS patches are independent of each other. With this assumption, the total log-likelihood is given by the summation of Eq. (5.52) in each CFHTLenS patch. In order to constrain $m_{\rm dm}$ and $\langle\sigma v\rangle$, we consider the 68 % confidence level of posterior distribution function of parameters. This is given by the contour line in the two dimensional space ($m_{\rm dm}$ and $\langle\sigma v\rangle$), which is defined as

$$\Delta\chi^2(\boldsymbol{p}) = \chi^2(\boldsymbol{p}) - \chi^2(\boldsymbol{\mu} = 0) = 2.30. \tag{5.54}$$

As discussed in Section 5.3.1, the minimum halo mass causes the uncertainty of the theoretical predictions by a factor of about ten. We therefore derive constraints based on the optimistic case with $M_{\rm min} = 10^{-6}M_\odot$ and on the conservative case with $M_{\rm min} = 10^6 M_\odot$.

[5] Strictly speaking, we need to consider other parameters associated with the model of substructure within DM haloes. These are, for example, the concentration parameter $c_{\rm vir}$ of host halo, subhalo density profile and subhalo mass function. Although we do not include these parameters explicitly in our analysis, we explore the overall effect by considering two cases with the different minimum halo mass $M_{\rm min}$ as the most important *effective* uncertainty of our benchmark model.

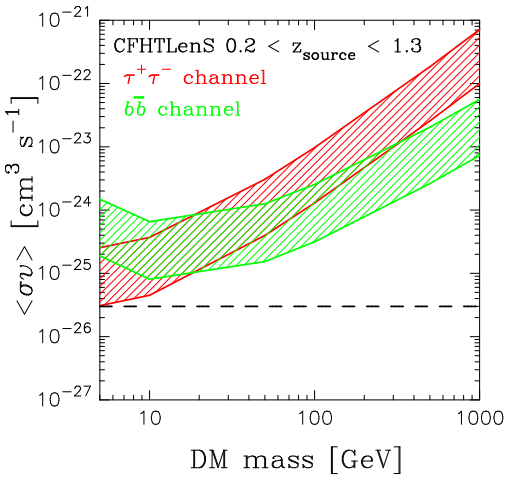

FIGURE 5.7: The 68 % confidence level upper limits on $\langle\sigma v\rangle$ as a function of DM mass (taken from [3]). The red shaded region represents the upper bound for the $\tau^+\tau^-$ channel and the green region is for the $b\bar{b}$ channel. Here, the widths of the shaded regions indicate the model uncertainty: for each shaded region, the upper curve is derived by our benchmark model with $M_{\rm min} = 10^6 M_\odot$ and the lower curve is obtained from the model with $M_{\rm min} = 10^{-6} M_\odot$.

In Figure 5.7, we show the result of our likelihood analysis on the DM parameter space $m_{\rm dm}$ and $\langle\sigma v\rangle$. We plot the constraints for two representative particle physics model, the $\tau^+\tau^-$ channel and the $b\bar{b}$ channel. We also show the results for the two choices of $M_{\rm min}$. The constraint for the case of $M_{\rm min} = 10^{-6} M_\odot$ is significantly stronger, as expected. At low DM mass, the annihilation cross-section is more severely constrained for the $\tau^+\tau^-$ channel, because of its harder gamma-ray spectra that contribute photons at sensitive energies than for the $b\bar{b}$ channel of the same DM mass. For reference, the horizontal dashed line indicates the canonical cross section of $\langle\sigma v\rangle = 3 \times 10^{-26}\,{\rm cm}^3\,{\rm s}^{-1}$ for a thermally produced DM.

5.5.2 Future forecast

It is interesting to explore the discovery potential of the upcoming cosmology surveys in terms of the DM particle properties. In this section, we consider two of these wide surveys with an area coverage of 1400 deg^2 (HSC) and 20000 deg^2 (LSST), by simply scaling the covariance matrix by a factor of 154/1400 or 154/20000, respectively. Assuming the same number density and redshift distribution of source galaxies as in the CFHTLenS, the expected constraints can be scaled by the effective survey area. The result suggests that the upper limit will be improved by a factor of $\sqrt{1400/154} \sim 3$ for HSC and by a factor of $\sqrt{20000/154} \sim 11$ for LSST. In particular, for a 100 GeV DM, the upper limit of $\langle\sigma v\rangle$ with 68 % confidence level could reach $2.7 - 22.2 \times 10^{-26}$ cm^3 s^{-1} for $b\bar{b}$ channel and $1.1 - 8.51 \times 10^{-25}$ cm^3 s^{-1} for $\tau^+\tau^-$ channel in the case of the LSST-like survey. It

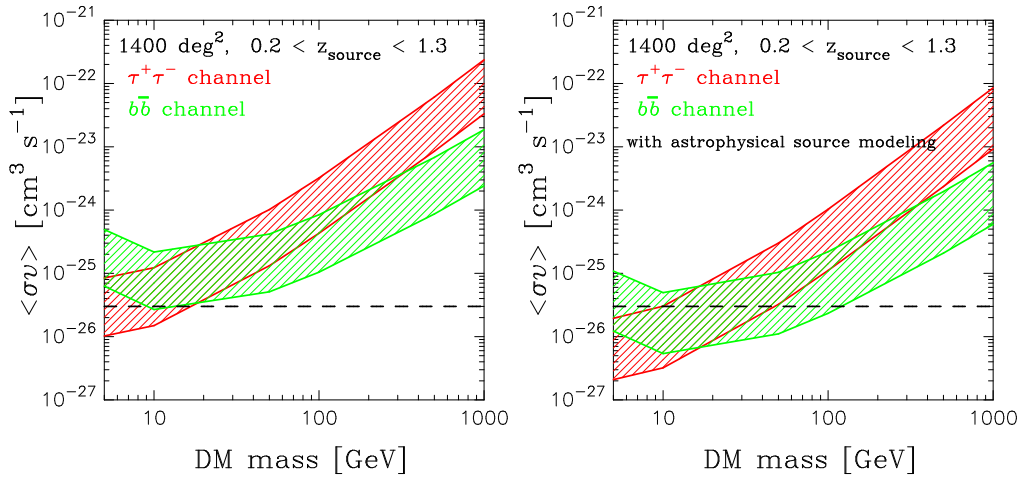

FIGURE 5.8: The expected 68 % confidence level upper limit on $\langle\sigma v\rangle$ as a function of the DM mass for upcoming surveys (taken from [3]). This figure shows the case with a sky coverage of survey area 1400 deg^2. The red shaded region corresponds to the expected upper limit for the $\tau^+\tau^-$ channel and the green one for the $b\bar{b}$ channel. The left panel represents that the conservative case assuming the DM annihilation contribution only, while the right panel shows the optimistic case taking into account astrophysical sources.

will be important to include the uncertainty in the model template of galactic emission and also the sampling variance that is neglected in this thesis. Then we will be able to derive robust and complementary probes of DM annihilation from the cross-correlation signal of cosmic shear and EGB.

As shown in Figure 5.3, the expected cross-correlation of astrophysical sources can be comparable to the DM annihilation signal with $m_{\rm dm} = 100$ GeV and $\langle\sigma v\rangle = 3 \times 10^{-26}$ cm^3 s^{-1}. Thus it will be even more important to accurately take into account of the contribution of astrophysical sources such as blazars and SFG for future surveys. We include the contribution from the astrophysical sources on the assumption that the contribution of blazars and SFGs can be estimated as in our benchmark model described in Section 5.3.1. The sum of the three contributions is given by

$$\xi_{\delta n-\gamma_t}(\theta) = \xi^{\rm dm}_{\delta n-\gamma_t}(\theta|m_{\rm dm}, \langle\sigma v\rangle) + \xi^{\rm blazer}_{\delta n-\gamma_t}(\theta) + \xi^{\rm SFG}_{\delta n-\gamma_t}(\theta). \tag{5.55}$$

Using this as a theoretical model template, we perform the likelihood analysis to make forecast for DM constraints. For simplicity, we assume that the observed cross-correlation is identical to the one of the CFHTLenS W1 patch but that the covariance matrix can be scaled by the survey area. The expected constraint from the HSC-like survey is found in Figure 5.8. The left panel represents the conservative case with no contribution from the astrophysical sources whereas the right panel shows the case with including the astrophysical sources. With the astrophysical sources in the model prediction, we can

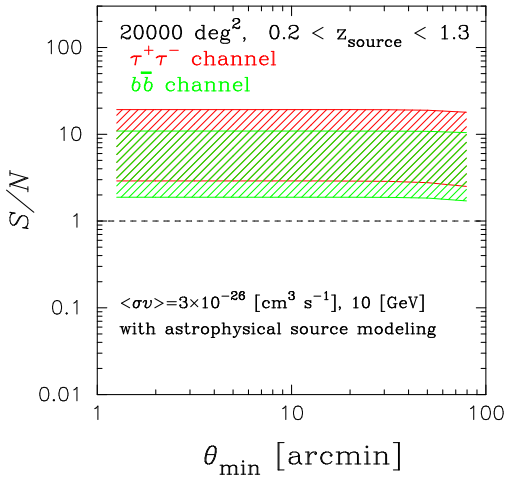

FIGURE 5.9: The cumulative signal-to-noise ratio for the cross-correlation of cosmic shear and the EGB (taken from [3]). The figure shows the case with a sky coverage of survey area 20000 deg^2, i.e., a LSST like survey. The red shaded region corresponds to the signal-to-noise ratio for the $\tau^+\tau^-$ channel and the green one for the $b\bar{b}$ channel. In this figure, we consider the sum of the DM annihilation contribution of a 10 GeV mass DM and the astrophysical sources for these plots.

place tighter upper bound by $\sim 40-70\%$ for the sky coverage of 1400 deg^2. It is clearly important to treat the contribution from the astrophysical sources carefully for future wide-field surveys.

We further study information content in the cross-correlation signal of cosmic shear and EGB. An important quantity is the cumulative signal-to-noise ratio S/N, which is defined by

$$(S/N)^2 = \sum_{i,j} \mu_i(\boldsymbol{p}) C_{ij}^{-1} \mu_j(\boldsymbol{p}). \tag{5.56}$$

In order to calculate S/N, we consider DM models with $\langle\sigma v\rangle = 3\times10^{-26}$ cm^3 s^{-1} for a 10 GeV and 100 GeV dark matter and use the covariance matrix estimated by the randomized method shown in Section 5.4.1.

Figure 5.9 shows the S/N as a function of the minimum angular scale included in the cross-correlation analysis. In this figure, we consider the annihilation signal of a 10 GeV DM particle and we set the maximum angular scale to 100 arcmin. Large-scale cross-correlations determine the information content, and including data at small angular scales does not improve the significance. The same can be said of a 100 GeV DM particle. This is simply because we can not extract information from cross-correlations on scales smaller than the size of the gamma-ray PSF. At large angular scales, $\theta \sim$ 100 arcmin, the signals are mainly contributed by the DM annihilation. We expect that the cross-correlation analysis with upcoming survey with a large sky converge of

$\sim$ 1000 deg^2 will be a powerful probe of dark matter annihilation. We also discuss the detectability of the cross-correlation signal with upcoming lensing surveys. In our benchmark model, the S/N is almost proportional to $\langle\sigma v\rangle$ because the DM contribution dominates over astrophysical contributions. We can thus *detect* at a 3-σ confidence level the DM signature with $\langle\sigma v\rangle \simeq 3 \times 10^{-26}$ cm^3 s^{-1} for a 10 GeV dark matter and $\langle\sigma v\rangle \simeq 1 \times 10^{-25}$ cm^3 s^{-1} for a 100 GeV dark matter in a LSST-like survey. It is important to note that S/N will likely increase significantly if cross-correlations at very large angular scales ($\gtrsim$ 100 arcmin) are included. In this thesis, the statistical error estimated from the real dataset is limited to the range of 1–100 arcmin. However, for upcoming wide-field surveys, we can measure the cross-correlation signal to much larger angular scales where the smoothing effect due to PSF is unimportant.

Chapter 6

Summary and Conclusion

In this thesis, we have paid special attention to statistical analyses of gravitational lensing for purpose of understanding the nature of dark energy and dark matter.

Lensing Minkowski Functionals

In order to constrain on the nature of dark energy, we consider the morphological statistics called Minkowski Functionals (MFs). We have studied various observational effects on lensing MFs with numerical simulations and real data set of cosmic shear in Chapter 4.

Subaru Suprime-Cam

At first, we have examined how mask regions affect the lensing MFs with a large number of numerical simulations. We found that the weak lensing MFs are affected by the lack of cosmic shear data due mostly to foreground contamination. The expected values of the MFs are biased even for a Gaussian convergence field. Masked regions induce the bias of lensing MFs due to (i) effective reduction in the number of sampling Fourier modes of cosmic shear and (ii) scatter of variance of the reconstructed weak lensing mass field for each field of view. The former can be corrected analytically as shown in AppendixA, while it is difficult to study the latter effect without numerical simulations.

Also, we have shown that masked regions significantly contaminate the *pure* gravitational signals in morphological analysis. We also have performed simple analysis to study the impact of masked regions on cosmological parameter estimation. From the cumulative signal-to-noise ratio for the lensing MFs, we have found that the effective survey

area largely determine the cosmological information content in the MFs. By studying the resulting distribution of χ^2 value for simulated maps with masks, we have shown that most of the resulting χ^2 values are found outside the expected one sigma region, when the mask is not considered. Thus, the mask bias could compromise significantly the cosmological parameter estimation.

Adopting the actual sky-mask used for a Subaru observation, we have compared the observed lensing MFs with the results of cosmological simulations to test the consistency of the observed MFs with the standard cosmological model. We have calculated the lensing MFs to the observed weak lensing shear map obtained from a Subaru Suprime-Cam imaging survey. Our analysis shows the resulting $\chi^2/n_{\rm dof} = 29.6/30$ for all the MFs suggests that the observed MFs are consistent with the adopted standard ΛCDM cosmology.

Canada-France-Hawaii Telescope Lensing Survey

Next, we have performed mock lensing observations by incorporating the three-dimensional distribution of the source galaxies and the effect of imperfect shape measurement in the same manner as in the analysis of the real Canada-France-Hawaii Telescope Lensing Survey (CFHTLenS) data. We have made realistic forecast for cosmological parameters from lensing MFs by using the mock catalogs and a Fisher analysis. We have also studied the possible systematics in the lensing MFs measurement that are crucial for cosmological studies. Finally, we have applied the developed method to real cosmic-shear data, to show that the lensing MFs are powerful probe of cosmology.

We found that the overall statistical error would be comparable to the sampling variance for the CFHT survey area. This leads that the accuracy of cosmological parameter constraints is degraded by a factor of ~ 2. Assuming that the statistical error in upcoming wide-field surveys scales to the effective survey area, we found that the lensing MFs can constrain the equation of state parameter of dark energy w_0 with an error of $\Delta w_0 \sim 0.25$ for Hyper Suprime-Cam survey with a sky coverage of ~ 1400 deg^2.

We then have investigated the effects of the two major systematics; the uncertainties in photometric redshifts of the source galaxies and the shear calibration correction. We have found that an error of $\Delta z = 0.05$ in the mean source redshift induces biased dark energy parameter estimation of $\Delta w_0 \sim 0.2$ for CFHTLenS. Furthermore, the shear calibration correction causes non-negligible errors that can bias cosmological parameter estimation as large as the 1σ confidence level for HSC survey.

We also have performed the Likelihood analysis with the lensing MFs template based on our mock catalogs. Although our mock catalogs consist of the limited cosmological models and our cosmological constraints shown in Chapter 4 would be biased, we found that the lensing MFs can, even in realistic case, break the degeneracy of cosmological parameters appeared in the two-point statistics of cosmic shear. This results indicate that lensing MFs enable us to constrain cosmological models by cosmic-shear observations even *without* any prior from the cosmic microwave background (CMB) anisotropies or from the galaxy clustering measurement. Since an independent probe is always important in cosmological analysis, lensing MFs provide a robust test of the standard ΛCDM model which is in good agreement with multiple cosmological analyses, e.g., CMB measurement.

Future Work

There still remain important issues when measuring the MFs from real data set.

With lensing MFs, we can probe the crucial length scales of structure where perturbative approaches break down because of the non-linear gravitational growth (e.g., [125, 209]). This means that we need accurate theoretical predictions of the lensing MFs beyond perturbation methods [120, 210] in order to sample accurately likelihood functions for a wide range of cosmological parameters. Another important issue is theoretical uncertainties associated with baryonic effects. Previous studies (e.g., [211, 212]) studied the effect of including baryonic components to the 2PCFs and consequently to cosmological parameter estimation. The baryonic effect could also be important for the MFs analysis because the MFs generally contain the information at arcminute scales, i.e., the typical virial radius of galaxy clusters. Ref. [213] shows appreciable baryonic effects on peak statistics using a simple model applied to dark-matter-only simulations. Obviously the most straightforward way to include the baryonic effect would be to perform weak-lensing simulations with outputs of hydrodynamic simulations. We continue studying the MFs along this idea.

There are also other possible systematics than those studied in this thesis. For example, source-lens clustering (e.g., [214]) and the intrinsic alignment (e.g., [41]) are likely to compromise cosmological parameter estimation. The statistical properties and the correlation of source galaxies and lensing structures are still uncertain but could be critical when making lensing mass maps. A promising approach in theoretical studies would be associating the source positions with their host dark matter halos on the light cone. This is along the line of our ongoing study using a large set of cosmological simulations in combination with actual observations.

Cross-Correlation Analysis of Cosmic Shear and Extragalactic Gamma-ray Background

In Chapter 5, we have studied the utility of a cosmic shear analysis in terms of probe of the nature of dark matter (DM). There, we have focused on a hypothetical annihilating DM and examined the detectability of the imprint of DM annihilation in real data sets.

We have performed cross-correlation analysis of cosmic shear and extragalactic gamma-ray background using observational data from the CFHTLenS and the *Fermi* satellite. We found that the measured cross-correlation signal is consistent with null detection for the 154 square-degrees sky coverage. Using theoretical models based on large-scale DM structure formation and the statistical error estimated from real data together with a large set of mock observations, we have placed constraints on the DM annihilation cross section. We have considered different DM annihilation channels and varied the minimum mass of DM halos. The derived constraint is $\langle \sigma v \rangle < 10^{-25} - 10^{-24}$ cm^3 s^{-1} for a 100 GeV DM, depending on the assumed parameters and annihilation channel. The constraint improves for smaller DM mass.

In fact, stronger constraints for DM annihilation is found in recent analyses of the *Fermi* observations of dwarf galaxies [215, 216, 217]. However, our constraints are derived using a completely different statistical method based on the cross-correlation of the EGB and cosmic shear. More importantly, our method is based on exactly extragalactic (or cosmological) scales where is completely different from galactic scales. Our limits compete favorably with the constraints of Ref. [218] that use galaxy clusters and those of Ref. [197] that use anisotropies of the EGB. Also, the cross-correlation signal provides an opportunity for testing the DM interpretation of a ∼GeV excess towards the Galactic center [219, 220, 221, 222, 223, 224, 225, 226]

We then have investigated the improvement expected with upcoming gravitational lensing survey with the sky coverage of 20000 square degrees. We have shown that constraints on DM annihilation cross section $\langle \sigma v \rangle$ would reach $2.7 - 22.2 \times 10^{-26}$ cm^3 s^{-1} for the $b\bar{b}$ channel and $1.1 - 8.51 \times 10^{-25}$ cm^3 s^{-1} for the $\tau^+\tau^-$ channel, both for a 100 GeV DM. For lighter DM motivated by the Galactic center excess, the constraints would reach $1.34 - 10.96 \times 10^{-26}$ cm^3 s^{-1} for the $b\bar{b}$ channel (assuming 40 GeV mass) and $0.39 - 3.24 \times 10^{-26}$ cm^3 s^{-1} for the $\tau^+\tau^-$ (assuming 10 GeV mass), allowing a test of the DM origin of the Galactic center excess. Furthermore, if we can made accurate modeling of astrophysical contributions to the cross-correlation, the expect constraints on $\langle \sigma v \rangle$ would be improved by 40-70% for a broad range of DM mass.

We have studied some systematic effects on gamma-ray data. In Chapter 5, we have used a conservative mask of 2° around each point-source. While more aggressive masks or point-source modeling will increase photon statistics, these must be weighed by their larger systematic uncertainties. Also, at present, when we adopt a smaller mask of 1° radius around each point source, we find that the errors on ξ improved by only 10%. For the galactic diffuse model subtraction, we have made an attempt to estimate the systematics by employing different gamma-ray datasets and different Galactic diffuse emission models. Table 5.1 shows the typical systematic error associated with *Fermi* photon analysis ($\Delta\chi^2 \sim 1$–5). In the case of a LSST-like survey (see Section 5.5.2), this difference could induce a systematic error of $\langle\sigma v\rangle$ for a 100 GeV DM on the level of $\sim 3 \times 10^{-26}$ cm^3 s^{-1} for both the $b\bar{b}$ channel and the $\tau^+\tau^-$ channel.

Future Work

There are a few issues in the cross-correlation analysis of cosmic shear and the EGB for upcoming surveys. First, in this thesis, we have only implemented a crude estimate of the systematic error associated with the gamma-ray foreground subtraction. Second, we have not included the sampling variance. While these are not expected to be a significant source of uncertainties at present, mainly because of the large statistical error in the current data sets, they would become more important for analyses using data from upcoming surveys.

Detailed comparisons with numerical simulations would also be required to test the accuracy of our benchmark model based on halo model approach (see also Appendix D). Combined with other observations such as the mean intensity of the EGB, angular correlation of the EGB and the cross-correlation of galaxy position and the EGB [227], one can expect that some of the degeneracies between the DM annihilation and astrophysical sources may be broken. It is therefore important to investigate how much information of the EGB can be extracted from such combined analyses using multiple astrophysical datasets. Gamma-ray analyses with future cosmological surveys would be very powerful methods for understanding the origin of the EGB and the indirect search of DM annihilation.

Appendix A

Effect of Masks on Variance of Smoothed Convergence Field

Here, we summarize the effect of masked regions on the variance of a smoothed convergence field $\mathcal{K}$. In the presence of masked regions in a survey area, one needs to follow a special procedure in order to construct a smoothed convergence field. Let us define the masked region $\mathcal{M}_s(\boldsymbol{\theta})$ in a survey area as

$$\mathcal{M}_s(\boldsymbol{\theta}) = \begin{cases} 1 & \text{where } \boldsymbol{\theta} \text{ lies in data region} \\ 0 & \text{otherwise.} \end{cases} \tag{A.1}$$

When the area with mask $\mathcal{M}_s(\boldsymbol{\theta})$ is smoothed, there would exist ill-defined pixels due to the convolution between $\mathcal{M}_s$ and a filter function for smoothing $U(\boldsymbol{\theta})$. We thus need to discard the ill-defined pixels to perform statistical analyses. The removal of the ill-defined pixels is equivalent to pasting a new mask $\mathcal{M}_1(\boldsymbol{\theta})$ so that we can mask the ill-defined pixels as well. We then get

$$\mathcal{K}^{\rm obs}(\boldsymbol{\theta}) \;=\; \mathcal{M}_1(\boldsymbol{\theta})\mathcal{K}_1(\boldsymbol{\theta}), \tag{A.2}$$

where

$$\mathcal{K}_1(\boldsymbol{\theta}) \;=\; \int \mathrm{d}^2\phi \; U(\boldsymbol{\theta}-\boldsymbol{\phi})\mathcal{M}_s(\boldsymbol{\phi})\kappa(\boldsymbol{\phi}). \tag{A.3}$$

The variance of the smoothed field is given by

$$\begin{aligned}
\sigma_0^2 &= \frac{1}{S}\int \mathrm{d}^2\theta \langle \mathcal{K}^{\rm obs}(\boldsymbol{\theta})^2\rangle \\
&= \frac{1}{S}\int \mathrm{d}^2\theta \mathcal{M}_1(\boldsymbol{\theta})\langle \mathcal{K}_1(\boldsymbol{\theta})^2\rangle \\
&= \frac{1}{S}\int \mathrm{d}^2\theta \mathcal{M}_1(\boldsymbol{\theta})\int \frac{\mathrm{d}^2\ell}{(2\pi)^2}\frac{\mathrm{d}^2\ell'}{(2\pi)^2}\langle \mathcal{K}_1(\boldsymbol{\ell})\mathcal{K}_1^*(\boldsymbol{\ell}')\rangle \exp\left(i(\boldsymbol{\ell}-\boldsymbol{\ell}')\cdot\boldsymbol{\theta}\right) \\
&= \frac{1}{S}\int \frac{\mathrm{d}^2\ell}{(2\pi)^2}\frac{\mathrm{d}^2\ell'}{(2\pi)^2}\mathcal{M}_1(\boldsymbol{\ell}-\boldsymbol{\ell}')\langle \mathcal{K}_1(\boldsymbol{\ell})\mathcal{K}_1^*(\boldsymbol{\ell}')\rangle, \qquad \text{(A.4)}
\end{aligned}$$

where we use the relation $\mathcal{M}_1(\boldsymbol{\theta})^2 = \mathcal{M}_1(\boldsymbol{\theta})$. The Fourier mode of $\mathcal{K}_1$ is given by

$$\begin{aligned}
\mathcal{K}_1(\boldsymbol{\ell}) &= \int \mathrm{d}^2\theta\mathrm{d}^2\phi\ U(\boldsymbol{\theta}-\boldsymbol{\phi})\mathcal{M}_s(\boldsymbol{\phi})\kappa(\boldsymbol{\phi})\exp\left(i\boldsymbol{\ell}\cdot\boldsymbol{\theta}\right) \\
&= U(\boldsymbol{\ell})\int \frac{\mathrm{d}^2\ell'}{(2\pi)^2}\mathcal{M}_s(\boldsymbol{\ell}')\kappa(\boldsymbol{\ell}-\boldsymbol{\ell}'), \\
\langle \mathcal{K}_1(\boldsymbol{\ell})\mathcal{K}_1^*(\boldsymbol{\ell}')\rangle &= U(\boldsymbol{\ell})U^*(\boldsymbol{\ell}')\int \frac{\mathrm{d}^2\ell_1}{(2\pi)^2}\frac{\mathrm{d}^2\ell_1'}{(2\pi)^2}\mathcal{M}_s(\boldsymbol{\ell}_1)\mathcal{M}_s^*(\boldsymbol{\ell}_1')\langle\kappa(\boldsymbol{\ell}-\boldsymbol{\ell}_1)\kappa^*(\boldsymbol{\ell}'-\boldsymbol{\ell}_1')\rangle \\
&= U(\boldsymbol{\ell})U^*(\boldsymbol{\ell}')\int \frac{\mathrm{d}^2\ell_1}{(2\pi)^2}\frac{\mathrm{d}^2\ell_1'}{(2\pi)^2}\mathcal{M}_s(\boldsymbol{\ell}_s)\mathcal{M}_s^*(\boldsymbol{\ell}_1')(2\pi)^2\delta^{(2)}(\boldsymbol{\ell}-\boldsymbol{\ell}_1-\boldsymbol{\ell}'+\boldsymbol{\ell}_1')P_\kappa(|\boldsymbol{\ell}-\boldsymbol{\ell}_1|) \\
&= U(\boldsymbol{\ell})U^*(\boldsymbol{\ell}')\int \frac{\mathrm{d}^2\ell_1}{(2\pi)^2}\mathcal{M}_s(\boldsymbol{\ell}_1)\mathcal{M}_s^*(\boldsymbol{\ell}_1+\boldsymbol{\ell}'-\boldsymbol{\ell})P_\kappa(|\boldsymbol{\ell}-\boldsymbol{\ell}_1|) \qquad \text{(A.5)}
\end{aligned}$$

Here, we assume that, with $\mathcal{M}_1(\boldsymbol{\theta})$, there remains only *clean* regions where the smoothed convergence is not affected by the original masked regions $\mathcal{M}_s(\boldsymbol{\theta})$. In this case, the measured $\mathcal{K}$ field is given by

$$\mathcal{K}^{\rm obs}(\boldsymbol{\theta}) \simeq \mathcal{M}_1(\boldsymbol{\theta})\int \mathrm{d}^2\phi\ U(\boldsymbol{\theta}-\boldsymbol{\phi})\kappa(\boldsymbol{\phi}). \qquad \text{(A.6)}$$

The fourier mode of $\mathcal{K}^{\rm obs}$ can then be given by

$$\begin{aligned}
\mathcal{K}^{\rm obs}(\boldsymbol{\ell}) &= \int \mathrm{d}^2\theta\ \mathcal{K}^{\rm obs}(\boldsymbol{\theta})\exp\left(i\boldsymbol{\ell}\cdot\boldsymbol{\theta}\right) \\
&\simeq \int \mathrm{d}^2\theta\ \mathcal{M}_1(\boldsymbol{\theta})\int \mathrm{d}^2\phi\ U(\boldsymbol{\theta}-\boldsymbol{\phi})\kappa(\boldsymbol{\phi})\exp\left(i\boldsymbol{\ell}\cdot\boldsymbol{\theta}\right) \\
&= \int \mathrm{d}^2\theta'\mathrm{d}^2\theta\mathrm{d}^2\phi\ \mathcal{M}_1(\boldsymbol{\theta}')\delta^{(2)}(\boldsymbol{\theta}-\boldsymbol{\theta}')U(\boldsymbol{\theta}-\boldsymbol{\phi})\kappa(\boldsymbol{\phi})\exp\left(i\boldsymbol{\ell}\cdot\boldsymbol{\theta}\right) \\
&= \int \frac{\mathrm{d}^2\ell'}{(2\pi)^2}\int \mathrm{d}^2\theta'\mathrm{d}^2\theta\mathrm{d}^2\phi\ \mathcal{M}_1(\boldsymbol{\theta}')U(\boldsymbol{\theta}-\boldsymbol{\phi})\kappa(\boldsymbol{\phi})\exp\left(i\boldsymbol{\ell}\cdot\boldsymbol{\theta}\right)\exp\left(-i\boldsymbol{\ell}'\cdot(\boldsymbol{\theta}-\boldsymbol{\theta}')\right) \\
&= \int \frac{\mathrm{d}^2\ell'}{(2\pi)^2}\mathcal{M}_1(\boldsymbol{\ell}')\int \mathrm{d}^2\theta\mathrm{d}^2\phi\ U(\boldsymbol{\theta}-\boldsymbol{\phi})\kappa(\boldsymbol{\phi})\exp\left(i(\boldsymbol{\ell}-\boldsymbol{\ell}')\cdot\boldsymbol{\theta}\right) \\
&= \int \frac{\mathrm{d}^2\ell'}{(2\pi)^2}\mathcal{M}_1(\boldsymbol{\ell}')U(\boldsymbol{\ell}-\boldsymbol{\ell}')\kappa(\boldsymbol{\ell}-\boldsymbol{\ell}'). \qquad \text{(A.7)}
\end{aligned}$$

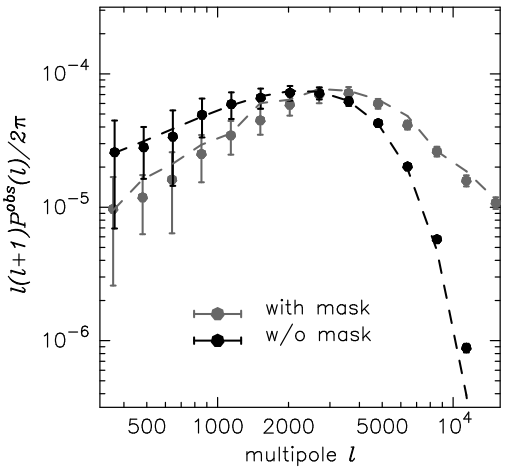

FIGURE A.1: The test the validity of Eq. (A.6). The figure is taken from [1]. The gray points with error bars represent $P^{\rm obs}(\ell)$ obtained from 1000 Gaussian maps with mask $\mathcal{M}_s(\boldsymbol{\theta})$. The gray dashed line is the theoretical prediction of Eq. (A.11). The black points with error bars show $P^{\rm obs}(\ell)$ obtained from 1000 maps without mask. The black dashed line is the input power spectrum smoothed by the Gaussian filter U.

The variance of the smoothed convergence field is calculated as

$$\begin{aligned}
\sigma_0^2 &= \frac{1}{S}\int \mathrm{d}^2\theta \langle \mathcal{K}^{\rm obs}(\boldsymbol{\theta})^2\rangle \\
&= \frac{1}{S}\int \mathrm{d}^2\theta \int \frac{\mathrm{d}^2\ell}{(2\pi)^2}\frac{\mathrm{d}^2\ell'}{(2\pi)^2}\langle \mathcal{K}^{\rm obs}(\boldsymbol{\ell})\mathcal{K}^{\rm obs}(\boldsymbol{\ell}')\rangle \exp\left(-i(\boldsymbol{\ell}-\boldsymbol{\ell}')\cdot\boldsymbol{\theta}\right) \\
&= \frac{1}{S}\int \frac{\mathrm{d}^2\ell}{(2\pi)^2}\ \langle \mathcal{K}^{\rm obs}(\boldsymbol{\ell})(\mathcal{K}^{\rm obs})^*(\boldsymbol{\ell})\rangle, \qquad \text{(A.8)}
\end{aligned}$$

where the ensemble average of the Fourier mode is

$$\begin{aligned}
\langle \mathcal{K}^{\rm obs}(\boldsymbol{\ell})(\mathcal{K}^{\rm obs})^*(\boldsymbol{\ell}')\rangle &\simeq \int \frac{\mathrm{d}^2\ell_1}{(2\pi)^2}\frac{\mathrm{d}^2\ell_1'}{(2\pi)^2}\mathcal{M}_1(\boldsymbol{\ell}_1)\mathcal{M}_1^*(\boldsymbol{\ell}_1')U(\boldsymbol{\ell}-\boldsymbol{\ell}_1)U^*(\boldsymbol{\ell}'-\boldsymbol{\ell}_1') \\
&\qquad \times\langle\kappa(\boldsymbol{\ell}-\boldsymbol{\ell}_1)\kappa^*(\boldsymbol{\ell}'-\boldsymbol{\ell}_1')\rangle \\
&= \int \frac{\mathrm{d}^2\ell_1}{(2\pi)^2}\frac{\mathrm{d}^2\ell_1'}{(2\pi)^2}\mathcal{M}_1(\boldsymbol{\ell}_1)\mathcal{M}_1^*(\boldsymbol{\ell}_1')U(\boldsymbol{\ell}-\boldsymbol{\ell}_1)U^*(\boldsymbol{\ell}'-\boldsymbol{\ell}_1') \\
&\qquad \times(2\pi)^2 P_\kappa(|\boldsymbol{\ell}-\boldsymbol{\ell}_1|)\delta^{(2)}(\boldsymbol{\ell}-\boldsymbol{\ell}_1-\boldsymbol{\ell}'+\boldsymbol{\ell}_1') \\
&= \int \frac{\mathrm{d}^2\ell_1}{(2\pi)^2}\mathcal{M}_1(\boldsymbol{\ell}_1)\mathcal{M}_1^*(\boldsymbol{\ell}_1+\boldsymbol{\ell}'-\boldsymbol{\ell})|U(\boldsymbol{\ell}-\boldsymbol{\ell}_1)|^2 P_\kappa(|\boldsymbol{\ell}-\boldsymbol{\ell}_1|) \qquad \text{(A.9)}
\end{aligned}$$

We have checked the validity of Eq. (A.6) by using 1000 Gaussian simulations. They are the same set of simulations as in Section 4.1.1. For each Gaussian simulation, we paste the observed masked region $\mathcal{M}_s(\boldsymbol{\theta})$ from the Subaru Suprime-Cam observation. We then smoothed the map with a Gaussian filter of Eq. (3.72) with smoothing scale of 1 arcmin. In order to avoid the ill-defined pixels, we paste a new mask $\mathcal{M}_1(\boldsymbol{\theta})$, which is constructed conservatively to cover the regions within two times the smoothing scale

from the boundary of the original mask $\mathcal{M}_s(\boldsymbol{\theta})$. We then calculate

$$P^{\rm obs}(\ell) \equiv \langle \mathcal{K}^{\rm obs}(\boldsymbol{\ell})(\mathcal{K}^{\rm obs})^*(\boldsymbol{\ell})\rangle/S. \tag{A.10}$$

If $\mathcal{K}^{\rm obs}$ can be well-approximated by Eq. (A.6), this quantity should be given by

$$P^{\rm obs}(\ell) \simeq \frac{1}{S}\int \frac{{\rm d}^2\ell_1}{(2\pi)^2}|\mathcal{M}_1(\boldsymbol{\ell}_1)|^2|U(\boldsymbol{\ell}-\boldsymbol{\ell}_1)|^2 P_\kappa(|\boldsymbol{\ell}-\boldsymbol{\ell}_1|). \tag{A.11}$$

Figure A.1 compares Eq. (A.6) and Eq. (A.11). Clearly Eq. (A.6) is an excellent approximation for the observed survey geometry. The ill-defined pixels are efficiently masked by $\mathcal{M}_1(\boldsymbol{\theta})$. We also find the variance σ_0^2 decreases by a factor of $O(5\%)$. This causes the bias of MFs even if the lensing field is Gaussian.

Appendix B

Effect of Source Redshift Clustering on Variance of Smoothed Convergence Field

Here, we summarize the effect of source redshift clustering on the variance of a smoothed convergence field. Weak lensing convergence κ is given by the integral of matter over density with a weight along the line-of-sight $\boldsymbol{\theta}$:

$$\kappa(\boldsymbol{\theta}, \chi_s) = \frac{3}{2}\left(\frac{H_0}{c}\right)^2 \Omega_{\rm m0} \int_0^{\chi_s} {\rm d}\chi_\ell \; g(\chi_s, \chi_\ell) \frac{\delta[r(\chi_\ell)\boldsymbol{\theta}, \chi_\ell]}{a(\chi_\ell)}, \tag{B.1}$$

$$g(\chi_s, \chi_\ell) = \frac{r(\chi_s - \chi_\ell) r(\chi_\ell)}{r(\chi_s)}, \tag{B.2}$$

where χ is comoving distance, $r(\chi)$ is angular diameter distance, and χ_s represents the comoving distance to a source. One can assign a probability distribution $p(\chi_s)$ of a source galaxy's position, or in fact $p(\chi_s)$ for a population of source galaxies, and integrate as,

$$\bar{\kappa}(\boldsymbol{\theta}) = \frac{3}{2}\left(\frac{H_0}{c}\right)^2 \Omega_{\rm m0} \int_0^{\chi H} {\rm d}\chi_s \; p(\chi_s) \int_0^{\chi_s} {\rm d}\chi_\ell \; g(\chi_s, \chi_\ell) \frac{\delta[r(\chi_\ell)\boldsymbol{\theta}, \chi_\ell]}{a(\chi_\ell)}. \tag{B.3}$$

In the conventional multiple lens plane algorithm, one can calculate the both convergence field κ and $\bar{\kappa}$ by using a suitable weight function in the integral. In practice in ray-tracing simulations, we shoot rays from the observer point to the source redshifts to obtain κ, whereas we shoot rays up to some certain (high-)redshift but with weight $p(\chi_s)$ along the line-of-sights to obtain $\bar{\kappa}$. In the former case, the full three-dimensional positions of the source galaxies are realized as in the observation considered, i.e., CFHTLenS in our case. The difference between κ and $\bar{\kappa}$ can be easily seen in a direct manner using the

two sets of simulations, and the resulting variances of smoothed convergence field can be explicitly compared.

The smoothed convergence field for κ is given by

$$\mathcal{K}(\boldsymbol{\theta}) = \sum_i U(\boldsymbol{\theta} - \boldsymbol{\phi}_i)\kappa(\boldsymbol{\phi}_i, \chi_{si}), \tag{B.4}$$

where $U(\boldsymbol{\theta})$ is the filter function for smoothing and the summation is taken over the source objects. The smoothed convergence field for $\bar{\kappa}$ is also obtained in the same way. The two-point correlation function of $\mathcal{K}$ is then given by

$$\begin{aligned}
\langle \mathcal{K}(\boldsymbol{\theta}_1)\mathcal{K}(\boldsymbol{\theta}_2)\rangle &= \langle \sum_i \sum_j U(\boldsymbol{\theta}_1 - \boldsymbol{\phi}_i)U(\boldsymbol{\theta}_2 - \boldsymbol{\phi}_j)\kappa(\boldsymbol{\phi}_i, \chi_{si})\kappa(\boldsymbol{\phi}_j, \chi_{sj})\rangle \\
&= \int \mathrm{d}^2\phi_1 \mathrm{d}^2\phi_2\, U(\boldsymbol{\theta}_1 - \boldsymbol{\phi}_1)U(\boldsymbol{\theta}_2 - \boldsymbol{\phi}_2) \\
&\times \int \mathrm{d}\chi_{s1}\, \mathrm{d}\chi_{s2}\; p(\chi_{s1})p(\chi_{s2})\left[1 + \xi_{ss}(\boldsymbol{\phi}_1 - \boldsymbol{\phi}_2, \chi_{s1}, \chi_{s2})\right] \\
&\qquad \times \langle \kappa(\boldsymbol{\phi}_1, \chi_{s1})\kappa(\boldsymbol{\phi}_2, \chi_{s2})\rangle,
\end{aligned} \tag{B.5}$$

where $\langle \cdots \rangle$ represents the operator of ensemble average and ξ_{ss} represents the two point correlation function of the sources. One can also calculate the two-point correlation of $\bar{\mathcal{K}}$ in the similar manner. We then obtain the non-vanishing difference between $\langle \bar{\mathcal{K}}\bar{\mathcal{K}}\rangle$ and $\langle \mathcal{K}\mathcal{K}\rangle$ as

$$\begin{aligned}
\langle \bar{\mathcal{K}}\bar{\mathcal{K}} - \mathcal{K}\mathcal{K}\rangle &= \int \mathrm{d}^2\phi_1 \mathrm{d}^2\phi_2\; U(\boldsymbol{\theta}_1 - \boldsymbol{\phi}_1)U(\boldsymbol{\theta}_2 - \boldsymbol{\phi}_2) \\
&\times \left[\bar{\xi}_{ss}(\boldsymbol{\phi}_1 - \boldsymbol{\phi}_2)w_{\rm pp}(\boldsymbol{\phi}_1 - \boldsymbol{\phi}_2) - V_{\rm pp}(\boldsymbol{\phi}_1 - \boldsymbol{\phi}_2)\right], \qquad \text{(B.6)} \\
\bar{\xi}_{ss}(\boldsymbol{\phi}_1 - \boldsymbol{\phi}_2) &= \int \mathrm{d}\chi_{s1}\mathrm{d}\chi_{s2}\; p(\chi_{s1})p(\chi_{s2})\xi_{ss}(\boldsymbol{\phi}_1 - \boldsymbol{\phi}_2, \chi_{s1}, \chi_{s2}), \qquad \text{(B.7)} \\
w_{\rm pp}(\boldsymbol{\phi}_1 - \boldsymbol{\phi}_2) &= \langle \bar{\kappa}(\boldsymbol{\phi}_1)\bar{\kappa}(\boldsymbol{\phi}_2)\rangle, \qquad \text{(B.8)} \\
V_{\rm pp}(\boldsymbol{\phi}_1 - \boldsymbol{\phi}_2) &= \frac{9}{4}\left(\frac{H_0}{c}\right)^4 \Omega_{\rm m0}^2 \int \mathrm{d}\chi_{s1}\mathrm{d}\chi_{s2}\; p(\chi_{s1})p(\chi_{s2})\xi_{ss}(\boldsymbol{\phi}_1 - \boldsymbol{\phi}_2, \chi_{s1}, \chi_{s2}) \\
&\times \int \mathrm{d}\chi_{\ell 1}\mathrm{d}\chi_{\ell 2}\; \frac{g(\chi_{s1}, \chi_{\ell 1})g(\chi_{s2}, \chi_{\ell 2})}{a(\chi_{\ell 1})a(\chi_{\ell 2})} \langle \delta[r(\chi_{\ell 1})\boldsymbol{\phi_1}, \chi_{\ell 1}]\delta[r(\chi_{\ell 2})\boldsymbol{\phi_2}, \chi_{\ell 2}]\rangle. \qquad \text{(B.9)}
\end{aligned}$$

This non-vanishing term arises if the source clustering ξ_{ss} evolves over redshift. Note also that the MFs of $\bar{\mathcal{K}}$ and those of $\mathcal{K}$ can be, in general, different if their variances differ (see, e.g. Ref. [1]).

In practice, the smoothed convergence field is often estimated from the shear field γ. In this case, one can calculate $\mathcal{K}$ using the following equation,

$$\mathcal{K}(\boldsymbol{\theta}) = \sum_i Q_t(\boldsymbol{\theta} - \boldsymbol{\phi}_i)\gamma_t(\boldsymbol{\phi}_i, \chi_{si}), \tag{B.10}$$

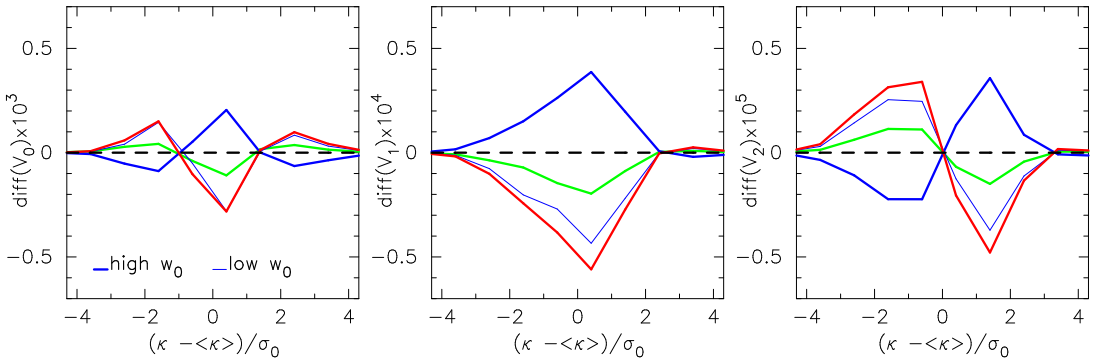

FIGURE B.1: Impact of a source redshift clustering on lensing MFs (taken from [2]). This figure shows the differences of average MFs over 40 catalogs between our fiducial cosmology and another one that includes a given systematic. The red line represents the impact of the difference of source redshift distribution and the green one shows the effect of source redshift clustering on lensing MFs. For comparison, the case of cosmological model with higher (lower) w_0 is also shown as the thick (thin) blue line.

where $Q_t(\boldsymbol{\theta})$ is the filter function for the shear field which is related to $U(\boldsymbol{\theta})$ by Equation (3.74) and $\gamma_t(\boldsymbol{\theta}, \chi_s)$ is the tangential component of shear at the position $\boldsymbol{\theta}$ when a source is at χ_s from the observer. Using Eq. (B.10), one can derive the correspoding non-vanishing term

$$\begin{aligned}
\langle \bar{\mathcal{K}}\bar{\mathcal{K}} - \mathcal{K}\mathcal{K} \rangle &= \int \mathrm{d}^2\phi_1 \mathrm{d}^2\phi_2 \; Q_t(\boldsymbol{\theta}_1 - \boldsymbol{\phi}_1) Q_t(\boldsymbol{\theta}_2 - \boldsymbol{\phi}_2) \\
&\times \left[\bar{\xi}_{ss}(\boldsymbol{\phi}_1 - \boldsymbol{\phi}_2) \langle \bar{\gamma}_t(\boldsymbol{\phi}_1) \bar{\gamma}_t(\boldsymbol{\phi}_2) \rangle - V^{\gamma}_{\mathrm{pp}}(\boldsymbol{\phi}_1 - \boldsymbol{\phi}_2) \right], \qquad \text{(B.11)} \\
V^{\gamma}_{\mathrm{pp}}(\boldsymbol{\phi}_1 - \boldsymbol{\phi}_2) &= \int \mathrm{d}\chi_{s1} \mathrm{d}\chi_{s2} \; p(\chi_{s1}) p(\chi_{s2}) \xi_{ss}(\boldsymbol{\phi}_1 - \boldsymbol{\phi}_2, \chi_{s1}, \chi_{s2}) \\
&\times \langle \gamma_t(\boldsymbol{\phi}_1, \chi_{s1}) \gamma_t(\boldsymbol{\phi}_2, \chi_{s2}) \rangle, \qquad \text{(B.12)} \\
\langle \bar{\gamma}_t(\boldsymbol{\phi}_1) \bar{\gamma}_t(\boldsymbol{\phi}_2) \rangle &= \frac{9}{4} \left(\frac{H_0}{c} \right)^4 \Omega^2_{\mathrm{m0}} \int_0^{\chi_H} \frac{\mathrm{d}\chi}{a^2(\chi)} \bar{W}^2(\chi) \\
&\times \int \frac{\ell d\ell}{2\pi} P_\delta \left(k = \frac{\ell}{r(\chi)}, z(\chi) \right) \left(\frac{J_0(\ell\phi_{12}) + J_4(\ell\phi_{12})}{2} \right), \qquad \text{(B.13)} \\
\bar{W}(\chi) &= \int_{\chi}^{\chi_H} \mathrm{d}\chi' p(\chi') \frac{r(\chi' - \chi)}{r(\chi')}, \qquad \text{(B.14)} \\
\langle \gamma_t(\boldsymbol{\phi}_1, \chi_{s1}) \gamma_t(\boldsymbol{\phi}_2, \chi_{s2}) \rangle &= \frac{9}{4} \left(\frac{H_0}{c} \right)^4 \Omega^2_{\mathrm{m0}} \int_0^{\min(\chi_{s1}, \chi_{s2})} \frac{\mathrm{d}\chi}{a^2(\chi)} \frac{r(\chi_{s1} - \chi)}{r(\chi_{s1})} \frac{r(\chi_{s2} - \chi)}{r(\chi_{s2})} \\
&\times \int \frac{\ell d\ell}{2\pi} P_\delta \left(k = \frac{\ell}{r(\chi)}, z(\chi) \right) \left(\frac{J_0(\ell\phi_{12}) + J_4(\ell\phi_{12})}{2} \right), \qquad \text{(B.15)}
\end{aligned}$$

where ϕ_{12} is the norm of $\boldsymbol{\phi}_1 - \boldsymbol{\phi}_2$ and $P_\delta(k, z)$ is the non-linear matter power spectrum at redshift z.

Although we have derived the difference between $\mathcal{K}$ and $\bar{\mathcal{K}}$ at the two-point statistics, it is extremely difficult to derive an explicit form for the corresponding difference in the lensing MFs. We thus resort to comparing directly the two sets of simulated lensing

MFs. One is our fiducial mock data used in Section 4.2.1.2. For the other, new set of simulations, we calculate $\bar{\kappa}$ at each source position on the sky using the source redshift distribution (weight) that is shown as the black histograms in Figure 4.12. Figure B.1 shows the results. The red line represents the difference caused by the two different source redshift distributions as described in Section 4.2.3. The green line shows the difference of the lensing MFs with and without source redshift clustering. For reference, the difference of lensing MFs between the different cosmological model by blue lines are also presented. The thick (thin) blue lines correspond to the case of the cosmological model with higher (lower) w_0. Although the impact of source clustering (green) is smaller than the effect of different source distribution (red), it or actually both could be a major source of systematics for future survey with the sky coverage of 20000 deg^2. The induced biases in cosmological parameters due to the source clustering are estimated by Eq. (4.19); the results are $\Delta\Omega_{\rm m0} = 0.00642$, $\Delta A_s = -0.00467 \times 10^9$ and $\Delta w_0 = 0.00487$.

Appendix C

Estimating the Minkowski Functionals Covariance Matrix

We describe an approximate way to evaluate the covariance matrix as given by Eq. (4.18) and test its validity in this Appendix. We first generate 40 noise-free lensing maps by the method in Section 3.4. For each realization of the 40 maps, we use a different random seed for the intrinsic ellipticities to make mock source galaxy catalogs described in Section 4.2.1.2. In this way, we generate $40 \times 40 = 1600$ catalogs in total, which can be used to estimate the full covariance of the MFs.

Let us denote a mock catalogue as $\mathcal{K}^{m,n}$, which is generated by the mth noise free lensing map with an nth random seed of the intrinsic ellipticity distribution. We then calculate the full covariance of V_0 as follows:

$$C_{ij}^{(40,40)} \equiv \frac{1}{1600-1}\sum_{m=1}^{40}\sum_{n=1}^{40}\sum_{i,j}(V_0(x_i^{m,n})-\bar{V}_0(x_i^{m,n}))(V_0(x_j^{m,n})-\bar{V}_0(x_j^{m,n})), \tag{C.1}$$

$$\bar{V}_0(x_i^{m,n}) \equiv \frac{1}{1600}\sum_{m=1}^{40}\sum_{n=1}^{40}V_0(x_i^{m,n}), \tag{C.2}$$

where $x_i^{m,n} = (\mathcal{K}_i^{m,n} - \langle\mathcal{K}^{m,n}\rangle)/\sigma_0^{m,n}$ and we here use five bins in the range of $x_i = [-3:3]$. We also calculate our estimator adopted in this thesis:

$$C_{ij} = C_{ij}^{(40,1)} + C_{ij}^{(1,40)}, \tag{C.3}$$

	x_1	x_2	x_3	x_4	x_5
x_1	1.96	0.35	1.96	4.07	1.87
x_2		1.53	1.51	1.27	1.46
x_3			1.82	2.12	1.92
x_4				1.14	0.98
x_5					1.82

TABLE C.1: The ratio of the full covariance of V_0 to our estimator (taken from [2]). The full covariance is derived from the new 1600 maps with Eq. (C.1), whereas our estimator is given by Eq. (C.3). x is defined by $(\mathcal{K} - \langle\mathcal{K}\rangle)/\sigma_0$.

where

$$C_{ij}^{(1,40)} \equiv \frac{1}{40-1}\sum_{n=1}^{40}\sum_{i,j}(V_0(x_i^{1,n}) - \bar{V}_0(x_i^{1,n}))(V_0(x_j^{1,n}) - \bar{V}_0(x_j^{1,n})), \quad \text{(C.4)}$$

$$C_{ij}^{(40,1)} \equiv \frac{1}{40-1}\sum_{m=1}^{40}\sum_{i,j}(V_0(x_i^{m,1}) - \bar{V}_0(x_i^{m,1}))(V_0(x_j^{m,1}) - \bar{V}_0(x_j^{m,1})), \quad \text{(C.5)}$$

$$\bar{V}_0(x_i^{1,n}) \equiv \frac{1}{40}\sum_{n=1}^{40} V_0(x_i^{1,n}), \quad \text{(C.6)}$$

$$\bar{V}_0(x_i^{m,1}) \equiv \frac{1}{40}\sum_{m=1}^{40} V_0(x_i^{m,1}). \quad \text{(C.7)}$$

The ratio $C_{ij}^{(40,40)}/C_{ij}$ then serves a check on the accuracy of our estimator. The ratio for each component is summarized in Table C.1. The simple estimator Eq. (C.3) indeed gives a good approximation to the full covariance. The ratio is typically within a factor of two, and the same is also found for V_1 and V_2. Even if the ratio of the full covariance and our estimator is 2 for all the matrix elements, the cosmological forecast shown in this thesis would be degraded only by a factor of $\sim 2^{1/3}$ (i.e., $\sim 20\%$).

Appendix D

Effect Of Dark Matter Halo Profile Uncertainties On Cross-Correlation Signals

Here, we quantity the effect of uncertainties of the DM halo profiles on the cross- correlation between cosmic shear and the EGB. In order to calculate the theoretical model of cross-correlation signals, we follow the halo model approach as in Section 5.3.1. In the halo model, there are mainly two contributions of the cross-correlation signal: the one-halo term and the two-halo term. For a given length scale k, the main contribution to the one-halo term as calculated by Eq. (5.26) comes from galaxy cluster size halos with $10^{13} - 10^{15} M_{\odot}$. This is valid for the two-halo term associated with density fluctuations (i.e., the first integral in Eq. (5.27)). On the other hand, the two-halo term associated with density squared (i.e., the second integral in Eq. (5.27)) is mainly determined by the smoothed profile contribution $\int \mathrm{d}V \rho_h^2(r|M,z)$ with dominant contribution from lower mass scales. Assuming the NFW profile and the concentration parameter $c_{\rm vir} = r_{\rm vir}/r_s \propto M^{\alpha}$ with $\alpha \sim -0.1$, $Mn(M,z) \int \mathrm{d}V \rho_h^2(r|M,z)$ would scaled as $\sim M^{3\alpha}$ for $M < 10^{12} M_{\odot}$. This fact indicates that the low mass halos dominates the two-halo term and that the overall amplitude of the two-halo term is sensitive to the minimum halo mass. Thus, along with M_{min}, $c_{\rm vir}(z,M)$ is one of the most important parameters in the halo model.

Recent numerical simulations (e.g. [70]) suggest a non-monotonic relation between the concentration parameter and the mass of DM haloes. In this appendix, we test the dependence of the cross-correlation signal on $c_{\rm vir}(z,M)$ by comparing a simple power-law model and the non-monotonic model. For the non-monotonic $c_{\rm vir}(z,M)$ model, we use the fitting function of Ref. [70] that determines $c_{\rm vir}$ as a function of the linear rms

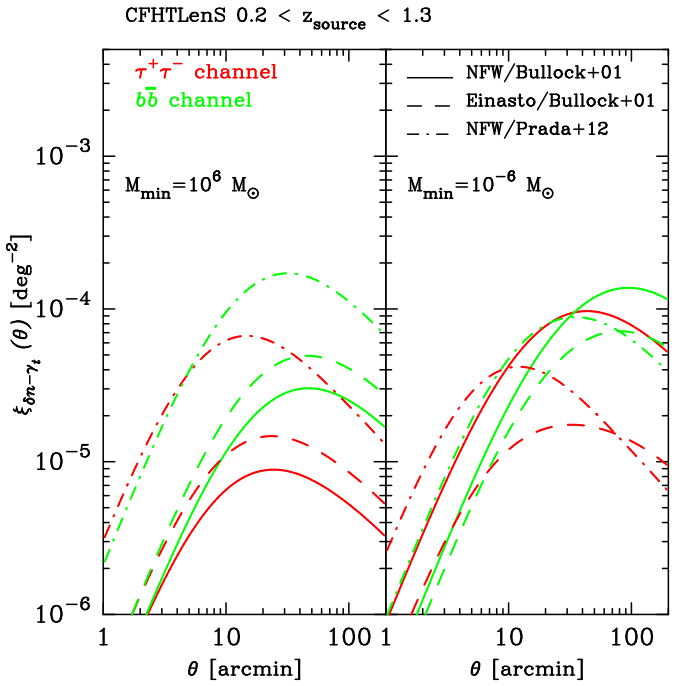

FIGURE D.1: The typical uncertainty of cross-correlation signals of cosmic shear and EGB from DM annihilation. We consider the signal from the annihilation of a 100 GeV mass DM particle with annihilation cross section $\langle\sigma v\rangle = 3 \times 10^{-26}$ cm^3 s^{-1} separately for the $\tau^+\tau^-$ channel (red lines) and the $b\bar{b}$ channel (green lines). The left panel shows the case of minimum DM halo mass $M_{\rm min} = 10^6 M_\odot$, while we assume $M_{\rm min} = 10^{-6} M_\odot$ in the right panel. The solid lines correspond to the halo model with the power-law model of $c_{\rm vir}$ with the NFW profile. The dashed lines represent the halo model with the power-law model of $c_{\rm vir}$ with the Einasto profile. The dashed-dotted lines show the halo model calculation with the non-monotonic model of $c_{\rm vir}$ and the NFW profile.

density fluctuation $\sigma(z, M)$. This fitting function successfully reproduces the complex feature of $c_{\rm vir}$ found in numerical simulations. For the power-law model, we apply the functional form shown in Ref. [69] as in our benchmark model.

Even if we can determine the halo profile concentration, the inner shape of density profile would make the cross-correlation signal uncertain. Although the inner slope of density profile of DM halo is still unconcluded, e.g., [207, 228], we here examine the alliterative model of DM density profile as proposed in Ref. [207]. This model is called Einasto profile, which is defined by

$$\rho_h(r) = \frac{\rho_s}{4} \exp\left\{\left(-\frac{2}{\alpha}\right)\left[\left(\frac{r}{r_s}\right)^{\alpha} - 1\right]\right\}, \tag{D.1}$$

where ρ_s and r_s represent the scale density and radius, and $\alpha = 0.17$. When using the Einasto profile, we simply use the power-law concentration in Ref. [69] and derive ρ_s and r_s in the same manner as in Section 5.3.1.

In Figure D.1, we summarize the comparison between the halo model calculations with

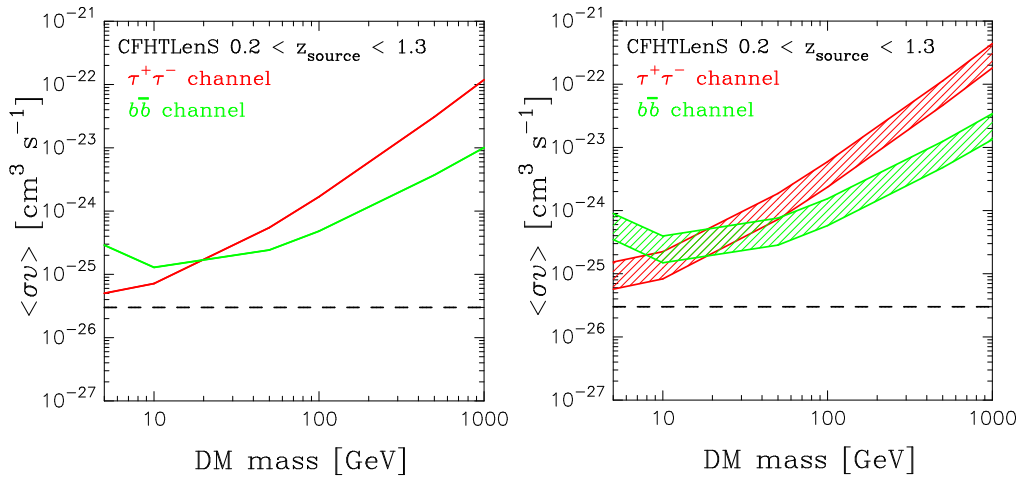

FIGURE D.2: The 68 % confidence level upper limits on $\langle\sigma v\rangle$ as functions of the DM mass (the left panel is taken from [3]). The left panel corresponds to the constraint derived by the model with the NFW profile and the non-monotonic model of $c_{\rm vir}$. The right panel represents the case where the model with the Einasto profile and the power-law model of $c_{\rm vir}$. The red shaded region corresponds to the upper limit for the $\tau^+\tau^-$ channel and the green one for the $b\bar{b}$ channel.

the power-law and non-monotonic models of $c_{\rm vir}$ and/or the different parameterizations of density profile. Each solid line is the same as our benchmark model, while each dashed line correspond to the case with the Einasto profile and the power-law model of $c_{\rm vir}$. The dashed-dotted lines show the halo model with the non-monotonic model of $c_{\rm vir}$. We assume the minimum halo mass $M_{\rm min} = 10^6 M_\odot$ and $10^{-6} M_\odot$ in the left and right panel, respectively. We also take into account the smoothing effect of gamma-ray point spread function (PSF) in Figure D.1.

For the non-monotonic model of $c_{\rm vir}$, we found that the final result is much less sensitive to the minimum halo mass because of the flattening feature of $c_{\rm vir}$ at low masses. The most important result is perhaps that the cross-correlation signals would be dominated by the one-halo term for the non-monotonic model. This is different from the result of our benchmark model and from previous work [179] mainly due to the higher concentration in massive DM haloes than in our benchmark model. Consequently, the expected signals for the non-monotonic model would be ten times as large as our benchmark model for smaller angular scale at $\theta < 10$ arcmin when we do not include the effect of gamma-ray PSF. However, for the angular scale larger than 30 arcmin, the two models with the different $c_{\rm vir}$ show quite similar amplitudes of the cross-correlation. Clearly, the choice of $c_{\rm vir}$ model would not affect the final constraints of DM annihilation significantly because most of the information about DM annihilation come from the large scale clustering as shown in Section 4.2.2.2. On the other hand, the inner slope of ρ_h has the larger impact on the calculation of the expected cross-correlation. Assuming the Einasto profile, the inner slope would gradually change as a function of radius. This induces the different

scaling of the volume integral $\int \mathrm{d}V\, \rho_h^2$ with respect to $c_{\rm vir}$. In both cases where $M_{\rm min} = 10^6 M_\odot$ and $10^{-6} M_\odot$, the two-halo term of the cross correlation signal would change with a level of $\sim 50 - 70$ %. Nevertheless, these uncertainties are smaller than an order of ~ 10, which is the model uncertainty in our benchmark model.

In Figure D.2, we show the 68 % confidence upper limit of DM annihilation obtained from the measurement shown in Section 5.4.2 with two different model of cross correlation signals as discussed above. For constraints, we simply assume that DM annihilation is the only contribution to the cross-correlation signals and take into account the smoothing effect due to PSF in the same manner shown in Section 5.3.1. When assuming the non-monotonic model of $c_{\rm vir}$, we found the constraints on $\langle \sigma v \rangle$ degrade by ~ 10 % over a wide mass range of 5–1000 GeV. Also, the constraints would be affected by the shape of DM density profile with a level of ~ 70 %.

Bibliography

[1] M. Shirasaki, N. Yoshida, and T. Hamana, *Effect of Masked Regions on Weak-lensing Statistics*, *Astrophys.J.* **774** (Sept., 2013) 111, [arXiv:1304.2164].

[2] M. Shirasaki and N. Yoshida, *Statistical and Systematic Errors in the Measurement of Weak-Lensing Minkowski Functionals: Application to the Canada-France-Hawaii Lensing Survey*, *Astrophys.J.* **786** (May, 2014) 43, [arXiv:1312.5032].

[3] M. Shirasaki, S. Horiuchi, and N. Yoshida, *Cross-Correlation of Cosmic Shear and Extragalactic Gamma-ray Background: Constraints on the Dark Matter Annihilation Cross-Section*, *Phys.Rev.* **D90** (2014) 063502, [arXiv:1404.5503].

[4] A. Einstein, *Kosmologische Betrachtungen zur allgemeinen Relativitätstheorie*, *Sitzungsberichte der Königlich Preußischen Akademie der Wissenschaften (Berlin), Seite 142-152.* (1917) 142–152.

[5] E. Hubble, *A Relation between Distance and Radial Velocity among Extra-Galactic Nebulae*, *Proceedings of the National Academy of Science* **15** (Mar., 1929) 168–173.

[6] C. T. Kowal, *Absolute magnitudes of supernovae.*, *Astronomical Journal* **73** (Dec., 1968) 1021–1024.

[7] M. Hamuy, M. M. Phillips, N. B. Suntzeff, R. A. Schommer, J. Maza, and R. Aviles, *The Absolute Luminosities of the Calan/Tololo Type IA Supernovae*, *Astronomical Journal* **112** (Dec., 1996) 2391, [astro-ph/9609059].

[8] A. G. Riess, W. H. Press, and R. P. Kirshner, *A Precise Distance Indicator: Type IA Supernova Multicolor Light-Curve Shapes*, *Astrophys.J.* **473** (Dec., 1996) 88, [astro-ph/9604143].

[9] M. M. Phillips, *The absolute magnitudes of Type IA supernovae*, *Astrophys.J.Lett.* **413** (Aug., 1993) L105–L108.

[10] B. P. Schmidt, N. B. Suntzeff, M. M. Phillips, R. A. Schommer, A. Clocchiatti, R. P. Kirshner, P. Garnavich, P. Challis, B. Leibundgut, J. Spyromilio, A. G. Riess, A. V. Filippenko, M. Hamuy, R. C. Smith, C. Hogan, C. Stubbs, A. Diercks, D. Reiss, R. Gilliland, J. Tonry, J. Maza, A. Dressler, J. Walsh, and R. Ciardullo, *The High-Z Supernova Search: Measuring Cosmic Deceleration and Global Curvature of the Universe Using Type IA Supernovae*, *Astrophys.J.* **507** (Nov., 1998) 46–63, [astro-ph/9805200].

[11] S. Perlmutter, S. Gabi, G. Goldhaber, A. Goobar, D. E. Groom, I. M. Hook, A. G. Kim, M. Y. Kim, J. C. Lee, R. Pain, C. R. Pennypacker, I. A. Small, R. S. Ellis, R. G. McMahon, B. J. Boyle, P. S. Bunclark, D. Carter, M. J. Irwin, K. Glazebrook, H. J. M. Newberg, A. V. Filippenko, T. Matheson, M. Dopita, and W. J. Couch, *Measurements of the Cosmological Parameters Omega and Lambda from the First Seven Supernovae at z ¿= 0.35*, *Astrophys.J.* **483** (July, 1997) 565–581, [astro-ph/9608192].

[12] A. G. Riess, A. V. Filippenko, P. Challis, A. Clocchiatti, A. Diercks, P. M. Garnavich, R. L. Gilliland, C. J. Hogan, S. Jha, R. P. Kirshner, B. Leibundgut, M. M. Phillips, D. Reiss, B. P. Schmidt, R. A. Schommer, R. C. Smith, J. Spyromilio, C. Stubbs, N. B. Suntzeff, and J. Tonry, *Observational Evidence from Supernovae for an Accelerating Universe and a Cosmological Constant*, *Astronomical Journal* **116** (Sept., 1998) 1009–1038, [astro-ph/9805201].

[13] S. Perlmutter, G. Aldering, G. Goldhaber, R. A. Knop, P. Nugent, P. G. Castro, S. Deustua, S. Fabbro, A. Goobar, D. E. Groom, I. M. Hook, A. G. Kim, M. Y. Kim, J. C. Lee, N. J. Nunes, R. Pain, C. R. Pennypacker, R. Quimby, C. Lidman, R. S. Ellis, M. Irwin, R. G. McMahon, P. Ruiz-Lapuente, N. Walton, B. Schaefer, B. J. Boyle, A. V. Filippenko, T. Matheson, A. S. Fruchter, N. Panagia, H. J. M. Newberg, W. J. Couch, and T. S. C. Project, *Measurements of Ω and Λ from 42 High-Redshift Supernovae*, *Astrophys.J.* **517** (June, 1999) 565–586, [astro-ph/9812133].

[14] R. A. Alpher, H. Bethe, and G. Gamow, *The Origin of Chemical Elements*, *Physical Review* **73** (Apr., 1948) 803–804.

[15] R. A. Alpher and R. C. Herman, *Remarks on the Evolution of the Expanding Universe*, *Physical Review* **75** (Apr., 1949) 1089–1095.

[16] W. Hu, N. Sugiyama, and J. Silk, *The physics of microwave background anisotropies*, *Nature* **386** (Mar., 1997) 37–43, [astro-ph/9504057].

[17] G. Hinshaw, D. N. Spergel, L. Verde, R. S. Hill, S. S. Meyer, C. Barnes, C. L. Bennett, M. Halpern, N. Jarosik, A. Kogut, E. Komatsu, M. Limon, L. Page,

G. S. Tucker, J. L. Weiland, E. Wollack, and E. L. Wright, *First-Year Wilkinson Microwave Anisotropy Probe (WMAP) Observations: The Angular Power Spectrum*, *Astron.Astrophys.Suppl.* **148** (Sept., 2003) 135–159, [astro-ph/0302217].

[18] D. J. Eisenstein, I. Zehavi, D. W. Hogg, R. Scoccimarro, M. R. Blanton, R. C. Nichol, R. Scranton, H.-J. Seo, M. Tegmark, Z. Zheng, S. F. Anderson, J. Annis, N. Bahcall, J. Brinkmann, S. Burles, F. J. Castander, A. Connolly, I. Csabai, M. Doi, M. Fukugita, J. A. Frieman, K. Glazebrook, J. E. Gunn, J. S. Hendry, G. Hennessy, Z. Ivezić, S. Kent, G. R. Knapp, H. Lin, Y.-S. Loh, R. H. Lupton, B. Margon, T. A. McKay, A. Meiksin, J. A. Munn, A. Pope, M. W. Richmond, D. Schlegel, D. P. Schneider, K. Shimasaku, C. Stoughton, M. A. Strauss, M. SubbaRao, A. S. Szalay, I. Szapudi, D. L. Tucker, B. Yanny, and D. G. York, *Detection of the Baryon Acoustic Peak in the Large-Scale Correlation Function of SDSS Luminous Red Galaxies*, *Astrophys.J.* **633** (Nov., 2005) 560–574, [astro-ph/0501171].

[19] **WMAP** Collaboration, G. Hinshaw, D. Larson, E. Komatsu, D. N. Spergel, C. L. Bennett, J. Dunkley, M. R. Nolta, M. Halpern, R. S. Hill, N. Odegard, L. Page, K. M. Smith, J. L. Weiland, B. Gold, N. Jarosik, A. Kogut, M. Limon, S. S. Meyer, G. S. Tucker, E. Wollack, and E. L. Wright, *Nine-Year Wilkinson Microwave Anisotropy Probe (WMAP) Observations: Cosmological Parameter Results*, *Astrophys.J.Suppl.* **208** (2013) 19, [arXiv:1212.5226].

[20] L. Anderson, É. Aubourg, S. Bailey, F. Beutler, V. Bhardwaj, M. Blanton, A. S. Bolton, J. Brinkmann, J. R. Brownstein, A. Burden, C.-H. Chuang, A. J. Cuesta, K. S. Dawson, D. J. Eisenstein, S. Escoffier, J. E. Gunn, H. Guo, S. Ho, K. Honscheid, C. Howlett, D. Kirkby, R. H. Lupton, M. Manera, C. Maraston, C. K. McBride, O. Mena, F. Montesano, R. C. Nichol, S. E. Nuza, M. D. Olmstead, N. Padmanabhan, N. Palanque-Delabrouille, J. Parejko, W. J. Percival, P. Petitjean, F. Prada, A. M. Price-Whelan, B. Reid, N. A. Roe, A. J. Ross, N. P. Ross, C. G. Sabiu, S. Saito, L. Samushia, A. G. Sánchez, D. J. Schlegel, D. P. Schneider, C. G. Scoccola, H.-J. Seo, R. A. Skibba, M. A. Strauss, M. E. C. Swanson, D. Thomas, J. L. Tinker, R. Tojeiro, M. V. Magaña, L. Verde, D. A. Wake, B. A. Weaver, D. H. Weinberg, M. White, X. Xu, C. Yèche, I. Zehavi, and G.-B. Zhao, *The clustering of galaxies in the SDSS-III Baryon Oscillation Spectroscopic Survey: baryon acoustic oscillations in the Data Releases 10 and 11 Galaxy samples*, *Mon.Not.Roy.Astron.Soc.* **441** (June, 2014) 24–62, [arXiv:1312.4877].

[21] F. Zwicky, *Die Rotverschiebung von extragalaktischen Nebeln*, *Helvetica Physica Acta* **6** (1933) 110–127.

[22] J. P. Ostriker and P. J. E. Peebles, *A Numerical Study of the Stability of Flattened Galaxies: or, can Cold Galaxies Survive?*, *Astrophys.J.* **186** (Dec., 1973) 467–480.

[23] M. L. Wilson and J. Silk, *On the anisotropy of the cosmological background matter and radiation distribution. I - The radiation anisotropy in a spatially flat universe*, *Astrophys.J.* **243** (Jan., 1981) 14–25.

[24] M. L. Wilson, *On the anisotropy of the cosmological background matter and radiation distribution. II - The radiation anisotropy in models with negative spatial curvature*, *Astrophys.J.* **273** (Oct., 1983) 2–15.

[25] J. R. Bond and G. Efstathiou, *Cosmic background radiation anisotropies in universes dominated by nonbaryonic dark matter*, *Astrophys.J.Lett.* **285** (Oct., 1984) L45–L48.

[26] A. Bosma, *21-cm line studies of spiral galaxies. I - Observations of the galaxies NGC 5033, 3198, 5055, 2841, and 7331. II - The distribution and kinematics of neutral hydrogen in spiral galaxies of various morphological types*, *Astronomical Journal* **86** (Dec., 1981) 1791–1846.

[27] K. G. Begeman, A. H. Broeils, and R. H. Sanders, *Extended rotation curves of spiral galaxies - Dark haloes and modified dynamics*, *Mon.Not.Roy.Astron.Soc.* **249** (Apr., 1991) 523–537.

[28] M. Markevitch, A. H. Gonzalez, L. David, A. Vikhlinin, S. Murray, W. Forman, C. Jones, and W. Tucker, *A Textbook Example of a Bow Shock in the Merging Galaxy Cluster 1E 0657-56*, *Astrophys.J.Lett.* **567** (Mar., 2002) L27–L31, [astro-ph/0110468].

[29] D. Clowe, A. Gonzalez, and M. Markevitch, *Weak-Lensing Mass Reconstruction of the Interacting Cluster 1E 0657-558: Direct Evidence for the Existence of Dark Matter*, *Astrophys.J.* **604** (Apr., 2004) 596–603, [astro-ph/0312273].

[30] N. A. Bahcall, L. M. Lubin, and V. Dorman, *Where is the Dark Matter?*, *Astrophys.J.Lett.* **447** (July, 1995) L81, [astro-ph/9506041].

[31] R. G. Carlberg, H. K. C. Yee, E. Ellingson, R. Abraham, P. Gravel, S. Morris, and C. J. Pritchet, *Galaxy Cluster Virial Masses and Omega*, *Astrophys.J.* **462** (May, 1996) 32, [astro-ph/9509034].

[32] A. Conley, J. Guy, M. Sullivan, N. Regnault, P. Astier, C. Balland, S. Basa, R. G. Carlberg, D. Fouchez, D. Hardin, I. M. Hook, D. A. Howell, R. Pain, N. Palanque-Delabrouille, K. M. Perrett, C. J. Pritchet, J. Rich, V. Ruhlmann-Kleider, D. Balam, S. Baumont, R. S. Ellis, S. Fabbro, H. K. Fakhouri, N. Fourmanoit, S. González-Gaitán, M. L. Graham, M. J. Hudson, E. Hsiao, T. Kronborg, C. Lidman, A. M. Mourao, J. D. Neill, S. Perlmutter, P. Ripoche, N. Suzuki, and E. S. Walker, *Supernova Constraints and Systematic Uncertainties from the First Three Years of the Supernova Legacy Survey*, *Astron.Astrophys.Suppl.* **192** (Jan., 2011) 1, [arXiv:1104.1443].

[33] N. Suzuki, D. Rubin, C. Lidman, G. Aldering, R. Amanullah, K. Barbary, L. F. Barrientos, J. Botyanszki, M. Brodwin, N. Connolly, K. S. Dawson, A. Dey, M. Doi, M. Donahue, S. Deustua, P. Eisenhardt, E. Ellingson, L. Faccioli, V. Fadeyev, H. K. Fakhouri, A. S. Fruchter, D. G. Gilbank, M. D. Gladders, G. Goldhaber, A. H. Gonzalez, A. Goobar, A. Gude, T. Hattori, H. Hoekstra, E. Hsiao, X. Huang, Y. Ihara, M. J. Jee, D. Johnston, N. Kashikawa, B. Koester, K. Konishi, M. Kowalski, E. V. Linder, L. Lubin, J. Melbourne, J. Meyers, T. Morokuma, F. Munshi, C. Mullis, T. Oda, N. Panagia, S. Perlmutter, M. Postman, T. Pritchard, J. Rhodes, P. Ripoche, P. Rosati, D. J. Schlegel, A. Spadafora, S. A. Stanford, V. Stanishev, D. Stern, M. Strovink, N. Takanashi, K. Tokita, M. Wagner, L. Wang, N. Yasuda, H. K. C. Yee, and T. Supernova Cosmology Project, *The Hubble Space Telescope Cluster Supernova Survey. V. Improving the Dark-energy Constraints above z ¿ 1 and Building an Early-type-hosted Supernova Sample*, *Astrophys.J.* **746** (Feb., 2012) 85, [arXiv:1105.3470].

[34] M. Tegmark, M. A. Strauss, M. R. Blanton, K. Abazajian, S. Dodelson, H. Sandvik, X. Wang, D. H. Weinberg, I. Zehavi, N. A. Bahcall, F. Hoyle, D. Schlegel, R. Scoccimarro, M. S. Vogeley, A. Berlind, T. Budavari, A. Connolly, D. J. Eisenstein, D. Finkbeiner, J. A. Frieman, J. E. Gunn, L. Hui, B. Jain, D. Johnston, S. Kent, H. Lin, R. Nakajima, R. C. Nichol, J. P. Ostriker, A. Pope, R. Scranton, U. Seljak, R. K. Sheth, A. Stebbins, A. S. Szalay, I. Szapudi, Y. Xu, J. Annis, J. Brinkmann, S. Burles, F. J. Castander, I. Csabai, J. Loveday, M. Doi, M. Fukugita, B. Gillespie, G. Hennessy, D. W. Hogg, Ž. Ivezić, G. R. Knapp, D. Q. Lamb, B. C. Lee, R. H. Lupton, T. A. McKay, P. Kunszt, J. A. Munn, L. O'Connell, J. Peoples, J. R. Pier, M. Richmond, C. Rockosi, D. P. Schneider, C. Stoughton, D. L. Tucker, D. E. vanden Berk, B. Yanny, and D. G. York, *Cosmological parameters from SDSS and WMAP*, *Phys.Rev.* **D69** (May, 2004) 103501, [astro-ph/0310723].

[35] **SDSS Collaboration** Collaboration, M. Tegmark et al., *Cosmological Constraints from the SDSS Luminous Red Galaxies*, *Phys.Rev.* **D74** (2006) 123507, [astro-ph/0608632].

[36] D. H. Weinberg, J. S. Bullock, F. Governato, R. Kuzio de Naray, and A. H. G. Peter, *Cold dark matter: controversies on small scales*, *ArXiv e-prints* (June, 2013) [arXiv:1306.0913].

[37] X. Chen, *Primordial Non-Gaussianities from Inflation Models*, *Advances in Astronomy* **2010** (2010) 72, [arXiv:1002.1416].

[38] M. Sato, T. Hamana, R. Takahashi, M. Takada, N. Yoshida, T. Matsubara, and N. Sugiyama, *Simulations of Wide-Field Weak Lensing Surveys. I. Basic Statistics and Non-Gaussian Effects*, *Astrophys.J.* **701** (Aug., 2009) 945–954, [arXiv:0906.2237].

[39] W. Hu and M. Tegmark, *Weak Lensing: Prospects for Measuring Cosmological Parameters*, *Astrophys.J.Lett.* **514** (Apr., 1999) L65–L68, [astro-ph/9811168].

[40] W. Hu, *Power Spectrum Tomography with Weak Lensing*, *Astrophys.J.Lett.* **522** (Sept., 1999) L21–L24, [astro-ph/9904153].

[41] C. M. Hirata and U. Seljak, *Intrinsic alignment-lensing interference as a contaminant of cosmic shear*, *Phys.Rev.* **D70** (Sept., 2004) 063526, [astro-ph/0406275].

[42] D. Kirk, A. Rassat, O. Host, and S. Bridle, *The cosmological impact of intrinsic alignment model choice for cosmic shear*, *Mon.Not.Roy.Astron.Soc.* **424** (Aug., 2012) 1647–1657, [arXiv:1112.4752].

[43] B. Joachimi, R. Mandelbaum, F. B. Abdalla, and S. L. Bridle, *Constraints on intrinsic alignment contamination of weak lensing surveys using the MegaZ-LRG sample*, *Astronomy and Astrophysics* **527** (Mar., 2011) A26, [arXiv:1008.3491].

[44] D. Huterer, M. Takada, G. Bernstein, and B. Jain, *Systematic errors in future weak-lensing surveys: requirements and prospects for self-calibration*, *Mon.Not.Roy.Astron.Soc.* **366** (Feb., 2006) 101–114, [astro-ph/0506030].

[45] R. Massey, H. Hoekstra, T. Kitching, J. Rhodes, M. Cropper, J. Amiaux, D. Harvey, Y. Mellier, M. Meneghetti, L. Miller, S. Paulin-Henriksson, S. Pires, R. Scaramella, and T. Schrabback, *Origins of weak lensing systematics, and requirements on future instrumentation (or knowledge of instrumentation)*, *Mon.Not.Roy.Astron.Soc.* **429** (Feb., 2013) 661–678, [arXiv:1210.7690].

[46] J. A. Tyson, F. Valdes, J. F. Jarvis, and A. P. Mills, Jr., *Galaxy mass distribution from gravitational light deflection*, *Astrophys.J.Lett.* **281** (June, 1984) L59–L62.

[47] L. van Waerbeke, *Scale dependence of the bias investigated by weak lensing*, *Astronomy and Astrophysics* **334** (June, 1998) 1–10, [astro-ph/9710244].

[48] P. Schneider, *Cosmic Shear and Biasing*, *Astrophys.J.* **498** (May, 1998) 43–47, [astro-ph/9708269].

[49] U. Seljak, A. Makarov, R. Mandelbaum, C. M. Hirata, N. Padmanabhan, P. McDonald, M. R. Blanton, M. Tegmark, N. A. Bahcall, and J. Brinkmann, *SDSS galaxy bias from halo mass-bias relation and its cosmological implications*, *Phys.Rev.* **D71** (Feb., 2005) 043511, [astro-ph/0406594].

[50] T. Baldauf, R. E. Smith, U. Seljak, and R. Mandelbaum, *Algorithm for the direct reconstruction of the dark matter correlation function from weak lensing and galaxy clustering*, *Phys.Rev.* **D81** (Mar., 2010) 063531, [arXiv:0911.4973].

[51] R. Mandelbaum, A. Slosar, T. Baldauf, U. Seljak, C. M. Hirata, R. Nakajima, R. Reyes, and R. E. Smith, *Cosmological parameter constraints from galaxy-galaxy lensing and galaxy clustering with the SDSS DR7*, *Mon.Not.Roy.Astron.Soc.* **432** (June, 2013) 1544–1575, [arXiv:1207.1120].

[52] M. Oguri and M. Takada, *Combining cluster observables and stacked weak lensing to probe dark energy: Self-calibration of systematic uncertainties*, *Phys.Rev.* **D83** (2011) 023008, [arXiv:1010.0744].

[53] W. Hu and B. Jain, *Joint galaxy-lensing observables and the dark energy*, *Phys.Rev.* **D70** (Aug., 2004) 043009, [astro-ph/0312395].

[54] F. Bernardeau, L. van Waerbeke, and Y. Mellier, *Weak lensing statistics as a probe of OMEGA and power spectrum.*, *Astronomy and Astrophysics* **322** (June, 1997) 1–18, [astro-ph/9609122].

[55] L. Hui, *Weighing the Cosmological Energy Contents with Weak Gravitational Lensing*, *Astrophys.J.Lett.* **519** (July, 1999) L9–L12, [astro-ph/9902275].

[56] M. Takada and B. Jain, *Cosmological parameters from lensing power spectrum and bispectrum tomography*, *Mon.Not.Roy.Astron.Soc.* **348** (Mar., 2004) 897–915, [astro-ph/0310125].

[57] I. Kayo, M. Takada, and B. Jain, *Information content of weak lensing power spectrum and bispectrum: including the non-Gaussian error covariance matrix*, *Mon.Not.Roy.Astron.Soc.* **429** (Feb., 2013) 344–371, [arXiv:1207.6322].

[58] T. Hamana, M. Takada, and N. Yoshida, *Searching for massive clusters in weak lensing surveys*, *Mon.Not.Roy.Astron.Soc.* **350** (2004) 893, [astro-ph/0310607].

[59] J. F. Hennawi and D. N. Spergel, *Shear-selected Cluster Cosmology: Tomography and Optimal Filtering*, *Astrophys.J.* **624** (May, 2005) 59–79, [astro-ph/0404349].

[60] L. Marian and G. M. Bernstein, *Dark energy constraints from lensing-detected galaxy clusters*, *Phys.Rev.* **D73** (June, 2006) 123525, [astro-ph/0605746].

[61] W. Fang and Z. Haiman, *Constraining dark energy by combining cluster counts and shear-shear correlations in a weak lensing survey*, *Phys.Rev.* **D75** (Feb., 2007) 043010, [astro-ph/0612187].

[62] M. Takada and S. Bridle, *Probing dark energy with cluster counts and cosmic shear power spectra: including the full covariance*, *New Journal of Physics* **9** (Dec., 2007) 446, [arXiv:0705.0163].

[63] L. Marian, R. E. Smith, S. Hilbert, and P. Schneider, *The cosmological information of shear peaks: beyond the abundance*, *Mon.Not.Roy.Astron.Soc.* **432** (June, 2013) 1338–1350, [arXiv:1301.5001].

[64] D. Bard, J. M. Kratochvil, C. Chang, M. May, S. M. Kahn, Y. AlSayyad, Z. Ahmad, J. Bankert, A. Connolly, R. R. Gibson, K. Gilmore, E. Grace, Z. Haiman, M. Hannel, K. M. Huffenberger, J. G. Jernigan, L. Jones, S. Krughoff, S. Lorenz, S. Marshall, A. Meert, S. Nagarajan, E. Peng, J. Peterson, A. P. Rasmussen, M. Shmakova, N. Sylvestre, N. Todd, and M. Young, *Effect of Measurement Errors on Predicted Cosmological Constraints from Shear Peak Statistics with Large Synoptic Survey Telescope*, *Astrophys.J.* **774** (Sept., 2013) 49, [arXiv:1301.0830].

[65] X. Liu, Q. Wang, C. Pan, and Z. Fan, *Mask Effects on Cosmological Studies with Weak-lensing Peak Statistics*, *Astrophys.J.* **784** (Mar., 2014) 31, [arXiv:1304.2873].

[66] Y. Utsumi, S. Miyazaki, M. J. Geller, I. P. Dell'Antonio, M. Oguri, M. J. Kurtz, T. Hamana, and D. G. Fabricant, *Reducing Systematic Error in Weak Lensing Cluster Surveys*, *Astrophys.J.* **786** (May, 2014) 93, [arXiv:1304.4656].

[67] T. Kitayama and Y. Suto, *Semianalytical predictions for statistical properties of x-ray clusters of galaxies in cold dark matter universes*, *Astrophys.J.* **469** (1996) 480, [astro-ph/9604141].

[68] J. F. Navarro, C. S. Frenk, and S. D. White, *The Structure of cold dark matter halos*, *Astrophys.J.* **462** (1996) 563–575, [astro-ph/9508025].

[69] J. S. Bullock, T. S. Kolatt, Y. Sigad, R. S. Somerville, A. V. Kravtsov, A. A. Klypin, J. R. Primack, and A. Dekel, *Profiles of dark haloes. Evolution, scatter, and environment*, *Mon.Not.Roy.Astron.Soc.* **321** (2001) 559–575, [astro-ph/9908159].

[70] F. Prada, A. A. Klypin, A. J. Cuesta, J. E. Betancort-Rijo, and J. Primack, *Halo concentrations in the standard LCDM cosmology*, *Mon.Not.Roy.Astron.Soc.* **428** (2012) 3018–3030, [arXiv:1104.5130].

[71] T. Ishiyama, S. Rieder, J. Makino, S. Portegies Zwart, D. Groen, K. Nitadori, C. de Laat, S. McMillan, K. Hiraki, and S. Harfst, *The Cosmogrid Simulation: Statistical Properties of Small Dark Matter Halos*, *Astrophys.J.* **767** (2013) 146, [arXiv:1101.2020].

[72] T. Ishiyama, *Hierarchical Formation of Dark Matter Halos and the Free Streaming Scale*, *Astrophys.J.* **788** (2014) 27, [arXiv:1404.1650].

[73] M. Persic, P. Salucci, and F. Stel, *The Universal rotation curve of spiral galaxies: 1. The Dark matter connection*, *Mon.Not.Roy.Astron.Soc.* **281** (1996) 27, [astro-ph/9506004].

[74] P. Salucci and M. Persic, *Dark Halos around Galaxies*, in *Dark and Visible Matter in Galaxies and Cosmological Implications* (M. Persic and P. Salucci, eds.), vol. 117 of *Astronomical Society of the Pacific Conference Series*, p. 1, 1997. astro-ph/9703027.

[75] C. O. Wright and T. G. Brainerd, *Gravitational lensing by nfw halos*, astro-ph/9908213.

[76] E. Komatsu and U. Seljak, *Universal gas density and temperature profile*, *Mon.Not.Roy.Astron.Soc.* **327** (2001) 1353–1366, [astro-ph/0106151].

[77] A. Cooray and R. K. Sheth, *Halo models of large scale structure*, *Phys.Rept.* **372** (2002) 1–129, [astro-ph/0206508].

[78] E. R. Harrison, *Fluctuations at the threshold of classical cosmology*, *Phys.Rev.* **D1** (1970) 2726–2730.

[79] Y. Zeldovich, *A Hypothesis, unifying the structure and the entropy of the universe*, *Mon.Not.Roy.Astron.Soc.* **160** (1972) 1P–3P.

[80] P. Peebles and J. Yu, *Primeval adiabatic perturbation in an expanding universe*, *Astrophys.J.* **162** (1970) 815–836.

[81] A. Lewis, A. Challinor, and A. Lasenby, *Efficient computation of CMB anisotropies in closed FRW models*, *Astrophys. J.* **538** (2000) 473–476, [astro-ph/9911177].

[82] D. J. Eisenstein and W. Hu, *Baryonic features in the matter transfer function*, *Astrophys.J.* **496** (1998) 605, [astro-ph/9709112].

[83] W. H. Press and P. Schechter, *Formation of galaxies and clusters of galaxies by selfsimilar gravitational condensation*, *Astrophys.J.* **187** (1974) 425–438.

[84] A. Jenkins, C. Frenk, S. D. White, J. Colberg, S. Cole, A. E. Evrard, H. M. P. Couchman, and N. Yoshida, *The Mass function of dark matter halos*, *Mon.Not.Roy.Astron.Soc.* **321** (2001) 372, [astro-ph/0005260].

[85] M. S. Warren, K. Abazajian, D. E. Holz, and L. Teodoro, *Precision determination of the mass function of dark matter halos*, *Astrophys.J.* **646** (2006) 881–885, [astro-ph/0506395].

[86] J. Tinker, A. V. Kravtsov, A. Klypin, K. Abazajian, M. Warren, G. Yepes, S. Gottlöber, and D. E. Holz, *Toward a halo mass function for precision cosmology: The Limits of universality*, *Astrophys.J.* **688** (2008) 709–728, [arXiv:0803.2706].

[87] R. K. Sheth and G. Tormen, *Large scale bias and the peak background split*, *Mon.Not.Roy.Astron.Soc.* **308** (1999) 119, [astro-ph/9901122].

[88] R. K. Sheth and G. Tormen, *An Excursion set model of hierarchical clustering : Ellipsoidal collapse and the moving barrier*, *Mon.Not.Roy.Astron.Soc.* **329** (2002) 61, [astro-ph/0105113].

[89] S. Cole and N. Kaiser, *Biased clustering in the cold dark matter cosmogony*, *Mon.Not.Roy.Astron.Soc.* **237** (1989) 1127–1146.

[90] B. Jain, U. Seljak, and S. D. White, *Ray tracing simulations of weak lensing by large scale structure*, *Astrophys.J.* **530** (2000) 547, [astro-ph/9901191].

[91] S. Seitz and P. Schneider, *Cluster lens reconstruction using only observed local data - an improved finite-field inversion technique*, *Astronomy and Astrophysics* **305** (1996) [astro-ph/9503096].

[92] **SDSS Collaboration** Collaboration, R. Scranton, B. Ménard, G. T. Richards, R. C. Nichol, A. D. Myers, B. Jain, A. Gray, M. Bartelmann, R. J. Brunner,

A. J. Connolly, J. E. Gunn, R. K. Sheth, N. A. Bahcall, J. Brinkman, J. Loveday, D. P. Schneider, A. Thakar, and D. G. York, *Detection of cosmic magnification with the Sloan Digital Sky Survey*, *Astrophys.J.* **633** (2005) 589–602, [astro-ph/0504510].

[93] H. Hildebrandt, L. van Waerbeke, and T. Erben, *CARS: The CFHTLS-Archive-Research Survey III. First detection of cosmic magnification in samples of normal high-z galaxies*, *Astronomy and Astrophysics* **507** (2009), no. 2 [arXiv:0906.1580].

[94] E. M. Huff and G. J. Graves, *Magnificent Magnification: Exploiting the Other Half of the Lensing Signal*, *Astrophys.J.* **780** (2014) L16, [arXiv:1111.1070].

[95] P. Schneider and C. Seitz, *Steps towards Nonlinear Cluster Inversion Through Gravitational Distortions. I. Basic Considerations and Circular Clusters*, *Astronomy and Astrophysics* **294** (1995), no. 2 [astro-ph/9407032].

[96] C. Seitz and P. Schneider, *Steps towards nonlinear cluster inversion through gravitational distortions. 3. Including a redshift distribution of the sources*, *Astronomy and Astrophysics* **318** (1997) [astro-ph/9601079].

[97] C. Heymans, L. Van Waerbeke, L. Miller, T. Erben, H. Hildebrandt, H. Hoekstra, T. D. Kitching, Y. Mellier, P. Simon, C. Bonnett, J. Coupon, L. Fu, J. Harnois Déraps, M. J. Hudson, M. Kilbinger, K. Kuijken, B. Rowe, T. Schrabback, E. Semboloni, E. van Uitert, S. Vafaei, and M. Velander, *CFHTLenS: the Canada-France-Hawaii Telescope Lensing Survey*, *Mon.Not.Roy.Astron.Soc.* **427** (Nov., 2012) 146–166, [arXiv:1210.0032].

[98] N. Kaiser, *Weak gravitational lensing of distant galaxies*, *Astrophys.J.* **388** (1992) 272.

[99] P. Schneider, L. van Waerbeke, M. Kilbinger, and Y. Mellier, *Analysis of two-point statistics of cosmic shear: I. estimators and covariances*, *Astron.Astrophys.* **396** (2002) 1–20, [astro-ph/0206182].

[100] M. Sato, M. Takada, T. Hamana, and T. Matsubara, *Simulations of Wide-Field Weak Lensing Surveys II: Covariance Matrix of Real Space Correlation Functions*, *Astrophys.J.* **734** (2011) 76, [arXiv:1009.2558].

[101] N. Kaiser and G. Squires, *Mapping the dark matter with weak gravitational lensing*, *Astrophys.J.* **404** (1993) 441–450.

[102] G. Fahlman, N. Kaiser, G. Squires, and D. Woods, *Dark matter in ms1224 from distortion of background galaxies*, *Astrophys.J.* **437** (1994) 56–62, [astro-ph/9402017].

[103] P. Schneider, *Detection of (dark) matter concentrations via weak gravitational lensing*, *Mon.Not.Roy.Astron.Soc.* **283** (1996) 837–853, [astro-ph/9601039].

[104] G. Kruse and P. Schneider, *Statistics of dark matter haloes expected from weak lensing surveys*, *Mon.Not.Roy.Astron.Soc.* (1998) [astro-ph/9806071].

[105] K. Reblinsky, G. Kruse, B. Jain, and P. Schneider, *Cosmic shear and halo abundances: analytical versus numerical results*, *Astron.Astrophys.* **351** (1999) 815–826, [astro-ph/9907250].

[106] B. Jain and L. V. Van Waerbeke, *Statistics of dark matter halos from gravitational lensing*, *Astrophys. J.* **530** (2000), no. 1 L1–L4, [astro-ph/9910459].

[107] M. Takada and B. Jain, *The Kurtosis of the cosmic shear field*, *Mon.Not.Roy.Astron.Soc.* **337** (2002) 875–894, [astro-ph/0205055].

[108] M. Jarvis, G. Bernstein, and B. Jain, *The skewness of the aperture mass statistic*, *Mon.Not.Roy.Astron.Soc.* **352** (2004) 338–352, [astro-ph/0307393].

[109] R. M. Soneira and P. J. E. Peebles, *A computer model universe - Simulation of the nature of the galaxy distribution in the Lick catalog*, *Astronomical Journal* **83** (July, 1978) 845–849.

[110] M. Joeveer and J. Einasto, *Has the universe the cell structure*, in *Large Scale Structures in the Universe* (M. S. Longair and J. Einasto, eds.), vol. 79 of *IAU Symposium*, pp. 241–250, 1978.

[111] J. R. Gott, III, M. Dickinson, and A. L. Melott, *The sponge-like topology of large-scale structure in the universe*, *Astrophys. J.* **306** (July, 1986) 341–357.

[112] D. H. Weinberg, J. R. Gott, III, and A. L. Melott, *The topology of large-scale structure. I - Topology and the random phase hypothesis*, *Astrophys. J.* **321** (Oct., 1987) 2–27.

[113] A. L. Melott, D. H. Weinberg, and J. R. Gott, III, *The topology of large-scale structure. II - Nonlinear evolution of Gaussian models*, *Astrophys. J.* **328** (May, 1988) 50–68.

[114] J. R. Gott, III, J. Miller, T. X. Thuan, S. E. Schneider, D. H. Weinberg, C. Gammie, K. Polk, M. Vogeley, S. Jeffrey, S. P. Bhavsar, A. L. Melott, R. Giovanelli, M. P. Hayes, R. B. Tully, and A. J. S. Hamilton, *The topology of large-scale structure. III - Analysis of observations*, *Astrophys. J.* **340** (May, 1989) 625–646.

[115] P. Coles, *Statistical geometry and the microwave background*, *Mon.Not.Roy.Astron.Soc.* **234** (Oct., 1988) 509–531.

[116] A. L. Melott, A. P. Cohen, A. J. S. Hamilton, J. R. Gott, III, and D. H. Weinberg, *Topology of large-scale structure. IV - Topology in two dimensions*, *Astrophys. J.* **345** (Oct., 1989) 618–626.

[117] J. R. Gott, III, C. Park, R. Juszkiewicz, W. E. Bies, D. P. Bennett, F. R. Bouchet, and A. Stebbins, *Topology of microwave background fluctuations - Theory*, *Astrophys. J.* **352** (Mar., 1990) 1–14.

[118] C. Hikage, T. Matsubara, P. Coles, M. Liguori, F. K. Hansen, and S. Matarrese, *Limits on Primordial Non-Gaussianity from Minkowski Functionals of the WMAP Temperature Anisotropies*, *Mon.Not.Roy.Astron.Soc.* **389** (2008) 1439–1446, [arXiv:0802.3677].

[119] C. Hikage and T. Matsubara, *Limits on Second-Order Non-Gaussianity from Minkowski Functionals of WMAP Data*, *Mon.Not.Roy.Astron.Soc.* **425** (2012) 2187–2196, [arXiv:1207.1183].

[120] T. Matsubara, *Statistics of Smoothed Cosmic Fields in Perturbation Theory. 1. Formulation and Useful Formulae in Second Order Perturbation Theory*, *Astrophys.J.* **584** (2003) 1–33.

[121] H. Tomita, *Curvature Invariants of Random Interface Generated by Gaussian Fields*, *Progress of Theoretical Physics* **76** (Oct., 1986) 952–955.

[122] J. Schmalzing and K. M. Gorski, *Minkowski functionals used in the morphological analysis of cosmic microwave background anisotropy maps*, *Mon.Not.Roy.Astron.Soc.* **297** (1998), no. 2 [astro-ph/9710185].

[123] T. Matsubara and B. Jain, *The topology of weak lensing fields*, *Astrophys.J.* **552** (2001) L89, [astro-ph/0009402].

[124] J. Sato, M. Takada, Y. Jing, and T. Futamase, *Implication of Omega$_m$ through the morphological analysis of weak lensing fields*, *Astrophys. J.* **551** (2001), no. 1 [astro-ph/0104015].

[125] A. Taruya, M. Takada, T. Hamana, I. Kayo, and T. Futamase, *Lognormal property of weak-lensing fields*, *Astrophys.J.* **571** (2002) 638–653, [astro-ph/0202090].

[126] J. M. Kratochvil, E. A. Lim, S. Wang, Z. Haiman, M. May, and K. Huffenberger, *Probing Cosmology with Weak Lensing Minkowski Functionals*, *Phys.Rev.* **D85** (2012) 103513, [arXiv:1109.6334].

[127] M. Shirasaki, N. Yoshida, T. Hamana, and T. Nishimichi, *Probing Primordial Non-Gaussianity with Weak Lensing Minkowski Functionals*, *Astrophys. J.* **760** (2012), no. 1 [arXiv:1204.4981].

[128] V. Springel, *The cosmological simulation code GADGET-2*, *Mon.Not.Roy.Astron.Soc.* **364** (2005) 1105–1134, [astro-ph/0505010].

[129] T. Nishimichi, A. Shirata, A. Taruya, K. Yahata, S. Saito, Y. Suto, R. Takahashi, N. Yoshida, T. Matsubara, N. Sugiyama, I. Kayo, Y. Jing, and K. Yoshikawa, *Modeling Nonlinear Evolution of Baryon Acoustic Oscillations: Convergence Regime of N-body Simulations and Analytic Models*, *Publ. Astron. Soc. Japan* **61** (Feb., 2009) 321–, [arXiv:0810.0813].

[130] P. Valageas and T. Nishimichi, *Combining perturbation theories with halo models*, *Astronomy and Astrophysics* **527** (Mar., 2011) A87, [arXiv:1009.0597].

[131] M. Crocce, S. Pueblas, and R. Scoccimarro, *Transients from initial conditions in cosmological simulations*, *Mon.Not.Roy.Astron.Soc.* **373** (Nov., 2006) 369–381, [astro-ph/0606505].

[132] M. J. White and W. Hu, *A New algorithm for computing statistics of weak lensing by large scale structure*, *Astrophys.J.* **537** (2000) 1–11, [astro-ph/9909165].

[133] T. Hamana and Y. Mellier, *Numerical study of statistical properties of the lensing excursion angles*, *Mon.Not.Roy.Astron.Soc.* **327** (2001) 169, [astro-ph/0101333].

[134] R. W. Hockney and J. W. Eastwood, *Computer simulation using particles*. 1988.

[135] M. Bolzonella, J.-M. Miralles, and R. Pello', *Photometric redshifts based on standard SED fitting procedures*, *Astron.Astrophys.* **363** (2000) 476–492, [astro-ph/0003380].

[136] N. Kaiser, *A New Shear Estimator for Weak-Lensing Observations*, *Astrophys.J.* **537** (July, 2000) 555–577, [astro-ph/9904003].

[137] T. Erben, L. Van Waerbeke, E. Bertin, Y. Mellier, and P. Schneider, *How accurately can we measure weak gravitational shear?*, *Astron.Astrophys.* **366** (Feb., 2001) 717–735, [astro-ph/0007021].

[138] C. Hirata and U. Seljak, *Shear calibration biases in weak-lensing surveys*, *Mon.Not.Roy.Astron.Soc.* **343** (Aug., 2003) 459–480, [astro-ph/0301054].

[139] C. Hikage, M. Takada, T. Hamana, and D. Spergel, *Shear power spectrum reconstruction using the pseudo-spectrum method*, *Mon.Not.Roy.Astron.Soc.* **412** (Mar., 2011) 65–74, [arXiv:1004.3542].

[140] R. E. Smith, J. A. Peacock, A. Jenkins, S. D. M. White, C. S. Frenk, F. R. Pearce, P. A. Thomas, G. Efstathiou, and H. M. P. Couchman, *Stable clustering, the halo model and non-linear cosmological power spectra*, *Mon.Not.Roy.Astron.Soc.* **341** (June, 2003) 1311–1332, [astro-ph/0207664].

[141] T. Hamana, M. Oguri, M. Shirasaki, and M. Sato, *Scatter and bias in weak lensing selected clusters*, *Mon.Not.Roy.Astron.Soc.* **425** (Sept., 2012) 2287–2298, [arXiv:1204.6117].

[142] E. Bertin, *Automatic Astrometric and Photometric Calibration with SCAMP*, in *Astronomical Data Analysis Software and Systems XV* (C. Gabriel, C. Arviset, D. Ponz, and S. Enrique, eds.), vol. 351 of *Astronomical Society of the Pacific Conference Series*, p. 112, July, 2006.

[143] E. Bertin, Y. Mellier, M. Radovich, G. Missonnier, P. Didelon, and B. Morin, *The TERAPIX Pipeline*, in *Astronomical Data Analysis Software and Systems XI* (D. A. Bohlender, D. Durand, and T. H. Handley, eds.), vol. 281 of *Astronomical Society of the Pacific Conference Series*, p. 228, 2002.

[144] E. Bertin and S. Arnouts, *SExtractor: Software for source extraction.*, *Astron.Astrophys.Suppl.* **117** (June, 1996) 393–404.

[145] N. Kaiser, G. Squires, and T. Broadhurst, *A Method for Weak Lensing Observations*, *Astrophys.J.* **449** (Aug., 1995) 460, [astro-ph/9411005].

[146] G. A. Luppino and N. Kaiser, *Detection of Weak Lensing by a Cluster of Galaxies at Z = 0.83*, *Astrophys.J.* **475** (Jan., 1997) 20, [astro-ph/9601194].

[147] H. Hoekstra, M. Franx, K. Kuijken, and G. Squires, *Weak Lensing Analysis of CL 1358+62 Using Hubble Space Telescope Observations*, *Astrophys.J.* **504** (Sept., 1998) 636.

[148] **WMAP Collaboration** Collaboration, D. N. Spergel, R. Bean, O. Doré, M. R. Nolta, C. L. Bennett, J. Dunkley, G. Hinshaw, N. Jarosik, E. Komatsu, L. Page, H. V. Peiris, L. Verde, M. Halpern, R. S. Hill, A. Kogut, M. Limon, S. S. Meyer, N. Odegard, G. S. Tucker, J. L. Weiland, E. Wollack, and E. L. Wright, *Wilkinson Microwave Anisotropy Probe (WMAP) three year results: implications for cosmology*, *Astrophys.J.Suppl.* **170** (2007) 377, [astro-ph/0603449].

[149] E. A. Lim and D. Simon, *Can we detect Hot or Cold spots in the CMB with Minkowski Functionals?*, *JCAP* **1201** (2012) 048, [arXiv:1103.4300].

[150] S. Winitzki and A. Kosowsky, *Minkowski functional description of microwave background Gaussianity*, *New Astronomy* **3** (Mar., 1998) 75–99, [astro-ph/9710164].

[151] S. Wang, Z. Haiman, and M. May, *Constraining Cosmology with High-Convergence Regions in Weak Lensing Surveys*, *Astrophys.J.* **691** (Jan., 2009) 547–559, [arXiv:0809.4052].

[152] T. Erben, H. Hildebrandt, L. Miller, L. van Waerbeke, C. Heymans, H. Hoekstra, T. D. Kitching, Y. Mellier, J. Benjamin, C. Blake, C. Bonnett, O. Cordes, J. Coupon, L. Fu, R. Gavazzi, B. Gillis, E. Grocutt, S. D. J. Gwyn, K. Holhjem, M. J. Hudson, M. Kilbinger, K. Kuijken, M. Milkeraitis, B. T. P. Rowe, T. Schrabback, E. Semboloni, P. Simon, M. Smit, O. Toader, S. Vafaei, E. van Uitert, and M. Velander, *CFHTLenS: the Canada-France-Hawaii Telescope Lensing Survey - imaging data and catalogue products*, *Mon.Not.Roy.Astron.Soc.* **433** (Aug., 2013) 2545–2563, [arXiv:1210.8156].

[153] L. Miller, C. Heymans, T. D. Kitching, L. van Waerbeke, T. Erben, H. Hildebrandt, H. Hoekstra, Y. Mellier, B. T. P. Rowe, J. Coupon, J. P. Dietrich, L. Fu, J. Harnois-Déraps, M. J. Hudson, M. Kilbinger, K. Kuijken, T. Schrabback, E. Semboloni, S. Vafaei, and M. Velander, *Bayesian galaxy shape measurement for weak lensing surveys - III. Application to the Canada-France-Hawaii Telescope Lensing Survey*, *Mon.Not.Roy.Astron.Soc.* **429** (Mar., 2013) 2858–2880, [arXiv:1210.8201].

[154] H. Hildebrandt, T. Erben, K. Kuijken, L. van Waerbeke, C. Heymans, and other, *CFHTLenS: improving the quality of photometric redshifts with precision photometry*, *Mon.Not.Roy.Astron.Soc.* **421** (Apr., 2012) 2355–2367, [arXiv:1111.4434].

[155] J. Benjamin, L. Van Waerbeke, C. Heymans, M. Kilbinger, T. Erben, H. Hildebrandt, H. Hoekstra, T. D. Kitching, Y. Mellier, L. Miller, B. Rowe, T. Schrabback, F. Simpson, J. Coupon, L. Fu, J. Harnois-Déraps, M. J. Hudson, K. Kuijken, E. Semboloni, S. Vafaei, and M. Velander, *CFHTLenS tomographic weak lensing: quantifying accurate redshift distributions*, *Mon.Not.Roy.Astron.Soc.* **431** (May, 2013) 1547–1564, [arXiv:1212.3327].

[156] N. Benítez, *Bayesian Photometric Redshift Estimation*, *Astrophys.J.* **536** (June, 2000) 571–583, [astro-ph/9811189].

[157] L. Van Waerbeke, J. Benjamin, T. Erben, C. Heymans, H. Hildebrandt, H. Hoekstra, T. D. Kitching, Y. Mellier, L. Miller, J. Coupon, J. Harnois-Déraps, L. Fu, M. Hudson, M. Kilbinger, K. Kuijken, B. Rowe, T. Schrabback, E. Semboloni, S. Vafaei, E. van Uitert, and M. Velander, *CFHTLenS: mapping the large-scale structure with gravitational lensing*, *Mon.Not.Roy.Astron.Soc.* **433** (Aug., 2013) 3373–3388, [arXiv:1303.1806].

[158] R. Takahashi, M. Sato, T. Nishimichi, A. Taruya, and M. Oguri, *Revising the Halofit Model for the Nonlinear Matter Power Spectrum*, *Astrophys.J.* **761** (Dec., 2012) 152, [arXiv:1208.2701].

[159] T. Eifler, P. Schneider, and J. Hartlap, *Dependence of cosmic shear covariances on cosmology. Impact on parameter estimation*, *Astron.Astrophys.* **502** (Aug., 2009) 721–731, [arXiv:0810.4254].

[160] M. Kilbinger, L. Fu, C. Heymans, F. Simpson, J. Benjamin, T. Erben, J. Harnois-Déraps, H. Hoekstra, H. Hildebrandt, T. D. Kitching, Y. Mellier, L. Miller, L. Van Waerbeke, K. Benabed, C. Bonnett, J. Coupon, M. J. Hudson, K. Kuijken, B. Rowe, T. Schrabback, E. Semboloni, S. Vafaei, and M. Velander, *CFHTLenS: combined probe cosmological model comparison using 2D weak gravitational lensing*, *Mon.Not.Roy.Astron.Soc.* **430** (Apr., 2013) 2200–2220, [arXiv:1212.3338].

[161] J. Hartlap, P. Simon, and P. Schneider, *Why your model parameter confidences might be too optimistic. Unbiased estimation of the inverse covariance matrix*, *Astron.Astrophys.* **464** (Mar., 2007) 399–404, [astro-ph/0608064].

[162] C. L. Bennett, D. Larson, J. L. Weiland, N. Jarosik, G. Hinshaw, N. Odegard, K. M. Smith, R. S. Hill, B. Gold, M. Halpern, E. Komatsu, M. R. Nolta, L. Page, D. N. Spergel, E. Wollack, J. Dunkley, A. Kogut, M. Limon, S. S. Meyer, G. S. Tucker, and E. L. Wright, *Nine-year Wilkinson Microwave Anisotropy Probe (WMAP) Observations: Final Maps and Results*, *Astrophys.J.Suppl.* **208** (Oct., 2013) 20, [arXiv:1212.5225].

[163] M. Kilbinger, K. Benabed, O. Cappe, J.-F. Cardoso, J. Coupon, G. Fort, H. J. McCracken, S. Prunet, C. P. Robert, and D. Wraith, *CosmoPMC: Cosmology Population Monte Carlo*, *ArXiv e-prints* (Jan., 2011) [arXiv:1101.0950].

[164] D. Wraith, M. Kilbinger, K. Benabed, O. Cappé, J.-F. Cardoso, G. Fort, S. Prunet, and C. P. Robert, *Estimation of cosmological parameters using adaptive importance sampling*, *Phys.Rev.* **D80** (July, 2009) 023507, [arXiv:0903.0837].

[165] M. Sato, K. Ichiki, and T. T. Takeuchi, *Precise Estimation of Cosmological Parameters Using a More Accurate Likelihood Function*, *Physical Review Letters* **105** (Dec., 2010) 251301, [arXiv:1011.4996].

[166] J. N. Fry, *The Galaxy correlation hierarchy in perturbation theory*, *Astrophys. J.* **279** (Apr., 1984) 499–510.

[167] L. Fu, M. Kilbinger, T. Erben, C. Heymans, H. Hildebrandt, H. Hoekstra, T. D. Kitching, Y. Mellier, L. Miller, E. Semboloni, P. Simon, L. Van Waerbeke, J. Coupon, J. Harnois-Déraps, M. J. Hudson, K. Kuijken, B. Rowe, T. Schrabback, S. Vafaei, and M. Velander, *CFHTLenS: cosmological constraints from a combination of cosmic shear two-point and three-point correlations*, *Mon.Not.Roy.Astron.Soc.* **441** (July, 2014) 2725–2743, [arXiv:1404.5469].

[168] E. W. Kolb and M. S. Turner, *The early universe.* 1990.

[169] G. Jungman, M. Kamionkowski, and K. Griest, *Supersymmetric dark matter*, *Phys.Rept.* **267** (Mar., 1996) 195–373, [hep-ph/9506380].

[170] R. Gilmore, R. Somerville, J. Primack, and A. Dominguez, *Semi-analytic modeling of the EBL and consequences for extragalactic gamma-ray spectra*, *Mon.Not.Roy.Astron.Soc.* **422** (2012) 3189–3207, [arXiv:1104.0671].

[171] S. Ando, *Gamma-ray background anisotropy from Galactic dark matter substructure*, *Phys.Rev.* **D80** (July, 2009) 023520, [arXiv:0903.4685].

[172] Y. Rasera, R. Teyssier, P. Sizun, B. Cordier, J. Paul, et al., *Soft gamma-ray background and light dark matter annihilation*, *Phys.Rev.* **D73** (2006) 103518, [astro-ph/0507707].

[173] S. Hofmann, D. J. Schwarz, and H. Stoecker, *Damping scales of neutralino cold dark matter*, *Phys.Rev.* **D64** (2001) 083507, [astro-ph/0104173].

[174] A. Loeb and M. Zaldarriaga, *The Small-scale power spectrum of cold dark matter*, *Phys.Rev.* **D71** (2005) 103520, [astro-ph/0504112].

[175] T. Bringmann, *Particle Models and the Small-Scale Structure of Dark Matter*, *New J.Phys.* **11** (2009) 105027, [arXiv:0903.0189].

[176] T. Goerdt, O. Y. Gnedin, B. Moore, J. Diemand, and J. Stadel, *The survival and disruption of CDM micro-haloes: Implications for direct and indirect detection experiments*, *Mon.Not.Roy.Astron.Soc.* **375** (2007) 191–198, [astro-ph/0608495].

[177] V. Berezinsky, V. Dokuchaev, and Y. Eroshenko, *Remnants of dark matter clumps*, *Phys.Rev.* **D77** (2008) 083519, [arXiv:0712.3499].

[178] S. Ando and E. Komatsu, *Anisotropy of the cosmic gamma-ray background from dark matter annihilation*, *Phys.Rev.* **D73** (2006) 023521, [astro-ph/0512217].

[179] S. Camera, M. Fornasa, N. Fornengo, and M. Regis, *A Novel Approach in the Weakly Interacting Massive Particle Quest: Cross-correlation of Gamma-Ray Anisotropies and Cosmic Shear*, *Astrophys.J.* **771** (2013) L5, [arXiv:1212.5018].

[180] W. L. Kraushaar, G. W. Clark, G. P. Garmire, R. Borken, P. Higbie, V. Leong, and T. Thorsos, *High-Energy Cosmic Gamma-Ray Observations from the OSO-3 Satellite*, *Astrophys.J.* **177** (Nov., 1972) 341.

[181] C. E. Fichtel, D. A. Kniffen, and R. C. Hartman, *Celestial diffuse gamma radiation above 30 mev observed by sas-2*, *Astrophys.J.Lett.* **186** (Dec., 1973) L99.

[182] **EGRET Collaboration** Collaboration, P. Sreekumar et al., *EGRET observations of the extragalactic gamma-ray emission*, *Astrophys.J.* **494** (1998) 523–534, [astro-ph/9709257].

[183] **Fermi-LAT collaboration** Collaboration, A. Abdo et al., *The Spectrum of the Isotropic Diffuse Gamma-Ray Emission Derived From First-Year Fermi Large Area Telescope Data*, *Phys.Rev.Lett.* **104** (2010) 101101, [arXiv:1002.3603].

[184] F. Stecker and M. Salamon, *The Gamma-ray background from blazars: A New look*, *Astrophys.J.* **464** (1996) 600–605, [astro-ph/9601120].

[185] T. Narumoto and T. Totani, *Gamma-ray luminosity function of blazars and the cosmic gamma-ray background: evidence for the luminosity dependent density evolution*, *Astrophys.J.* **643** (2006) 81–91, [astro-ph/0602178].

[186] Y. Inoue and T. Totani, *The Blazar Sequence and the Cosmic Gamma-Ray Background Radiation in the Fermi Era*, *Astrophys.J.* **702** (2009) 523–536, [arXiv:0810.3580].

[187] **Fermi LAT Collaboration** Collaboration, M. Ackermann et al., *Anisotropies in the diffuse gamma-ray background measured by the Fermi LAT*, *Phys.Rev.* **D85** (2012) 083007, [arXiv:1202.2856].

[188] **Fermi-LAT Collaboration** Collaboration, A. Abdo et al., *The Fermi-LAT high-latitude Survey: Source Count Distributions and the Origin of the Extragalactic Diffuse Background*, *Astrophys.J.* **720** (2010) 435–453, [arXiv:1003.0895].

[189] M. Ajello, M. Shaw, R. Romani, C. Dermer, L. Costamante, et al., *The Luminosity Function of Fermi-detected Flat-Spectrum Radio Quasars*, *Astrophys.J.* **751** (2012) 108, [arXiv:1110.3787].

[190] J. P. Harding and K. N. Abazajian, *Models of the Contribution of Blazars to the Anisotropy of the Extragalactic Diffuse Gamma-ray Background*, *JCAP* **1211** (2012) 026, [arXiv:1206.4734].

[191] A. Cuoco, E. Komatsu, and J. Siegal-Gaskins, *Joint anisotropy and source count constraints on the contribution of blazars to the diffuse gamma-ray background*, *Phys.Rev.* **D86** (2012) 063004, [arXiv:1202.5309].

[192] **Fermi LAT Collaboration** Collaboration, M. Ackermann et al., *GeV Observations of Star-forming Galaxies with Fermi LAT*, *Astrophys.J.* **755** (2012) 164, [arXiv:1206.1346].

[193] Y. Inoue, *Contribution of the Gamma-ray Loud Radio Galaxies Core Emissions to the Cosmic MeV and GeV Gamma-Ray Background Radiation*, *Astrophys.J.* **733** (2011) 66, [arXiv:1103.3946].

[194] M. Su, T. R. Slatyer, and D. P. Finkbeiner, *Giant Gamma-ray Bubbles from Fermi-LAT: AGN Activity or Bipolar Galactic Wind?*, *Astrophys.J.* **724** (2010) 1044–1082, [arXiv:1005.5480].

[195] **Fermi-LAT Collaboration** Collaboration, M. Ackermann et al., *The Fermi Large Area Telescope On Orbit: Event Classification, Instrument Response Functions, and Calibration*, *Astrophys.J.Suppl.* **203** (2012) 4, [arXiv:1206.1896].

[196] S. Ando, E. Komatsu, T. Narumoto, and T. Totani, *Angular power spectrum of gamma-ray sources for GLAST: Blazars and clusters of galaxies*, *Mon.Not.Roy.Astron.Soc.* **376** (2007) 1635–1647, [astro-ph/0610155].

[197] S. Ando and E. Komatsu, *Constraints on the annihilation cross section of dark matter particles from anisotropies in the diffuse gamma-ray background measured with Fermi-LAT*, *Phys.Rev.* **D87** (2013), no. 12 123539, [arXiv:1301.5901].

[198] M. Cirelli, G. Corcella, A. Hektor, G. Hutsi, M. Kadastik, et al., *PPPC 4 DM ID: A Poor Particle Physicist Cookbook for Dark Matter Indirect Detection*, *JCAP* **1103** (2011) 051, [arXiv:1012.4515].

[199] M. Cirelli, P. D. Serpico, and G. Zaharijas, *Bremsstrahlung gamma rays from light Dark Matter*, *JCAP* **1311** (2013) 035, [arXiv:1307.7152].

[200] L. Bergstrom, T. Bringmann, M. Eriksson, and M. Gustafsson, *Gamma rays from heavy neutralino dark matter*, *Phys.Rev.Lett.* **95** (2005) 241301, [hep-ph/0507229].

[201] D. N. Limber, *The Analysis of Counts of the Extragalactic Nebulae in Terms of a Fluctuating Density Field. II*, *Astrophys.J.* **119** (1954) 655.

[202] R. de Putter and M. Takada, *Halo-Galaxy Lensing: A Full Sky Approach*, *Phys.Rev.* **D82** (2010) 103522, [arXiv:1007.4809].

[203] R. K. Sheth, H. Mo, and G. Tormen, *Ellipsoidal collapse and an improved model for the number and spatial distribution of dark matter haloes*, *Mon.Not.Roy.Astron.Soc.* **323** (2001) 1, [astro-ph/9907024].

[204] L. Gao, C. Frenk, A. Jenkins, V. Springel, and S. White, *Where will supersymmetric dark matter first be seen?*, *Mon.Not.Roy.Astron.Soc.* **419** (2012) 1721, [arXiv:1107.1916].

[205] K. C. Y. Ng, R. Laha, S. Campbell, S. Horiuchi, B. Dasgupta, et al., *Resolving Small-Scale Dark Matter Structures Using Multi-Source Indirect Detection*, arXiv:1310.1915.

[206] M. A. Sanchez-Conde and F. Prada, *The flattening of the concentration-mass relation towards low halo masses and its implications for the annihilation signal boost*, arXiv:1312.1729.

[207] J. F. Navarro, A. Ludlow, V. Springel, J. Wang, M. Vogelsberger, S. D. M. White, A. Jenkins, C. S. Frenk, and A. Helmi, *The diversity and similarity of simulated cold dark matter haloes*, *Mon.Not.Roy.Astron.Soc.* **402** (Feb., 2010) 21–34, [arXiv:0810.1522].

[208] G. Rodighiero, M. Vaccari, A. Franceschini, L. Tresse, O. L. Fevre, et al., *Mid- and Far-infrared Luminosity Functions and Galaxy Evolution from Multiwavelength Spitzer Observations up to z 2.5*, *aa* **515** (2010) A8, [arXiv:0910.5649].

[209] A. Petri, Z. Haiman, L. Hui, M. May, and J. M. Kratochvil, *Cosmology with Minkowski functionals and moments of the weak lensing convergence field*, *Phys.Rev.* **D88** (Dec., 2013) 123002, [arXiv:1309.4460].

[210] D. Munshi, L. van Waerbeke, J. Smidt, and P. Coles, *From weak lensing to non-Gaussianity via Minkowski functionals*, *Mon.Not.Roy.Astron.Soc.* **419** (Jan., 2012) 536–555, [arXiv:1103.1876].

[211] E. Semboloni, H. Hoekstra, and J. Schaye, *Effect of baryonic feedback on two- and three-point shear statistics: prospects for detection and improved modelling*, *Mon.Not.Roy.Astron.Soc.* **434** (Sept., 2013) 148–162, [arXiv:1210.7303].

[212] A. R. Zentner, E. Semboloni, S. Dodelson, T. Eifler, E. Krause, and A. P. Hearin, *Accounting for baryons in cosmological constraints from cosmic shear*, *Phys.Rev.* **D87** (Feb., 2013) 043509, [arXiv:1212.1177].

[213] X. Yang, J. M. Kratochvil, K. Huffenberger, Z. Haiman, and M. May, *Baryon impact on weak lensing peaks and power spectrum: Low-bias statistics and self-calibration in future surveys*, *Phys.Rev.* **D87** (Jan., 2013) 023511, [arXiv:1210.0608].

[214] T. Hamana, S. T. Colombi, A. Thion, J. E. G. T. Devriendt, Y. Mellier, and F. Bernardeau, *Source-lens clustering effects on the skewness of the lensing convergence*, *Mon.Not.Roy.Astron.Soc.* **330** (Feb., 2002) 365–377, [astro-ph/0012200].

[215] A. Geringer-Sameth and S. M. Koushiappas, *Exclusion of canonical WIMPs by the joint analysis of Milky Way dwarfs with Fermi*, *Phys.Rev.Lett.* **107** (2011) 241303, [arXiv:1108.2914].

[216] **Fermi-LAT collaboration** Collaboration, M. Ackermann et al., *Constraining Dark Matter Models from a Combined Analysis of Milky Way Satellites with the Fermi Large Area Telescope*, *Phys.Rev.Lett.* **107** (2011) 241302, [arXiv:1108.3546].

[217] **Fermi-LAT Collaboration** Collaboration, M. Ackermann et al., *Dark Matter Constraints from Observations of 25 Milky Way Satellite Galaxies with the Fermi Large Area Telescope*, *Phys.Rev.* **D89** (2014) 042001, [arXiv:1310.0828].

[218] S. Ando and D. Nagai, *Fermi-LAT constraints on dark matter annihilation cross section from observations of the Fornax cluster*, *JCAP* **1207** (2012) 017, [arXiv:1201.0753].

[219] L. Goodenough and D. Hooper, *Possible Evidence For Dark Matter Annihilation In The Inner Milky Way From The Fermi Gamma Ray Space Telescope*, arXiv:0910.2998.

[220] D. Hooper and L. Goodenough, *Dark Matter Annihilation in The Galactic Center As Seen by the Fermi Gamma Ray Space Telescope*, *Phys.Lett.* **B697** (2011) 412–428, [arXiv:1010.2752].

[221] A. Boyarsky, D. Malyshev, and O. Ruchayskiy, *A comment on the emission from the Galactic Center as seen by the Fermi telescope*, *Phys.Lett.* **B705** (2011) 165–169, [arXiv:1012.5839].

[222] D. Hooper and T. Linden, *On The Origin Of The Gamma Rays From The Galactic Center*, *Phys.Rev.* **D84** (2011) 123005, [arXiv:1110.0006].

[223] K. N. Abazajian and M. Kaplinghat, *Detection of a Gamma-Ray Source in the Galactic Center Consistent with Extended Emission from Dark Matter Annihilation and Concentrated Astrophysical Emission*, *Phys.Rev.* **D86** (2012) 083511, [arXiv:1207.6047].

[224] C. Gordon and O. Macias, *Dark Matter and Pulsar Model Constraints from Galactic Center Fermi-LAT Gamma Ray Observations*, *Phys.Rev.* **D88** (2013) 083521, [arXiv:1306.5725].

[225] K. N. Abazajian, N. Canac, S. Horiuchi, and M. Kaplinghat, *Astrophysical and Dark Matter Interpretations of Extended Gamma Ray Emission from the Galactic Center*, arXiv:1402.4090.

[226] T. Daylan, D. P. Finkbeiner, D. Hooper, T. Linden, S. K. N. Portillo, et al., *The Characterization of the Gamma-Ray Signal from the Central Milky Way: A Compelling Case for Annihilating Dark Matter*, arXiv:1402.6703.

[227] J.-Q. Xia, A. Cuoco, E. Branchini, M. Fornasa, and M. Viel, *A cross-correlation study of the Fermi-LAT γ-ray diffuse extragalactic signal*, *Mon.Not.Roy.Astron.Soc.* **416** (2011) 2247–2264, [arXiv:1103.4861].

[228] J. Diemand, M. Zemp, B. Moore, J. Stadel, and C. M. Carollo, *Cusps in cold dark matter haloes*, *Mon.Not.Roy.Astron.Soc.* **364** (Dec., 2005) 665–673, [astro-ph/0504215].